Alma Mater Studiorum
Università degli studi di Bologna

Scuola di Dottorato in Scienze Matematiche, Fisiche ed Astronomiche

DOTTORATO DI RICERCA IN ASTRONOMIA

CICLO XXVI

The evolution of massive clumps in star forming regions

Dottorando:

Andrea Giannetti

Supervisore:

Dr. **Jan Brand**

Relatore:

Chiar.ma Prof.ssa **Loretta Gregorini**

Coordinatore:

Chiar.mo Prof. **Lauro Moscardini**

Settore Concorsuale: 02/C1 - Astronomia, Astrofisica, Fisica della Terra e dei Pianeti
Settore Scientifico-Disciplinare: FIS/05 - Astronomia e Astrofisica

Esame finale anno 2014

Questa tesi è stata svolta nell'ambito delle attività di ricerca
dell'Istituto di Radioastronomia
(Istituto Nazionale di Astrofisica, Bologna)

The research presented in this thesis was carried out as part of the scientific
activities of the Istituto di Radioastronomia (INAF, Bologna)

Contents

Chapter 1

Introduction

Human beings have always had the instinct of looking up at the sky. The stars there are the fundamental building blocks that make the visible Universe the way we see it, and they are born and die over timescales much longer than the human life span; thus the celestial sphere may appear to the eye as static and immutable for thousands of years. However, though stars were certainly formed in large numbers in the past, star formation is occurring even now in our own Galaxy. To understand that star formation is a process active even today took a long time, and this idea did not come up until the middle of the last century (Ambartsumian 1947, 1949), because stars are born in the densest parts of molecular clouds, and the whole process is hidden from view by the very same gas and dust out of which they are formed. To penetrate this obscuring curtain we must use longer wavelengths than our eye is able to perceive.

The effort to unveil what happens behind this curtain is well motivated: not only do stars determine how galaxies appear to us, but they are also crucial for life. On the one hand, within them almost all the elements heavier than helium are formed and then released into the interstellar medium in the final phases of their lives; on the other hand, complex organic molecules are commonly observed in sites of active star formation. Among the complex species detected in interstellar space there is the simplest sugar, glycolaldehyde (e.g., Hollis et al. 2000; Beltrán et al. 2009), a precursor of ribose, which forms part of the backbone of RNA. Last but not least, star formation is connected to the formation of planetary systems like the Solar system (e.g., Williams & Cieza 2011, for a review on proto-planetary disks). Thus, in the end, understanding the process of star formation has deep implications for understanding the formation of the Earth, how life developed here and ultimately whether the conditions of the Solar system are unique, or quite

common in the Universe.

1.1 Interstellar Medium

Stars. Planets. These are the first things that come in mind when one thinks of our Galaxy. However, they occupy only a minor fraction of space in the Milky Way; the rest, the large volume between stars, is filled with diffuse gas, dust and radiation, generally referred to as the Interstellar Medium (ISM). The first indication of its existence was the presence of dark patches devoid of stars compared to nearby areas, in the photographic atlas of the Milky Way (Barnard et al. 1927). Since then, the ISM has been observed both in absorption and emission, in the continuum and in atomic and molecular lines.

The quantity and state of gas contained in a galaxy has relevant effects on its appearance, especially through star formation. The quantity of gas as a fraction of baryonic mass varies strongly between different types of galaxies and also amongst galaxies of the same type. Typical values range from $\sim 1\%$ for elliptical galaxies, to $\sim 10\%$ for spirals and even more for irregular galaxies. The ISM is mainly composed of hydrogen, while helium and metals (in the "astronomical" sense, i.e. all elements heavier than helium) represent respectively $\sim 10\%$ and $\sim 1\%$ (in number) of the atoms. Despite their low abundance, metals are crucial for the physical and chemical evolution of the interstellar matter (through heating & cooling).

The ISM is characterised by a wide range of temperatures and densities, and it can be both ionised and neutral. Because of this, the ISM is usually divided in three different states or phases: hot, warm and cold, according to its temperature. The typical temperature of each phase is such that they are in approximate pressure equilibrium. However, regions that are not in pressure equilibrium clearly exist, such as HII regions, that are overpressurised and expanding, or molecular clouds, that may be self-gravitating. The ISM phases are also classified according to their state of ionisation. Therefore, as a first approximation, the ISM can be separated into: hot ionised medium, warm ionised/neutral medium and cold neutral medium. The typical properties of these distinct phases are summarised in Table 1.1.

This simple picture of discrete ISM phases is complicated by turbulence, continuously mixing the interstellar matter, and, in some cases, thermal instability becomes a second order effect. The efficiency of turbulence in turning discrete phases into a continuum is still matter of debate (see, e.g., Audit & Hennebelle 2008; Vazquez-Semadeni 2009).

Table 1.1: Physical properties of ISM phases, from Draine (2010) and Hennebelle & Falgarone (2012).

Phase	Temperature (K)	Density (cm^{-3})	Filling factor
HIM	$> 3 \times 10^5$	4×10^{-3}	≈ 0.5
WIM & HII regions	$3 \times 10^3 - 10^4$	$0.3 - 10^4$	≈ 0.1
WNM	$500 - 8 \times 10^3$	$0.3 - 0.6$	≈ 0.4
CNM[(1)]	100	30	≈ 0.01
CNM[(2)]	$10 - 50$	10^{3-6}	$\approx 10^{-4}$

Notes. [(1)] Diffuse clouds; [(2)] Molecular clouds

1.2 Molecular clouds

The vast majority of the molecular gas ($\sim$ 80% in the Milky Way) resides in giant cloud complexes. The filling factor of molecular gas is very low, i.e. the fraction of volume occupied by molecular clouds is very small compared to that occupied by atomic gas (see Table 1.1). However, these clouds are also the densest component of the interstellar medium, accounting for a significant fraction ($\sim$ 13%) of the mass of the ISM ($\sim 7 \times 10^9$ $M_\odot$ in the Milky Way; Draine 2010). The typical properties of molecular clouds are shown in Table 1.2. The bulk of molecular gas is usually very cold, with temperatures around 10 – 20 K. Molecular rotational transitions may have very low energies above the fundamental state; CO, for example, has the lowest rotational transition only at 5.5 K above the ground state, and can thus be easily excited even in the very cold environments of molecular clouds, that therefore appear bright in some molecular lines. The line emission from molecules critically depends on the physical properties of the emitting medium, and one can use their emission to infer the conditions of the gas, such as its temperature and density.

The molecular gas is embedded in a more diffuse, atomic medium, which partially shields the cloud from radiation, allowing the formation of molecules. In fact, molecules are always observed above a certain critical value of visual extinction A_V ($\approx$ 3 mag, Tielens & Hollenbach 1985). The linear sizes of the atomic envelopes are typically several times larger than those of the embedded molecular complexes, with masses that can be comparable to those of the molecular gas (Blitz 1993).

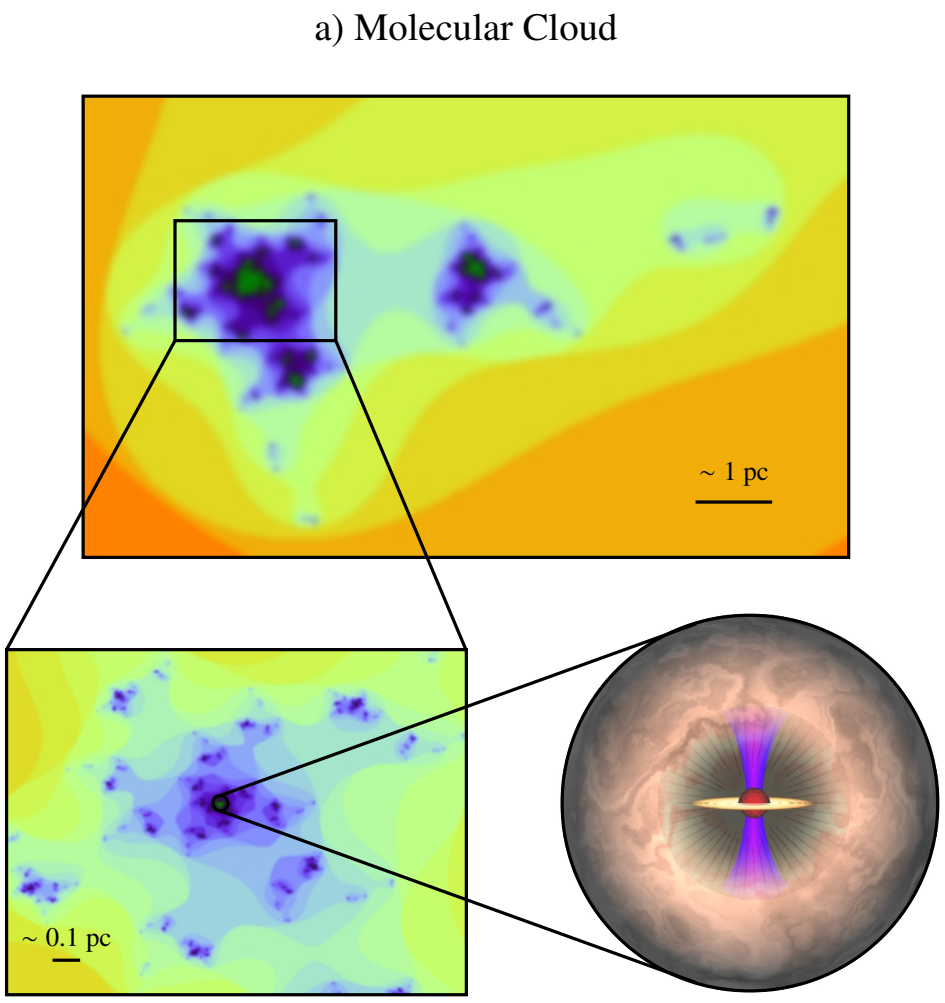

Figure 1.1: Clumpy structure of a molecular cloud. The panels show different spatial scales: a) cloud, b) clump, and c) core and its embedded protostar. In a) and b) the linear scale is indicated in the bottom left or right corner.

Table 1.2: Physical properties of molecular clouds complexes and their components. The columns show typical values of the average particle number density, size, mass, linewidths and extinction in the optical, respectively. Adapted from Draine (2010).

Category	$n_{\rm tot}$ ($\rm cm^{-3}$)	Size (pc)	M ($\rm M_\odot$)	Linewidth ($\rm km\ s^{-1}$)	A_V (mag)
GMC complex	50 – 300	25 – 200	10^5 – $10^{6.8}$	4 – 17	3 – 10
Dark Cloud Complex	10^2 – 10^3	4 – 25	10^3 – $10^{4.5}$	1.5 – 5	4 – 12
GMC	10^3 – 10^4	2 – 20	10^3 – $10^{5.3}$	2 – 9	9 – 25
Dark Cloud	10^2 – 10^4	0.3 – 6	5 – 500	0.4 – 2	3 – 15

Figure 1.1 illustrates that giant molecular clouds are highly structured entities (e.g., Blitz & Williams 1999), showing a hierarchical structure. Each cloud typically contains several dense and compact regions of size of the order of 1 pc, called molecular *clumps*. The space between the various clumps is filled with lower density gas. From observations we know that a fraction of this material is certainly molecular, while the remainder is atomic, with a higher temperature (20 – 40 K) with respect to the molecular component. The inter-clump gas represents only a minor fraction of the mass of the complex. Clumps are easily detectable at mm wavelengths through optically thin dust emission or molecular transitions. Moving to smaller spatial scales, clumps, like clouds, are not homogeneous. The smallest and densest regions in a clump are called *cores*. They have sizes of the order of 0.1 pc and they are often sites of active star formation, as revealed by the presence of embedded young stellar objects (YSOs) visible as point sources at infrared (IR) wavelengths.

1.2.1 Dust

Interstellar dust is the main source of extinction at long wavelengths, due to absorption or scattering of non-ionising photons; it dominates the Spectral Energy Distribution (SED) of the ISM for wavelengths longer than that of the Lyα line (λ = 1215.67 Å), shortwards of which H ionisation occurs. In fact, the grains absorb photons from the far-UV to the visible, and re-emit them at IR wavelengths.

The IR emission of diffuse interstellar matter shows two clear components, reflecting a real difference in the grain size distribution. These two components have different temperatures: one is cold, with a temperature typically around 15 – 20 K,

while the other is hot, with $T \sim 500-1000$ K. The cold component is due to thermal emission from large grains (~ 0.1 μm). These are in radiative equilibrium with the interstellar radiation field and self-radiate according to the Planck formula modified by the grain emissivity. The second component is generated, on the other hand, by very small grains (< 50 Å) and Polycyclic Aromatic Hydrocarbons (PAHs), that absorb a single far-UV photon, reaching temperatures of approximately 500 – 1000 K, and after which they rapidly re-radiate the energy at mid-IR and near-IR wavelengths.

Dust grains also play a very important role in the chemistry of the ISM. In fact, they offer a surface where atoms can accrete, encounter and react, redistributing the excess energy to the grain itself. This makes it possible for species like H_2 to be formed much more easily in the interstellar space, because grains act as catalysts, thus making the reactions through which molecules are formed faster than those that happen in the gas phase. Furthermore, the dust competes with the gas to absorb far-UV photons. This is particularly relevant in molecular clouds, where dust shields the molecules from photons that can destroy them, in addition to the self-shielding effect (i.e. the molecules at the edge absorb the dissociating photons, protecting those deeper in the cloud) of some molecules such as H_2 or, to a lesser degree, CO.

Dust also controls the abundances of metals in the gas phase, through accretion of these atoms onto the grains and destruction of the dust particles. A visible effect of these processes is, for example, the depletion of heavy elements in the interstellar medium, especially of those capable of forming refractory solids. The issue of grain composition has been widely debated and it is still not completely certain. It seems, however, that silicates and graphite or amorphous carbon are important components of interstellar dust.

1.3 Star formation

How molecular clouds are formed is still matter of debate; on the one hand they may be long-lived entities, supported against collapse by magnetic fields (e.g., Shu et al. 1987; Lada & Kylafis 1991) or, on the other hand, they can be transient structures, like atmospheric clouds (e.g., Glover & Mac Low 2007).

In Sect. 1.2 we saw how molecular clouds are not homogeneous entities, but present a significant substructure (cf. Fig. 1.1 and 1.2; a sketch and real data, respectively). Dense and filamentary structures are commonly observed within giant molecular clouds (e.g., Bally et al. 1987; Mizuno et al. 1995). These

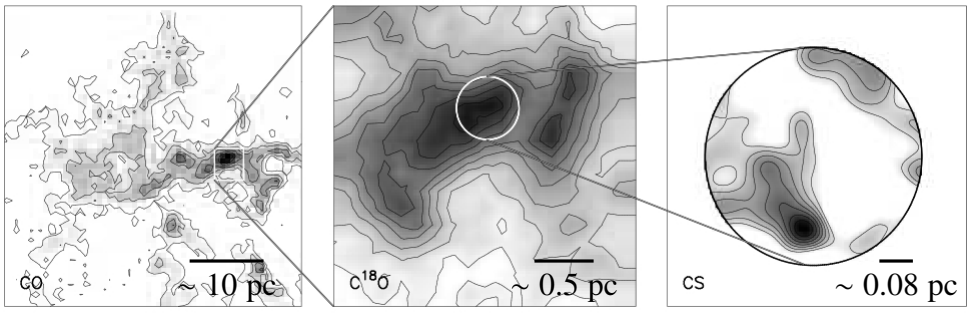

Figure 1.2: Hierarchical structure of a cloud as observed in real data (Rosette cloud). The panels show a representative view of clouds, clumps and cores, respectively. Different tracers are used to make the different scales stand out: CO for the large-scale structure of an entire cloud, the optically thin $C^{18}O$ to isolate the column density peaks corresponding to clumps and the high density tracer CS to identify cores, the densest regions within the clumps. The Figure is taken from Blitz & Williams (1999).

structures in turn host clumps, out of which entire star clusters are formed, and cores, forming a single star or a small multiple stellar system.

For stars with a final mass above ≈ 8 $M_\odot$ (see Sect. 1.3.2) the contraction timescale of the protostar is shorter than the time needed to accrete all of its mass. This changes the evolution of the object with respect to its lower-mass counterparts, and therefore in the following we make a distinction between the formation of low- and high-mass stars.

1.3.1 Low-mass star formation

Solar-mass stars form following a (now) well-known sequence of evolutionary stages that can be easily observed in nearby molecular clouds. A classification of the evolutionary stages based on the SED slope at near-IR and mid-IR wavelengths was developed by Lada (1987), and shown in Fig. 1.3.

Figure 1.3 also shows a sketch of these phases, from a dense core within a molecular cloud to the "naked" star. The evolutionary phases can be summarised as follows:

1. **Prestellar —** Not all cores in a cloud are destined to collapse to form a star. Those that have the "right" initial conditions to permit collapse (i.e. they are

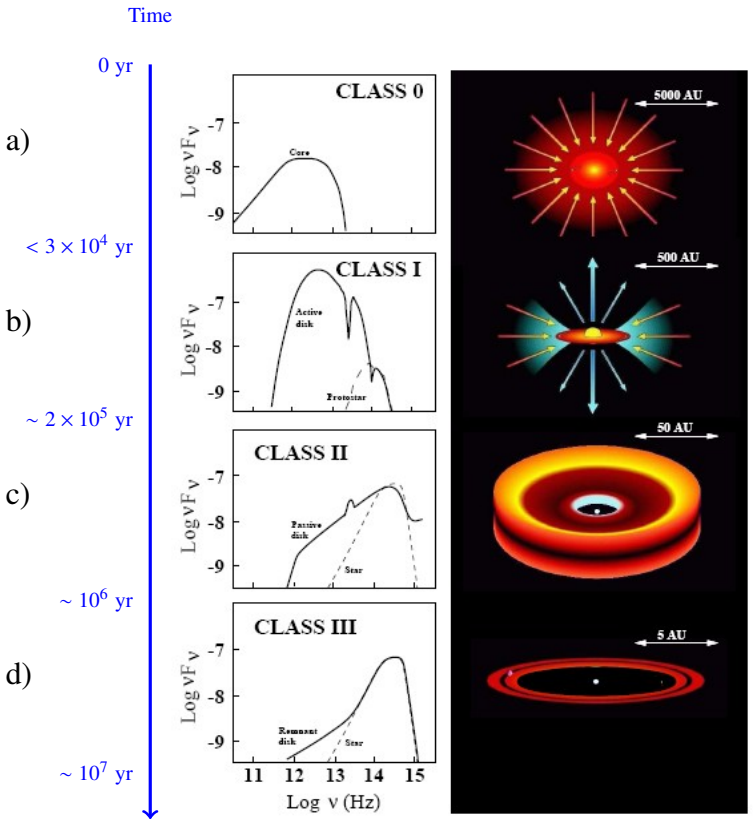

Figure 1.3: Spectral Energy Distributions (left) and sketch of the circumstellar environment (right), for Classes 0-III (see text for a description). Taken from Isella (2006).

or will become gravitationally unstable) are called prestellar cores. They are quiescent objects, made up of dense and cold material, typically embedded in an envelope of less dense gas. The cores are contracting, thus progressively increasing their density (this phase is not shown in Fig. 1.3).

2. **Class 0 —** A core with a sufficiently high density collapses under the action of gravity, marking the initial act of the star formation process. The regions with higher density become unstable first, and the collapse proceeds inside-out, progressively including material from more external regions in the cocoon, and accreting it onto the central object, increasing its mass. Any angular momentum from the original cocoon is conserved, increasing its

rotation velocity as the radius shrinks, and giving rise to flattened structures. Molecular outflows perpendicular to the axis of rotation have been observed already in these stages (e.g., Saraceno et al. 1996; Bourke et al. 2005), implying that the outflow phenomenon appears very early in the process of star formation, and is directly linked to mass accretion. In fact, outflows help to remove angular momentum, thus allowing/facilitating accretion. Objects in such an early evolutionary stage are visible only at mm-/far-IR wavelengths (cf. panel (a) of Fig. 1.3).

3. **Class I —** The collapse of the core proceeds, making the density in the central parts increase so much that the material becomes opaque to its own infrared radiation. This causes the temperature to rise steadily, and the material is eventually dissociated and ionised. At this point the collapse has halted in the central regions, where a protostellar nucleus can be found, whose material is supported by thermal pressure. The material surrounding the embryo is now arranged in a circumstellar accretion disk, that continues accreting from the envelope. The protostellar nucleus is in turn accreting material from the disk; part of the angular momentum of the material is dissipated through a collimated bipolar outflow, allowing the gas to fall onto the protostar. The central object is still deeply embedded in a molecular and dusty envelope, and its emission is thus heavily extincted. From an observational point of view, disks, outflows and jets can be seen, e.g., through molecular line emission. During this stage, the protostar will become visible at near-IR wavelengths (cf. panel (b) of Fig. 1.3); it has a strong near-IR excess, mainly caused by the emission of the disk. This can be qualitatively reproduced modelling the disk as a superposition of black-bodies with different temperatures.

4. **Class II —** After $\sim$ few $\times 10^5$ yr most of the surrounding material has joined the circumstellar disk and the central object can be seen also in the optical. Mass accretion onto the protostar is still continuing. Classical T-Tauri stars are in this evolutionary stage. Class II objects still show signs of accretion and have a near-IR excess (cf. panel (c) of Fig. 1.3).

5. **Class III —** The material in the disk is slowly consumed (being accreted onto the central object or expelled by e.g. outflows) thus reducing the mass accretion. The central object does not show any near-IR excess any more (cf. panel (d) of Fig. 1.3). Due to the strong magnetic field of the protostars, they are much more luminous in X-rays than main sequence stars (e.g., Feigelson & Montmerle 1999) of the same mass.

6. **Main Sequence —** After $\sim 10^7$ yr H-burning is initiated: the star reaches the zero age main sequence (ZAMS), the disk is completely evaporated and a planetary system may have formed from the disk. At this point, the radiation from the newly-formed star comes entirely from the stellar photosphere, and the star is visible in the optical.

1.3.1.1 Mass-Luminosity diagram

The evolutionary sequence identified in the low-mass regime (class 0-III, see Sect. 1.3.1) on the basis of the objects' spectral slope in the IR was taken a step further by Saraceno et al. (1996). The authors collected and classified a sample of objects from class 0 to class II, and then constructed a diagnostic diagram comparing the mass of the circumstellar envelope and the total luminosity of the source.

Saraceno et al. (1996) show that classes 0 to II are found in different regions of the diagram (cf. Fig. 1.4, grey symbols and lines). For a given mass, less evolved objects have a lower luminosity. The evolution of a protostar in the low-mass regime is controlled mainly by its mass, that determines the total luminosity L, and by the quantity of circumstellar material M. M and L can be directly derived from the observations, and their combination provides a straightforward method to determine the evolutionary phase of a low-mass protostar. In the diagram, time increases in the vertical direction at first and then from right to left.

Molinari et al. (2008) extended this method to the high-mass regime (Fig. 1.4, black symbols and lines), finding that the mass-luminosity plot may also be used to infer the evolutionary stage of massive objects. In Fig. 1.4 black open circles show sources in the earliest evolutionary stage, and progressively more evolved objects are indicated by filled circles, asterisks and pluses. The evolutionary phase of the sources is inferred by their mm- and IR properties (see Chapter 3), and with the models described in Robitaille et al. (2006) and Robitaille et al. (2007). The curves represent the evolution of clumps with different initial envelope masses. Time evolves as in the low-mass case, increasing first in the vertical direction, and then from right to left (see also Sect. 3.6.1). The black solid line is the best fit to the sources likely hosting a ZAMS star. Whereas low mass-stars may form in isolation and can be relatively nearby, high-mass stars virtually always form in clusters (cf. Sect. 1.3.2) and since they are typically at larger distances due to their rarity, one cannot reach the same spatial resolution, and confusion with other sources in the cluster is an issue. Therefore, in this case, the luminosity and the mass are typically those of an entire high-mass star-forming region, rather than of

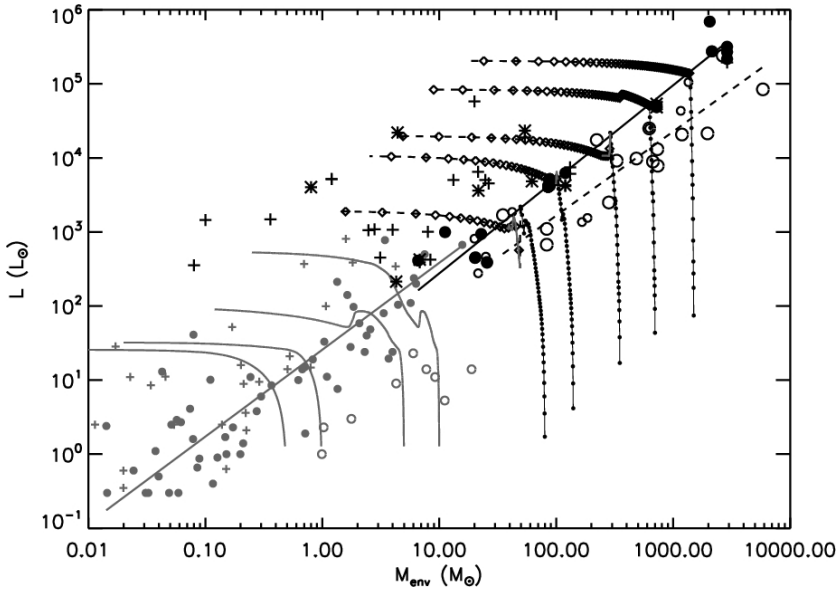

Figure 1.4: Mass-Luminosity diagram for low- (grey) and high-mass (black) regimes. Lines and symbols in grey are from Saraceno et al. (1996), for the low-mass regime. Class 0, I and II sources are represented respectively by open circles, filled circles and crosses, with the solid grey line representing the log-log linear fit to the Class I source distribution. The grey curves show the protostellar evolution in the low-mass regime, for different values of the final stellar mass. The black lines and symbols represent the sources in Molinari et al. (2008), for the high-mass regime; open circles show sources in the earliest evolutionary stage, and progressively more evolved objects are indicated by filled circles, asterisks and pluses. The curves represent the evolution of clumps with different initial envelope masses. The black solid line is the best fit for those clumps likely hosting a Zero Age MS star. The black dashed line is the log-log fit to the less-evolved massive sources. In both regimes, time increase in the vertical direction at first and then from right to left. Taken from Molinari et al. (2008).

a single (proto)star.

1.3.1.2 Depletion and deuteration in low-mass starless cores

Low-mass starless cores have been studied extensively, with a high spatial resolution thanks to their general nearness. These observations made it possible to derive the physical structure as a function of radius in the core; their column density-, volume density- and temperature at different radii are now well known, making it possible to study the chemical properties of the cores in detail.

At the low temperatures found in dense and quiescent regions of the clouds, the molecules can stick onto the dust grains, forming an ice coating (see e.g., Caselli 2011). One can calculate the rate at which molecules stick onto the grains, following the expression:

$$k = \sigma v(T) n_g S, \tag{1.1}$$

where σ is the cross section of the grains, $v(T)$ is the mean value of the Maxwellian function describing the velocity distribution of the particles in a gas with temperature T, n_g is the volume density of the grains and S is the sticking probability. For CO at 10 K, and assuming $S = 1$ in these conditions (meaning that each time a gas particle hits a grain it sticks to it), the adsorption (or freeze-out) timescale $\tau_{\rm ads}$ is (see Bergin & Tafalla 2007):

$$\tau_{\rm ads} = 1/k \approx \frac{5 \times 10^9}{n({\rm H_2})[{\rm cm^{-3}}]} \ {\rm yr}, \tag{1.2}$$

shorter than the free-fall timescale for $n({\rm H_2}) \gtrsim 10^4$ cm^{-3}. Bacmann et al. (2002) suggest that, from the comparison of CO and dust emission, the freeze-out becomes important for densities of molecular hydrogen above $\sim 3 \times 10^4$ cm^{-3}.

Dust emission traces well the H_2, thus identifying the core and the location where column density is maximal. Clear differences are found in the behaviour of carbon- and sulphur-bearing molecules and nitrogen hydrides comparing the distribution of the emission of these different classes of molecules with that of the dust in the (sub-)mm regime. It is commonly found that the abundance of C- and S-bearing molecules tend to rapidly decrease towards the centre in low-mass starless cores (Caselli et al. 1999; Bergin et al. 2002; Tafalla et al. 2002; Zhang et al. 2009), where the density is higher and the temperature is lower, while nitrogen hydrides have constant- or much more slowly decreasing abundances. Figure 1.5 shows a clear example of this situation: on the one hand the $C^{18}O$ emission is

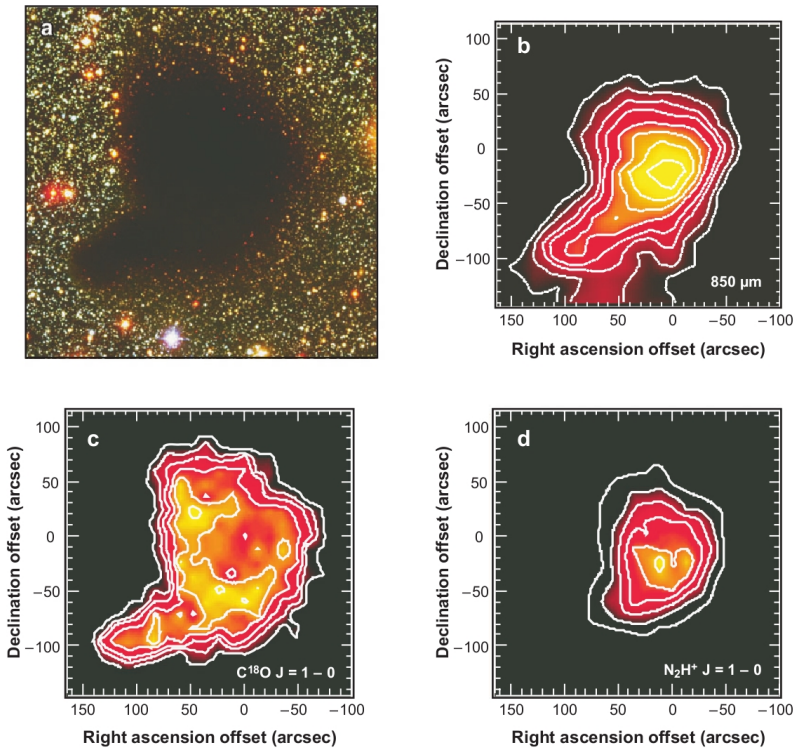

Figure 1.5: Multiwavelength image of the molecular core B68, taken from Bergin & Tafalla (2007). The top left panel shows the obscuration region observed in the optical. The top right panel shows the dust continuum emission at 850 μm. The bottom panels show the integrated molecular emission of $C^{18}O(1-0)$ (left) and $N_2H^+(1-0)$ (right). The different spatial distribution is clear, with $N_2H^+(1-0)$ closely following the emission profile of the dust, while $C^{18}O$ shows a ring-shaped emission around the dust sub-mm emission peak.

ring-like, with a hole coincident with the peak of dust emission (and thus of the column density), on the other hand the emission of N_2H^+ closely resembles that of the dust. The different behaviour of these classes of molecules depends on the effects of the removal of CO from the gas phase, that triggers important changes in the chemistry of the core. An additional explanation may be that the atomic N, which has a low probability of sticking to grains (≈ 0.1, Flower et al. 2006) is only slowly converting into molecular nitrogen (Hily-Blant et al. 2010), which has similar sticking coefficient and binding energy as CO (Öberg et al. 2005; Bisschop

et al. 2006). In particular, CO has a dominant role in the destruction of the N_2H^+ molecule (Bergin & Tafalla 2007, and references therein). Thus, the abundance of this molecule (and of ammonia, that is formed from N_2H^+; see e.g. Aikawa et al. 2005) increases where CO is depleted (e.g., Jørgensen et al. 2004). As long as N_2 does not reach abundances below those of N_2H^+ and NH_3, they can still form and trace the dense gas where other molecules have a large degree of depletion, i.e. very reduced abundances. The same happens for deuterated molecules, which can become more abundant even by several orders of magnitude, with respect to normal conditions (e.g., Roueff et al. 2000; Loinard et al. 2001, 2002). As deuterium bonds are stronger than bonds with the most common hydrogen isotope, ion-molecule reactions are thought to be at the basis of these increased abundances (Millar et al. 1989). The presence of the ions at the beginning of the reactions is ensured by the cosmic rays ionisation. The driving reaction for deuterium chemistry in the cold and dense environments of starless molecular cores is:

$$H_3^+ + HD \leftrightarrow H_2D^+ + H_2 + 230\ K, \tag{1.3}$$

which is slightly exothermic in the forward sense, favouring the formation of H_2D^+ at 10 K, and increasing the deuteration of species involved in ion-molecule chemistry. Moreover, considering also the following reactions

$$H_2D^+ + HD \leftrightarrow D_2H^+ + H_2 + 180\ K \tag{1.4}$$

$$D_2H^+ + HD \leftrightarrow D_3^+ + H_2 + 230\ K, \tag{1.5}$$

one can reproduce the observed abundances of doubly or triply deuterated species (Roueff et al. 2000; Lis et al. 2002). Finally, because CO is the primary destroyer for H_3^+ and H_2D^+, the ratio between deuterated- and non-deuterated species may increase even more (e.g., Caselli et al. 2002; Bacmann et al. 2003).

1.3.2 High-mass star formation

Whereas for low-mass stars the formation process is quite well-understood both theoretically and observationally, the analogous process in the high-mass regime is still far from being clear on both fronts, despite the attention dedicated to it in the last decades. This is because of several reasons. First of all, from an observational point of view, high-mass stars are very rare compared to low-mass stars; for

example, assuming a Salpeter IMF, there are 100 times more stars like our Sun than there are stars with $M_* = 30$ M$_\odot$, and they have very different lifetimes τ with $\tau(M_* = 1\ \mathrm{M}_\odot) \approx 2000 \times \tau(M_* = 30\ \mathrm{M}_\odot)$. Therefore, at any given time there are about $2{\times}10^5$ more stars of 1 M$_\odot$ than there are stars of 30 M$_\odot$; the luminosity is still dominated by the massive stars, because $L(M_* = 30\ \mathrm{M}_\odot) \approx 10^5 \times L(M_* = 1\ \mathrm{M}_\odot)$. Because of their rarity, massive stars are typically found at larger distances than their low-mass counterparts, and therefore it is very difficult, if not impossible, to match the spatial resolution reached in the study of low-mass objects. Secondly, the relevant phases of the process are very short-lived with respect to the low-mass regime. The characteristic timescale over which a protostar contracts towards the conditions of temperature and density that permit hydrogen fusion is the Kelvin-Helmholtz timescale:

$$\tau_{KH} = \frac{GM_*^2}{R_* L_*}, \tag{1.6}$$

where M_*, R_* and L_* are the mass, radius and luminosity of the protostar, respectively. The Kelvin-Helmholtz timescale equals the accretion timescale for stars that reach final masses of ≈ 8 M$_\odot$, the exact value depending on the accretion rate. For high-mass stars the Kelvin-Helmholtz timescale is shorter than the accretion timescale, therefore they start hydrogen fusion while still accreting large quantities of material and a significant fraction of their final mass. Because of the short duration of these phases, they take place while still deeply embedded in molecular and dusty material, making long-wavelength observations ($\lambda \gtrsim$ mid-/far-IR) the only way to penetrate this cocoon and investigate the process directly. An additional complication is that massive stars virtually always form in clusters (Lada & Lada 2003), where the environment is complex, usually with several OB- and hundreds, if not thousands of low-mass stars. The limited spatial resolution can thus be a critical issue in such studies, and powerful interferometers are needed to unveil the details of the process for single star-forming units.

From the theoretical point of view, the problem of star formation in general is complex, because of the very large number of physical processes that must be taken into account, such as heating and cooling of gas and dust, magnetic fields, gas-phase and solid-phase chemistry, dust properties and evolution, accretion from the envelope onto the disk and from the disk onto the star. Even more so for the high mass regime, where strong mechanical- and radiative feedback have a dominant role and cannot be neglected. When the accreting objects start the H-burning, their luminosity becomes so high that it exerts a radiation pressure on the dust grains, which in turn are coupled to the gas (Wolfire & Cassinelli 1987), large enough

that it is capable of halting accretion, if it proceeds in a spherically symmetric way. This means that one cannot describe the mass accretion in high-mass stars under the simplifying approximation of spherical symmetry. The models in this regime also lack many observational constraints for the reasons explained above.

1.3.2.1 Evolutionary phases of high-mass stars

Despite all the difficulties on both observational and theoretical fronts, there is much we do know of the process of massive star formation. High-mass stars are short-lived (cf. 1.3.2) and they spend a significant part of their life ($\gtrsim 10\%$) within the molecular material from which they originated. The availability of radio-, mm- and IR facilities allows one to study these embedded phases. An important step was the identification of infrared-dark clouds (IRDCs; Perault et al. 1996; Egan et al. 1998) as the most promising locations for the next generation of massive stars in our Galaxy.

Based on sub-mm-, IR- and radio observations, different evolutionary phases can be broadly distinguished:

1. The densest, coldest and most compact regions within IRDCs are likely very good places to study the initial conditions of high-mass stars/clusters formation (e.g., Menten et al. 2005). In order to study the physical conditions of the medium before star formation begins, one has to identify *starless cores*. However, this is not straightforward, as optical depth (for molecular lines) and/or extinction (for IR observations) may make embedded protostars undetectable. Observations at mm-, sub-mm and far-IR wavelengths are still among the best probes to derive the physical conditions of the gas. Some molecular line- and continuum observation were carried out to derive the physical properties of apparently starless sources (e.g., Rygl et al. 2010, 2013; Sánchez-Monge et al. 2013b). These objects have large masses and high column densities of molecular hydrogen, of the order of few $\times 10^{2-3}$ $M_\odot$ and 10^{22-24} cm^{-2}, respectively; volume densities of the order of 10^5 cm^{-3}, temperatures in the range $10-20$ K, and linear sizes ~ 0.5 pc (see Zinnecker & Yorke 2007, for a summary). A theoretical threshold of surface density $\Sigma = 1$ g cm^{-2} was proposed by Krumholz & McKee (2008) for massive star formation to occur, but some observational evidence, such as the detection of massive molecular outflows, methanol masers and UCHII (López-Sepulcre et al. 2010; Urquhart et al. 2013a,b), shows that lower values of Σ in high-mass clumps ($\sim 0.05 - 0.3$ g cm^{-2}) seem to be sufficient for the formation

of massive stars to initiate. A detailed study of massive starless clumps and cores was carried out by Butler & Tan (2012). This work suggests that starless sources may have lower Σ (typically $0.2 - 0.3$ g cm^{-2}) than more evolved sources where high-mass stars are already present, studied in, e.g., Mueller et al. (2002).

2. The so-called *Hot Core phase* is characterised by the presence of high abundances of complex organic molecules in the gas phase, which can be readily observed at mm-/sub-mm wavelengths. Because of their complex structure, these molecules usually have several transitions very close in frequency, which can be observed simultaneously. Using rotation diagrams (Goldsmith & Langer 1999) the gas temperature can be derived, and it is found to be high ($\sim$ 100 K); these objects also have large masses and small sizes ($M \sim 10 - 1000$ M$_\odot$, $R \lesssim 0.1$ pc; Cesaroni 2005, and references therein). It is commonly thought that several complex organic molecules are formed on the grain surfaces (see Herbst & van Dishoeck 2009, for a review), and then evaporated in the gas phase by the energetic output of the embedded object(s). Hot molecular cores are usually associated with maser (CH_3OH, H_2O) activity (Cesaroni 2005).

3. As time proceeds, the massive star(s) produce small pockets of ionised gas, visible in radio continuum observations (van der Tak & Menten 2005), commonly referred to, depending on their properties (size and density), as *hyper- or ultra- compact H*II (HC/UCHII) *regions* (Kurtz 2002). The ionised material is still confined close to the star by its gravitational attraction. HCHII regions likely represent an individual massive star photoevaporating its disk (e.g., Keto 2007), while UCHII are produced when diskless massive stars ionise the material of the envelope that surrounds them (Hoare et al. 2007).

4. The last phase includes the *compact- and classical H*II *regions*, where the gas is usually ionised by the combined action of several massive stars, and where the ionised material expands hydrodynamically as a whole. Molecules are dissociated and the cloud is dispersed revealing the embedded cluster (Carpenter et al. 1993; Testi et al. 1998; Massi et al. 2003, 2006). At this point a gravitationally bound cluster or an unbound OB association is visible in the sky even at optical wavelengths.

From the theoretical side, three different mechanisms have been proposed to describe the process of formation of massive stars: monolithic collapse, competitive accretion and stellar mergers.

- The *monolithic collapse* scenario (e.g., McKee & Tan 2003) is essentially a scaled-up version of low-mass star formation, in terms of the general scheme. The gas that will be accreted onto the central star starts as gravitationally bound in a massive core, the overdense region possibly generated by turbulence. This structure collapses and the material falls onto the central object through an accretion disk, transferring the angular momentum towards its outer regions. The presence of an accretion disk around a forming high-mass star makes it possible to overcome the difficulties connected to the stellar feedback in the case of spherical accretion. The energetic output of the massive star evacuates cavities in the polar direction (perpendicular to the disk), through which the photons can escape. On the other hand, the feedback removes only a small quantity of gas from the disk, not sufficient to prevent the inward flow of material within the disk. One (of several) possibility to trigger the rapid transfer of material from the disk to the massive object are tidal effects of nearby stars, which could explain why massive stars are commonly found in multiple systems (e.g., Mason et al. 1998). Outside of the disk evaporation radius (i.e. where the sound speed is equal to the escape velocity) the accretion disk is photoevaporated on a timescale of $\sim 10^5$ yr, and the interplay between the evaporation and the accretion sets the final mass of the star, and it may even set the upper limit for the stellar masses (Zinnecker & Yorke 2007).

- Contrary to the case of monolithic collapse, in the *competitive accretion* scenario (e.g., Bonnell et al. 2001) the gas that will eventually be accreted onto a star is not gravitationally bound to it. The build-up of the material can thus occur during the process of star formation, and not before its beginning, as for the monolithic collapse. From high-mass clumps, several low-mass seeds are formed through fragmentation. All seeds are similar at the time of their formation: their evolution (and thus the final mass of the star) is set by how "fortunate" a seed is; the most lucky embryos have an easy way to success, and will likely become massive stars. The first condition that is important for the seed's growth in mass is the location at which the seed is born: if the protostellar embryo is formed in a privileged place (such as the bottom of the clump's potential well) where more material is available for accretion, its growth may be significantly enhanced, increasing the final mass of the star. The seeds that were most successful in accreting material with respect to the average object, progressively increase even more their ability to gain mass: the region from which a protostar may accrete material

(its accretion domain) gets larger with its current mass, due to the increased gravitational attraction of the object. As the embryos grow in mass, their accretion domains start to overlap, and they have to compete for the material still available for accretion, from which the "competitive accretion" scenario derives its name. For a protostar to become a massive star it has to be in favourable conditions at all stages, explaining why high-mass stars are so rare. In this scenario massive stars must always be surrounded by lower-mass objects, formed by all the remaining "not-as-lucky" embryos (Bonnell et al. 2003), and massive starless cores should not exist. For larger clump masses, more material from the cloud is affected and directed towards the forming stars, increasing the reservoir of gas that can be accreted onto the stars. The competitive accretion scenario presents a natural way to explain the power-law shape of the IMF, as shown by Bonnell et al. (2007).

- Finally, in the *stellar mergers* scenario, massive stars are formed in the collision of lower-mass sources. This was one of the first attempts to overcome the problems related to the accretion feedback (e.g., Bonnell et al. 1998). However, stellar mergers are rare, and thus may be important only in the densest regions of tightly-packed clusters, especially for the formation of the most massive stars.

The processes described above are not mutually exclusive, and all of them may happen, depending on the environmental conditions.

1.4 The influence of high-mass stars on their environment

High-mass stars have a completely different internal structure (i.e. with a convective core and a radiative envelope, whereas low-mass stars have a radiative core and a convective envelope, like our Sun), they emit a significant part of their energy output at ultraviolet wavelengths, and they end their lives as supernovae. Stars with $M \gtrsim 8$ M$_\odot$ reach temperatures and densities high enough to start the fusion of helium into carbon in a weakly- or non-degenerate environment, by means of the triple-α reaction. Stars with masses $M \gtrsim 11$ M$_\odot$ are also capable of burning heavier elements (O, Ne, S, etc.), all the way up to ^{56}Fe. Figure 1.6 shows the onion-like structure of the core in these massive objects, at the end of their life.

When they explode as Supernovae, part of the heavy nuclei in the core are dispersed into the interstellar space, enriching the ISM in the surroundings of the

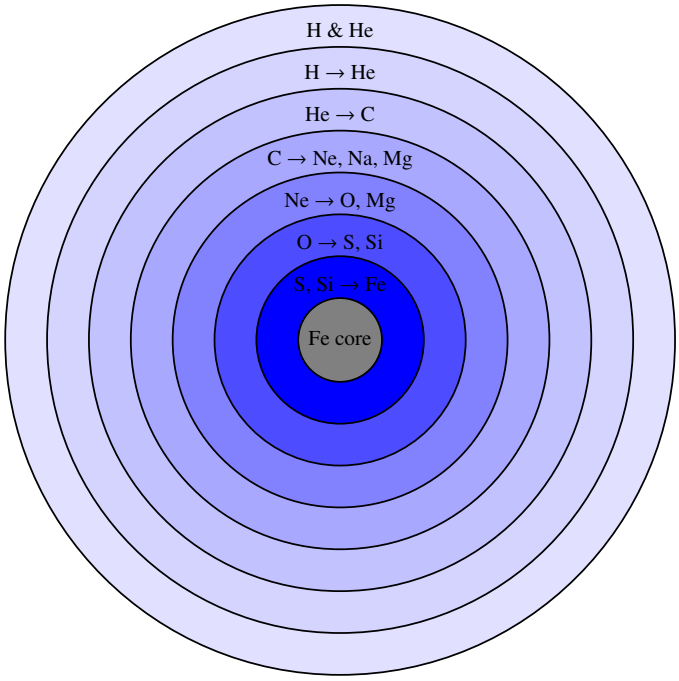

Figure 1.6: Core of a massive star in the last phases of its life, before it explodes as a supernova.

dying star. Elements heavier than ^{56}Fe are created mainly through reactions of neutron capture during the supernova event. The production of heavy elements is particularly important for the chemistry and the energetic balance of the ISM, because they are the dominant actors for the cooling of the interstellar medium. Massive stars strongly modify their surroundings, ionising the nearby gas, injecting significant amounts of energy into the ISM and mixing it through supernova explosions, winds and expanding HII regions. High-mass stars are thus of primary importance in determining the physical-, chemical- and morphological properties of galaxies, for their evolution, and even for the evolution of the Universe itself.

Considering their potentially destructive impact on their surroundings, high-mass stars may be expected to affect star-formation activity as well.

Several scenarios were explored in the literature, starting from the classical idea of *Collect & Collapse* (e.g., Elmegreen 1998). The basic principle behind this mechanism is that the material around the star is swept up on the edge of an expanding HII region, and that the mass of the collected material eventually

becomes large enough to be gravitationally unstable, forming a new generation of stars. Events of triggered star formation have been observed around HII regions in the Galaxy (e.g., Deharveng et al. 2005; Zavagno et al. 2006; Snider et al. 2009; Brand et al. 2011). The Collect & Collapse mechanism is only able to generate less-massive stars in the subsequent stellar generations, but the fraction of massive stars may be larger than in the case of spontaneous star formation (Elmegreen & Lada 1977; Walborn & Parker 1992; Deharveng & Zavagno 2011).

Another mechanism through which massive stars may induce subsequent events of star formation is the so-called radiative implosion of cores. This process may work beyond an ionisation front produced by the massive stars, which is preceded by a shock front compressing the gas. The compression of gas may induce the collapse of pre-existing condensations that would otherwise be dispersed, and may accelerate the collapse of cores that would have collapsed anyway. For typical properties of the ionisation front and of the shocked layer, the ionisation front overcomes these cores in a time comparable to the accretion timescale of low-mass stars, thus possibly halting the accretion for some of them, by photoevaporating the remaining material still available. This may influence the IMF, that would peak at even lower masses, an effect observed in some regions (e.g., Goodwin et al. 2004).

The death of a star as a supernova can also be responsible for inducing star formation, simultaneously favouring the formation of high-mass stars. This would explain the existence of OB subgroups and the coevality of the stars (cf. Zinnecker & Yorke 2007, and references therein).

Massive stars may, however, also quench the formation of successive stellar generations. For example, they can limit the final mass of the surrounding stars (as in the radiative implosion scenario), remove the remaining gas from the surrounding environment, or they can disperse or photoevaporate cores or delay their collapse (Dale et al. 2012, 2013), transferring to them energy and momentum, through radiation and winds.

All these processes seem to be at work in the regions surrounding massive stars in our Galaxy; which of them dominates depends on the specific conditions of the environment.

1.5 Outline of the thesis

In the high-mass regime the identification of different evolutionary stages is not as clear as in the low-mass regime. To understand the details of the process and test the predictions of the models one needs to understand what are the initial

conditions in the clumps before the onset of high-mass star formation, and how the clump properties change with time due to the feedback of the newly-formed stars. In this thesis I use all available observational material to determine the relative age of a sample of massive clumps. I investigate the physical conditions and -properties of massive clumps in different stages of their early evolution, and the degree of CO depletion in such objects. Comparing the typical properties of the evolutionary classes we bring out the variations therein, induced by the process of high-mass star- and cluster formation in the parent clump. Having defined an evolutionary sequence in terms of physical parameters one can now use already publicly available observations to arrange a larger sample of clumps on a timeline, and then use an instrument like ALMA to study objects in a certain evolutionary phase in great detail.

I also investigate the physical properties and star formation activity in molecular material in the vicinity of a young massive cluster, that has already dispersed the clump out of which it formed.

The thesis is organised as follows. In Chapter 2, I briefly describe the concepts of Bayesian statistics used throughout this work. In Chapter 3, I select a sample of massive clumps that are in different evolutionary phases, based on their mm- and IR properties. Then, I derive the gas and dust temperature, mass and density of these clumps, and analyse the variation of these properties from quiescent clumps, without any sign of active star formation, to clumps likely hosting a ZAMS star. In the same chapter I investigate the velocity gradients in these clumps, and briefly discuss CO depletion and recent observations of several molecular species, tracers of Hot Cores and/or shocked gas, for a subsample of these clumps. In Chapter 4, I study CO depletion in some of the brightest sources in the ATLASGAL survey, investigate how it changes from dark clouds to more evolved objects, and compare its evolution to what happens in the low-mass regime. In Chapter 5, I derive the physical properties of the molecular gas in the photon-dominated region adjacent to the HII region G353.2+0.9 in the vicinity of Pismis 24, a young, massive cluster, containing some of the most massive and hottest stars known in our Galaxy. I derive the IMF of the cluster and study the star formation activity in its surroundings. Finally, in Chapter 6, I present a short summary of the results obtained in this work.

Chapter 2

The Bayesian approach to statistics

In order to know more of the world that surrounds us, we have to observe nature, then formulate hypotheses on the laws governing it and gather data to test them. The paradigm according to which scientific theories have to confront reality was a revolution for science.

Drawing general conclusions from these data is how we make science progress. Because the data we have will always be incomplete and fragmentary, our knowledge of the world will necessarily be probabilistic. Statistics is the science that allows us to connect a set of data to specific problems, and to draw the general conclusions we need through statistical inference.

A well-canonised method is now at the basis of the physical sciences, resting on a few premises:

1. A theory cannot be proven to be true beyond any doubt;

2. Until a theory is proven to be false, it is assumed to be an useful representation of the physical world;

3. If two or more theories can explain a phenomenon, the simplest one is to be preferred, following Ockham's razor, unless the added complexity is justified by the data.

Two main philosophical approaches to statistics are available, based on different definitions of probability. In the following I will describe them briefly, with special attention to the Bayesian approach, used throughout this thesis.

This chapter is based on the D'Agostini (2003), Gregory (2005) and Bolstad (2007) books.

2.1 The Frequentist approach

Following the frequentist approach to statistics, probability is identified with the long-run frequency of an event. The procedures are evaluated on the basis of how they perform in the long run, over all possible samples that can be drawn from a given population. In the frequentist approach parameters are fixed, but unknown constants. Because parameters are not treated as random variables, probabilistic statements cannot be made about their value, i.e. the proposition "the true value is between x and y with a probability of z" is not allowed in the frequentist approach. This can generate confusion and create a problem of interpretation. In order to explain this issue, let's consider the following example (D'Agostini 2003): we design a simple experiment to measure a quantity, for example the length of a pen. If we repeat the experiment n times, neglecting any systematic effect, we can derive the average of the measurement results $\overline{x}$, and the uncertainty associated with the measurement would be $\sigma/\sqrt{n}$, if the uncertainty associated with the single measurement is σ. The relation

$$\mu = \overline{x} \pm \frac{\sigma}{\sqrt{n}} \tag{2.1}$$

connects the true value of the length of the pen μ with the result of the experiment. Equation 2.1 merely states that:

$$P\left(\mu - \frac{\sigma}{\sqrt{n}} \leq \overline{X} \leq \mu + \frac{\sigma}{\sqrt{n}}\right) = 68\%, \tag{2.2}$$

not increasing our knowledge about μ itself, even though this is what we seek in doing the experiment in the first place. Here $\overline{X}$ is used, because it represents a random variable, rather than the numerical value $\overline{x}$ it can assume. It is easy to see that, on the contrary, Eq. 2.2 is often interpreted as:

$$P\left(\overline{x} - \frac{\sigma}{\sqrt{n}} \leq \mu \leq \overline{x} + \frac{\sigma}{\sqrt{n}}\right) = 68\%. \tag{2.3}$$

However, this does not make sense in the frequentist approach, as μ is not a random variable and thus we cannot make probabilistic statements about its value. In this case there is a clear role reversal between the true value μ, for which we are in a state of uncertainty, and the observation $\overline{x}$, which is considered a random variable (D'Agostini 2003).

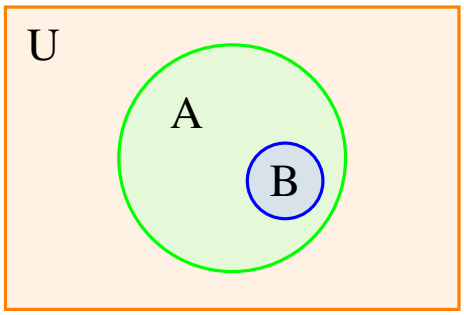

Figure 2.1: In this case, if B is true, then also A is true. Deduction is possible.

2.2 The Bayesian approach

The Bayesian approach has a completely different philosophy: probability is defined either as the degree of belief of an event to turn out to be true, or as a real number expressing the plausibility of a proposition A, given the truth of proposition B; the latter is at the foundation of the Bayesian statistic as an extended logic (Gregory 2005). Either of these definitions have several advantages over the frequentist one: they are completely general and can be applied to any event, independently of the possibility of repeating a measurement n times under identical conditions; it also allows the definition of the probability of the true value of a physical quantity or of an hypothesis. In fact, after a measurement, we find ourselves in a state of uncertainty about the true value of the parameter that we want to infer. The concept of probability and the interpretation of the results of an experiment in the Bayesian approach allow us to consider the parameter as a random variable, in turn giving the possibility to make probabilistic statements on the parameter itself, solving the problem of interpretation described in Sect. 2.1.

The Bayesian approach rests on the laws of probability, as they are at the heart of the statistical inference on the parameters and are used to extend logic to deal with uncertainty, as we usually do in everyday life, adjusting our beliefs about something on the basis of whether another event happened or not (Bolstad 2007).

To clarify this, let's consider the following example taken from Bolstad (2007): suppose we have two propositions, A (e.g., "I own a motorbike") and B (e.g., "My motorbike is a Ducati"). If B is true, then A is also true, the only conclusion consistent with the given condition. Also, if one knows that A is false, one can safely affirm that B is false too. In both cases we can use deduction. Using Venn diagrams, the situation can be represented graphically as in Fig. 2.1. On the other

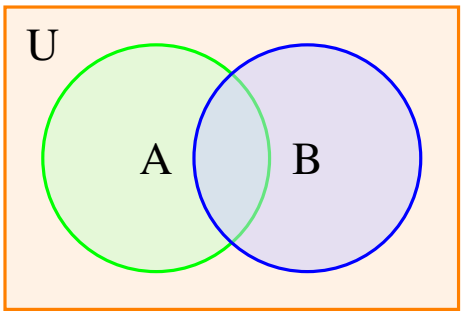

Figure 2.2: In this case, deduction is not possible, and traditional logic tells us nothing of B, if we know that A is true, and viceversa.

hand, consider that I say "I don't have a Ducati": using traditional logic you can't say anything about me having a motorbike or not, i.e. you can say nothing about the truth of proposition A, knowing that B is false. In the same way, if I only say that A is true, you cannot say anything about the brand of my motorbike. However, intuitively, in the first case it is less plausible that I have a motorbike, because one of the ways A could be true was removed; conversely, in the second case, the plausibility of B to be true increases, as you already know I have a motorbike. One can visualise this with the help of Fig. 2.1 and a simple numerical example. Suppose we have 20 numbers in a hat, and we have to extract one of them. Proposition A could be "a number less than or equal to 10 is extracted" and B could be "a number less than or equal to 3 is extracted". So, the probability of A of being true is $1/2$ and that of B is $3/20$. However, if we know that B is false (i.e. a number larger than 3 is extracted) the probability of A to be true is just $7/17$. Conversely, if we know that A is true, then the probability of B to be true is $3/10$.

The above example is only the simplest of the possible cases. Figure 2.2 shows a more general case: if one of the two statements A or B is true, the other can still be either true or false. With the Bayesian approach we can formalise the qualitative, intuitive variation in plausibility of the previous example, and translate the plausibility of a proposition or event into numbers, and update it on the basis of the occurrence or non-occurrence of another event. This process is called an induction.

Measures of plausibility should have some specific properties:

1. Plausibilities have to be non-negative, real numbers, and have to agree with our common sense, for example associating larger numbers to larger plausibilities.

2. When the possibility exists to represent a proposition in more than one way, then all representations must be consistent and give the same plausibility.

3. In the process of evaluation, all available information must be taken into account.

4. To equivalent states of knowledge we have to assign the same plausibility.

It can be demonstrated (Cox 1946; De Finetti 1974) that all plausibilities satisfying these requirements obey the laws of probability, which are then used in the Bayesian approach to revise our beliefs, given the data. All this permits the creation of a very general theory of uncertainty, able to take into account any source of systematic or statistical error, whichever is their distribution.

2.2.1 The rules of probability and the Bayes theorem

Three axioms are at the basis of the rules of probability, important for their internal consistency: $P(\mathrm{A}) \geq 0$ for any event A; $P(\mathrm{U}) = 1$ (U is the universe, cf. Figures 2.1 and 2.2); $P(\mathrm{A} \cup \mathrm{B}) = P(\mathrm{A}) + P(\mathrm{B})$, if the events are disjoint. As a simple reminder, $\cup$ and $\cap$ are the operation of union and intersection between ensembles, respectively; $\emptyset$ is the empty set, and $\overline{\mathrm{E}}$ is the complement of the event E. Everything that follows can be demonstrated starting from these axioms (cf. Appendix A).

$$P(\mathrm{E}) = 1 - P(\overline{\mathrm{E}}); \tag{2.4}$$

$$P(\emptyset) = 0; \tag{2.5}$$

$$P(\mathrm{A} \cup \mathrm{B}) = P(\mathrm{A}) + P(\mathrm{B}) - P(\mathrm{A} \cap \mathrm{B}); \tag{2.6}$$

$$P(\mathrm{A} \cup \mathrm{B}) \geq P(\mathrm{A} \cap \mathrm{B}); \tag{2.7}$$

If B is a subset of A, as in Fig. 2.1, the probability of A is greater or equal than that of B:

$$P(\mathrm{A}) \geq P(\mathrm{B}). \tag{2.8}$$

Another important definition is that of conditional probability, which is the probability of occurrence of an event A, after the occurrence of event B, indicated as $P(\mathrm{A}|\mathrm{B})$. Suppose the situation is that shown in Fig. 2.2. If we are aware that B occurred, then we are positive that $\overline{\mathrm{B}}$ did not, implying that all that is outside B is no longer possible. This redefines a new universe, corresponding to B, that has to obey the second axiom. Therefore $P(\mathrm{A}|\mathrm{B}) = P(\mathrm{A} \cap \mathrm{B})/P(\mathrm{B})$, so that $P(\mathrm{A}|\mathrm{B}) + P(\overline{\mathrm{A}}|\mathrm{B}) = 1$, $P(\mathrm{B}) = 1$. If two events are independent $P(\mathrm{A}|\mathrm{B}) = P(\mathrm{A})$, and thus

$$P(\mathrm{A} \cap \mathrm{B}) = P(\mathrm{A}) \times P(\mathrm{B}). \tag{2.9}$$

When this is no longer valid, the events are called correlated, positively or negatively if $P(\mathrm{A}|\mathrm{B}) > P(\mathrm{A})$ or $P(\mathrm{A}|\mathrm{B}) < P(\mathrm{A})$, respectively. Consider now the set of all mutually exclusive hypotheses H_i that may influence the event A. To know what is the probability of the various H_i, given the occurrence of B is the typical problem of any kind of measurement, i.e. to derive the probability of the causes responsible for the observed data. The frequentist approach lacks this, using an indirect approach based on confidence, which is prone to generate the problems discussed in Sect. 2.1, arbitrarily interpreting Eq. 2.2 as 2.3. This is an intuitive process, explained by D'Agostini (2003) with the dog and the hunter example: suppose that we know that a hunter goes hunting with his dog, and that there is a 50% probability to find the dog within 100 m from the hunter. What can we say about the position of the hunter if we observe the dog? Intuitively, one would say that there is a 50% probability of finding the hunter within 100 m from the dog. The answer is correct only if the hunter may be anywhere around the dog (if this is not the case, one has a case physically analogous to measurement at the edge of a physical region; cf. Example 1 in the following), and if there is no preferential direction from which the dog approaches (non-flat distribution of a physical quantity; cf. Example 2). Remaining on the dog-hunter example, suppose there is a path in the woods and the hunter moves only along this path. If we observe the dog farther than 100 m from the road, then we know that the hunter *cannot* be within 100 m from the dog. Suppose now that the dog is eager to run in the woods and tends to precede the hunter. With the aid of the Bayes theorem one can easily show that the probability of finding the hunter within 100 m from the dog will, in general, be different from 50%. Physical examples of these problematic cases are described in D'Agostini (2003) and reported in the boxes at the end of the Section.

The Bayesian approach can easily take the above situations into account. To see how, let's start from the derivation of the single tool used for inference, the

Bayes theorem.

Imagine we divide the universe into N mutually exclusive hypotheses H_i. In order to calculate the probability of the causes behind an event E, $P(E|H_i)$, we can rewrite Eq. 2.9 as:

$$P(E \cap H_i) = P(E|H_i)P(H_i), \tag{2.10}$$

and by symmetry:

$$P(H_i \cap E) = P(E \cap H_i) = P(H_i|E)P(E). \tag{2.11}$$

Combining equations 2.10 and 2.11:

$$P(E|H_i)P(H_i) = P(H_i|E)P(E), \tag{2.12}$$

we derive one of the forms of the Bayes theorem

$$P(H_i|E) = \frac{P(E|H_i)P(H_i)}{P(E)}. \tag{2.13}$$

Because the hypotheses are disjoint, i.e. $H_i \cap H_j = \emptyset$ and they are exhaustive, i.e. $\cup_i H_i = U$, we can write

$$P(E) = P\left(\bigcup_i (E \cap H_i)\right) = \sum_i P(E \cap H_i) = \sum_i P(E|H_i)P(H_i). \tag{2.14}$$

Substituting this into Eq. 2.13, we get the standard way of writing the Bayes theorem:

$$P(H_i|E) = \frac{P(E|H_i)P(H_i)}{\sum_i P(E|H_i)P(H_i)}. \tag{2.15}$$

In Eq. 2.15 the expression in the denominator is only a normalisation factor, so that $\Sigma_i P(H_i|E) = 1$. $P(E|H_i)$ is called *likelihood* and expresses the probability that a cause produces a given effect. $P(H_i|E)$ is the updated probability of H_i, given the effect E, after the measurement, or *posterior*. Finally, $P(H_i)$ is the initial, *a priori* probability of the hypothesis H_i available without the data obtained with the current experiment. This is called *prior*. The use of priors has been criticised as subjective, but it is important to realise that the only thing that objectivity requires in a scientific approach is that different investigators with the same state of knowledge reach the same conclusion (De Finetti 1974; Jaynes & Bretthorst

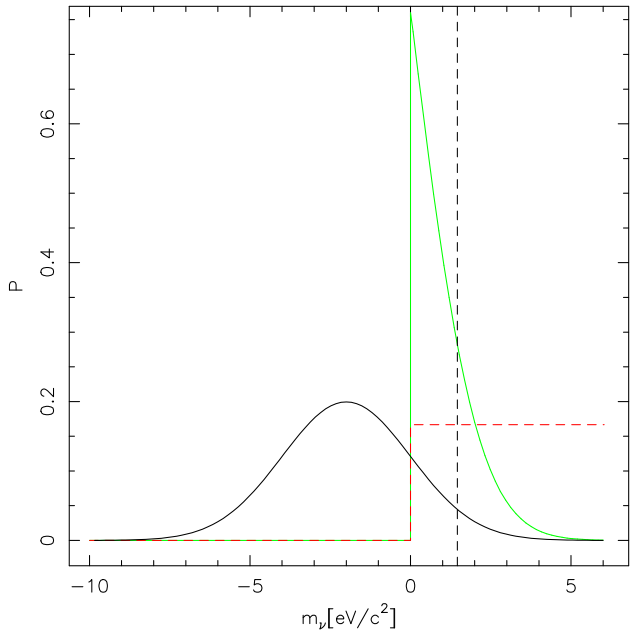

Figure 2.3: Example of measurement at the edge of a physical region, e.g. the neutrino mass (see text). The dashed red line is the prior, the solid black line is the likelihood and the solid green line is the posterior. The black dashed line shows the shortest 68% interval of the posterior.

2003). Besides, the use of priors is the only natural way to include any previous knowledge in the analysis.

The set of competing hypotheses we want to assign probabilities to is called hypothesis space. After applying the Bayes theorem to all the hypotheses, we have a probability distribution function in the case of discrete quantities or a probability density function in the continuous case, in both cases abbreviated as PDF. A PDF describes our state of knowledge, or better, ignorance, about a parameter. The true value of a parameter is not distributed over the PDF, it has a definite value, but our state of uncertainty allows us to treat it as a random variable.

Practical examples of the use of the Bayes Theorem for astronomical data are shown in the following Chapters; the PDF of the quantities we are interested in is derived explicitly for simple cases in Sections 4.6.3.2, 5.2.3.8 and B.2.

The very scheme of the Bayesian approach can be seen as a model for the process of learning (Gregory 2005), being the tool that lets us update our knowledge of the physical world on the basis of the observed data. Firstly we define our state of

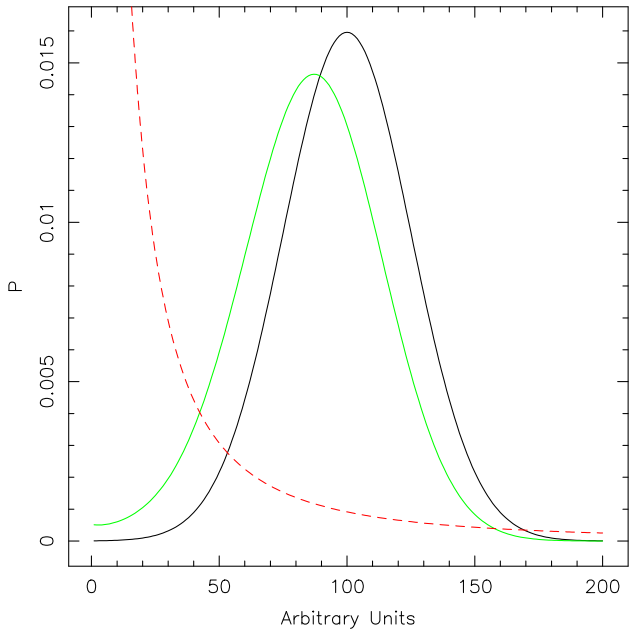

Figure 2.4: Example of measurement of a quantity with a non-flat distribution, e.g. the energy of cosmic rays (see text). The dashed red line is the prior, the solid black line is the likelihood and the solid green line is the posterior.

knowledge, based on the available information before the experiment, formalising it into a prior; secondly we gather the new data to construct a likelihood, and finally we use the Bayes theorem to combine it with the *a priori* information, to revise our information about the parameter deriving a posterior. The posterior can then be used as a prior, when new data become available.

The solution of a problem in the Bayesian paradigm is usually conceptually simple. However, a major drawback for using this approach is that it could be difficult or computationally very expensive to derive the posterior, typically requiring the integration of functions with many dimensions.

The Monte Carlo Markov Chains (MCMC) methods are one of the possible solutions to this problem, trying to simulate direct drawing from a complex distribution. This class of algorithms derives its name from the fact that it uses the current value of the sample to randomly generate the next one, producing a Markov Chain (Walsh 2004). A Markov chain is a system with a finite or countable number of states. It moves successively from one state to another: each transition is called a *step*. If the chain is in state i it will move to the next state j (which can also be

Example 1 – Measurement at the edge of a physical region. To measure the mass of the electron-neutrino, an experiment was designed, with a resolution $\sigma = 2$ eV/c^2, assumed to be independent of the mass for simplicity. The analysis of the data from this experiment gives a neutrino mass of $m_\nu = -4$ eV/c^2. How is one to interpret these data? Certainly it does not make sense to express the results in one of the following ways: $m_\nu = -4 \pm 2$ eV/c^2, $P(-6 \text{ eV/c}^2 \leq m_\nu \leq -2 \text{ eV/c}^2) = 68\%$ or even $P(m_\nu \leq 0) = 98\%$. Figure 2.3 illustrates this situation. In the Bayesian approach, one can interpret the experiment results as a likelihood (the black solid line), and use a prior like the red dashed line. Combining them with the Bayes theorem, we get the posterior shown as a green solid line: on this basis we can write $P(m_\nu \leq 1.5 \text{ eV/c}^2) \approx 68\%$.

Example 2 – Non-flat distribution of a physical quantity. Suppose that we have previous evidence that a specific quantity has a probability distribution similar to that of the red dashed line in Fig. 2.4, with low values much more probable than the high ones. This could qualitatively represent the energy of bremsstrahlung photons or of cosmic rays. We know that the probability distribution of an observable value X can be represented as a Gaussian with a certain dispersion around the true value μ, independently of its actual value. Suppose we measure $x = 100$, in arbitrary units. Intuitively, we expect that the true value that caused the observation has more probability to be on the left of the measured value. In Fig. 2.4 the posterior shows this, being shifted to the left. This also shows why the probability to find the hunter around the "eager" dog is no longer 50%.

the same) with a transition probability p_{ij}. These probabilities depend only on the actual state of the chain, and not on the previous ones.

Among the various MCMC methods, Gibbs Sampling (Geman & Geman 1984) is particularly suited for Bayesian inference, because it can be used in a very broad class of problems (Gelfand & Smith 1990). Gibbs sampling is very useful to derive posteriors (Smith & Roberts 1993), and several softwares (such as JAGS) offer an implementation of this algorithm. The power of a Gibbs sampler resides in the fact that it only needs univariate (of a single random variable) conditional distributions, that are much easier to simulate than the full joint distribution. Therefore, one simply has to simulate n random variables sequentially from their

univariate distributions, conditional on the current value of the other variables, rather than a vector of n elements from the joint distribution (Walsh 2004).

The samples produced are correlated, because the transition probabilities between two states depend on the most recent value of the sample, being Markov Chains. Moreover, the initial values may not approximate properly the joint distribution. The usual approach is to discard these initial values (*burn-in*), and in order to obtain independent samples, resort to *thinning*, i.e. sampling the chain only every k values.

Such methods are used in all the following Chapters to propagate the uncertainty, connected to the measured continuum- or line fluxes, to the inferred physical parameters (cf. e.g. Sections 3.5.2, 4.5.2, and 5.2.3.8). A practical example of the analysis of the output of JAGS is shown below.

The chains produced by JAGS are in the form of plain text files. Each of them appear like:

```
# parameter 1
5001  17.0438
5011  10.0482
5021  8.03154
5031  27.0869
5041  11.9768
5051  18.8083
5061  12.1218
5071  14.3282
5081  18.5156
...
# parameter 2
5001  1019.52
5011  1109.04
5021  1221.6
5031  106.971
5041  527.163
5051  401.684
5061  725.182
5071  493.271
5081  284.345
...
```

where the first column is an index that identifies the iteration, and the second is the value of the parameter. From the first column it is clear that in this case a *burn in* of 5000 iterations and a thinning of 10 were used. Figure 2.5 shows the trace plot (iteration vs. parameter value) for parameter 1 in the example above, for three different chains. This is a first simple way to assess the convergence. From the parameter values one can derive their mean and median values. The marginal distribution of each parameter is derived simply by constructing a histogram like the one shown in Fig. 2.6 (normalised to have sum equal to 1), from which one can derive e.g., the shortest 68% interval or the mode.

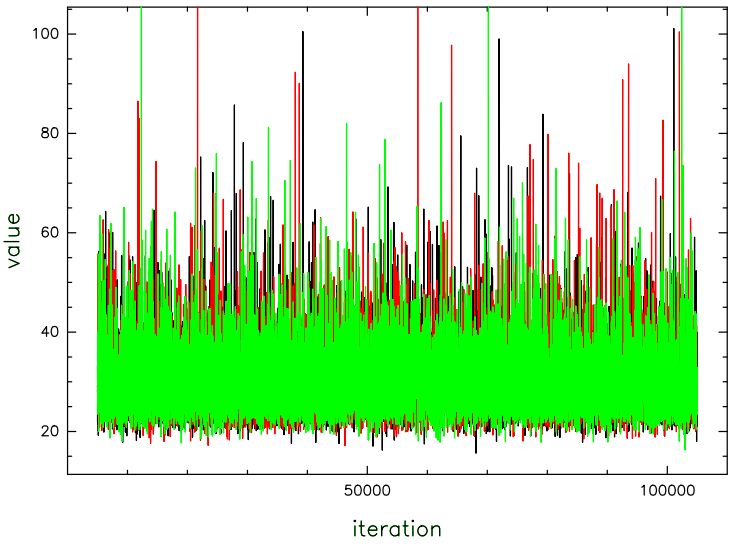

Figure 2.5: Trace plot of a parameter. Three chains are considered (and show similar results), each of them is plotted in a different colour.

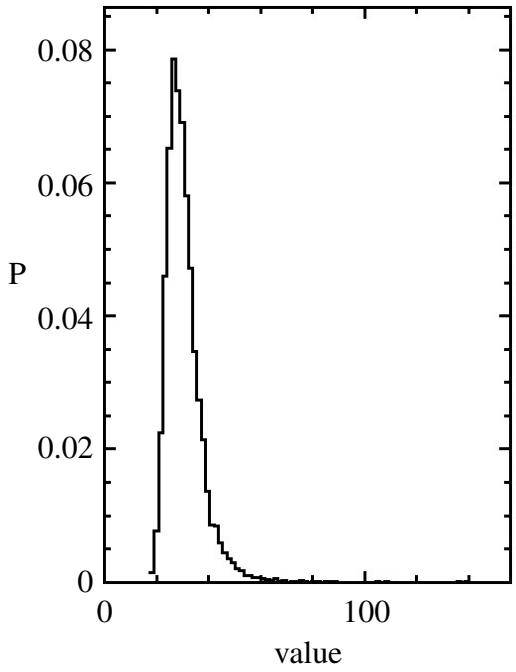

Figure 2.6: Normalised histogram of the marginal distribution of the same parameter shown in Fig. 2.5.

2.2.2 Marginalisation

Often, the models we use will have more than one parameter, but we may be interested in only a subset of them. For example, we may want to know only the temperature of the gas, whichever is its density (cf. Fig. 4.14). In such a situation, the parameters we are not interested in are called *nuisance parameters*. The result of applying the Bayes theorem is always the full joint posterior PDF for all parameters (Gregory 2005).

The Bayesian approach has an easy way of dealing with nuisance parameters, through marginalisation. This is one of the major technical advantages of this approach, because the frequentistic approach lacks a consistent and general way to deal with nuisance parameters, from which they derive their name. To explain how marginalisation works, consider a simple example with a sinusoidal wave (Gregory 2005), where we have two parameters (the amplitude A and the phase ψ), but we are interested in only one of them, for example the phase. For the sake of simplicity, let's assume that the amplitude may assume only discrete values. Therefore, for some value of the amplitude A_i the boolean proposition $\sum_i A_i$ is true. This simply means that the wave has an amplitude among those considered. Thus one has $P(\sum_i A_i) = 1$. Because we are only interested in ψ, we want to know $P(\psi|D, I)$, the probability to have a phase ψ, given the data D and any previous information I we have, previously left out of the notation for simplicity. Here, the parameters play the role of the hypotheses, and the data of the events that these *hypotheses* (i.e. the value of the parameters) can produce. The composite proposition $\psi, \sum_i A_i|D, I$ is true if both ψ and $\sum_i A_i$ are true, and its probability to be true is represented by $P(\psi, \sum_i A_i|D, I)$. Using the product rule to expand this proposition we can write:

$$P\left(\psi, \sum_i A_i|D, I\right) = P(\psi|D, I) \times P\left(\sum_i A_i|D, I\right) = P(\psi|D, I). \tag{2.16}$$

Using the boolean algebra and because the propositions ψA_i are independent for different i we can rewrite the left hand side of Eq. 2.16:

$$P\left(\psi, \sum_i A_i|D, I\right) = P\left(\sum_i \psi A_i|D, I\right) = \sum_i \left(P(\psi, A_i|D, I)\right). \tag{2.17}$$

Combining Equations 2.16 and 2.17 we get:

$$P(\psi|D, I) = \sum_i \left(P(\psi, A_i|D, I)\right), \tag{2.18}$$

	1	**2**	**3**	**4**	**5**	***P*(col)**
Black	$\frac{5}{120}$	$\frac{3}{120}$	$\frac{3}{120}$	$\frac{1}{120}$	$\frac{7}{120}$	$\frac{\mathbf{19}}{\mathbf{120}}$
Orange	$\frac{6}{120}$	$\frac{3}{120}$	$\frac{5}{120}$	$\frac{5}{120}$	$\frac{5}{120}$	$\frac{\mathbf{24}}{\mathbf{120}}$
Red	$\frac{7}{120}$	$\frac{4}{120}$	$\frac{6}{120}$	$\frac{2}{120}$	$\frac{8}{120}$	$\frac{\mathbf{27}}{\mathbf{120}}$
Green	$\frac{9}{120}$	$\frac{5}{120}$	$\frac{3}{120}$	$\frac{8}{120}$	$\frac{1}{120}$	$\frac{\mathbf{26}}{\mathbf{120}}$
Blue	$\frac{3}{120}$	$\frac{6}{120}$	$\frac{2}{120}$	$\frac{9}{120}$	$\frac{4}{120}$	$\frac{\mathbf{24}}{\mathbf{120}}$
***P*(number)**	$\frac{\mathbf{30}}{\mathbf{120}}$	$\frac{\mathbf{21}}{\mathbf{120}}$	$\frac{\mathbf{19}}{\mathbf{120}}$	$\frac{\mathbf{25}}{\mathbf{120}}$	$\frac{\mathbf{25}}{\mathbf{120}}$	

Figure 2.7: Simple example of marginalisation. 120 coloured balls are in a box, and on each of them there is a number. The probabilities of drawing a ball of a specific colour or with a specific number is given at the margins of the matrix containing the probabilities of extracting a ball of a specific colour *and* number.

or extending this result to continuous variables:

$$P(\psi|D,I) = \int P(\psi, A|D,I)dA. \tag{2.19}$$

This equation shows that we can obtain the marginal distribution of ψ (and ψ only) simply by integrating out any nuisance parameter we might have.

In Fig. 2.7 I give a very simple example of how marginalisation works. Suppose we have a box containing 120 coloured balls, each with a number between 1 and 5. The matrix elements are probabilities: there are 7 red balls with number 1 in the box, so the probability to extract one of them is $7/120$, and so on. Suppose that one draws a ball. What is the probability of drawing a ball of a specific colour? Or to extract a specific number? One simply has to marginalise the probabilities in the matrix. The marginal distributions are indicated in the figure as P(col) and P(number), for a specific colour and number, respectively. Another useful form for the operation of marginalisation can be obtained expanding Eq. 2.19 with the Bayes theorem, assuming that the priors for ψ and A are independent:

$$P(\psi|D,I) \propto P(\psi|I) \int P(A|I)P(D|\psi,A,I)dA; \tag{2.20}$$

this expresses the marginal posterior probability in terms of the weighted average of the likelihood with weights $P(A|I)$, the prior on A.

2.2.3 Model comparison and Ockham's razor

"Ockham's razor" says that when comparing different models, the simpler one should be favoured, unless there is enough evidence in favour of the other. This principle is incorporated in the Bayesian approach for model comparison: the Bayes theorem automatically penalises complex models, also quantitatively defining the amount of evidence needed to prefer one model over another. The more complex model is favoured only if the additional complication is justified by the complexity of the data, as a crucial consequence of the marginalisation operation.

The obvious condition to perform model comparison is that at least two competing models exist to reproduce the data. We can denote each model as M_i, and calculate their probabilities:

$$P(M_i|D, I) = \frac{P(M_i|I)P(D|M_i, I)}{P(D|I)}. \tag{2.21}$$

$P(D|M_i, I)$ is the global likelihood of the model M_i, and can be evaluated with the continuous counterpart of $P(D|I) = \sum_i P(M_i|I)P(D|M_i, I)$:

$$P(D|M) = \int P(\theta|M)P(D|\theta, M)d\theta = \mathcal{L}(M), \tag{2.22}$$

where θ is the parameter of the model and the global likelihood is now indicated with $\mathcal{L}(M)$. This shows that model comparison is perfectly analogous to parameter estimation. The model PDF is again the product of priors and global likelihood, only for the distinct models we want to compare.

To illustrate how the Bayesian approach favours simpler models let's consider a case where we want to compare two alternative models, one with a parameter θ and the other a subcase of the first, with $\theta = \theta_0$, therefore without free parameters. Figure 2.8 offers a useful support for the following discussion. We can calculate the odds ratio O_{ij} in favour of the first model (M_1) over the second (M_0), as the ratio of their probabilities:

$$O_{10} = \frac{P(M_1|D, I)}{P(M_0|D, I)} = \frac{P(M_1|I)}{P(M_0|I)} \frac{P(D|M_1, I)}{P(D|M_0, I)}, \tag{2.23}$$

where the first factor is the prior odds ratio and the second is the Bayes factor B_{10}.

To calculate B_{10} one has to evaluate Eq. 2.22, to derive the global likelihood for M_1. On the other hand, for M_0 the global likelihood would be equal to the likelihood function of M_1 for $\theta = \theta_0$. If the new data from the experiment add some more information about the parameters than we had before performing the experiment, the likelihood function $\mathcal{L}(\theta) = P(D|\theta, M, I)$ will be "narrower" than the prior $P(\theta|M, I)$. Suppose that $\Delta\theta$ is the characteristic width of the prior, thus if we use a flat prior we have $\int_{\Delta\theta} P(\theta|M_1, I)d\theta = P(\theta|M_1, I)\Delta\theta = 1$, so that $P(\theta|M_1, I) = 1/\Delta\theta$. Let's indicate with $\delta\theta$ the characteristic width of the likelihood defined by:

$$\int_{\Delta\theta} P(D|\theta, M_1, I)d\theta \approx P(D|\hat{\theta}, M_1, I)\delta\theta. \tag{2.24}$$

Thus the global likelihood 2.22 can be approximated as the maximum likelihood times the characteristic width of the likelihood divided by the characteristic width of the prior:

$$\begin{aligned} P(D|M_1, I) &= \int P(D|\theta, M_1, I)P(\theta|M_1, I)d\theta = \mathcal{L}(M_1) = \frac{1}{\Delta\theta}\int P(D|\theta, M_1, I)d\theta \\ &\approx P(D|\hat{\theta}, M_1, I)\frac{\delta\theta}{\Delta\theta} = \mathcal{L}(\hat{\theta})\frac{\delta\theta}{\Delta\theta}. \end{aligned} \tag{2.25}$$

$\mathcal{L}(M_0)$ is instead

$$\mathcal{L}(M_0) = P(D|M_0, I) = P(D|\theta_0, M_1, I) = \mathcal{L}(\theta_0), \tag{2.26}$$

and therefore:

$$B_{10} = \frac{P(M_1|I)}{P(M_0|I)}\,\frac{\mathcal{L}(M_1)}{\mathcal{L}(M_0)} \approx \frac{P(M_1|I)}{P(M_0|I)}\,\frac{\mathcal{L}(\hat{\theta})}{\mathcal{L}(\theta_0)}\,\frac{\delta\theta}{\Delta\theta}. \tag{2.27}$$

If we do not have reasons to prefer one model over another, the prior odds is equal to 1. The likelihood ratio cannot favour M_0 because it is a sub case of M_1. On the other hand, $\delta\theta/\Delta\theta < 1$, because the posterior is narrower than the prior. The complex model is penalised for the parameter space that is considered in the prior and ruled out by the data. M_1 is thus favoured only if the likelihood ratio is large enough to compensate the penalisation. This notion can be generalised to n models without difficulty. The approximation we used for the global likelihood is a general way of writing it, as the maximum of the likelihood function times a factor Ω_θ. Ω_θ

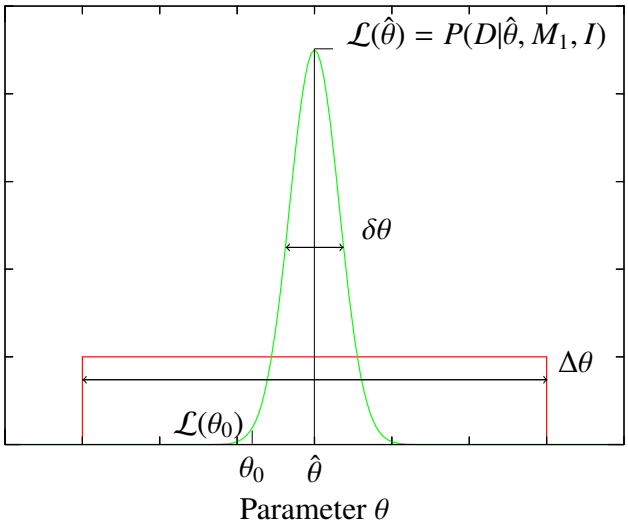

Figure 2.8: Example prior $P(\theta|M_1, I) = 1/\Delta\theta$ (red) and likelihood $\mathcal{L}(\theta) = P(D|\theta, M_1, I)$ (green) to illustrate the Bayesian model comparison.

is called Ockham's factor associated with the parameter θ, because it corrects the likelihood ratio, quantifying the qualitative idea that the simpler model should be preferred, unless there is evidence that justifies the added complexity. Ω_θ can be interpreted as the ratio of the region of parameter space covered by the posterior and that covered by the prior (cf. Fig. 2.8).

2.2.4 The advantages of the Bayesian approach

Summarising, the Bayesian approach offers several advantages over the frequentist approach, listed below (cf. Gregory 2005; Bolstad 2007).

- First of all, it rests on a single tool, the Bayes theorem is always the starting point. It gives an elegant, rational and simple way to answer scientific questions in the optimal way;
- It allows one to take explicitly into account any previous information one might have, usually leading to better performances;
- Given the different definition of probability, one can make probabilistic statements directly on the parameters, without having to use the non-intuitive concept of confidence;

- If offers a straightforward way to deal with nuisance parameters through marginalisation (see Sect. 2.2.2);
- The Bayes theorem presents a powerful way of comparing different models, and incorporates the principle of Ockham's razor (see Sect. 2.2.3);
- It provides a way to obtain predictive distributions for future observations.

The drawback represented by the difficulties of finding a closed form for- or to perform numerical integration of the posterior is now overcome, thanks to e.g., the algorithms described in Sect. 2.2.1. Therefore, the Bayesian approach is experiencing a growing interest in the scientific community.

Chapter 3

Physical properties of high-mass clumps in different stages of evolution

This chapter is adapted from Giannetti, Brand, Sánchez-Monge, Fontani, Cesaroni, Beltrán, Molinari, Dodson and Rioja (2013, A&A, 556, A16), and Fontani, Giannetti, Beltrán, Dodson, Rioja, Brand, Caselli and Cesaroni (2012, MNRAS, 423,2342).

3.1 Chapter summary

The details of the process of massive star formation are still elusive. A complete characterisation of the first stages of the process from an observational point of view is needed to constrain theories on the subject. In the past 20 years we have made a thorough investigation of colour-selected IRAS sources over the whole sky. The sources in the northern hemisphere were studied in detail and used to derive an evolutionary sequence based on their spectral energy distribution.

To investigate the first stages of the process of high-mass star formation, we selected a sample of massive clumps previously observed with the Swedish-ESO Sub-millimetre Telescope at 1.2 mm and with the ATNF Australia Telescope Compact Array at 1.3 cm. The selection criteria used were: (i) source declination $\delta < -30^{\circ}$; (ii) comparable numbers of MSX-dark and -bright sources; (iii) clumps as isolated as possible, i.e. with a separation greater than one SEST beam ($24''$) between MSX and non-MSX emitters to limit confusion; (iv) masses in excess

of $\sim$ 40 $M_\odot$ in the Beltrán et al. (2006) catalogue. We want to characterise the physical conditions in such sources, and test whether their properties depend on the evolutionary stage of the clump.

With ATCA we observed the selected sources in the NH_3(1,1) and (2,2) transitions and in the $H_2O(6_{16} - 5_{23})$ maser line. Ammonia lines are a very good temperature probe that allow us to accurately determine the mass and the column, volume, and surface densities of the clumps. We also collected all data available to construct the spectral energy distribution of the individual clumps and to determine if star formation is already occurring through observations of its most common signposts, thus putting constraints on the evolutionary stage of the source. We fitted the spectral energy distribution between 1.2 mm and 70 μm with a modified black-body to derive the dust temperature and independently determine the mass. With APEX we observed several molecular species, allowing us to measure CO depletion, investigate the presence of Hot Cores and identify lines that appear early in the process of star formation, while undetected in quiescent sources.

We find that the clumps are cold ($T \sim 10-30$ K), massive ($M \sim 10^2 - 10^3$ $M_\odot$), and dense ($n(H_2) \gtrsim 10^5$ cm^{-3}) and that they have high column densities ($N(H_2) \sim 10^{23}$ cm^{-2}). All clumps appear to be potentially able to form high-mass stars. The most massive clumps appear to be gravitationally unstable, if the only sources of support against collapse are turbulence and thermal pressure, which possibly indicates that the magnetic field is important in stabilising them. Several sources show velocity gradients, in the range $0.5 - 3$ km s^{-1} pc^{-1}.

After investigating how the average properties depend on the evolutionary phase of the source, we find that the temperature and central density progressively increase with time. Sources likely hosting a ZAMS star show a steeper radial dependence of the volume density and tend to be more compact than starless clumps. CO depletion appear to be substantial in massive clumps in early evolutionary stages: the sources have unexpectedly high depletions, in the range $5 - 78$, marginally higher in IR-dark clumps. A preliminary look at the APEX data show that $SO(6_5 - 5_4)$ and $H_2CO(3_{2,1} - 2_{2,0})$ seem to be good indicators of ongoing star formation, and become detectable in the early phases of the process.

3.2 Introduction

Massive stars spend a significant part ($\gtrsim$ 10%) of their lives embedded in their parental molecular cloud, making it difficult to investigate their early evolutionary stages. The discovery of IR-dark clouds (IRDCs; e.g., Perault et al. 1996; Egan et al. 1998) seen in absorption against the mid-IR Galactic background made it possible to identify the most likely birthplaces of high-mass stars. These clouds are usually filamentary, hosting complexes of cold ($T \lesssim 25$ K) and dense ($n \gtrsim 10^5$ cm^{-3}) clumps, with high H_2 column densities ($N \gtrsim 10^{23}$ cm^{-2}) and masses that usually exceed 100 $M_\odot$ (though not all of them will form massive stars; e.g., Kauffmann & Pillai 2010). Clouds with such low temperatures have a spectral energy distribution (SED) that peaks at far-IR (FIR) wavelengths and are optically thin in the millimetre/sub-millimetre regime. The emission at these wavelengths usually matches the IR absorption very well (e.g., Rathborne et al. 2006; Pillai et al. 2006), and makes it easy to identify the cold and dense gas concentrations. Some clumps within IRDCs show signs of active star formation, such as 24 μm emission, presence of extended excess emission at 4.5 μm[1], masers and SiO emission from outflows (e.g., Beuther et al. 2005b; Rathborne et al. 2005; Chambers et al. 2009).

The pre/protostellar phase for high-mass stars is very short ($\sim 3 \times 10^4$ yr), according to statistical studies (Motte et al. 2007), when compared to the low-mass regime ($\sim 3 \times 10^5$ yr, Kirk et al. 2005). The accretion timescale is longer than the Kelvin-Helmoltz timescale and nuclear fusion starts before the star has reached its final mass, thus continuing to accrete a significant quantity of material even in this phase. The entire life of the protostar and part of the main sequence is therefore spent inside the parental clump. Objects in these early phases of evolution and their influence on the surrounding material, can be investigated at frequencies that can penetrate the cocoon in which the objects are enshrouded.

In the last 2 decades we have made a thorough investigation of a sample of luminous IRAS sources distributed over the whole sky, selected on the basis of FIR colours typical of YSOs (e.g, Palla et al. 1991). Our expectation that this sample contains high-mass YSOs in different evolutionary stages has been supported by a large number of observations at both low- and high-angular resolution (e.g., Molinari et al. 1996, 1998a,b; Brand et al. 2001; Fontani et al. 2005; Beltrán et al. 2006). Those with $\delta < 30°$ have been observed with the SEST in the continuum at 1.2-mm (SIMBA) and in CS (Fontani et al. 2005; Beltrán et al. 2006). The

[1]The excess at 4.5 μm, typically named Extended Green Object or "green fuzzy" is commonly interpreted as arising from H_2 and CO lines, likely tracing shocks (e.g., Noriega-Crespo et al. 2004; Marston et al. 2004).

mm-continuum maps often show the presence of several clumps around a single IRAS source. A comparison with MSX (and later Spitzer) images revealed that some of these clumps are associated with mid-IR emission, while others appear IR-dark (Beltrán et al. 2006).

A first attempt to exploit such large amount of data to define an evolutionary sequence for the clumps and their embedded sources was carried out by Molinari et al. (2008), who distinguished three different types of objects, on the basis of their mm- and IR properties: **(Type 1)** objects with dominant mm emission, and not associated with a mid-IR source; **(Type 2)** objects with both IR- and mm emission; and **(Type 3)** objects with clearly dominant IR emission. Using a simple model, the authors could explain these different types in terms of an evolutionary scenario, in order of increasing age: (Type 1) starless cores and/or (proto)stars embedded in dusty clumps; (Type 2) deeply embedded Zero-Age Main Sequence OB star(s) still accreting material from the parental clump, and (Type 3) OB stars surrounded only by the remnants of the molecular cloud. From our recent ATCA 1.3 cm continuum- and line (H_2O maser at 22 GHz) observations (Sánchez-Monge et al. 2013a) of a large number ($\sim$ 200) of these massive clumps selected from the SEST mm-continuum observations, we found that Type 1 sources are rarely associated with cm-continuum emission (8%), Types 2 (75%) and 3 (28%) more frequently. At the same time, H_2O maser emission was found associated with 13%, 26%, and 3% of sources of Type 1, 2 and 3, respectively. These findings corroborate the evolutionary sequence derived by Molinari et al. (2008).

In this chapter we will explore how the gas and dust properties in massive clumps depend on the evolutionary phase, as determined from the source type and the presence of signposts of high-mass star formation.

The chapter is organised as follows: in Sect. 3.3 we briefly describe the sample selection, in Sect. 3.4 we describe the observations performed with the Australia Telescope Compact Array, and describe the data reduction procedure; in Sect. 3.5 we show the results for the quantities directly derived from the observations; in Sect. 3.6 we discuss how the sample is divided into "star-forming" and "quiescent" clumps, and into clumps likely hosting a ZAMS star (Types 2 and 3) and clumps that are starless or with a deeply embedded (proto)star (Type 1). The mean clump properties are investigated to search for differences as a function of evolutionary phase. In Sect. 3.7 we give a sketch of the different classes of objects identified and finally in Sect. 3.8 we summarise our findings.

Table 3.1: Central coordinates of the observed fields, names of the clumps in the field and their coordinates.

Phase Centre (J2000)		Clump	Clump Coordinates (J2000)	
RA	DEC		RA	DEC
08:49:35.13	−44:11:59.0	08477-4359c1	08:49:35.13	−44:11:59.0
09:00:40.50	−47:25:55.0	08589-4714c1	09:00:39.71	−47:26:11.0
10:10:41.70	−57:44:36.0	10088-5730c2	10:10:41.70	−57:44:36.0
12:32:52.10	−61:35:42.0	12300-6119c1	12:32:49.86	−61:35:34.0
13:07:09.40	−63:47:12.0	13039-6331c1	13:07:08.19	−63:47:12.0
13:59:33.04	−61:49:13.0	13560-6133c1	13:59:31.91	−61:48:41.0
		13560-6133c2	13:59:33.04	−61:49:13.0
13:59:55.50	−61:24:25.0	13563-6109c1	13:59:57.73	−61:24:33.0
14:20:21.74	−61:31:13.0	14166-6118c1	14:20:19.50	−61:31:53.0
		14166-6118c2	14:20:21.74	−61:31:13.0
14:22:21.54	−61:06:42.0	14183-6050c3	14:22:21.54	−61:06:42.0
15:07:32.52	−58:40:33.0	15038-5828c1	15:07:32.52	−58:40:33.0
15:11:07.90	−59:06:30.0	15072-5855c1	15:11:08.94	−59:06:46.0
15:31:44.17	−56:32:08.0	15278-5620c1	15:31:45.13	−56:30:48.0
		15278-5620c2	15:31:44.17	−56:32:08.0
15:48:40.82	−53:40:35.0	15454-5335c2	15:48:40.82	−53:40:35.0
15:51:28.24	−54:31:42.0	15470-5419c1	15:51:28.24	−54:31:42.0
15:51:01.62	−54:26:46.0	15470-5419c3	15:51:01.62	−54:26:46.0
15:50:56.12	−54:30:38.0	15470-5419c4	15:50:56.12	−54:30:38.0
15:59:36.20	−52:22:58.0	15557-5215c1	15:59:40.57	−52:23:30.0
		15557-5215c2	15:59:36.20	−52:22:58.0
15:59:39.70	−52:25:14.0	15557-5215c3	15:59:39.70	−52:25:14.0
16:01:52.83	−53:11:57.0	15579-5303c1	16:01:46.60	−53:11:41.0
16:02:08.86	−53:08:53.0	15579-5303c3	16:02:08.86	−53:08:53.0
16:10:06.61	−50:50:29.0	16061-5048c1	16:10:06.61	−50:50:29.0
16:09:57.30	−50:57:09.0	16061-5048c2	16:10:02.38	−50:49:33.0
16:10:06.61	−50:57:09.0	16061-5048c4	16:10:06.61	−50:57:09.0
16:13:05.20	−50:23:05.0	16093-5015c1	16:13:01.85	−50:22:41.0
16:12:55.46	−51:43:22.0	16093-5128c1	16:12:49.45	−51:43:30.0
		16093-5128c2	16:12:55.46	−51:43:22.0
16:12:49.45	−51:36:34.0	16093-5128c8	16:12:49.45	−51:36:34.0
16:20:24.51	−49:35:34.0	16164-4929c2	16:20:18.75	−49:34:54.0
		16164-4929c3	16:20:24.51	−49:35:34.0
16:20:31.92	−49:35:26.0	16164-4929c6	16:20:31.92	−49:35:26.0
16:20:24.33	−48:44:58.0	16164-4837c2	16:20:24.33	−48:44:58.0
16:29:00.89	−48:50:31.0	16254-4844c1	16:29:00.89	−48:50:31.0
16:47:01.70	−41:15:18.0	16428-4109c1	16:47:01.70	−41:15:18.0
16:46:46.81	−41:14:22.0	16428-4109c2	16:46:46.81	−41:14:22.0
16:47:33.13	−45:22:51.0	16435-4515c3	16:47:33.13	−45:22:51.0
16:51:44.59	−44:46:50.0	16482-4443c2	16:51:44.59	−44:46:50.0
17:00:33.38	−42:25:18.0	16573-4214c2	17:00:33.38	−42:25:18.0
17:07:58.78	−40:02:24.0	17040-3959c1	17:07:58.78	−40:02:24.0
17:23:00.30	−38:13:54.0	17195-3811c1	17:23:00.98	−38:13:54.0
17:23:00.30	−38:14:58.0	17195-3811c2	17:23:00.30	−38:14:58.0
		17195-3811c3	17:23:00.98	−38:15:38.0
17:38:49.87	−32:43:27.0	17355-3241c1	17:38:49.87	−32:43:27.0

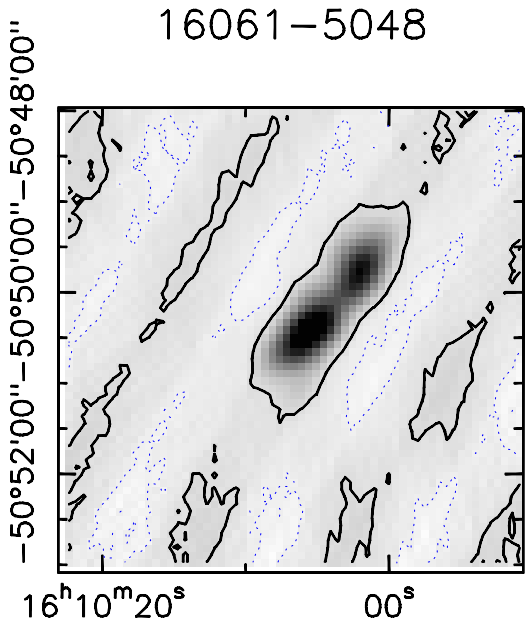

Figure 3.1: Typical map for a source in which we filter out the extended emission. The contours are ±3% of the intensity peak of 628.3 mJy.

3.3 Sample and tracer

The 39 fields considered in this work were selected from the Beltrán et al. (2006) survey at 1.2 mm, carried out with SEST/SIMBA towards IRAS sources, and contain 46 massive millimetre clumps. The coordinates of the field centres and of the clumps are listed in Table 3.1. Each field contains at least one massive clump. The selection of fields was done according to simple criteria: (i) source declination $\delta < -30°$; (ii) comparable numbers of MSX-dark and -bright sources; (iii) clumps as isolated as possible, i.e. with a separation greater than one SEST beam (24″) between MSX and non-MSX emitters to limit confusion; (iv) masses in excess of $\sim$ 40 $M_\odot$ in the Beltrán et al. (2006) catalogue. In this work we will use the gas temperature derived from ammonia observations and the dust temperature derived from a modified black-body fit to the SED to obtain a more accurate estimate of the mass and related quantities. For a spectroscopic tool we selected ammonia, which is an ideal tracer for cold, dense gas, not depleting up to high number densities ($\gtrsim 10^6$ cm^{-3}) and an excellent thermometer (Ho & Townes 1983). The ammonia inversion transitions are split into five electric quadrupole hyperfine components (cf. Fig. B.3, for (1,1) and (2,2) transitions), a main one at

the centre of the spectrum and four satellites, from the intensity-ratio of which one can derive the optical depth τ. This allows a direct estimate of the column density. The five lines are further split into several closely-spaced components by magnetic interactions between the nuclei; however, these lines are typically not resolved observationally.

3.4 Observations and data reduction

The fields were observed in the ammonia (1,1) and (2,2) inversion transitions (23694.50 MHz and 23722.63 MHz, respectively) and in the $H_2O(6_{16} - 5_{23})$ maser line (22235.08 MHz), with the Australia Telescope Compact Array (ATCA). The observations were performed between the 4th and 8th of March 2011, for a total telescope time of 48 hours. We used the array in configuration 750D, providing baselines from 31 m to 4469 m. The primary beam of the telescope at these frequencies is $\sim 2.5'$. The flux density scale was determined by observing the standard primary calibrator PKS1934−638 (0.78 Jy at 23650MHz), with an uncertainty expected to be $\lesssim$ 10%. Gain calibration was performed through frequent observations of nearby compact quasars; 0537−441 was used as the bandpass calibrator. Pointing corrections were derived from nearby quasars and applied online. Weather conditions were generally good, with a weather path noise $\sim$ 400 μm or better.

The total time on source was divided into series of snapshots with a variable duration of between 3 and 5 minutes observed over a range as large as possible in hour angle, to improve the uv-coverage for each target. As a consequence of the observing strategy, the total on source integration time varies, and is typically between $\sim$ 30 min and $\sim$ 1 hour. The CABB correlator provided two zoom bands of 64 MHz each, with a spectral resolution of 32 kHz ($\sim$ 0.4 km s^{-1} at $\sim$ 23.7 GHz). The two ammonia inversion transitions were observed in one band, and the other was centred on the H_2O maser line.

The data were edited and calibrated with the MIRIAD software package, following standard procedures. Deconvolution and imaging were performed in AIPS with the "imagr" task, applying natural weighting to the visibilities. Ammonia emission lines were visible only on the shortest baselines, thus we discarded all baselines $\gtrsim$ 30 kλ. In order to obtain images with the same angular resolution, we reconstructed all of them with a clean circular beam of diameter 20″, except for 17195−3811, 17040−3959c1 and 16428−4109c1. These sources have a poorer uv-coverage, resulting in a beam of roughly 20″ ×40″. Moreover, 16254−4844c1

and 16573−4214c2 were observed with a very limited range for the hour angle, making the 'clean' impossible. Ammonia spectra were extracted from the data cubes in two different ways: from a circular area of diameter 20″ centred at the peak emission, or averaged over the (larger) region enclosed in the 3σ contour of the NH_3(1,1) integrated emission. The spectra extracted from the data cube were imported in CLASS[2], and the lines were fitted using METHOD NH3 for the NH_3(1,1) inversion transition, that takes into account the hyperfine splitting of the line, thus giving as output also the optical depth of the main line. This method was also used for the (2,2) transition, in order to obtain a better estimate of the full width at half maximum (FWHM) linewidth ΔV and τ for the 9 sources for which we detected the (2,2) hyperfine structure. The spectral rms ranges from 3 to 55 mJy, with typical values around 10 mJy. The value of the rms for each spectrum is given in Table 3.2.

H_2O maser emission is detected on all baselines, allowing us to achieve the highest angular resolution allowed by the array configuration ($\sim 1-2''$). For 16254−4844c1 and 16573−4214c2, we could only establish whether there is maser emission or not, and we do not derive positions for the maser spots.

3.5 Results and analysis

3.5.1 Ammonia line profiles and properties

The NH_3(1,1) integrated emission (zeroth moment) is shown in panels (a) and (b) of Fig. B.1 together with the SEST 1.2 mm emission. Of the 46 clumps listed in Table 3.1, 36 were detected in both NH_3(1,1) and (2,2); 43 have been detected in NH_3(1,1). Three clumps were not detected in NH_3 at all: 15454−5335c2, 14166−6118c1 and 16164−4929c2. We discuss them in more detail in Appendix B.1. It is evident from the data that we filter out extended emission for some objects: Figure 3.1 shows that the lack of information on the largest spatial scales of emission causes the persistence of negative features in the corresponding maps. The general morphology of the ammonia emission traces well the mm-continuum emission. The peaks of NH_3(1,1) may show significant displacement with respect to the millimetre peak. For some sources this may be caused by a low signal-to-noise ratio of the NH_3 emission. Alternatively, the offset could be the result of optical depth or chemical effects. Twelve clumps have optical depths larger than

[2]Part of the GILDAS (Grenoble Image and Line Data Analysis Software `http://iram.fr/IRAMFR/GILDAS/`) package

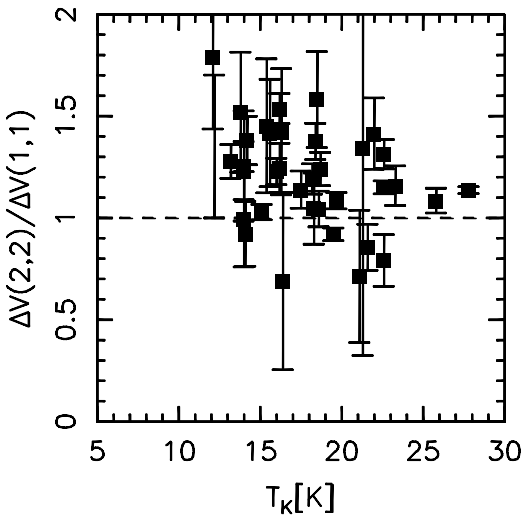

Figure 3.2: Ratio of the line FWHM ΔV for the NH_3(2,2) and (1,1) lines as a function of kinetic temperature, derived from our data assuming $\Delta V(2,2) = \Delta V(1,1)$.

1.5 in the main line and a reliable map, but only 3 of them show an offset. We also made maps of the emission of one of the satellite lines, (that are likely to be optically thin, as their optical depth is $\sim$ 4 times smaller than that of the main line), for the 7 sources showing the largest displacement between ammonia and millimetre peak. In only one source (15470-5419c1) is the peak of the satellite line emission coincident with the millimetre peak; in the others the offset remains unchanged. Thus, optical depth effects cannot be the dominant cause for the offset.

The peak flux of the two ammonia transitions, the rms of the spectra, ΔV, the optical depth τ, the systemic velocity $V_{\rm LSR}$ of the line, the rotation temperature $T_{\rm rot}$, the kinetic temperature $T_{\rm K}$ and the ammonia column density $N(NH_3)$ are listed in Table 3.2. The optical depth of the (1,1) transition ranges from $\ll$ 1 to $\sim$ 4, showing that ammonia emission is moderately thick in these objects.

Figure 3.2 shows that the FWHM ΔV of the (2,2) transition is on average slightly larger than that of the (1,1), indicating that the two transitions do not trace exactly the same volume of gas, the (2,2) transition being more sensitive to regions with a higher degree of turbulence due to its higher energy. The same result is found by Rygl et al. (2010). To estimate a rotation temperature (e.g., Mangum et al. 1992; Busquet et al. 2009) from the line ratio the two ammonia transitions must trace the same volume of gas. Thus, if this assumption is correct, the ΔV

should be the equal. The difference in ΔV that we measure is sufficiently small not to invalidate our assumption that the emission from NH_3(1,1) and (2,2) comes from the same region. We thus consider our temperature estimates reliable.

The kinematic distances were recomputed for the clumps with the $V_{\rm LSR}$ derived from NH_3 and the rotation curve of Brand & Blitz (1993), and were found to be in agreement with those given in Beltrán et al. (2006), except for 08477−4939c1, 16061−5048c1 and c2, 16093−5128c1, and 17040−3959c1. We choose to use the Brand & Blitz (1993) instead of the more recent one of Reid et al. (2009) because it still the best sampled in terms of Heliocentric- and Galactocentric distances and Galactocentric azimuth. A comparison shows that the kinematic distances derived with the Reid et al. (2009) curve are systematically smaller by $< 10 - 15\%$ for virtually all of our sources.

In the inner Galaxy, objects along the line-of-sight on either side of the tangent point have the same radial velocity, which leads to an ambiguity in the kinematic distance ("near" and "far") for several of our targets. Thus, we checked all our sources for associated 8 μm absorption features in the Spitzer/GLIMPSE images, for HI self-absorption observations towards them in the literature and for the height with respect to the Galactic midplane. The near distance is chosen if the complex is observed in absorption against the Galactic mid-InfraRed (MIR) background or if the source at the far distance is further than 150 pc from the Galactic plane ($\sim 2-3$ times the scaleheight of the molecular gas distribution; see Dame et al. 1987; Brand & Blitz 1993; Dame & Thaddeus 1994). Twenty-two of our sources meet the first criterion, and eight targets would be located at more than 150 pc from the midplane of the Milky Way at the far distance. Finally, Green & McClure-Griffiths (2011) report HI self-absorption measurements for 7 HII regions near our observed fields (containing 12 clumps in total). They locate 3 HII region/clump complexes at the far distance. However, we are confident that 2 (15557-5215 and 17040-3959) of those 3 are instead at the near distance as the 8 μm images show a clear absorption patch, and this is unlikely if the sources were on the far side of the Galactic centre. Hence the far distance was assigned to only 1 of our fields (containing 1 clump). The distances adopted are listed in Table 3.2. Where the near-far ambiguity could not be resolved (8 sources), the near distance was assumed.

3.5.2 Temperatures from ammonia

We derive the rotation temperature ($T_{\rm rot}$), and the molecular column density, following the method described in Busquet et al. (2009). This assumes that the transitions between the inversion doublets can be approximated as a two level system (see Ho

& Townes 1983), and that the excitation temperature and line widths are the same for both the (1,1) and (2,2) transition (see Sect. 3.5.1). The kinetic temperature T_K was then extrapolated from T_{rot} using the empirical method outlined in Tafalla et al. (2004). This relation gives results accurate to a 5% level for temperatures $\lesssim$ 20 K. This procedure was used to derive the gas temperature both from the spectra extracted from an area equal to that of the beam around the peak of the ammonia emission, and from those averaged over the whole area of NH_3(1,1) emission.

In order to also have an estimate of the uncertainty, the method to derive T_{rot}, T_K and ammonia column density $N(NH_3)$ was implemented in JAGS[3] (Just Another Gibbs Sampler). JAGS is a program for the analysis of Bayesian models, based on Markov Chain Monte Carlo simulations. It computes the *posterior* probability distribution, summarising our knowledge of the quantities considered, given a user-defined model (i.e. the equations and the assumptions of Gaussianity for the quantities directly derived from the fit in our case), the data and our prior knowledge of the quantities involved (Andreon 2011). This program was used to derive T_{rot}, T_K and $N(NH_3)$ and their uncertainty, propagating the Gaussian uncertainty of the parameters of the fit, as given by CLASS. Constant *priors* were used on these parameters, i.e. $T\tau$ and τ. To check the dependency of the results on the choice of the *prior*, we used also a Gaussian *prior* with a large σ. The results show that the derived parameters are virtually independent of the *prior* choice.

The temperatures and $N(NH_3)$ derived from the peak spectrum in this way are listed in Table 3.2, with their uncertainties. On the other hand, Table B.6 shows the observed spectral parameters for the spectra averaged over the whole NH_3(1,1) emission, the rotation and kinetic temperatures and the average ammonia column density, with the respective uncertainties. T_K obtained from the spectra extracted from both the peak of the NH_3 and those obtained from the whole area of emission are in the range between $\sim$ 10 and $\sim$ 28 K. T_{rot} and T_K calculated from the two sets of ammonia spectra agree very well in most cases. Few exceptions exist, where the 68% credibility intervals for the kinetic temperature do not overlap (3 cases), but with differences of $\sim$ 5 K at most, possibly due to dilution of the NH_3(2,2) emission, averaged over the same area as the (1,1). Thus in the following we use the T_K derived at the peak of ammonia emission

The gas temperatures derived from ammonia imply that the average ΔV of the ammonia lines (between $\sim$ 0.7 and 3.7 km s^{-1}) is well in excess of the thermal broadening in such cold gas ($\sim$ 0.15 km s^{-1} for T_K = 20 K), indicating that

[3] `http://mcmc-jags.sourceforge.net/`

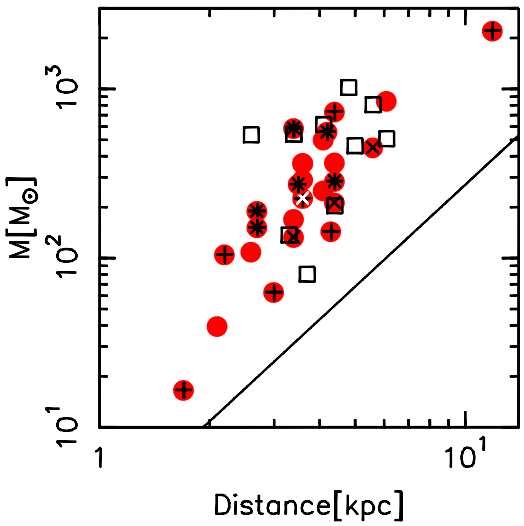

Figure 3.3: Mass of the clumps as a function of distance. The black solid line indicates the typical mass sensitivity for the SEST images (see text). The sources with signs of active star formation are shown as red filled circles, those without as black open squares (see Sect. 3.6). Associated MSX emission is indicated as a black plus, and radio-continuum emission as a black cross. The white cross indicates 17195-3811c1 (see text).

turbulence may play a major role in supporting the clumps.

3.5.3 Ammonia abundances

To determine characteristic ammonia abundances we used the spectra averaged over all the NH_3 emission. We derived $N(H_2)$ from the average 1.2 mm emission, collected over the same area as the ammonia, assuming that the clump is homogeneous (see Sect. 3.5.4), and divided the NH_3 column density (derived according to Sect. 3.5.2) by $N(H_2)$. The total range of abundances for all the sources in the sample lies between $\sim 10^{-9}$ and $\sim 10^{-7}$. For most of the objects the abundances are in the typical range of $\sim 10^{-8} - 10^{-7}$ (cf. Wienen et al. 2012, and references therein). We compared the NH_3 abundance derived in this way with the abundance derived at the peak of ammonia emission: we find this latter quantity is typically slightly greater than the former, with ratios in the range $\sim 0.6 - 10$ and mean and median values of 2.5 and 1.2, respectively. A sub-sample of the clumps observed in ammonia was also observed in $C^{18}O$ and N_2H^+ with APEX (Fontani et al. 2012).

The carbon monoxide was found to be heavily depleted in these sources, showing that they are in an early phase of evolution (cf. Sect. 3.6.2.7 and Chapter 4). On the contrary, the observed ammonia abundances indicate that NH_3 is not depleted on a large scale in these clumps, in agreement with studies of clumps in low-mass star-forming regions, whereas CO is also depleted (e.g., Tafalla et al. 2002).

3.5.4 Clump masses, diameters and gas densities

Determining accurate masses for the clumps is crucial to determine the evolutionary phase of the clump from a mass-luminosity plot (Molinari et al. 2008), and to see if the clump is massive enough to form high-mass stars. With our temperature determination (assuming that the gas, dust and kinetic temperatures T_g, $T_{\rm d}$ and $T_{\rm K}$ are equal) we are able to compute more accurate masses than those listed in Beltrán et al. (2006), that were derived assuming $T_d = 30$ K. The clump masses are calculated from the integrated 1.2 mm (250 GHz) flux through (Hildebrand 1983):

$$\mathrm{M_{gas}} = \gamma \frac{\mathrm{S_{250}} D^2}{\kappa_{250} \mathrm{B_{250}}(T_{\rm d})}, \tag{3.1}$$

where $\mathrm{S_{250}}$ is the total flux density at 250 GHz, D is the distance, γ is the gas-to-dust ratio, $\mathrm{B_{250}}(T_{\rm d})$ is the emission of a black-body with temperature equal to $T_{\rm d}$ at 250 GHz, and $\kappa_{250} \equiv \kappa_0 (250\ \mathrm{GHz}/\nu_0[\mathrm{GHz}])^\beta$ is the dust opacity per unit mass at the indicated frequency. We used $\kappa_0 = 0.8$ cm g^{-1} at $\nu_0 = 230.6$ GHz, as recommended by Ossenkopf & Henning (1994). The index β was derived from the modified black-body fit to the spectral energy distribution of the clumps, using only the SEST and Hi-GAL fluxes (see Sect. 3.5.5), where the data were available, otherwise we chose $\beta = 2$, as in Beltrán et al. (2006).

The masses and their uncertainties are again estimated with JAGS, taking into account the probability distribution of $T_{\rm K}$, as derived from the ammonia observations, the uncertainty of the integrated 1.2-mm flux (determined with standard techniques from the flux density rms in the images) and a 15% calibration uncertainty. We find systematically higher masses than Beltrán et al. (2006), because the temperatures are always lower than 30 K. The masses of the clumps tend to increase with the distance (see Fig. 3.3), as a result of the fact that nearby high-mass clumps are rare and that at large distances one cannot always separate individual clumps. In Fig. 3.3 we show the minimum detectable mass from the 1.2 mm maps, calculated from Eq. 3.1 for unresolved sources, with a typical 3σ flux density of 100 mJy/beam and a $T_{\rm d} = 15$ K. In this work we adopted the

Table 3.2: Parameters of the ammonia spectra extracted from an area equal to that of the beam, around the NH_3 emission peak. The columns indicate the clump name, the peak flux of the (1,1) transition and the rms of the spectrum, the V_{LSR} of the emission, the ΔV of NH_3(1,1), the opacity of the (1,1) line and its uncertainty, the peak flux of the (2,2) transition and the rms of the spectrum, and the ΔV of NH_3(2,2), T_{rot}, T_K and ammonia column density, with their uncertainties, the near and far kinematic distance. The clumps above the horizontal line are those classified as star-forming, while the clump below it are those classified as quiescent (see Sect. 3.6).

Clump	F_{max}(1,1)	RMS	V_{LSR}	ΔV(1,1)	τ(1,1)	$\sigma_{\tau(1,1)}$	F_{max}(2,2)	RMS	ΔV(2,2)	T_{rot}	68% int.	T_K	68% int.	$N(NH_3)$	68% int.	D_{near}	D_{far}	Notes
	(mJy)	(mJy)	(km s^{-1})	(km s^{-1})			(mJy)	(mJy)	(km s^{-1})	(K)	(K)	(K)	(K)	(10^{15} × cm^{-2})	(10^{15} × cm^{-2})	(kpc)	(kpc)	
08477-4359c1	341.9	9.0	10.9	1.3	0.3	0.1	78.8	8.0	1.7	14.4	12.6 – 15.9	16.2	13.8 – 18.0	0.63	0.53 – 0.67	2.2	–	
08589-4714c1	29.7	5.0	5.5	1.7	0.1	0.3	…	5.0	…	–	–	–	–	–	–	1.5	–	(1)
12300-6119c1	82.7	6.0	–42.3	1.3	0.3	0.3	31.8	6.0	1.7	17.8	16.0 – 19.1	21.3	18.4 – 23.3	0.19	0.10 – 0.24	4.3	4.3	
13039-6331c1	28.0	7.0	27.8	0.7	…	…	…	7.0	…	–	–	–	–	–	–	12.1	–	(1)
13560-6133c1	261.7	10.0	–56.4	1.7	1.2	0.1	138.0	1.10	2.0	18.9	15.1 – 21.0	23.3	16.8 – 26.1	1.07	0.95 – 1.14	5.6	5.6	
13563-6109c1	47.0	5.0	–53.2	1.2	0.1	0.2	…	4.0	…	–	–	–	–	–	–	5.6[a]	5.6	(1)
14166-6118c1	…	11.0	…	…	…	…	…	11.0	…	–	–	–	–	–	–	3.3[c]	8.4	(1)
15072-5855c1	36.8	6.0	–40.3	0.9	0.1	0.2	18.8	6.0	0.7	17.5	13.3 – 19.8	21.1	13.9 – 23.6	0.07	0.01 – 0.09	3.0[a]	10.0	
15278-5620c1	397.0	19.0	–48.8	1.5	1.4	0.2	182.1	16.0	1.8	16.2	15.2 – 16.6	18.7	17.3 – 19.7	2.26	1.48 – 2.47	3.4[a]	10.3	
15278-5620c2	455.7	17.0	–48.7	1.3	2.3	0.2	239.7	15.0	1.3	16.1	15.2 – 17.1	18.6	17.2 – 20.0	1.87	1.73 – 1.98	3.4[a]	10.3	
15470-5419c1	362.0	18.0	–60.8	2.6	1.4	0.1	148.2	17.0	2.7	15.6	11.7 – 18.0	18.3	12.0 – 20.9	2.61	1.98 – 2.56	4.1[a]	10.2	
	120.0	18.0	–58.9	3.7	2.1	0.4	50.0	17.0	4.7	–	–	–	–	–	–	4.1[a]	10.2	(1)
15470-5419c3	461.6	11.0	–61.0	1.8	1.7	0.1	222.1	10.0	1.7	16.8	16.5 – 17.0	19.5	18.8 – 19.9	2.07	2.00 – 2.14	4.1[a]	10.2	
15557-5215c1	347.0	18.0	–67.8	1.3	2.0	0.3	161.7	16.0	2.0	15.7	11.5 – 18.2	18.5	11.6 – 21.1	1.59	1.36 – 1.65	4.4[a]	10.2	
15557-5215c2	384.7	13.0	–67.2	1.3	3.0	0.2	278.6	16.0	1.7	18.7	17.6 – 19.7	22.6	20.1 – 24.0	1.92	1.83 – 2.02	4.4[a]	10.2	
15579-5303c1	354.1	10.0	–49.1	2.7	1.2	0.1	240.5	10.0	3.0	21.7	21.6 – 22.2	27.8	26.8 – 28.8	1.84	1.78 – 1.90	3.5[a]	11.1	
16061-5048c1	628.3	16.0	–66.9	2.4	1.2	0.1	383.1	16.0	2.6	20.5	18.6 – 22.1	25.8	21.3 – 27.9	2.58	2.45 – 2.67	4.4[a]	10.6	
16061-5048c2	810.3	18.0	–67.1	1.9	2.9	0.1	517.1	15.0	2.3	18.8	18.3 – 19.4	22.6	22.1 – 23.4	2.86	2.65 – 2.98	4.4[a]	10.6	
16061-5048c4	428.8	16.0	–51.6	1.0	4.5	0.3	170.1	16.0	1.3	12.2	11.7 – 12.4	13.2	12.8 – 13.5	3.47	3.22 – 3.72	3.6[a]	11.4	
16093-5015c1	376.6	8.0	–42.4	1.2	0.1	0.0	95.5	8.0	1.3	15.3	14.5 – 16.2	17.5	16.3 – 18.3	0.47	0.44 – 0.49	3.1	11.9[b]	
16093-5128c1	481.8	17.0	–63.1	1.2	2.4	0.2	216.3	15.0	1.9	14.5	14.0 – 15.3	16.2	15.2 – 17.0	2.05	1.89 – 2.18	4.2[a]	10.7	
16093-5128c8	93.6	7.0	–95.9	1.0	1.0	0.4	25.6	6.0	0.7	14.2	8.9 – 17.8	16.4	9.2 – 19.5	4.84	2.24 – 4.88	6.1[c]	8.9	
16164-4929c2	…	5.0	…	…	…	…	…	4.0	…	–	–	–	–	–	–	2.6[a]	12.6	(1)
16254-4844c1	439.7	55.0	–44.7	1.6	2.6	0.6	274.4	56.0	2.3	18.2	14.9 – 19.1	22.0	17.2 – 23.5	2.45	2.05 – 2.81	3.4[a]	12.0	(2)
16428-4109c1	265.1	8.0	–24.5	1.3	0.2	0.0	90.0	8.0	1.7	16.0	15.0 – 16.8	18.4	17.5 – 20.1	0.39	0.36 – 0.41	2.7[a]	13.6	
16428-4109c2	471.7	9.0	–25.1	1.1	1.2	0.1	207.6	7.0	1.2	16.9	16.8 – 17.3	19.7	19.2 – 20.4	1.06	1.01 – 1.10	2.7[a]	13.6	
16573-4214c2	536.7	52.0	–27.3	1.4	2.1	0.4	218.0	45.0	2.0	14.0	12.7 – 15.1	15.6	13.5 – 17.1	2.51	2.01 – 2.92	2.6[a]	13.7	(2)
17040-3959c1	138.9	8.0	–15.6	1.9	3.5	0.3	87.5	8.0	2.2	15.9	15.1 – 16.5	18.2	16.8 – 18.8	2.13	1.97 – 2.28	2.1[a]	14.4	
17195-3811c1	181.3	10.0	–25.7	1.4	2.9	0.3	81.9	10.0	1.2	17.8	13.2 – 20.3	21.6	14.0 – 24.5	0.61	0.50 – 0.69	3.6[a]	13.2	
17195-3811c2	387.3	6.0	–25.5	0.8	1.2	0.0	120.9	6.0	1.0	14.3	14.0 – 14.4	16.0	15.4 – 16.3	0.78	0.75 – 0.80	3.6[a]	13.2	
17195-3811c3	163.8	6.0	–25.3	0.8	1.0	0.2	65.2	5.0	1.2	13.0	12.2 – 13.7	14.2	13.4 – 15.4	1.02	0.91 – 1.10	3.6[a]	13.2	
17355-3241c1	130.4	6.0	–3.5	1.0	0.2	0.2	59.0	6.0	0.8	18.7	17.3 – 19.9	22.6	20.1 – 24.7	0.17	0.13 – 0.20	1.7[a]	15.3	
10088-5730c2	12.0	5.0	–4.6	0.7	…	…	…	4.0	…	–	–	–	–	–	–	1.2[c]	2.5	(1)
13560-6133c2	114.5	13.0	–56.5	1.3	2.7	0.6	55.1	10.0	1.9	13.5	8.8 – 15.7	15.4	8.6 – 18.2	1.59	0.91 – 1.71	5.6	5.6	
14166-6118c2	257.7	11.0	–39.6	1.1	0.5	0.2	60.0	11.0	1.3	12.8	11.6 – 14.1	14.0	12.2 – 15.4	0.53	0.39 – 0.61	3.3[c]	8.4	
14183-6050c3	52.3	6.0	–44.4	0.8	1.5	0.7	9.0	3.0	1.4	11.2	8.3 – 13.2	12.1	8.5 – 14.6	0.61	0.25 – 0.66	3.4[a]	8.4	
15038-5828c1	154.7	11.0	–68.7	1.8	1.4	0.3	38.6	10.0	2.7	12.6	11.7 – 13.5	13.8	12.4 – 14.7	1.15	0.94 – 1.34	5.0[a]	8.0	
15454-5335c2	…	55.0	…	…	…	…	…	55.0	…	–	–	–	–	–	–	…	…	(1)
15470-5419c4	340.9	12.0	–58.6	1.2	2.1	0.2	86.7	11.0	1.1	12.7	9.8 – 14.1	14.1	10.4 – 15.6	1.90	1.32 – 2.05	4.1[a]	10.2	
15557-5215c3	314.7	9.0	–68.6	1.3	3.0	0.1	129.4	9.0	1.3	13.7	12.6 – 14.5	15.1	13.8 – 16.4	2.13	1.93 – 2.28	4.4[a]	10.2	
15579-5303c3	123.2	9.0	–74.2	1.2	0.1	0.1	24.6	8.0	1.6	11.3	9.3 – 12.9	12.2	9.3 – 13.8	0.26	0.17 – 0.32	4.8[a]	9.8	
16093-5128c2	135.1	12.0	–96.9	2.0	1.7	0.3	42.6	14.0	2.0	12.8	11.2 – 13.7	14.0	11.7 – 15.3	1.49	1.17 – 1.73	6.1[c]	8.9	
16164-4929c3	398.1	8.0	–31.8	1.4	1.7	0.1	84.6	8.0	1.7	12.8	10.5 – 14.4	14.0	11.1 – 15.8	1.73	1.32 – 1.88	2.6[a]	12.6	
16164-4929c6	25.4	5.0	–32.6	0.8	3.3	1.5	…	4.0	0.7	–	–	–	–	–	–	2.6[a]	12.6	(1)
16164-4837c2	69.8	5.0	–51.2	0.8	1.0	0.5	…	4.0	0.8	–	–	–	–	–	–	3.6[a]	11.7	(1)
16435-4515c3	43.6	5.0	–51.7	1.1	1.3	0.6	…	4.0	1.4	–	–	–	–	–	–	4.0[c]	12.0	(1)
16482-4443c2	206.7	11.0	–42.4	1.2	0.6	0.3	48.8	10.0	1.7	14.2	10.1 – 16.6	16.3	10.6 – 18.9	0.59	0.45 – 0.61	3.7[c]	12.4	

Notes. (1) Source excluded from the analysis due to non-detection in NH_3(2,2) (signal-to-noise< 3).
(2) Source with a single observation: spectra extracted from non-cleaned maps.
[a] The distance ambiguity was resolved for this source. We chose the near distance.
[b] The distance ambiguity was resolved for this source. We chose the far distance.
[c] Distance ambiguity not resolved. The near distance was assumed for this source.

mass computed within the FWHM contour, in order to consider only the inner regions of the clump, excluding the external envelope (see Sect. 3.6), and because the measured diameter depends on the signal-to-noise ratio. Therefore when we generically speak of the mass we refer to masses computed within the FWHM contour. In this way the mass could be underestimated by a factor of 2, if the source is Gaussian and the envelope contribution is negligible. Our mass estimates are thus conservative, and the possible variation is indicated in figures 3.4 and 3.11 for comparison. The masses are listed in Table B.1. For completeness, masses and densities computed within the 3σ contour are shown in Table B.2.

Angular diameters were derived from 1.2 mm maps. The beam-corrected angular diameters θ of the clumps at FWHM level are estimated assuming that the sources are Gaussian, using the relation $\theta = \sqrt{\mathrm{FWHP}^2 - \mathrm{HPBW}^2}$, with FWHP = $2\sqrt{\mathrm{A}/\pi}$, where A is the area within the contour at half peak intensity, and HPBW is the SEST half-power beam width. If the angular size derived in this way is less than half the beam size, the source is deemed unresolved and we set an upper limit to its size equal to half the HPBW (Wilson et al. 2005). The linear diameters at FWHM level range from ~ 0.2 to ~ 2.0 pc (Table B.1).

Kauffmann & Pillai (2010) derived an empirical relation between mass and radius to separate the clumps that are able to form high-mass stars from those that are not. With the mass now much better constrained, we can use this relation to test if our clumps have the potential of forming massive stars. In Fig. 3.4 we show the mass and size of our clumps, compared to the Kauffmann & Pillai (2010) relation, scaled to the same dust opacity as used in the present work. From the figure we observe that the vast majority of our sources lie above the Kauffmann & Pillai (2010) relation, indicated as a dashed line, corroborating the idea that the whole sample is constituted of similar objects and suggesting that virtually all of them could form massive stars. This makes our sample a good one to study the evolution of massive clumps potentially able to form massive stars.

The column- and volume-densities of molecular hydrogen were calculated using the mass and the diameters, assuming spherical symmetry and correcting for helium ($\sim 8\%$ in number; e.g., Allen 1973). These two quantities are found to lie between $\sim 0.1 - 6 \times 10^{23}$ cm^{-2}, and $0.2 - 20 \times 10^5$ cm^{-3}, respectively: values like these are typical of IRDCs (e.g., Egan et al. 1998; Carey et al. 1998, 2000; Pillai et al. 2006). The surface density Σ was determined by averaging the mass over the deconvolved FWHM area of emission at 1.2 mm. Σ for the clumps in this sample is found to lie between 0.03 and 1.5 g cm^{-2}.

The mass, volume-, column-, and surface densities with their 68% credibility intervals for all the clumps are listed in Table B.1.

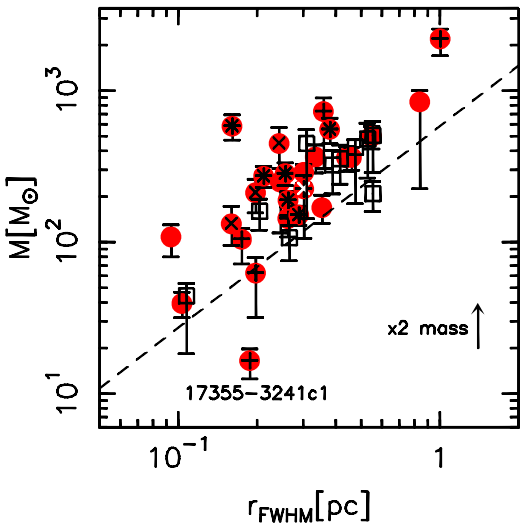

Figure 3.4: Mass-radius plot; $r_{\rm FWHM}$ is the beam-corrected radius at FWHM level. The symbols are the same as in Fig. 3.3. The boundary for massive-star formation derived by Kauffmann & Pillai (2010) ($M[\mathrm{M}_\odot] = 870(r/\ \mathrm{pc})^{1.33}$, rescaled to match our dust opacity) is indicated as a dashed line. Sources above this line are able to form massive stars. The uncertainty in mass is shown for each point. A variation of a factor of 2 in mass (see text) is indicated in the bottom right corner.

3.5.5 Spectral energy distribution

Important insights in the evolutionary state of a source can be gained through its L/M ratio, as proposed by Saraceno et al. (1996) for the low-mass regime and by Molinari et al. (2008) for the high-mass regime. We constructed the Spectral Energy Distribution (SED) for the sources in our sample complementing the SEST data with Herschel[4]/Hi-GAL (500 μm, 350 μm, 250 μm, 160 μm, 70 μm; Molinari et al. 2010), MIPSGAL (24 μm; Carey et al. 2009), MSX (band A 8.28 μm, C 12.13 μm, D 14.65 μm, E 21.30 μm; Price et al. 2001) and GLIMPSE (8.0 μm, 5.8 μm, 4.5 μm, 3.6 μm; Benjamin et al. 2003; Churchwell et al. 2009) data. We smoothed all the images to a common resolution of 25″ (the approximate resolution of the 350 μm image) except that at 500 μm, which has a resolution of ∼ 36″. Two different polygons were defined for each wavelength: one to derive the flux density of the source, and the other for the background in the region. The bolometric

[4]Pilbratt et al. 2010. Here we use the PACS (Poglitsch et al. 2010) and SPIRE (Griffin et al. 2010) instruments.

luminosity was calculated by integrating the fluxes over frequency, interpolating linearly between the measured fluxes at different frequencies in logarithmic space. The uncertainty was estimated by simply interpolating between the lower and upper limit of the 68% credibility interval of the fluxes used to derive the luminosity, respectively.

The fluxes at the longest wavelengths in the SED can be used to infer the typical properties of the dusty envelope. With this in mind we fitted the SED fluxes, down to 70 μm with a modified black-body. The point at 70 μm was included in the fit to better constrain the temperature in the case where the SED has its peak shortward of 160 μm. The inclusion of the flux at 70 μm implies that we will measure a higher $T_{\rm d}$, because we are tracing the warm dust layers near the embedded (proto)star. The fit procedure is described in Appendix B.2. The results of the modified black-body fit, the luminosity derived integrating the SED from 1.2 mm down to 3.6 μm, and the uncertainties in these quantities for each clump are listed in Table 3.3. In the table we list only the clumps with data in all the five Herschel/Hi-GAL bands. Figures B.5 and B.6 show the SED with the fit results. 17195-3811c1 is on the edge of the Herschel/HiGAL 160/70 μm maps, thus is not included here. However we use the lower limits on the fluxes at these wavelengths for the fit with the Robitaille models (see below) for this latter source.

From Fig. 3.5 we can see that the characteristic $T_{\rm d}$ obtained from the fit of a modified black-body to the SED down to 70 μm is usually in good agreement with $T_{\rm K}$ derived from the ammonia observations. Seven sources have $|T_{\rm K} - T_{\rm d}| \geq 5$ K and uncertainties not large enough to explain this difference, implying a statistically significant discrepancy. Four of these objects have $T_{\rm d} > T_{\rm K}$: these are also the cases where $T_{\rm d}$ is high, always above 20 K. The discrepancy may arise from a combination of different causes: the fact that the ratio of the two lowest transitions of ammonia is optimal to derive temperatures only up to $20 - 25$ K, that ammonia and dust emission are probing different regions of the clump, and that the strong emission in these clumps from warm dust, heated by the central star and visible at 70 μm, is biasing the modified black-body fit towards higher $T_{\rm d}$.

The gas masses obtained from the modified black-body fit usually agree, within the uncertainties, with those derived simply from the 1.2 mm continuum, and lie between the mass within the 3σ and that within the FWHM contour (Fig. 3.6). As not all sources have a complete SED, and considering the reasonable agreement between masses determined from the 1.2 mm integrated flux and from the modified black-body fit to the SED, we decided to use the former in the following analysis, so that we could also assign a size to the source consistently.

Table 3.3: Parameters derived from the modified black-body fit of the SED down to 70 μm, and luminosity of the clumps (integrated from 1.2 mm and 3.6 μm). The clumps above the horizontal line are those classified as star-forming, while the clump below it are those classified as quiescent (see Sect. 3.6). The columns show the dust temperature ($T_{\rm d}$), the mass (M) of the gas and the dust emissivity index β from the modified black-body fit, and the luminosity of the clumps derived integrating the SED, with their uncertainties.

Clump	$T_{\rm d}$	68% int.	M	68% int.	β	68% int.	L	68% int.
	(K)	(K)	($10^2 \times M_\odot$)	($10^2 \times M_\odot$)			($10^2 \times L_\odot$)	($10^2 \times L_\odot$)
13560-6133c1	24.3	22.8 – 25.5	6.2	5.3 – 7.2	1.4	1.2 – 1.5	30.1	25.6 – 34.3
13563-6109c1	22.0	20.8 – 23.3	2.4	2.0 – 2.9	1.8	1.6 – 2.0	27.3	24.2 – 30.4
15072-5855c1	26.5	25.0 – 28.0	0.5	0.4 – 0.6	1.7	1.5 – 1.9	11.4	10.2 – 12.6
15278-5620c1	27.8	26.0 – 29.3	6.0	5.1 – 7.0	1.8	1.6 – 1.9	266.2	241.1 – 291.1
15278-5620c2	11.2	9.8 – 12.3	4.4	3.5 – 5.3	2.1	1.7 – 2.4	1.4	0.8 – 1.8
15470-5419c1	16.6	15.8 – 17.3	4.0	3.5 – 4.8	1.5	1.3 – 1.7	4.0	3.2 – 4.5
15470-5419c3	19.2	18.3 – 20.0	3.6	3.1 – 4.3	1.6	1.4 – 1.8	7.9	6.7 – 8.9
15557-5215c1	23.8	22.3 – 25.0	5.3	4.5 – 6.3	1.8	1.6 – 2.0	76.2	68.0 – 84.4
15557-5215c2	15.6	14.8 – 16.8	3.6	2.9 – 4.5	2.1	1.8 – 2.3	7.4	5.9 – 8.5
15579-5303c1	24.5	23.0 – 25.5	5.3	4.6 – 6.1	1.9	1.7 – 2.0	84.8	75.9 – 93.6
16061-5048c1	19.9	19.0 – 20.8	6.0	5.1 – 7.0	2.0	1.8 – 2.1	33.8	29.7 – 37.6
16061-5048c2	21.3	20.3 – 22.3	5.9	5.1 – 7.0	2.2	2.0 – 2.3	86.3	77.0 – 95.5
16061-5048c4	9.5	8.8 – 10.3	8.5	7.0 – 10.2	2.5	2.2 – 2.8	2.1	1.4 – 2.6
16093-5015c1	20.8	19.8 – 21.8	20.9	17.8 – 24.3	1.6	1.4 – 1.8	90.0	77.5 – 101.5
16093-5128c1	23.8	22.5 – 25.0	4.6	4.0 – 5.3	2.2	2.0 – 2.4	256.9	234.4 – 279.3
16093-5128c8	13.8	12.8 – 15.3	1.8	1.5 – 2.2	2.3	2.0 – 2.6	3.5	2.4 – 4.2
16254-4844c1	17.6	16.8 – 18.3	2.6	2.2 – 3.1	1.6	1.5 – 1.8	4.1	3.4 – 4.6
16573-4214c2	16.0	15.3 – 16.5	2.1	1.8 – 2.4	1.8	1.6 – 1.9	2.6	2.2 – 3.0
17040-3959c1	17.2	16.5 – 17.8	0.5	0.4 – 0.6	2.3	2.2 – 2.5	2.5	2.2 – 2.8
17355-3241c1	23.8	22.5 – 24.8	0.35	0.3 – 0.4	2.1	1.9 – 2.2	19.0	17.1 – 21.0
14166-6118c2	18.1	15.3 – 20.8	0.5	0.4 – 0.6	1.7	1.2 – 2.0	1.3	0.8 – 1.7
14183-6050c3	16.1	15.0 – 17.0	1.0	0.7 – 1.2	1.9	1.6 – 2.3	2.3	1.5 – 2.7
15038-5828c1	12.2	11.3 – 13.3	5.4	4.5 – 6.5	2.1	1.8 – 2.4	3.3	1.9 – 3.8
15470-5419c4	11.1	10.3 – 12.0	6.2	5.1 – 7.5	2.4	2.0 – 2.6	2.9	1.9 – 3.7
15557-5215c3	9.6	8.5 – 10.5	3.6	2.9 – 4.5	2.9	2.5 – 3.3	1.8	1.1 – 2.6
15579-5303c3	15.6	14.5 – 17.0	3.4	2.7 – 4.3	1.6	1.3 – 1.9	3.9	2.1 – 4.8
16093-5128c2	10.4	9.0 – 11.5	5.1	4.0 – 6.1	2.7	2.3 – 3.0	3.2	1.7 – 4.0
16164-4929c3	9.2	8.3 – 10.3	4.7	3.8 – 5.7	2.6	2.2 – 2.9	1.0	0.6 – 1.7
16164-4929c6	11.0	10.3 – 12.0	1.1	0.9 – 1.4	2.4	2.1 – 2.7	0.7	0.4 – 1.0
16164-4837c2	8.1	7.5 – 8.8	3.2	2.7 – 3.9	3.0	2.7 – 3.4	0.8	0.5 – 1.0
16435-4515c3	10.5	9.8 – 11.3	4.3	3.5 – 5.1	2.7	2.4 – 2.9	2.9	1.8 – 3.6
16482-4443c2	8.7	8.0 – 9.5	1.9	1.6 – 2.3	3.1	2.8 – 3.5	0.8	0.5 – 1.0

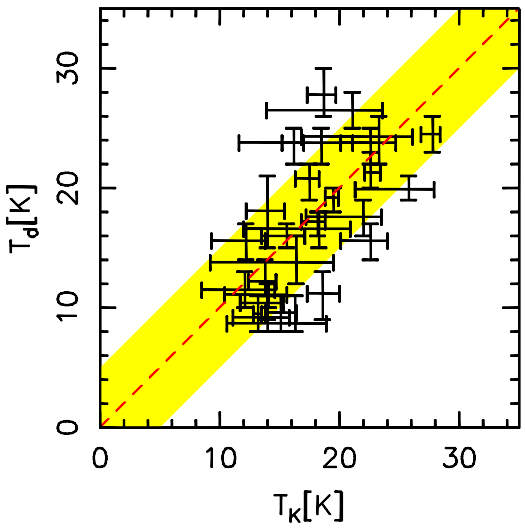

Figure 3.5: Comparison between the kinetic temperature ($T_{\rm K}$) derived from ammonia and the dust temperature ($T_{\rm d}$) from the SED-fit. The dashed line indicates equal temperatures and the yellow-shaded region shows a difference of ±5 K between the two temperatures.

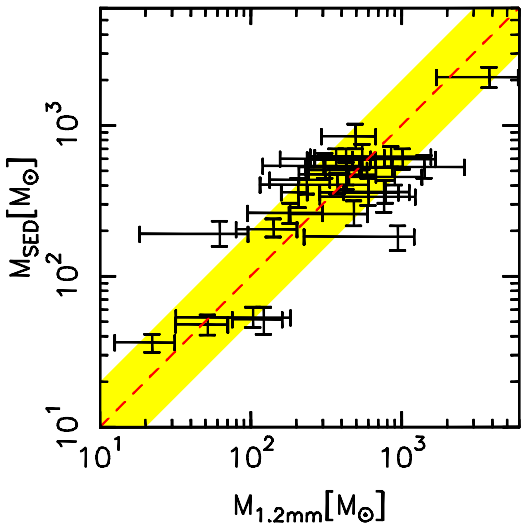

Figure 3.6: Comparison between the mass derived from the 1.2 mm continuum and from the SED fit. The uncertainties in $M_{\rm SED}$ are indicated. The bars for the 1.2 mm continuum range from the lower limit of the mass within the FWHM contour to the upper limit of the 3σ contour. The dashed line indicates equal masses and the yellow-shaded region shows a difference of a factor of two.

Robitaille et al. (2006) developed a code to compute the SED of axisymmetric YSOs. This code considers a central YSO with a rotationally flattened infalling envelope, the presence of bipolar cavities and a flared accretion disk, making use of a Monte Carlo radiation transfer algorithm to compute the flux of the object at wavelengths from the mm- to the near-IR regimes.

A vast range of stellar masses and of evolutionary phases are covered, from the earliest stages of strong infall to the late phase where only the circumstellar disk remains around the central object, and the envelope is completely dispersed. Following the discussion in Molinari et al. (2008), we use these models only for clumps that clearly contain an embedded source, and with detectable fluxes shortward of 70 μm in the smoothed images. Otherwise, only the modified black-body fit is done. To fit the SED with the Robitaille models, we make use of the online SED fitting tool[5] (Robitaille et al. 2007). In the tool, we allowed the foreground interstellar extinction to range between 1 and 2 mag kpc^{-1} (e.g., Allen 1973; Lynga 1982; Scheffler 1982). The stellar masses obtained from the fit range between $\sim$ 5 and $\sim$ 30 $M_{\odot}$, corresponding to spectral types approximately B7-O8. The luminosities derived vary between $\sim$ 600 and 65000 $L_{\odot}$, agreeing with those derived by simply integrating the SED, interpolating linearly in the log-log space. Our estimate of L tends to be lower, as the linear interpolation in the log-log space gives a lower limit for the luminosity and because of the model assumptions. However, for consistency, in the following we will use our estimate of the luminosity for all sources.

The envelope mass from the fit of the Robitaille models is greater than that derived either from the modified black-body fit or from the 1.2 mm-continuum. In this regard, Offner et al. (2012) compared synthetic SEDs of deeply embedded protostars, derived from simulated observation obtained with a 3D radiative transfer code for dust emission, for a vast range of parameters, with the best fit obtained from the standard grid of Robitaille models. These authors showed that usually the fit recovers the true luminosity and stellar mass, although with large uncertainties, but systematically overestimates the mass of the envelope, mainly due to the assumption of a different dust model. The difference is more pronounced in the mm-regime, strongly influencing the mass determination. Our assumption of dust opacity is similar to that used by Offner et al. (2012) in the mm-regime, explaining the discrepancy between our mass estimates and the envelope mass from the fit with the online SED fitting tool.

A summary of the results of the fits with the Robitaille models is shown in

[5] `http://caravan.astro.wisc.edu/protostars/`

Table 3.4: Summary of the properties derived from the fit of the Robitaille models to the SED of the objects with significant mid-IR emission. Our estimated range in L is shown for comparison. The ranges in M_*, L_{Rob} and $M_{\rm env}$ are those spanned by the best ten models. The masses are derived with a different dust model, and thus deviate from our estimate.

Clump	M_* ($M_\odot$)	L_{Rob} ($10^2 \times L_\odot$)	L ($10^2 \times L_\odot$)	$M_{\rm env}$ ($10^2 \times M_\odot$)
13560-6133c1	9.6 – 15.4	25 – 43	26 – 34	15.0 – 36.0
13563-6109c1	9.7 – 13.8	27 – 49	24 – 30	5.5 – 18.0
15072-5855c1	5.9 – 8.8	6 – 28	10 – 13	1.6 – 15.0
15278-5620c1	14.7 – 22.9	307 – 665	241 – 291	16.0 – 28.0
15557-5215c1	10.1 – 27.4	37 – 234	68 – 84	5.2 – 23.0
15557-5215c2	6.0 – 9.6	6 – 15	6 – 9	7.3 – 15.0
15579-5303c1	13.4 – 17.8	149 – 334	76 – 94	14.0 – 34.0
16061-5048c1	12.5 – 18.5	52 – 116	30 – 38	23.0 – 40.0
16061-5048c2	11.0 – 24.4	83 – 781	77 – 96	16.0 – 21.0
16093-5015c1	12.8 – 21.9	45 – 209	78 – 102	19.0 – 52.0
16093-5128c1	14.8 – 24.2	104 – 638	234 – 279	9.8 – 40.0
17195-3811c1	9.3 – 12.9	23 – 138	–	7.2 – 31.0
17355-3241c1	7.6 – 8.2	21 – 34	17 – 21	2.2 – 2.5

Table 3.4.

3.5.6 Stability and dynamics of the clumps

To investigate the stability of the clumps, we performed the simplest virial analysis, without taking into account magnetic or rotational support.

Equation (3) in MacLaren et al. (1988) gives a simple expression to evaluate the virial mass in the case of a spherical clump of radius R, with a given density profile:

$$M_{\rm vir}[M_\odot] = k\, R[\rm pc]\, \Delta V^2[\rm km\ s^{-1}], \tag{3.2}$$

where R is the radius and ΔV is the FWHM of the line. To derive the virial mass we assumed a constant density profile, which implies that $k = 210$. In this way we obtain an upper limit for the virial mass. Power law radial profiles for the gas volume density in the clumps can reduce the virial mass: the steeper the profile,

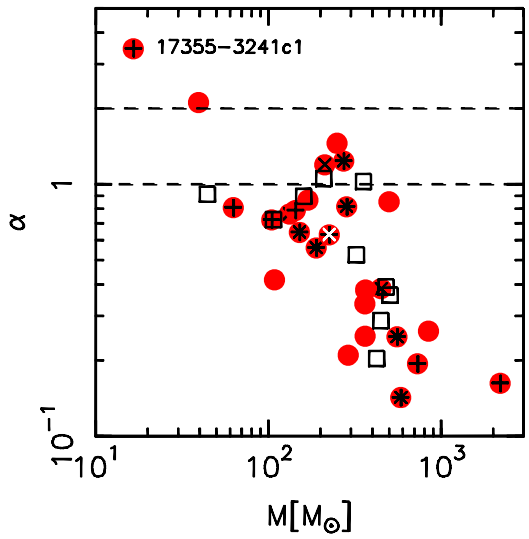

Figure 3.7: Virial parameter $\alpha = M_{\rm vir}/M$ as a function of M. The symbols are the same as in Fig. 3.3. The dashed lines indicate $\alpha = 2$ (clump gravitationally bound), and $\alpha = 1$ (clump in virial equilibrium).

the lower the virial mass. A radial dependence like $n(\mathrm{H_2}) \propto (r/r_0)^{-2}$ reduces the virial mass by about a factor of 2 (cf. MacLaren et al. 1988). The virial parameter $\alpha = M_{\rm vir}/M$ is used as an indicator for gravitational stability; $\alpha < 2$ implies that the clumps are gravitationally bound, and $\alpha = 1$ indicates virial equilibrium. Due to our choice of homogeneous clumps to derive the virial mass, the values that we derive for the virial parameter α are upper limits. Figure 3.7 shows that for virtually all the clumps we find $\alpha \lesssim 1$, implying that they are dominated by gravity. In Sect. 3.6.2.6 we discuss in detail the observed values of α.

3.5.6.1 Velocity gradients

The maps of the first moment of the ammonia (1,1) transition, computed from the main line, reveal the presence of velocity gradients in some of the sources. In order to investigate the gradients we masked the moment map at a level of about $1 - 5\%$ of the peak integrated emission. Then, the pixel value and coordinates are used as input to fit a plane to the masked map, to derive the direction- and the magnitude of the velocity gradients. The fit was performed with JAGS, allowing for an intrinsic scatter, and using a Gaussian with a dispersion for the measured mean velocity of 0.1 km s^{-1}, 25% of the width of a channel of the ATCA observations. The first

Table 3.5: Velocity gradients for the sources in Fig. 3.8. θ indicates the direction of the "red" velocities, east of north.

Source	θ (deg)	68%int. (deg)	Gradient (km s^{-1})	68%int. (km s^{-1})	Intr. scatter ($10^{-1} \times$ km s^{-1})	68%int. ($10^{-1} \times$ km s^{-1})
08477-4359c1	113.2	111.1 – 115.4	3.1	2.9 – 3.3	1.4	1.2 – 1.6
13560-6133c2	200.4	190.0 – 215.2	0.6	0.5 – 0.7	0.7	0.3 – 0.9
15038-5828c1	357.0	348.4 – 7.1	0.8	0.7 – 0.9	1.1	0.8 – 1.4
15470-5419c1	221.6	217.0 – 227.2	3.2	2.9 – 3.5	5.1	4.5 – 5.6
15470-5419c3	148.9	142.8 – 154.5	1.4	1.2 – 1.5	2.8	2.5 – 3.0
15470-5419c4	89.8	85.0 – 95.0	0.7	0.6 – 0.8	0.5	0.0 – 0.8
15557-5215c2	256.9	254.0 – 259.9	1.2	1.1 – 1.3	0.2	0.0 – 0.3
15579-5303c1	356.4	352.2 – 0.5	1.9	1.8 – 2.0	2.8	2.5 – 3.1
16061-5048c1	230.7	227.1 – 233.8	1.8	1.6 – 2.0	2.8	2.5 – 3.1
16061-5048c2	92.9	82.4 – 100.6	0.7	0.5 – 0.8	2.1	1.9 – 2.4
16061-5048c4	292.2	289.9 – 294.3	1.5	1.4 – 1.6	1.2	1.0 – 1.4
16093-5128c1	326.3	323.3 – 329.2	0.9	0.8 – 1.0	0.2	0.0 – 0.3
16164-4929c3	78.7	76.5 – 80.9	2.6	2.5 – 2.7	0.6	0.3 – 0.7
16428-4109c2	315.8	312.6 – 318.7	1.6	1.5 – 1.7	0.4	0.3 – 0.5

moment maps are shown in Figure 3.8. The typical magnitude of the gradients ranges between ~ 0.5 and 3 km s^{-1} pc^{-1}. The results are summarised in Table 3.5.

It is not easy to infer the nature of the observed gradients: some are possibly caused by stellar feedback, both from embedded and external sources (e.g. 16061-5048c4, cf. Sect. B.1), others may be the result of the superposition of different sources, or of rotation. If the gradients are due to rotation, from the measured gradients one can calculate the ratio of rotational kinetic energy to gravitational energy, usually indicated as β. The expression to estimate this parameter is (Goodman et al. 1993):

$$\beta = \frac{1}{2}\frac{p}{q}\frac{\omega^2 R^3}{GM}, \tag{3.3}$$

where $\overrightarrow{\omega}$ is the angular velocity vector. For spherical, homogeneous clumps $p/q = 2/3$; using the appropriate values for the clumps, and correcting for a random inclination (multiplying by $3/2$; see Goodman et al. 1993) we find typical values of $\beta \sim 0.05$. In only one case we find $\beta \sim 0.15$, for 16164-4929c3. However, the clump is not elongated perpendicular to the presumed rotation axis, thus suggesting that the gradient is not due to solid-body rotation. If the clump is not homogeneous, β diminishes: for an r^{-2} profile the ratio is reduced by a factor ~ 3. Such low values of β show that rotation is not important in supporting massive clumps. Similar values of β are commonly found in molecular condensations (cf., e.g. Goodman et al. 1993).

A more detailed analysis is to be carried out, combining MALT90 data with our ammonia observations to investigate the velocity field on larger scales.

3.5.7 Water maser emission

Thirteen clumps in our sample show maser emission. The spectra were extracted from the data cubes at each position where emission was detected (see Fig. B.4) within a polygon comparable to the beam dimensions (between $\sim 1''$ and $\sim 2''$), and imported in CLASS. The lines were then fitted with Gaussians. Two sources have very strong lines, reaching nearly ~ 100 Jy. We typically find multiple velocity components (up to 22) towards a single clump. A summary of the maser emission properties is shown in Table 3.6. The water maser range of velocities usually straddles the systemic velocity of the clump, as shown in Fig. 3.9 (cf. Brand et al. 2003). The positions of the maser spots are indicated in Fig. B.2 as white open squares. A comparison with Sánchez-Monge et al. (2013a) shows that 2 sources detected in their study are not detected in our observations, while 2 targets that we detect, were not detected in Sánchez-Monge et al. (2013a) (cf. Table B.3), as expected because of the well-known variability of water masers (e.g., Felli et al. 2007). All of these sources show other signs of active star formation.

3.6 Discussion

In order to investigate how the clump properties depend on their evolutionary state, the sources were first separated into two sub-samples, according to the presence or absence of signposts of active star formation. In particular, we considered the presence of water maser(s), "green fuzzies", 24 μm and radio-continuum emission.

- 24 μm emission: We overlaid the Spitzer MIPSGAL images at 24 μm and the SEST 1.2 mm maps of Beltrán et al. (2006), in order to identify those clumps with and without IR emission. If a 24 μm source is found at the location of the 1.2 mm emission peak, then it is considered as being associated with it. MIPSGAL images cover 41 of the clumps in this sample, the remaining 5 are covered by MSX images. Twenty-five clumps are IR-bright at 24 μm as shown in Fig. B.2, and 3 among those without Spitzer 24 μm data show emission in the 21 μm MSX image.
- "Green Fuzzies": extended 4.5 μm emission produced by shock-excited molecular lines, commonly associated with Class II CH_3OH masers (Cy-

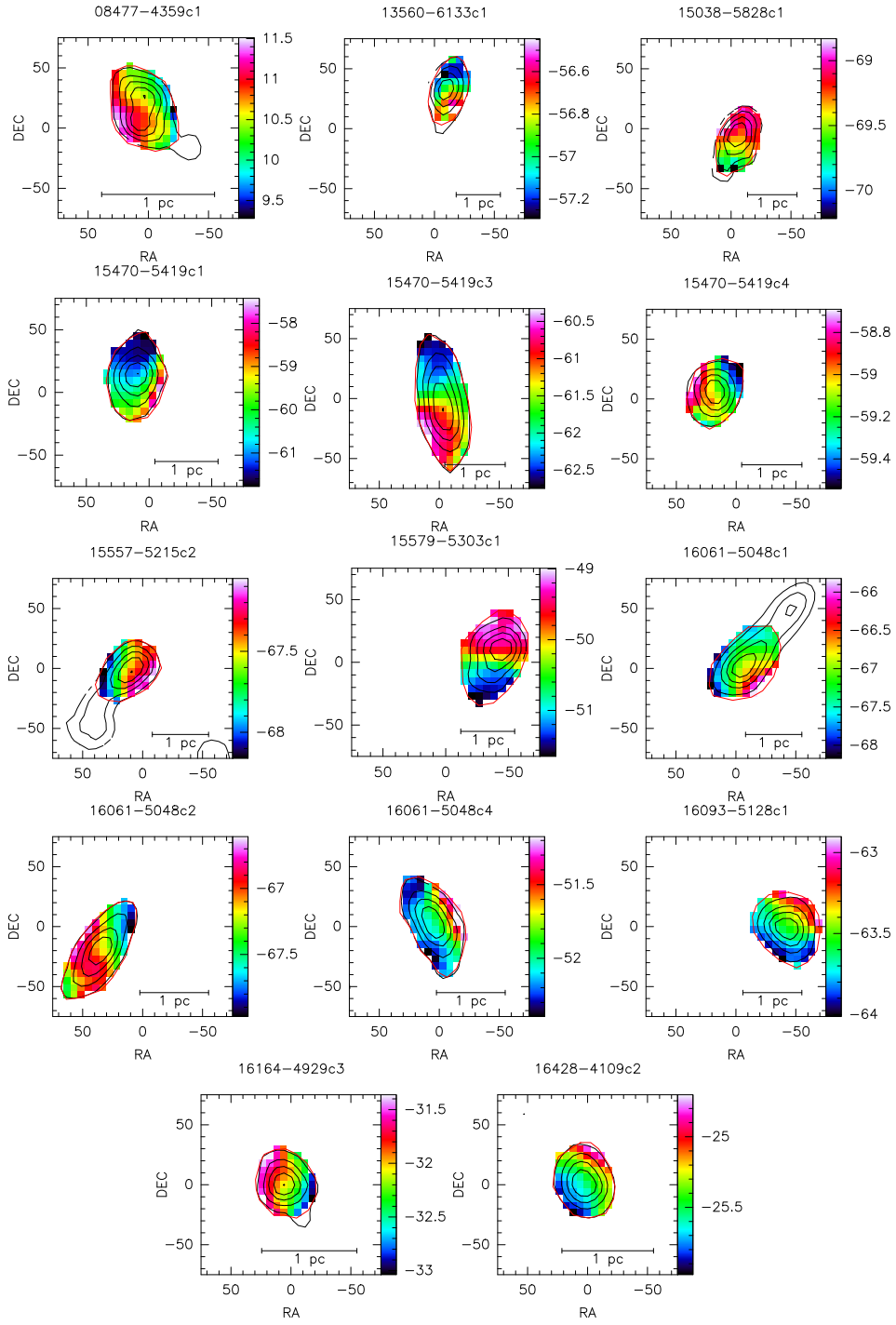

Figure 3.8: First moment maps of the sources showing a velocity gradient. The red contour indicates the area considered for the fit. To clarify the figure, we excluded from the maps the signal outside this contour.

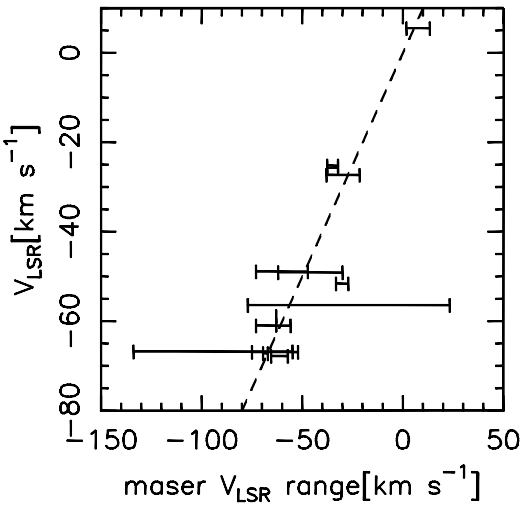

Figure 3.9: Range of velocity of the water maser *vs.* $V_{\rm LSR}$ of the clump. The dashed line indicates $V_{\rm H_2O} = V_{\rm LSR}$, i.e. a maser velocity equal to the systemic velocity of the clump.

ganowski et al. 2009). To identify the "green fuzzies", we followed the procedure described in Chambers et al. (2009). Again, only 41 clumps out of the 46 are covered by GLIMPSE data. Sixteen clumps show the presence of extended, excess 4.5 μm emission.

- Water masers: 13 clumps in our sample show maser emission. The water maser is a known indicator of star formation, thought to appear in the early stages of the process (Breen & Ellingsen 2011), and is observed both in low- and high-mass star formation regions.

- Radio-continuum: 40 of the clumps in our sample were observed with ATCA at 22 GHz and 18 GHz (Sánchez-Monge et al. 2013a). Twelve sources were detected, and 3 more have a tentative detection at about 3σ at one of the frequencies. The radio-continuum alone is not always considered sufficient to classify a source as star forming. This is because we find one source (16061−5048c4) in the sample where the radio emission is likely to come from an ionization front in the outer layers of the clump, based on the morphology of the emission or the lack of an IR source in the Spitzer/Hi-GAL images. This special case is discussed in the Appendix.

Table 3.6: Summary of the emission characteristics of H_2O masers.

Clump	Maser	$V_{\rm LSR}$(min, max)	$F_{\rm peak}$	$\int F dv$	$L_{\rm H_2O}$	$V_{\rm LSR}$ S.C.	ΔV S.C.	Offset (Ph.C.)
		(km s^{-1})	(Jy)	(Jy km s^{-1})	($10^{-7} \times L_\odot$)	(km s^{-1})	(km s^{-1})	($''$)
08589-4714c1	3	0.5; 14.8	1.67	2.4	1.3	4.8	1.2	2, −10
13560-6133c1	22	−78.2; 26.0	5.78	37.4	272.0	−53.3	1.1	−15, 35
15278-5620c1	6	−68.2; −43.5	84.5	85.4	228.9	−47.5	0.8	10, 79
15470-5419c1	1	−64.6; −61.2	1.95	2.1	8.2	−63.0	1.0	26, −8
15470-5419c3	4	−63.7; −51.9	3.93	9.3	36.3	−60.0	1.1	−2, 10
	2	−75.5; −64.1	0.57	1.2	4.7	−66.4	1.3	−31, −50
15557-5215c1	2	−68.4; −52.4	3.54	7.5	33.7	−57.2	1.6	42, −7
	2	−67.9; −60.4	9.03	11.3	50.7	−65.4	1.0	6, −57
15557-5215c2	1	−71.0; −67.8	2.56	2.3	9.4	−69.4	0.8	32, 33
	1	−69.4; −67.1	0.18	0.15	0.7	−67.1	0.8	7, 4
15579-5303c1	9	−63.1; −27.7	75.4	120.4	643.3	−47.7	0.9	−53, 13
	1	−38.5; −33.7	0.59	0.67	3.6	−35.8	1.0	−54, 15
16061-5048c1	6	−78.7; −50.9	19.6	23.3	104.6	−67.0	0.8	−3, 2
	2	−71.2; −68.1	0.47	0.51	2.3	−69.0	0.8	−9, 4
16061-5048c2	2	−79.5; −69.6	1.50	2.7	12.1	−77.7	1.6	45, −27
	3	−135.8; −63.5	0.54	1.8	8.1	−65.1	0.9	35, −20
	3	−79.6; −52.0	0.46	0.75	3.4	−54.8	1.8	42, −24
16061-5048c4	3	−35.6; −25.1	0.70	2.1	6.3	−33.2	1.5	−5, −2
16573-4214c2	5	−39.6; −20.2	1.30	2.5	3.9	−29.9	0.7	–[a]
17195-3811	5	−39.7; −29.5	8.39	10.4	31.3	−32.2	1.0	–[a]

Notes. [(a)] These sources have poor uv-coverage, thus no position for the maser spots is given.
The columns show the clump name, the number of Gaussian components in the spectrum, the range of $V_{\rm LSR}$ over which we detect emission, the flux density peak, the integrated emission, the water maser luminosity, the $V_{\rm LSR}$ and ΔV of the strongest component (S.C.), and the offset of the maser spot with respect to the phase centre (Ph.C.). No correction was performed for the primary beam.

If any of these signposts is observed (except radio continuum in the special case discussed in the Appendix), a clump is indicated as star-forming. Based on these criteria, of the 46 objects observed, 31 were classified as star-forming and 15 as quiescent. A summary of the clumps with specific indicators of ongoing star formation is given in Fig. 3.10. All the star formation signposts in each clump are presented in Table B.3. Figure B.2 shows all the observed fields of view and clumps (dashed and solid red circles, respectively), with the SEST emission (contours) superimposed on the MIPS 24 μm image, and the position of maser spots (white open squares) and "green fuzzies" (green open circles). Removing those clumps with no NH_3(2,2) detection, 26 and 10 clumps remain in the star-forming and in the quiescent sub-samples, respectively.

In the following, we compare the average properties of the clumps using the parameters we have derived, for the two sub-samples, to look for systematic differences in the physical properties characterising the two classes. Note that

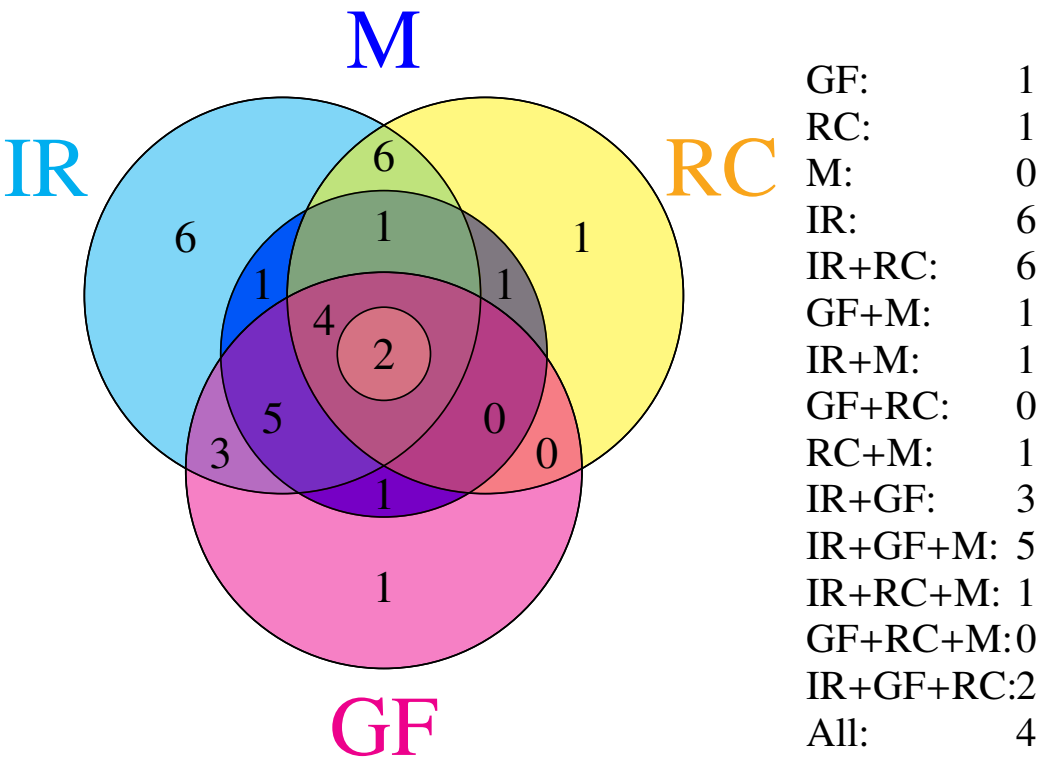

Figure 3.10: Summary of specific star formation indicators in the clumps. The labels correspond to green fuzzies (GF), mid-IR emission (IR), H_2O maser (M), and radio continuum emission (RC) (see Sect. 3.6 for details). For example, the small central circle shows the combination IR+GF+RC, with no maser detection, while the "triangular" area with a darker shade surrounding the small circle represents the presence of all four signposts of star formation.

hereafter the quiescent and star-forming sub-samples will be denoted with the acronyms **QS** and **SFS**, respectively.

3.6.1 The mass-luminosity diagram

To refine the separation in different evolutionary phases we make use of the mass-luminosity ($M - L$) plot, which is an efficient and well-established diagnostic tool to disentangle the different evolutionary phases of star formation in the low-mass regime (Saraceno et al. 1996, see Sect. 1.3.1.1). Molinari et al. (2008) proposed that it could also be used for high-mass stars, under the hypothesis that

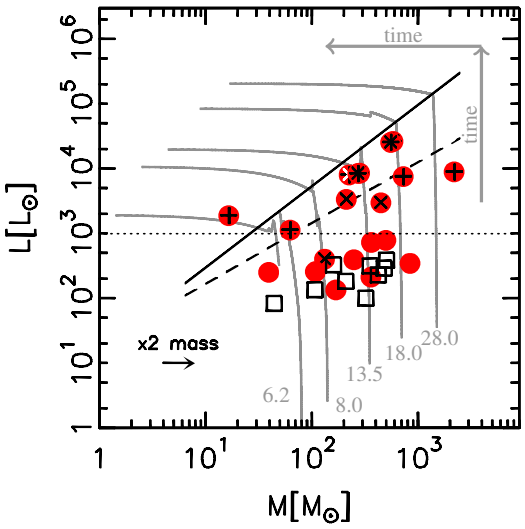

Figure 3.11: Mass-Luminosity plot for the sources in our sample with Hi-GAL observations. The mass is computed within the FWHM contour of 1.2 mm emission. The symbols are the same as in Fig. 3.3. The black solid line indicates the ZAMS locus, according to Molinari et al. (2008), while the dashed line indicates the ZAMS locus as determined by Urquhart et al. (2013a). The grey lines show the evolution of cores of different masses; the lines are labelled with the final mass of the most massive star (in $M_\odot$). Time increases from bottom to top and from right to left, as indicated. Radio-continuum emission and MSX emission are found nearly exclusively in clumps near the ZAMS. A variation of a factor of 2 in mass (see text) is indicated in the bottom left corner.

star formation at high- and low-mass proceeds in a similar fashion, with accretion from the surrounding environment playing a major role (e.g., Krumholz et al. 2009). Molinari et al. (2008) built a simple model for the evolution of a clump, based on the turbulent core prescriptions of McKee & Tan (2003), ranging from the early collapse phase to the complete disruption of the dusty envelope by the central object.

Figure 3.11 shows the $M - L$ plot for the sources in our sample for which we were able to derive the luminosity (see Sect. 3.5.5 and Table 3.3) from the integration of the SED (with the linear interpolation in the log-log space) and the mass derived from the 1.2 mm emission, for which we used the temperature determination obtained from the ammonia observations (Sect. 3.5.2). The black solid line indicates the ZAMS locus, according to Molinari et al. (2008), while the

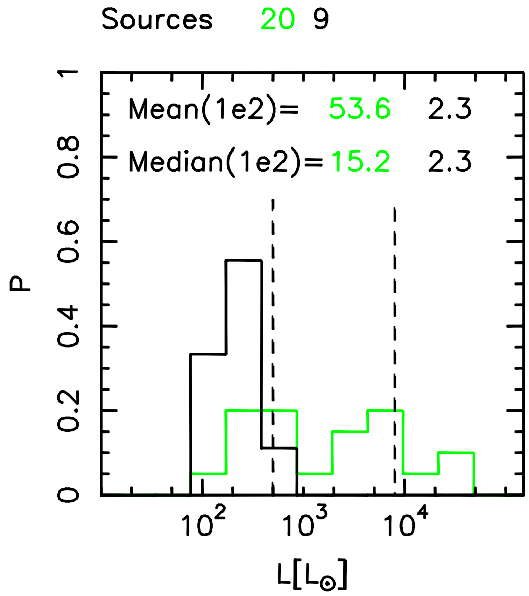

Figure 3.12: Normalised histogram of the luminosities for the SFS (green) and for the QS (black). 500 $L_\odot$ and 8000 $L_\odot$ are indicated by the dashed lines.

dashed line indicates the ZAMS locus as determined by Urquhart et al. (2013a). The latter authors consider clumps showing methanol maser emission and with a luminosity from the Red MSX Sources survey (Urquhart et al. 2008). 90% of the sources studied by Urquhart et al. (2013a) have $L > 10^3$ $L_\odot$, the remaining 10%, with $L < 10^3$ $L_\odot$, have low gas masses ($10^1 - 10^2$ $M_\odot$), and could be forming intermediate-mass stars. Objects classified as either YSO or UCHII regions were used to determine the ZAMS locus, as no statistically significant difference is found between the two classes. The difference in slope between the two ZAMS-lines could be due to the fact that in Molinari et al. (2008) the luminosities were determined from the Robitaille models, using IRAS fluxes in the FIR, and could thus be overestimated. The grey curves show the evolution of the source predicted by the simple model, for different final masses, from $\sim$ 6 to $\sim$ 30 $M_\odot$. Time increases in the direction of the arrows shown in the upper right part of the plot. In the collapse phase, before the central object reaches the ZAMS, the mass of the core envelope does not change by much, but the luminosity increases rapidly. After the central star reaches the ZAMS, the luminosity does not vary much, and the energetic radiation and wind begin to destroy the parental clump, visible as a steady decrease in envelope mass.

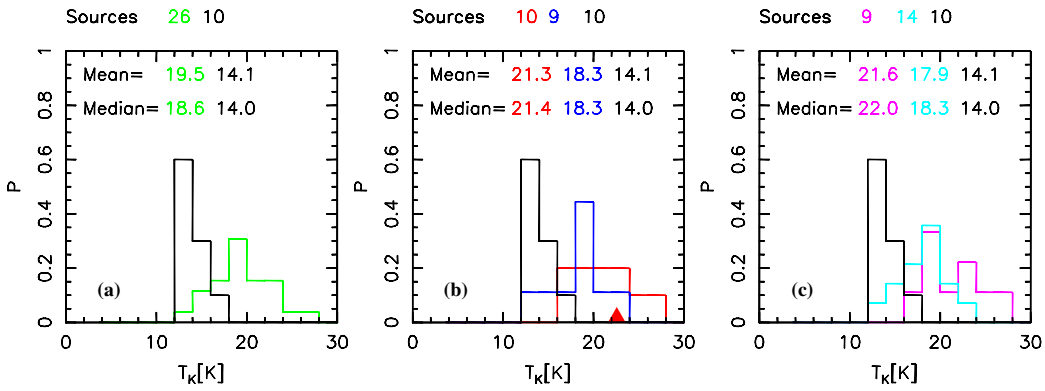

Figure 3.13: Normalised histogram (to the total number of sources in each class) of kinetic temperature for **(a)** the SFS (green), and the QS (black); **(b)** the same as **(a)**, but the SFS-2, with $L > 10^3$ $L_\odot$ (in red) are separated from the SFS-1 (in blue), the red triangle shows the temperature for the Type 3 source; **(c)** the same as **(a)**, but the SFS were divided into clumps with (magenta) and without (cyan) radio-continuum emission. Mean and median values of the temperature are indicated in each panel. The total number of sources in each class is shown above each panel.

Comparing the distribution of sources in the plot with the evolutionary tracks of the Molinari et al. (2008) model, our objects span the total range in envelope masses, for final masses of the star between about 6 and 30 $M_\odot$. The stellar masses are in agreement with those derived from the fit of the SED with the Robitaille models for the objects near the ZAMS, for which the final mass is similar to the current mass, as the main accretion phase is over. Massive stars appear to form virtually always in clusters (e.g., Lada & Lada 2003). In both the Molinari et al. (2008) and the Robitaille models the luminosity is considered as being dominated by the most massive object formed in the cluster. The derived bolometric luminosity and stellar mass could thus be overestimated.

A first macroscopic difference between the SFS and the QS sources is the luminosity. As can be seen in Fig. 3.12, the clumps in the QS have low luminosities, distributed between $\sim$ 100 and 500 $L_\odot$. On the other hand, the sources in the SFS show a peak at $\sim$ 500 $L_\odot$, but also a second peak at $L \sim 8 \times 10^3$ $L_\odot$ (both indicated as dashed lines in the figure). The distribution of the sources in the $M - L$ plot indicates that part of the sources in the SFS (10 out of 20, including 17195-3811c1, with the mean luminosity derived with the online SED fitting tool) are likely hosting

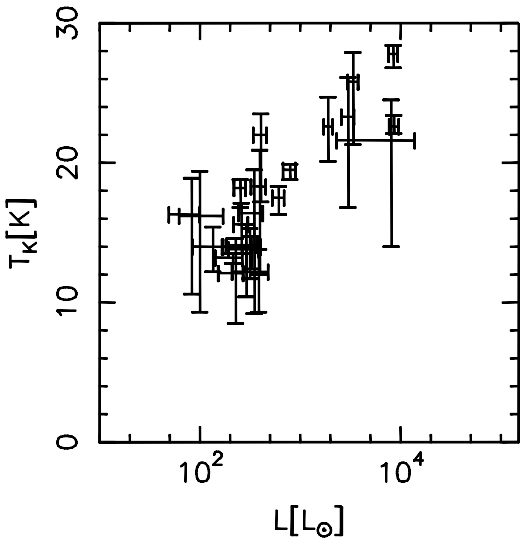

Figure 3.14: Correlation between luminosity and kinetic temperature. The uncertainties for L and T_K are indicated in the figure.

a ZAMS star and have stopped the accelerating accretion phase, according to the model of Molinari et al. (2008). The sources with signs of active star formation, but well below the ZAMS loci, are essentially indistinguishable from the quiescent ones in terms of luminosities. Figure 3.11 shows that in our sample all sources with $L > 10^3$ $L_\odot$ have strong IR (MSX) and/or radio continuum emission, while those below this threshold do not. The radio emission from the sources near the ZAMS locus, with final masses greater than 8 $M_\odot$ shows that the interpretation of the $M - L$ plot is essentially correct, and that the prediction of the end of the accelerating accretion phase is reasonably good.

The small range of luminosity and its low average value for the QS shows that this is a homogeneous sample, with all the clumps in an early phase of evolution. On the other hand, the SFS appear to include clumps in widely different evolutionary stages: the points in the diagram go from clumps similar to those of the QS, to clumps containing a ZAMS star and beyond, where the star is dispersing the envelope. For our sample, a simple criterion in luminosity is sufficient to separate the sources that likely have an embedded ZAMS star from the rest. Thus, in the following we will refer to objects containing a ZAMS star as those with $L > 10^3$ $L_\odot$. In Fig. 3.11 these objects fall in the region encompassed by the ZAMS loci, except 13560−6133c1 and 16093−5015c1, slightly below the Urquhart et al. (2013a) ZAMS locus.

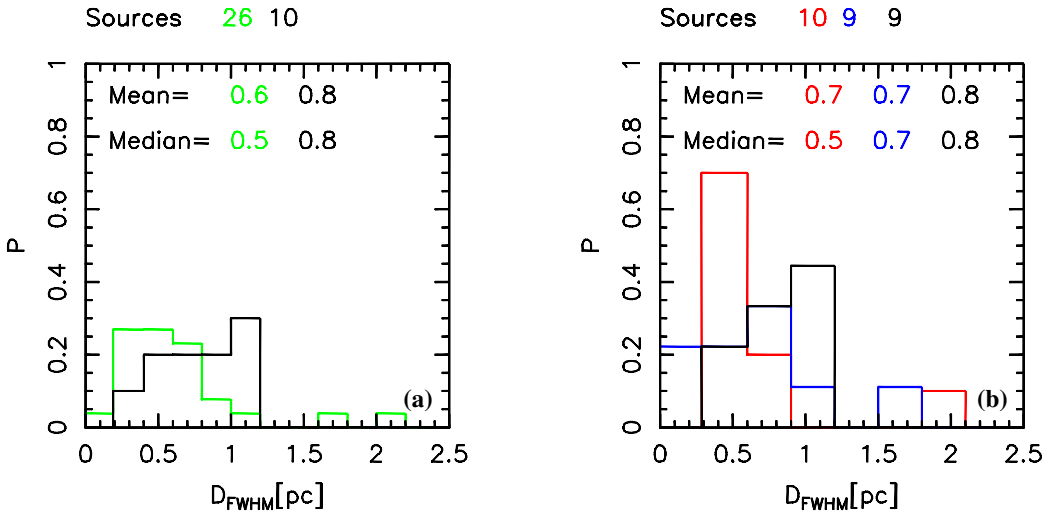

Figure 3.15: Histograms of the diameters of the clumps. Panel **(a)** shows the diameters of the SFS (green) *vs.* the QS (black). In panel **(b)** we show the SFS-2 in red, the SFS-1 in blue, and the QS in black. The total number of sources in each class is shown above each panel.

We can easily divide the clumps in this sample in Type 1, 2 and 3 according to the $M - L$ plot (see Molinari et al. 2008, and cf. Sect. 3.2); the classification of sources in one of the three types is shown in Table B.3. The clumps between the two ZAMS loci, with $L > 10^3$ $L_\odot$ would be Type 2 clumps (including the two sources slightly below the Urquhart et al. ZAMS locus, 13560−6133c1 and 16093−5015c1, the former of which shows also radio continuum emission), while the rest of the SFS and the QS would be Type 1. Type 1 sources include both pre-stellar and protostellar sources in early stages of evolution, for which the development of an HII region may be quenched by the high accretion rates. The leftmost point in the mass luminosity plot (Fig. 3.11) identifies the most evolved source in our sample, 17355−3241c1, with a relatively low mass and a high luminosity. This clump is the only Type 3 source in our sample, and has very strong emission even in the IRAC bands. 17355−3241c1 exemplifies the last phase of the evolution in the $M - L$ plot, when the parent cloud is dispersed by the destructive action of the central star. This source is discussed in more detail in Appendix B.1.

Thus, the $M - L$ plot and the signposts of active star formation give complementary information about the evolutionary state of the clump, allowing us to refine the Molinari et al. (2008) classification, separating objects likely hosting a

ZAMS star from the other sources in the SFS. Our original sample is thus finally divided into three different classes (without considering Type 3 objects): Type 1 quiescent clumps, apparently starless, Type 1 with signs of active star formation, but still a low luminosity and Type 2 sources, hereafter QS, SFS-1 and SFS-2, respectively. Table B.5 shows explicitly that SFS-1 and SFS-2 have very different luminosity-to-mass ratios. The clumps in the SFS-1 can be in a very early phase of the process of formation of a high-mass object; alternatively, the signposts of active star formation could be generated by more evolved lower-mass stars.

3.6.2 Properties of sources in different stages of evolution

3.6.2.1 Temperatures

The temperature of gas and dust may be influenced by the presence of a (proto)star deeply embedded in a clump. Figure 3.13a shows the histogram of temperatures for the two samples. The normalised counts of the SFS are shown in green, and those of the QS in black. We find that it is possible to observe temperature differences on a large scale, comparing the average values of $T_{\rm K}$ and $T_{\rm d}$ of the QS and the SFS. The typical $T_{\rm K}$ of the star-forming clumps is greater than that of the QS, with mean values of $T_{\rm K} = 19.5^{+1.5}_{-2.9}$ K and $14.1^{+1.8}_{-3.2}$ K, for the SFS and QS, respectively. Thus, the average temperature increases as evolution proceeds.

In Fig. 3.13b we can see that the SFS-2 (in red) show a slightly higher $T_{\rm K}$ ($T_{\rm K} = 21.4^{+1.7}_{-3.8}$ K) than the SFS-1 (in blue) ($T_{\rm K} = 18.3^{+1.4}_{-3.0}$ K). Figure 3.13b shows also the QS, to underline that both the SFS-1 and SFS-2 sources on average have a higher $T_{\rm K}$. Figure 3.13c shows that the SFS with 1.3 cm radio-continuum emission are hotter than those without it. A similar conclusion is found by Sánchez-Monge et al. (2013b), studying NH_3(1,1) and (2,2) at high angular resolution in cores in clustered high- and intermediate-mass star forming regions. They find that starless cores have an average $T \sim 15$ K, lower than $T \sim 21$ K found for protostellar cores. These values are very close to those found in this work. Sánchez-Monge et al. (2013b) show that the higher temperatures in starless cores in clustered environments with respect to more isolated cases can be explained considering external heating from the nearby massive stars. Also Rygl et al. (2010) and Urquhart et al. (2011) find that actively star-forming clumps are slightly hotter than the quiescent ones. A behaviour similar to that of the kinetic temperature is observed for $T_{\rm d}$ as a function of evolutionary phase, not unexpected given the good agreement of the two temperatures (see Sect. 3.5.5; Fig. 3.5). The mean values are $T_{\rm d} = 24.0^{+1.5}_{-1.6}$; $15.8^{+1.4}_{-1.6}$; $11.8^{+1.7}_{-1.5}$ K for SFS-2, SFS-1 and QS, respectively.

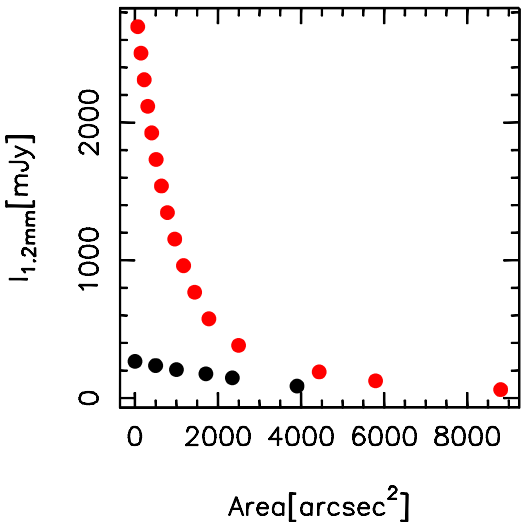

Figure 3.16: 1.2 mm intensity level as a function of the area within the contour for a typical QS (black) and SFS-2 (red) source, respectively.

Disregarding the 7 points with $|T_K - T_d| \geq 5$ K and non-overlapping 68% credibility intervals, we find a correlation between the luminosity and the kinetic temperature, shown in Fig. 3.14. A correlation between T_K and L_{bol} was also found by e.g., Churchwell et al. (1990), Wu et al. (2006), Urquhart et al. (2011), and by Sánchez-Monge et al. (2013b), for cores in clustered environments, using the luminosity of the whole region.

3.6.2.2 Sizes

From the panel (a) of Fig. 3.15 we note that the SFS tend to have smaller FWHM diameters than the QS. From the distribution of sizes shown in panel (b) we note that the SFS-2 have a peak at the smallest linear dimensions. Plotting the area within a specific intensity contour of 1.2 mm emission as a function of the intensity level and extrapolating linearly to zero intensity we get an idea of the source extent if we could observe with infinite sensitivity (cf. Brand & Wouterloot 1994). Figure 3.16 shows the 1.2 mm intensity level as a function of the area within the contour for representative sources in QS and SFS-2. For the SFS-2 we ignore the central emission peak for the fit. This method allow us to estimate the effect of the lower temperature on the clump size at the typical noise levels of the SEST maps.

This procedure shows that with our noise levels we miss $\sim$ 30% of the emission

area for a typical QS, while only $\sim 10-15\%$ is lost for a typical SFS-2. The SFS-1 usually show an intermediate behaviour. The larger fraction of emission area below the noise level for the QS confirms that we are not able to detect the external envelope of the coldest clumps, and that the actual linear size of QS sources is very similar to that of SFS-2 objects. On the other hand, the area within the FWHM contour is smaller for SFS-2 sources, possibly indicating that sources hosting a ZAMS object are more compact and centrally concentrated. We investigate an alternative possibility, namely that the observed FWHM size may be T-dependent, performing a simple test using a 1D simulation with RATRAN (Hogerheijde & van der Tak 2000), constructing a clump with a typical radial dependence of the density ($\propto r^{-1.7}$, cf. Beuther et al. 2002; Mueller et al. 2002), and comparing the continuum at 250 GHz with and without a central luminous heating source. The radial temperature dependence is assumed to be $\propto (r/r_0)^{-0.4}$ (e.g., Wolfire & Cassinelli 1986). We observe that the clump with the embedded source, has a smaller (by $20-30\%$) FWHM. This could explain the smaller sizes derived for SFS-2.

Urquhart et al. (2013a), also conclude that high-mass star forming clumps showing methanol maser emission are more compact and centrally concentrated than the rest of sources in the ATLASGAL survey (Schuller et al. 2009), comparing the "compactness" of the sources by means of the ratio of the peak and integrated sub-mm flux, for a much larger sample.

3.6.2.3 Densities

The mean column-, volume- and surface-densities are compared for QS and SFS, and for SFS-1 and SFS-2 in Fig. 3.17 and 3.18, respectively.

The histogram of the SFS is shifted towards higher densities; Chambers et al. (2009) obtain the same result, with star-forming sources on average denser than the quiescent ones. Taking into account the separation into SFS-1 and SFS-2, the density histograms show that the SFS-2 usually have higher values of column-, volume- and surface-densities than either QS or SFS-1; the latter two classes have density distributions peaking at similar values, with that of the SFS-1 showing a tail with values similar to those of the SFS-2. Thus, the clumps hosting a ZAMS star have higher densities, indicating that as star formation proceeds, the clumps appear to become denser in the central parts. The same is found by Butler & Tan (2012), comparing their sample of starless cores to a sample of more evolved objects (from Mueller et al. 2002). We caution that, as the source size could be underestimated due to the presence of a central heating source, causing the clump to appear more

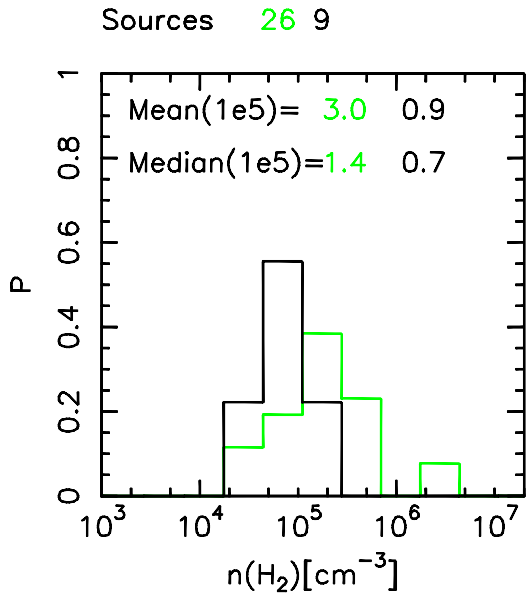

Figure 3.17: Normalised histogram of volume density of molecular hydrogen averaged within the FWHM contour. We show the SFS in green and the QS in black. The total number of sources in each class is shown above the panel.

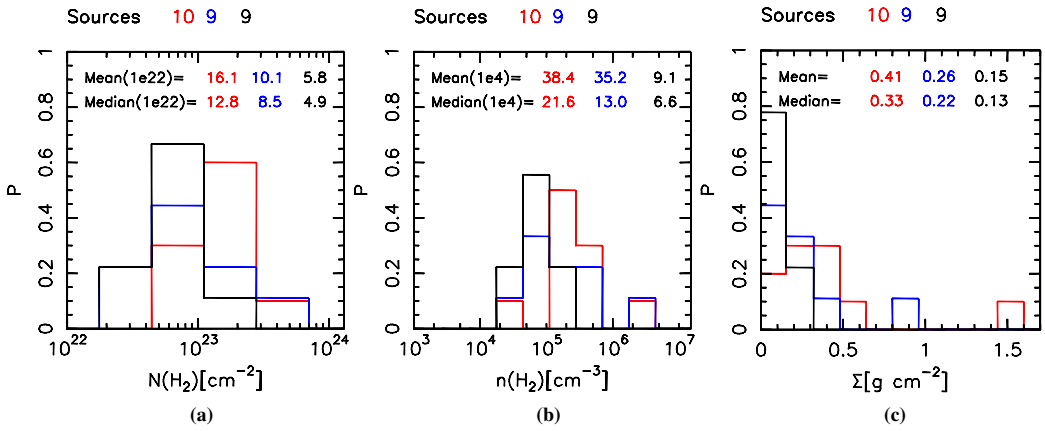

Figure 3.18: Normalised histograms of **(a)** column-, **(b)** volume- and **(c)** surface-densities of molecular hydrogen averaged within the FWHM contour. We show the SFS-2 in red, SFS-1 in blue and the QS in black. The total number of sources in each class is shown above the panels.

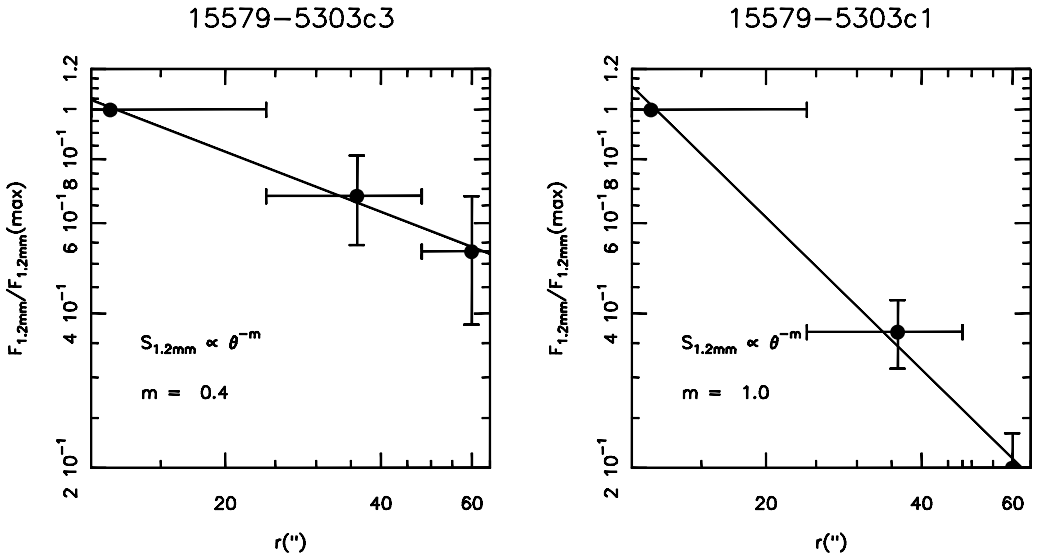

Figure 3.19: Average 1.2 mm flux, normalised to the maximum, as a function of the radius of the largest circle of the annulus for a typical QS (left) and SFS-2 (right) source. The uncertainty on the average flux in indicated. The beam FWHM size is indicated as an errorbar in x. In the bottom left corner the slope m is indicated.

centrally peaked (see Sect. 3.6.2.2), the densities could be overestimated for the SFS-2, thus explaining the observed differences with both QS and SFS-1.

Rygl et al. (2013) argue that star formation signposts are not present in clumps with a column density below a value of 4×10^{22} cm^{-2}. No such threshold effect for the onset of star formation is observed in our sample, but only two of our clumps of any type have column densities well below 4×10^{22} cm^{-2} (cf. Table B.1).

We note that the values of the mass surface density are typically lower than the theoretical threshold of $\Sigma = 1$ g cm^{-2} for massive star formation, on average by a factor $2 - 6$. The theoretical threshold for Σ given by Krumholz & McKee (2008) holds for a single core, stabilised against fragmentation only by radiative heating. López-Sepulcre et al. (2010) show that massive star formation, indicated by the presence of massive molecular outflows, most probably driven by massive YSOs, is occurring also in clumps with a much lower mass surface density, of the order of $\Sigma \sim 0.3$ g cm^{-2}. Butler & Tan (2012) show that similar values of the mass surface density Σ are typical also of massive starless cores, assuming a gas-to-dust ratio of 150, thus consistent with our average value of ~ 0.2 g cm^{-2} for the QS, for a gas-to-dust ratio of 100.

We investigate in more detail the possibility that the radial dependence of the density changes in different classes of objects, by fitting a power law to the average radial 1.2 mm intensity profile calculated in concentric annuli centred on the clump. Figure 3.19 shows the normalised 1.2 mm emission as a function of the angular radius of the largest circle of the annulus. The beam FWHM size is indicated as an errorbar in x. Following the notation in Ward-Thompson et al. (1994) (and references therein), the power law indices of the mm emission m, of the density p and of the temperature q are related by $m = p + Q(\nu, T)q - 1$, where $Q(\nu, T)$ is a coefficient depending on the wavelength and the temperature, near to unity for $h\nu/(k_B T) \ll 1$ (see Adams 1991). We find typical power law indices for mm emission $m \simeq 0.2 - 0.4$ for QS and $\sim 1.0 - 1.3$ for SFS-2 clumps, respectively. We assumed that quiescent clumps are isothermal and that Type 2 sources are likely to have a radial gradient in temperature, described by $T \propto (r/r_0)^q$, with $q = -0.4$ (e.g., Wolfire & Cassinelli 1986). This implies that the power law index p for volume density is $\sim 1.5 - 1.8$ in SFS-2 sources, steeper than in QS sources, with $p \sim 1.2 - 1.4$. The value of p is highly uncertain, because of the assumptions made and because of the very limited number of points for each source, however we are mainly interested in the difference between the QS and SFS-2, and not the specific value of p. As the clumps in QS and SFS have similar masses and total sizes (see Sect. 3.5.4 and 3.6.2.2), this difference in density profile suggests that SFS-2 clumps may indeed be denser in the central regions. Other authors investigated the differences in the density power law index for sources in different stages of evolution. Beuther et al. (2002) also derive an average radial power law dependence for density with $p \sim 1.5 - 2.0$. These authors find that the density distribution is flatter for sources in the very early stages ($p \sim 1.5$), then it becomes steeper during the collapse and accretion phase ($p \sim 1.9$), and finally it flattens again ($p \sim 1.5$) in the dispersal phase. A similar result is reported by Butler & Tan (2012), who compared power law indices for density in starless clumps ($p \sim 1.1$), obtained with a very different technique, with the same quantity derived by Mueller et al. (2002) for more evolved objects ($p \sim 1.8$). This conclusion is also supported by numerical simulations by Smith et al. (2009). The authors show how massive clumps evolve from diffuse and filamentary morphologies to more dense and centrally condensed structures around the most massive sink particles, as the low-density gas is focused towards the progenitors of high-mass stars, through gravitational contraction. The simulations by Smith et al. (2009) also predict that more evolved objects should have a simpler and less structured morphology at high resolution. This prediction may be tested with ALMA observations. A cycle 1 proposal (2012.1.00366.S, PI: F. Fontani) was accepted to study fragmentation in

eleven massive clumps among those investigated here, to assess the importance of magnetic field in supporting the cores (see Commerçon et al. 2011). However, the sample include both sources from QS and from SFS-1, potentially allowing us to study differences in the fragmentation degree as time proceeds, and determine the mass of starless cores. We will be able to obtain some insights on the star formation mechanism, through these masses: in fact, the monolithic collapse scenario predicts the existence of massive starless cores, while if high-mass stars form through competitive accretion, they should be at most of intermediate mass (Zinnecker & Yorke 2007; Smith et al. 2009).

3.6.2.4 Mass

The masses measured for our clumps are in the range 10−2000 $M_\odot$, which indicates that we are probing the low-mass end of the Kauffmann & Pillai (2010) relation (cf. their Fig. 2b and Fig. 3.4 in this work). With respect to more massive clumps, those in this sample will probably form a very limited number of stars with $M > 8$ $M_\odot$, making the assumption of a single massive star in the clump plausible. On the other hand, we know that massive stars are being formed in some objects, as we observe compact radio continuum emission, likely arising in HII regions (Sánchez-Monge et al. 2013a).

Comparing the source size and densities (Fig. 3.15 and 3.18) SFS-2 sources are typically the most compact, suggesting that an evolution of the clumps towards more compact entities with evolution might indeed occur. However, as time proceeds and the massive stars dissociate the molecular gas they move down and to the right in the $M - r$ plot (Fig. 3.4), as shown by 17355−3241c1.

3.6.2.5 Velocity and linewidth

The velocity gradients found for the clumps ($1 - 2$ km s^{-1} pc^{-1}; Sect. 3.5.6.1) are comparable for the SFS and QS, and also the fraction of clumps showing gradients is similar: about 50% of the objects.

From the second moment map we find that the clumps in the SFS have larger linewidths, with an average value of 2.2 km s^{-1} compared to 1.6 km s^{-1} for the sources in the QS. For 08477−4359c1, 13560−6133c1, 15557−5215c1 and c2, 15579−5303c1 and 16093−5015c1 we find an increase of the linewidth between the position of a 24 μm source and the rest of the clump of $\sim 10-30$%. Figure 3.20 shows an example of this increase in linewidth at the location of a 24 μm source. These sources always have a ΔV of the (2,2) line larger than that of the (1,1) at this

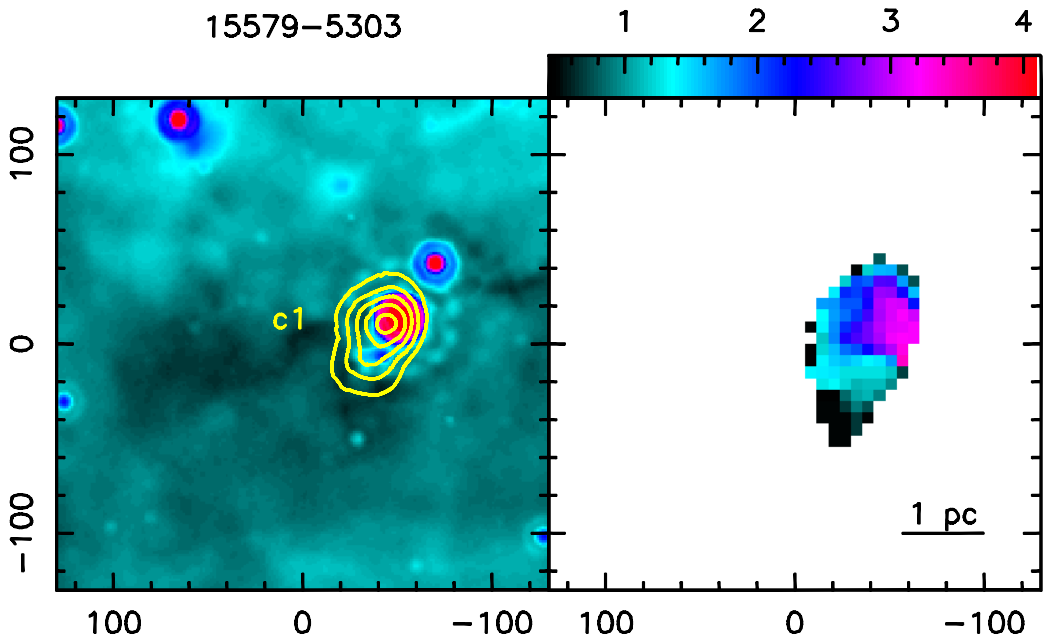

Figure 3.20: Example of $NH_3(1,1)$ second moment map. Left panel shows Spitzer/MIPSGAL 24 μm image in colourscale and $NH_3(1,1)$ integrated emission in contours, while the right panel shows the second moment map.

position. This indicates that we are probing the regions where the embedded source is injecting turbulence. All these sources have a luminosity in excess of 10^3 $L_\odot$, except 15557−5215c2 (L = 740 $L_\odot$), and 08477−4359c1, for which we do not have Herschel data. Similar linewidths are found in dense cores located within clustered massive star forming regions (Sánchez-Monge et al. 2013b): $\sim$ 1.2 km s^{-1} and $\sim$ 2.0 km s^{-1} for starless and protostellar cores, respectively.

3.6.2.6 Virial parameter

Figure 3.7 presents the virial parameter $\alpha \equiv M_{\rm vir}/M$ as a function of M. As already noted, all clumps in our sample appear dominated by gravity. Moreover, these are upper limits for α as the virial mass should be reduced by up to a factor of 2 (see MacLaren et al. 1988) as a consequence of the density gradients found in the clumps; another factor of 2 may arise because the mass was was computed within the FWHM contour. Two sources in the SFS have $\alpha \gtrsim 2$: this could be due to the action of the embedded YSO(s) disrupting the parental cloud. The value of the virial parameter tends to decrease as the clump mass increases.

Let's explore a few possibilities to explain $\alpha < 1$ for such a large number of sources. The first is that we might be underestimating the gas/dust temperature, and are thus overestimating the mass from the 1.2 mm continuum. As NH_3(1,1) and (2,2) essentially trace cold gas and they could be optically thick, this may be a possibility. An independent determination of the temperature in the clumps is given by the dust temperature derived from the modified black-body fit of the mm-FIR part of the SED. Dust emission is optically thin in this regime, thus probing even the inner regions of the clump. Comparing T_K and T_d we find that the two temperatures are usually in good agreement, as discussed in Sect. 3.5 and shown in Fig. 3.5. Therefore we do not expect the bulk of the gas in the clump to have temperatures systematically higher than those adopted here, and consequently lower masses. Moreover, also quiescent clumps have $\alpha \ll 1$, and the temperature in this case should not be underestimated, as no central heating source is present in these sources. Even if it were the case, it is difficult to account for a factor of $3 - 10$. The independent estimate of the mass through the SED essentially confirms that the mass of the clumps is correct.

Another possibility is that we are underestimating the radius of the clump, leading us to underestimate the virial mass. Panagia & Walmsley (1978) show that if the source is not Gaussian, we may underestimate the radius by even a factor of 2. However, it is not clear why the most massive clumps should be different from the others. The same holds for the uncertainty connected to the gas-to-dust ratio, assumed to be 100.

Fontani et al. (2002) and López-Sepulcre et al. (2010) reach opposite conclusions regarding the stability of the clumps in their samples. In the former work the authors show that the ratio between M_{vir}/M reaches values as low as ours, using as a tracer CH_3CCH, while López-Sepulcre et al. (2010) obtain $\alpha \sim 1$ using the mass derived from dust emission and the virial mass from the $C^{18}O$ line emission. Also Hofner et al. (2000) find $\alpha < 1$ using the less abundant $C^{17}O$. Some of the clumps in our sample have been observed in $C^{18}O(3 - 2)$ by Fontani et al. (2012), and these authors find that the clumps are in virial equilibrium or even have virial masses greater than the clump mass (i.e., $\alpha \gtrsim 1$). Comparing the $C^{18}O$ and the NH_3 linewidths we find that the former are larger, typically by a factor of 1.6 and even up to ~ 2.6. As a consequence, the virial masses calculated using the $C^{18}O$ linewidth would be larger by a factor 2.7 (up to 6.8), and α would increase accordingly. Olmi et al. (2010) discuss in detail the differences found in linewidths between $^{13}CO(2 - 1)$, NH_3 and N_2H^+ in the Vela-D cloud; the former should provide an upper limit to the internal energy of the cores, while the latter N-bearing species should give a more accurate estimate of this quantity (see also Morales

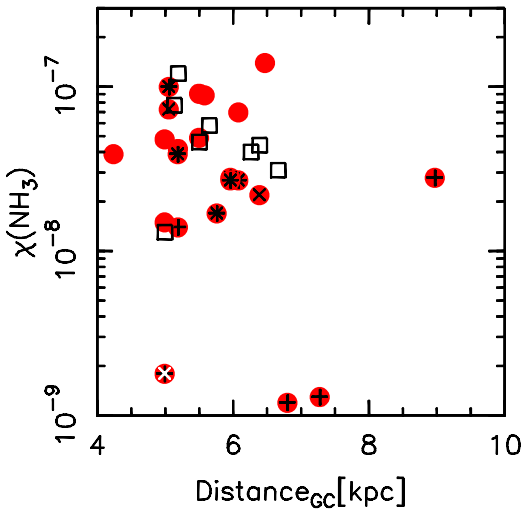

Figure 3.21: Ammonia abundance as a function of Galactocentric distance. The symbols are the same as in Fig. 3.3.

Ortiz et al. 2012). Olmi et al. (2010) find that the average ^{13}CO(2 − 1)-to-N_2H^+ line ratio is ∼ 1.6, similar to what we find in the massive clumps investigated here. While they find that the cores are seemingly gravitationally unbound using the ^{13}CO(2 − 1) linewidths, using those of N_2H^+ shows that they are likely gravitationally bound (Olmi et al. 2010). Sánchez-Monge et al. (2013b) find ammonia linewidths for cores in high-mass star forming regions similar to those found in this study, while Morales Ortiz et al. (2012) find even lower linewidths for low-mass cores in the Vela-D molecular cloud (∼ 1.4 km s^{-1} and ∼ 1.6 km s^{-1} for starless- and protostellar sources, respectively), using optically thin transitions from several molecular species, including ammonia. The difference in linewidth between NH_3 and C^{18}O may be explained by the fact that C^{18}O is tracing a more extended and diffuse region, where ΔV may be larger due to the effects of the environment in which the clump is embedded, or due to the presence of several gas concentrations along the line of sight (i.e., additional indistinguishable velocity components in the spectra), not dense/massive enough to be visible in NH_3, or by the presence of velocity gradients across the clumps. Moreover, C^{18}O is more prone to be entrained in outflows driven by objects already formed in the clump. In conclusion, α may be underestimated, nevertheless, even taking into account the possibilities discussed above, α would still be < 1 for the sources with the highest masses. Moreover, the contribution of external pressure helps gravity.

If these clumps were supported only by turbulence and thermal pressure, they

would collapse on the timescale of the free-fall time. Given the short timescales set by the free-fall time $t_{ff} = \sqrt{3\pi/(32G\rho)} \sim 5 \times 10^4$ yr, this may suggest that magnetic field plays a significant role in stabilising the clumps. Following the relation for virial equilibrium given in McKee et al. (1993), neglecting the surface pressure term, we get the expression for the equilibrium magnetic field

$$B = 1.4 \times 10^{-5} \left[\left(\frac{M}{100\ \mathrm{M}_\odot} \right) \left(\frac{R}{1\ \mathrm{pc}} \right)^{-4} \right]^{0.5} \times \left[\left(\frac{M}{100\ \mathrm{M}_\odot} \right) - 0.71 \left(\frac{R}{1\ \mathrm{pc}} \right) \left(\frac{\Delta V}{2\ \mathrm{km\ s^{-1}}} \right)^2 \right]^{0.5} [G], \tag{3.4}$$

where M is the clump mass, R is the clump radius and ΔV is the FWHM of the line. Using appropriate numbers for these parameters we find that $|\vec{B}| \approx 0.1 - 1$ mG is sufficient to stabilise the clumps. Such values of the magnetic field have been observed towards regions undergoing massive star formation (e.g., Crutcher 2005; Girart et al. 2009).

3.6.2.7 CO depletion

Despite the identification of many thousands of IRDCs, the number of studies that address their chemical (and physical) properties still remains limited, especially in the Southern hemisphere (e.g., Vasyunina et al. 2009; Miettinen et al. 2011; Miettinen 2013; Liu et al. 2013). In particular, CO depletion is a key parameter for the chemistry of prestellar cores in the low-mass regime (Bergin & Tafalla 2007): the disappearance of CO from the gas phase triggers important changes in the chemical properties of such objects, such as much increased abundances for nitrogen hydrides and (multiply) deuterated species. The amount of CO depletion in massive clumps still remains controversial, with some studies showing large depletions (e.g., a factor of ~ 5, Hernandez et al. 2011), and others indicating canonical abundances (e.g., Miettinen et al. 2011).

With APEX we observed the $(3-2)$ transition of $C^{18}O$ in twenty-one sources (see Table 1 in Fontani et al. 2012). This transition has a higher critical density ($\sim 5\times10^4$ cm^{-3}) than $C^{18}O(1-0)$ or $(2-1)$, and should therefore be more sensitive to depletion, which should be important for $n(H_2) \gtrsim 10^4$ cm^{-3} (Bergin & Tafalla 2007; Caselli 2011). We also observed $N_2H^+(3-2)$ and $N_2D^+(4-3)$ for twelve and ten of the sources for which we have $C^{18}O$, respectively (8 sources have both transitions), to investigate the deuteration fraction. Details about observations and methods can be found in Fontani et al. (2012).

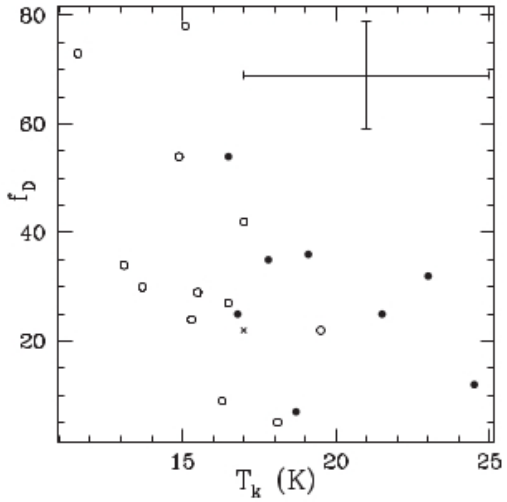

Figure 3.22: CO depletion factor f_D as a function of T_K. A typical uncertainty is shown in the top right corner. The filled and open circles represent the sources detected and undetected at 24 μm, respectively, according to Table 1 in Fontani et al. (2012). The cross indicates a source for which the image at 24 μm is not available.

Using the expressions in Beuther et al. (2002) for $N(H_2)$ and assuming that $C^{18}O$ is in LTE, we find surprisingly high depletion factors f_D, between $5-78$, with a mean value of 32 and median of 29. Separating the sources in IR-bright and dark we find that the latter class has a marginally higher average f_D (35 vs. 28). We also find a faint anti-correlation between T_K and f_D (Fig. 3.22), consistent with the fact that CO depletion should be more important for colder sources.The derived values are higher than those found in other high-mass clumps (e.g., Chen et al. 2011; Miettinen et al. 2011) and higher even than what is found in some low-mass prestellar cores (Crapsi et al. 2005), possibly due to the transition used to derive it.

Although $N_2H^+(3-2)$ is detected in all the twelve observed sources, only one (15557-5215c2) is marginally detected in $N_2D^+(4-3)$, most likely due to the very high critical density of the line ($\sim 3\times10^7$ cm^{-3}), thus likely suffering from enormous beam dilution. This is the first time that this line is detected in an IRDC. The derived deuteration fraction of 0.003 and the upper limits for the remaining sources ($0.003-0.5$) do not allow us to draw firm conclusions about this parameter in the observed sources.

Table 3.7: Molecular transitions observed with APEX.

Line	E_u (K)	ν (MHz)
$C^{18}O(2-1)$	15.8	219560.36
$SO(6_5-5_4)$	35.0	219949.44
$SO_2(11_{1,11}-10_{0,10})$	60.4	221965.21
$OCS(18-17)$	99.8	218903.36
$HNCO(10_{0,10}-9_{0,9})$	58.0	219798.32
$H_2CO(3_{2,1}-2_{2,0})$	68.1	218760.08
$H_2^{13}CO(3_{1,2}-2_{1,1})$	32.9	219908.53
$CH_3OH(8_{0,8}-7_{1,6})$	96.6	220078.49
$CH_3CN(12_0-11_0)$	68.9	220747.26
$CH_3CN(12_1-11_1)$	76.0	220743.01
$CH_3CN(12_2-11_2)$	97.4	220730.26
$CH_3CN(12_3-11_3)$	133.2	220709.02
$CH_3CN(12_4-11_4)$	183.1	220679.29
$CH_3CN(12_5-11_5)$	247.4	220641.09
$CH_3CN(12_6-11_6)$	325.9	220594.43
$CH_3CN(12_7-11_7)$	418.6	220539.33
$CH_3C_2H(13_0-12_0)$	74.6	222166.97
$CH_3C_2H(13_1-12_1)$	81.8	222162.73
$CH_3C_2H(13_2-12_2)$	103.4	222150.01
$CH_3C_2H(13_3-12_3)$	139.4	222128.81

3.6.2.8 Chemical tracers of Hot Cores and star formation

In a recent run of observations with APEX (on 1-2 Sept. 2012) we targeted a sub-sample of sources among the three groups (QS, SFS-1, SFS-2). The aim of the observations was to search for molecular emission that works as an early signpost of star formation, and to identify Hot Cores among the SFS. The observed transitions are listed in Table 3.7.

The analysis is still in progress and the data are to be complemented with archival data and new observations; here we show preliminary results.

Figure 3.23 shows the observed sources and the spectra for each of the observed transitions, with the respective fit for the sources with detected emission. The names of the sources are colour-coded: black for QS, green for SFS-1 and red SFS-2. The

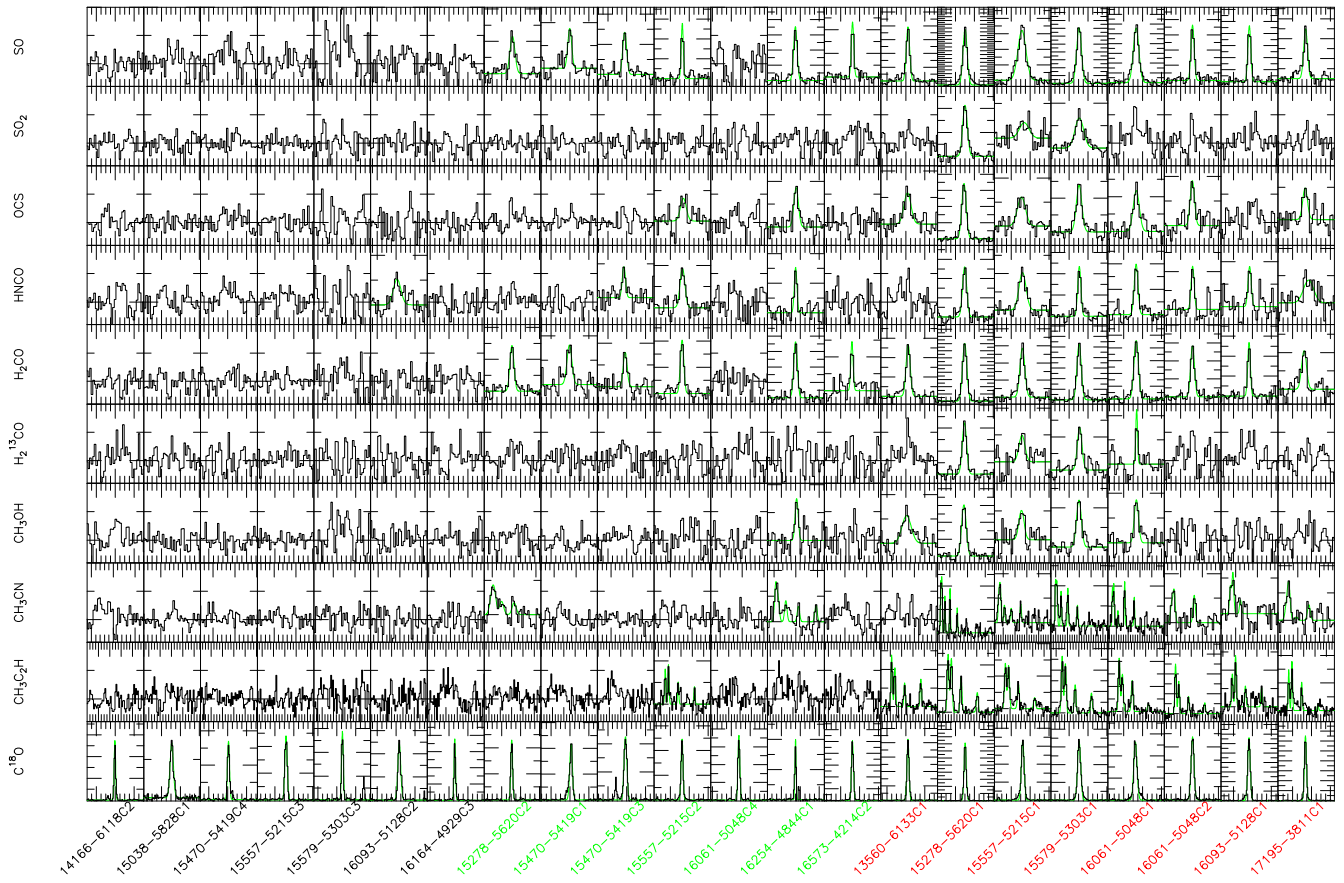

Figure 3.23: Spectra observed for a selection of 22 sources (cf. Table 3.1). The molecular species and the sources are indicated. The specific transitions are shown in Table 3.7. The Gaussian fits are indicated in green. The source names are colour-coded: red = SFS-2, green = SFS-1, black = QS. The spectra have different *y*-scales, to highlight the faint emission, however, the tickmarks are the same for all species (0.05 K small, 0.1 K big), except $C^{18}O$ (0.5 K small, 1.0 K big). The spectra show a range of ±30 km s^{-1} around the velocity of the ammonia line, listed in Table 3.2. CH_3C_2H and CH_3CN are the exception: for the former the *x* axis covers 100 km s^{-1}, and for the latter its extent is between 130 – 240 km s^{-1}, depending on the number of detected lines.

richness of the spectra clearly increases from QS to SFS-2. This can be both due to increased abundances of the observed species or the lack of the proper excitation conditions in the quiescent clumps, because most of the transitions have rather high energies above the fundamental state. In either case, transitions that are detectable at early stages of the process of high-mass star/cluster formation can be used as simple, efficient tracers of ongoing star formation. Figure 3.24 shows the integrated line fluxes as a function of the L/M ratio, indicating the source evolutionary stage (e.g., Molinari et al. 2008; López-Sepulcre et al. 2011). There is a tendency of the sources to show larger line fluxes in more evolved stages, albeit with a large scatter. The scatter could be due to different distances (and thus different filling factors for the high-excitation lines) and/or to the different physical properties in the region surrounding the exciting source(s). It is interesting to note the behaviour of SO and H_2CO: these transitions become detectable shortly after the star formation process begins, also in sources with a rather low luminosity and L/M ratios like those in SFS-1. Thus, they could be used to select clumps in the earliest stages of the process.

Among the star-forming sources we detected nine objects both in $CH_3CN(12-11)$ and in $CH_3C_2H(13-12)$. The detection of line emission from Hot Core tracers in some SFS-1 (cf. Fig. 3.24) indicates that high-mass stars may actually be forming there. The emission of $CH_3CN(12-11)$ is usually very weak, and we could derive a temperature through a Boltzmann plot for only five of the nine sources detected. Also, two of these sources show a large scatter in the diagram. The best examples of Boltzmann plots are shown in Fig. 3.25. Tables 3.8 and 3.9 show the temperature and column density from the Boltzmann plot for $CH_3CN(12-11)$ and $CH_3C_2H(13-12)$, respectively. In the tables, we list the mean, median and mode of the derived parameters, in addition to the shortest 68% interval, to better characterise their distribution. The temperatures derived from $CH_3CN(12-11)$ are high, between $100-300$ K, the emission coming from the hot gas around the central object, constituting the "Hot Core". The beam-averaged abundances of this molecule with respect to H_2 are of the order of 10^{-10}. Considering the energy of the upper levels of the transitions (cf. Table 3.7), the temperature calculated from the emission of $CH_3C_2H(13-12)$ is rather low. Again, the emission from this molecule is detected only for the more evolved and luminous sources (plus 15557−5215c2); the temperatures are higher than those measured from the ammonia inversion lines, suggesting that we are tracing deeper layers in the clumps. The beam-averaged abundances of CH_3C_2H with respect to molecular hydrogen are approximately 10^{-9}.

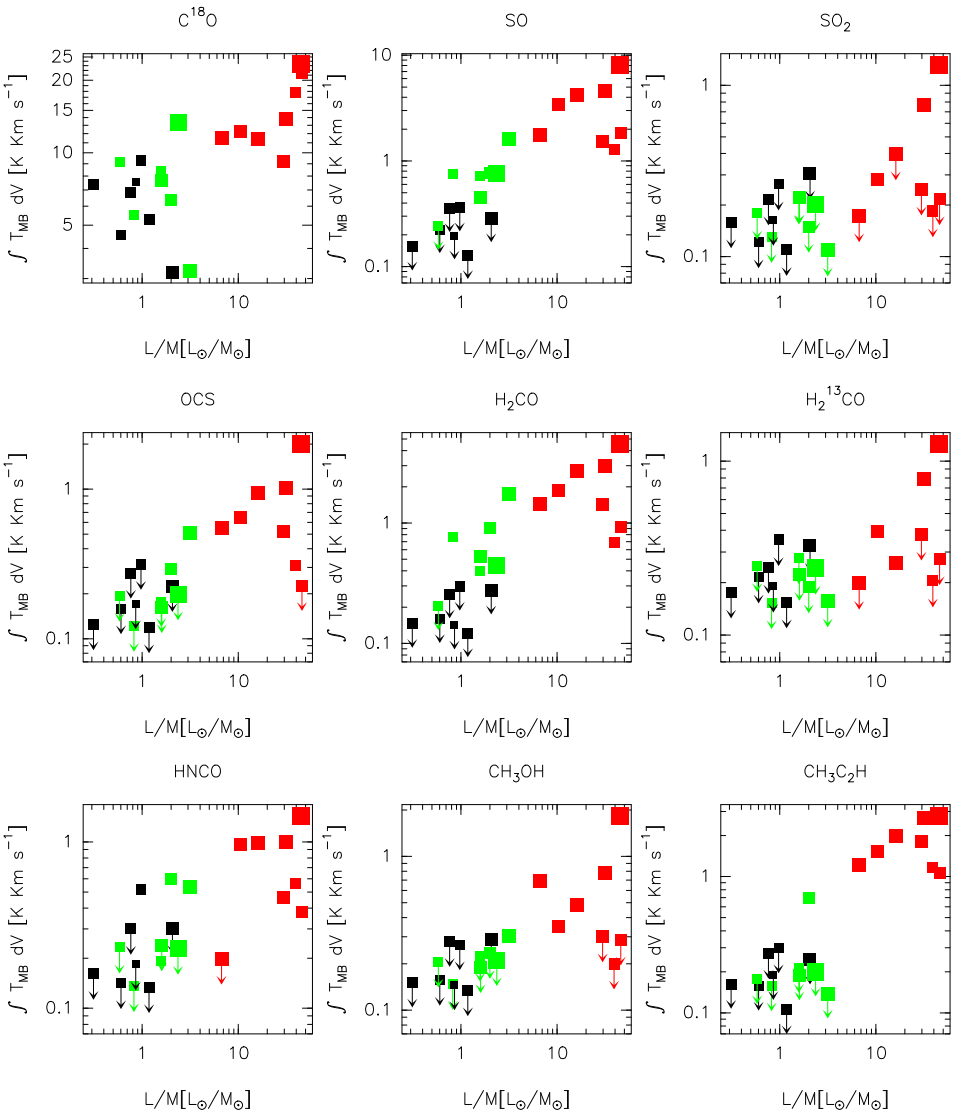

Figure 3.24: Integrated line fluxes as a function of L/M ratio, indicating the source evolutionary stage. The colours indicate red = SFS-2, green = SFS-1, black = QS. The symbol size is proportional to the logarithm of the source number density. Undetected sources are indicated as 3σ upper limits.

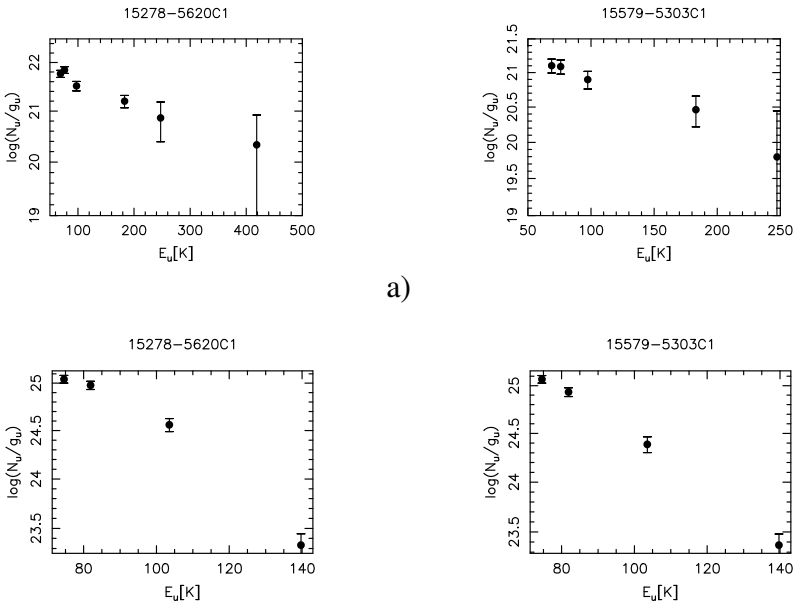

Figure 3.25: Examples of Boltzmann plots for: a) CH_3CN and b) CH_3C_2H.

Table 3.8: Results of the linear fit to the Boltzmann plot for $CH_3CN(12-11)$.

Source	T_{rot}(mean) (K)	T_{rot}(median) (K)	T_{rot}(mode) (K)	68% int. (K)	N_{CH_3CN}(mean) ($10^{12} \times$ cm^{-2})	N_{CH_3CN}(median) ($10^{12} \times$ cm^{-2})	N_{CH_3CN}(mode) ($10^{12} \times$ cm^{-2})	68% int. ($10^{12} \times$ cm^{-2})
15278-5620c1	207	201	191	148 – 251	38.5	36.5	31.2	25.3 – 45.9
15557-5215c1	197	190	169	114 – 252	13.7	12.5	10.4	7.2 – 16.4
15579-5303c1	175	167	156	109 – 219	15.9	14.4	12.7	9.1 – 18.3
16061-5048c1	216	211	207	140 – 285	16.0	14.5	14.0	8.3 – 20.1
16254-4844c1	174	165	148	84 – 231	10.4	9.1	6.5	4.4 – 13.1

Table 3.9: Results of the linear fit to the Boltzmann plot for $CH_3C_2H(13-12)$.

Source	T_{rot}(mean) (K)	T_{rot}(median) (K)	T_{rot}(mode) (K)	68% int. (K)	$N_{CH_3C_2H}$(mean) ($10^{13} \times$ cm^{-2})	$N_{CH_3C_2H}$(median) ($10^{13} \times$ cm^{-2})	$N_{CH_3C_2H}$(mode) ($10^{13} \times$ cm^{-2})	68% int. ($10^{13} \times$ cm^{-2})
13560-6133c1	61.8	53.0	44.2	25.2 – 75.9	16.4	14.9	13.7	10.9 – 18.3
15278-5620c1	40.7	37.6	32.9	20.3 – 51.9	44.0	39.8	35.5	27.1 – 50.2
15557-5215c1	35.1	32.2	30.6	18.1 – 49.4	30.0	25.7	21.2	14.6 – 34.9
15557-5215c2	54.6	45.0	36.0	23.3 – 74.3	10.8	9.3	8.5	5.8 – 11.8
15579-5303c1	41.1	38.0	33.1	21.1 – 51.2	41.2	37.8	32.7	25.4 – 46.5
16061-5048c1	34.2	30.4	24.4	18.1 – 49.7	45.2	36.5	29.5	19.4 – 51.7
16061-5048c2	33.3	30.7	30.7	18.0 – 49.9	36.4	31.3	25.3	17.0 – 40.9
16093-5128c1	52.4	43.1	33.8	20.9 – 65.8	17.1	14.4	12.0	9.1 – 19.1
17195-3811c1	50.4	38.2	29.0	16.3 – 67.1	25.3	19.6	15.4	11.1 – 26.6

3.7 Observational classification of high-mass clumps

Figure 3.26 shows a sketch of the different evolutionary phases identified in this work, with representative values for the observed properties indicated in the yellow rectangles. The arrows connecting the different source types show how the evolution proceeds. In addition to the properties listed in the figure, we find that the SFS-2 have smaller FWHM diameters, that can be due to an intrinsically smaller size and/or just an observational effect caused by the presence of a temperature gradient generated by the heating of the embedded massive (proto)stars (see Sect. 3.6.2.2). The density profile seems to be steeper in the SFS-2 clumps than in the QS, even when allowing for a temperature gradient in the former sub-sample. Thus the central density may indeed be higher for clumps with a similar size and mass. More detailed studies are needed to confirm this result.

Mean and median values for various parameters of the QS and SFS, and of the SFS-1 and SFS-2 are listed in Tables B.4 and B.5.

3.8 Summary and conclusions

From ATCA NH_3 observations of 46 clumps previously observed with the SEST in the 1.2-mm continuum we derived the average properties of the gas for a sample of 36 of these, detected in both NH_3(1,1) and (2,2). The clumps were selected with declination below $-30°$, in comparable numbers among MSX-dark and -bright sources, with a separation greater than one SEST beam ($24''$) between MSX and non-MSX emitters to limit confusion, and with masses in excess of ~ 40 $M_\odot$ in the Beltrán et al. (2006) catalogue. With a reliable and independent temperature estimate through the NH_3 (1,1) and (2,2) line ratio, we determined the mass of the gas.

We performed the simplest virial analysis to investigate the stability of the clumps against gravity. All sources, but one, show a virial parameter $\alpha \lesssim 2$ (Fig. 3.7), showing that gravity is the dominating force. The most massive clumps typically show $\alpha < 1$, and we showed that this is likely to be real (see Sect. 3.6.2.6). The role of the magnetic field in stabilising the sources against gravitational collapse is thus a major one. The required strength of the field was estimated to be $|\overrightarrow{B}| \approx 0.1 - 1$ mG, in agreement with the sparse measurements in regions of high-mass star formation (Sect. 3.6.2.6).

We find ammonia abundances to be in between $10^{-7} - 10^{-9}$, but within the range canonical values of $\sim 10^{-7} - 10^{-8}$ for the vast majority of the sample, showing that

this molecule is not depleted, as opposed to CO in these clumps (cf. Sect. 3.6.2.7 for a summary and Fontani et al. 2012, for a detailed description of the results).

Our data were complemented with Herschel/Hi-GAL, Spitzer/MIPS, MSX and Spitzer/IRAC data, to construct the SEDs of the sources (Sect. 3.5.5). From the SEDs we derived the luminosity of 32 sources (i.e. those with Herschel/Hi-GAL data), out of which we have 29 sources with a reliable ammonia detection in both lines, so that we could locate the clumps in a $M - L$ plot (Fig. 3.11). The sample was divided into sub-samples of clumps in different phases of evolution on the basis of the presence or absence of signs of ongoing star formation and on the location of the sources in the $M - L$ plot. To classify a clump as star-forming, we considered the presence of at least one of the following tracers: 24 μm emission, 1.3 cm continuum emission, water masers, and "green fuzzies" (excess emission at 4.5 μm). The star-forming sub-sample (SFS) includes these sources, while the quiescent sub-sample (QS) contains those without detectable signs of ongoing star formation.

We used the $M - r$ relation found by Kauffmann & Pillai (2010) to assess if also the clumps without clear signs of ongoing massive star formation in our sample are potentially able to form high-mass stars. Virtually all sources lie above of the empirical relation, confirming that our sample is a good one to study evolution in the first stages of the formation of high-mass stars.

We find that more or less smooth velocity gradients are present in $\sim$ 50% of the sources with a strong ammonia emission and a reliable map, including clumps in all evolutionary stages. Typical gradients are found to be in the range $0.5 - 3$ km s^{-1} pc^{-1}. If the observed gradients are due to rotation, the latter does not play an important role in supporting the clumps against collapse.

We explored if and how the average properties of a clump depend on the presence of active star formation and on its evolutionary phase (Sect. 3.6). The information from the $M - L$ plot and that on the presence of ongoing star formation are complementary: we find that Type 1 sources include both the star forming clumps with a low luminosity, well below the ZAMS loci in the $M - L$ plot, and the clumps in the QS, while Type 2 sources are the clumps in the SFS hosting a ZAMS star. For our sample, a convenient criterion based on L was enough to separate Type 1 and Type 2 objects (cf. Fig. 3.11): sources with $L > 10^3$ L$_\odot$ are likely to host a ZAMS star. This idea is corroborated by the large fraction of these sources that are encompassed by the two determinations of the ZAMS locus (Molinari et al. 2008; Urquhart et al. 2013a), and show radio-continuum and strong mid-IR emission, i.e. an UCHII region. Therefore we define the following classes of objects using both the information obtained from the $M - L$ plot and from classical signposts of star

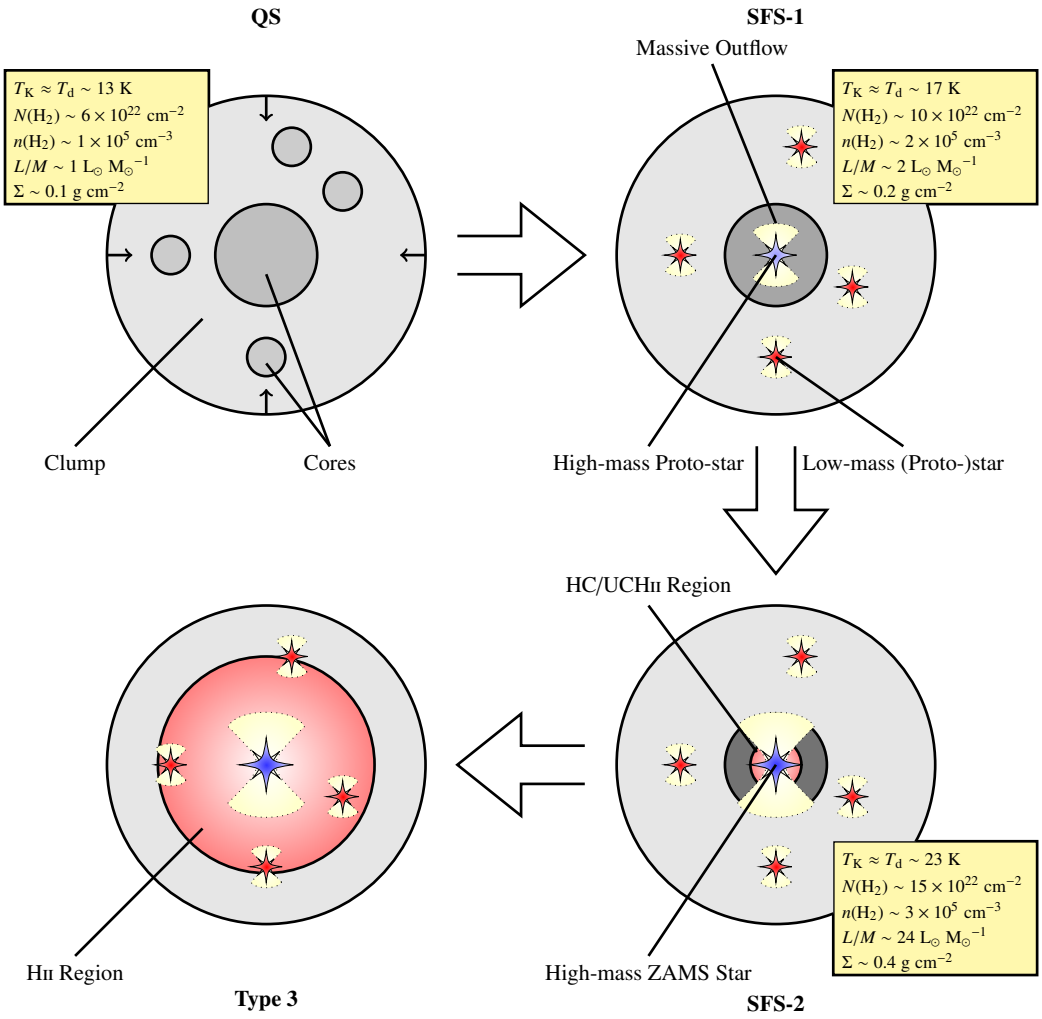

Figure 3.26: A simple sketch of the evolutionary phases considered in this chapter for massive star formation. The representative properties of clumps in the different evolutionary stages as derived in this work are listed in the yellow rectangles.

formation: QS for quiescent Type 1 sources, SFS-1 for Type 1 sources with signs of active star formation, and SFS-2 for Type 2 sources. A sketch of these phases with the typical values for the physical parameters derived in this work is shown in Fig. 3.26. Analyzing the typical properties of the clumps in our sample we find that they depend on the evolutionary phase of the source. The differences found can be summarised as follows:

- SFS-2 sources always show radio continuum or strong mid-IR emission, suggesting the presence of an HII region, while QS and SFS-1 objects do not.
- The average temperature (both kinetic and dust) of the three evolutionary classes slowly increases from the QS, to SFS-1, to SFS-2 sources, with typical values of $\sim$ 13 K, 17 K and $\sim$ 23 K, respectively.
- The temperature of the clumps appears to be correlated with the luminosity of the source (Fig. 3.14).
- SFS-2 objects have smaller FWHM diameters (median values of 0.5 *vs.* 0.8 pc for SFS-2 and QS, respectively), due to the presence of strong and compact peaks of emission at mm wavelengths. This could be caused by the presence of a temperature gradient in the SFS-2.
- As a consequence, clumps classified as SFS-2 on average have higher volume-, column- and surface densities inside the FWHM intensity contour of the 1.2 mm continuum emission.
- Assuming that density (for all clumps) and temperature (for SFS-2 clumps) both vary as power laws as a function of clump radius, we derived the power law indices for density, and found them to be steeper in more evolved sources. Typical power law indices for the molecular hydrogen volume density are $p \sim 1.2 - 1.4$ for QS and $\sim 1.5 - 1.8$ for SFS-2 sources. These results indicate that more evolved sources are indeed denser and more centrally concentrated.
- The fact that SFS-2 sources are the most extreme in terms of compactness suggests that QS sources are still contracting.
- Considerable CO depletion (a factor between $5 - 78$) is found for SFS-1 and QS sources, weakly correlating with $T_{\rm K}$. The average value of the depletion factor is marginally higher for IR-dark sources, as defined in Fontani et al. (2012).

- We observed several molecular lines with rather high excitation requirements (plus $C^{18}O$ and $^{13}CO(2-1)$) towards twenty-two of these objects, equally distributed among QS, SFS-1 and SFS-2. We find that QS sources are detected in the lines from the CO isotopologues, while $SO(6_5 - 5_4)$ and $H_2CO(3_{2,1} - 2_{2,0})$ are already detected in the SFS-1, thus in sources with a low L/M ratio, and can likely be used as early tracers of the SF process. The integrated line fluxes tend to increase with L/M, even though they show a large scatter.

Acknowledgements
The Australia Telescope is funded by the Commonwealth of Australia for operation as a National Facility managed by CSIRO. This work is based in part on observations made with the Spitzer Space Telescope, which is operated by the Jet Propulsion Laboratory, California Institute of Technology under a contract with NASA. This research made use of data products from the Midcourse Space Experiment. Processing of the data was funded by the Ballistic Missile Defense Organisation with additional support from NASA Office of Space Science. This research has also made use of the NASA/ IPAC Infrared Science Archive, which is operated by the Jet Propulsion Laboratory, California Institute of Technology, under contract with the National Aeronautics and Space Administration. This research made use of the NASA ADS database.

Chapter 4

ATLASGAL-selected massive clumps in the inner Galaxy: CO Depletion and Isotopic Ratios

This chapter is taken from Giannetti, Wyrowski, Brand, Csengeri, Fontani, Walmsley, Nguyen Luong, Güsten and Menten, in preparation.

4.1 Chapter summary

In the low-mass regime, molecular cores have spatially resolved temperature- and density profiles allowing a detailed study of their chemical properties. It is found that the abundances of C-bearing molecules rapidly decrease with radius in starless cores, where the density is very high and the temperature is very low. Here the molecules tend to stick to the grains, forming ice mantles.

We investigate CO depletion in a large sample of massive clumps, and test its correlation with evolutionary stage-, and with the physical parameters of the source. Moreover, we study the gradients in $[^{12}C]/[^{13}C]$ and $[^{18}O]/[^{17}O]$ isotopic ratios across the inner Galaxy, and the virial stability of the clumps.

From the ATLASGAL 870 μm survey we selected 102 clumps, which have masses between $\sim 10^2 - 3 \times 10^4$ $M_\odot$ sampling different evolutionary stages. We use low-J emission lines of CO isotopologues and the dust continuum emission to infer the depletion factor f_D. RATRAN one-dimensional models were also used to determine f_D and investigate the presence of depletion above a density threshold. The isotopic ratios and optical depths were derived with a Bayesian approach.

We find a significant number of clumps with a large CO depletion, up to ~ 20. Larger values of depletion are found for colder clumps, thus for earlier evolutionary phases. For typical lifetimes of massive starless clumps depletion holes with radii $\lesssim 0.1$ pc may be present. The value of the $[^{12}C]/[^{13}C]$ ratio is found to increase with distance from the Galactic centre, with a value of $\sim 66 \pm 12$ for the Solar neighbourhood. The $[^{18}O]/[^{17}O]$ ratio is approximately constant (~ 4) across the inner Galaxy between 2 and 8 kpc, albeit with a large range ($\sim 2 - 6$). Clumps with total masses derived from dust continuum emission up to ~ 20 times higher than $M_{\rm vir}$ are found, especially among the less evolved sources.

CO depletion in high-mass clumps seems to behave like in the low-mass regime, with less evolved clumps showing larger values for the depletion than their more evolved counterparts, and increasing for denser sources. $[^{12}C]/[^{13}C]$ and $[^{18}O]/[^{17}O]$ are consistent with previous determinations, and show a large intrinsic scatter.

4.2 Introduction

The fundamental role of massive stars in shaping their direct environment and the galaxies they are in, makes the understanding of the process through which they form one of the major objectives yet to be achieved by astrophysicists. Progress in this sense requires a detailed observational knowledge of high-mass star-forming regions from a physical and chemical point of view. Molecular line- and dust continuum emission in the sub-mm regime are among the main tools to study the first stages of massive star formation, where the sources are still embedded in the molecular gas.

In the low-mass regime, molecules such as CO and CS tend to freeze onto the dust grains in the densest and coldest part of starless cores (e.g., Caselli et al. 1999; Kramer et al. 1999; Bergin & Tafalla 2007; Caselli 2011). This is observed as an abundance drop for these molecules (referred to as depletion) in the central parts of the core, identified by means of dust continuum emission (e.g., Tafalla et al. 2002, and references therein). The evolution of the abundance of different molecules on large scales can be reproduced with time-dependent models for gas-phase chemistry (e.g., Langer et al. 2000). Comparing observations of starless cores in the mm-continuum and in molecular lines from (among other species) CO isotopologues, Tafalla et al. (2002) find that depletion of CO can be substantial, with abundances with respect to H_2 in the central regions that are up to $1-2$ orders of magnitude below the canonical ones. CO depletion is a temperature- and density-sensitive process; at low temperatures and high densities the depletion is higher, because under those conditions it is easier for the molecules to attach themselves to the grains. When protostars are formed in the core, the temperature increases, and at temperatures $T \sim 20-25$ K (commonly found in high-mass clumps, e.g. Wienen et al. 2012, and Chapter 3) the molecules evaporate from grains back into the gas phase, and the abundance returns to canonical levels (for CO $\sim 10^{-4}$ with respect to molecular hydrogen, in the solar neighbourhood; e.g., Fontani et al. 2006). The depletion in a molecular core can thus vary substantially during the process of star formation, and can be used as an evolutionary indicator.

APEX[1] (Güsten et al. 2006) is a $12-$m sub-mm telescope located on Chajnator plane in Chile. The APEX Telescope Large Area Survey of the Galaxy (ATLASGAL, Schuller et al. 2009) is the first complete survey of the Inner Galactic plane, carried out in the sub-mm continuum at 870 μm (345 GHz), and thus sensitive

[1]This publication is based on data acquired with the Atacama Pathfinder Experiment (APEX). APEX is a collaboration between the Max-Planck-Institut für Radioastronomie, the European Southern Observatory, and the Onsala Space Observatory.

also to very cold dust, potentially tracing the pristine condensations where the process of star formation still has to begin. Contreras et al. (2013) compiled a catalogue of compact sources (extracted with SExtractor, Bertin & Arnouts 1996) of the ATLASGAL survey, and Csengeri et al. (submitted to A&A) filtered the extended emission and decomposed the remainder into Gaussian components using the GAUSSCLUMPS algorithm (Stutzki & Güsten 1990). The properties of a sample of massive star forming clumps in the ATLASGAL survey were studied by Urquhart et al. (2013a) and Urquhart et al. (2013b), searching for sources associated with methanol masers (from the methanol multi-beam survey, Green et al. 2009a; Caswell et al. 2010; Green et al. 2009b; Caswell et al. 2011; Green et al. 2012) and (ultra-)compact HII regions (from the CORNISH survey, Hoare et al. 2012; Purcell et al. 2013), respectively.

On the other hand, the starless-phase in the high-mass regime is elusive, due to its short duration (e.g., Motte et al. 2007; Tackenberg et al. 2012). Candidates have been found looking for compact and massive molecular condensations without signs of active star formation (e.g., Chambers et al. 2009; Rygl et al. 2010; Butler & Tan 2012; Rygl et al. 2013; Giannetti et al. 2013). Recent Herschel observations have also been used to search for massive starless objects (Nguyen Luong et al. 2011). These clumps show lower temperatures than their star-forming counterparts ($10 - 15$ K vs. $20 - 40$ K), which are characterised by active star formation signposts, such as infrared (IR), radio continuum and maser emission. A number of studies, usually targeting a limited sample of sources, have been carried out to investigate depletion in high-mass clumps (e.g., Zinchenko et al. 2009; Miettinen et al. 2011; Hernandez et al. 2011; Rygl et al. 2013; Liu et al. 2013), and very few address the variation with time of this key parameter for the chemistry of the source (Fontani et al. 2012). Discordant evidence for depletion exists for high-mass objects, with both claims of significant CO freeze-out onto grains (Hernandez et al. 2011; Fontani et al. 2012; Rygl et al. 2013) and of canonical abundances (Zinchenko et al. 2009; Miettinen et al. 2011). In this work we investigate the CO abundance in a large sample of massive clumps, selected from ATLASGAL, by means of its rarer (optically thin) isotopologues. The clumps have been selected to be in different evolutionary phases, so that we can also study changes in CO abundance in massive clumps during their evolution.

The chapter is organised as follows: in Sect. 4.3 I describe the sample and its selection, and in Sect. 4.4 I briefly describe the observations. In Sect. 4.5 I derive the physical properties of the clumps, and the carbon and oxygen isotopic ratios across the inner Galaxy; Sect. 4.6 is dedicated to the discussion of these results, to the derivation of the CO-depletion factor ($f_D = X^E/X^O$, where X^O and X^E are the

Table 4.1: Frequencies of the observed transitions and angular size of the beam (FWHP).

Receiver	Transition	ν (GHz)	$\theta_{\rm beam}$ ($''$)
APEX/FLASH	$^{12}C^{17}O(3-2)$	337.06099	19
APEX/APEX-1	$^{13}C^{16}O(2-1)$	220.39868	28
	$^{12}C^{18}O(2-1)$	219.56035	28
IRAM 30-m/EMIR	$^{13}C^{16}O(1-0)$	110.20135	22
	$^{12}C^{18}O(1-0)$	109.78217	22
	$^{12}C^{17}O(1-0)$	112.35898	21
	$^{13}C^{18}O(1-0)$	104.71140	23

observed and expected abundances, respectively) and to the study of the physical and chemical changes occurring in the sources as they evolve. Finally, in Sect. 4.7 I draw some general conclusions and summarise our findings.

4.3 The Sample

The ATLASGAL survey constitutes an excellent tool for selecting massive clumps. To select sources in various evolutionary phases, the clumps were extracted from the survey database with the following criteria, each one defining a group of objects:

- The 32 brightest sources of the whole survey, excluding the Central Molecular Zone (i.e., the central few $\times 10^2$ pc) are called IRB group. These clumps are also detected in the IR;

- The 25 brightest sources, that are classified as a Massive Young Stellar Object (MYSO) in the Red MSX Sources survey (Urquhart et al. 2008), are hereafter referred to as the RMS group;

- The 23 brightest objects dark at 8 μm constitute the D8 group;

- Finally, the 22 brightest sources that are dark at 24 μm, are hereafter called D24.

Above, "brightest" refers to the sub-mm flux at 870 μm. The member of each group were selected from the ATLASGAL catalogue after removing those of the preceding groups. The properties of the sources (coordinates, distances and classifications) are shown in Tables C.1 to C.3. This sample is termed the TOP100 sample of the ATLASGAL survey. Clumps in the first two groups of objects most likely contain high-mass stars and/or massive young stellar objects, while the other two are in an earlier phase of evolution (cf. Motte et al. 2007; Nguyen Luong et al. 2011), hosting very deeply embedded (and thus heavily extincted) (proto)stars or being still starless. Separating the sample in these four categories allows us to study possible variations of depletion as a function of evolution.

4.4 Observations

Single-pointing observations were carried out for all sources in the TOP100 sample with APEX/FLASH (Heyminck et al. 2006) in $C^{17}O(3-2)$, between June 2011 and July 2012. Lower-excitation lines have been observed with APEX-1 for southern sources (^{13}CO, $C^{18}O(2-1)$; observations carried out on 13-15 November 2008, and on 30 October and 1-2 November 2009), and with the EMIR on the IRAM 30-m telescope for northern sources ($C^{18}O$, ^{13}CO, $C^{17}O$, $^{13}C^{18}O(1-0)$; on 8-11 April 2011). The frequency of each transition and the beam size are listed in Table 4.1. To easily distinguish the data available for a source, we divide the sample in the following way: **Sub-sample S1** (35 positions), with EMIR follow-ups; **Sub-sample S2** (45 positions), with APEX-1 follow-ups and **Sub-sample S3** (23 positions) with only the FLASH observations. Single Gaussians were fitted to the spectra for ^{13}CO, $C^{18}O$ and $^{13}C^{18}O$ lines, while for $C^{17}O(3-2)$ and $C^{17}O(1-0)$ the appropriate hyperfine splitting was taken into account. The line parameters are listed in Tables C.4 to C.9. The velocity resolution and the rms of the spectra are typically between $0.3-0.5$ km s^{-1} and $0.05-0.10$ K (in units of main beam temperature, $T_{\rm MB}$), respectively.

4.5 Results

4.5.1 Distance

In order to derive the masses and to investigate the relative abundance of different isotopes as a function of Galactocentric distance, we searched the literature for

a distance determination for each of the sources in our sample. We use direct maser parallax or spectrophotometric measurements where available (7 and 16 sources respectively), otherwise (79 sources) we use the kinematic distance (using the rotation curve of Brand & Blitz 1993), resolving the near-far ambiguity with HI self-absorption data from Wienen et al., in prep. (personal communication), or from the literature. After this process, only 2 sources out of 102 still have a distance ambiguity, and for these we use the near kinematic distance. On the other hand, no such ambiguity is present for the Galactocentric distance. Our findings are summarised in Tables C.1-C.3.

4.5.2 Excitation Temperatures

The excitation temperature ($T_{\rm ex}$) is derived from the ratio R_{ij} of the integrated line intensities of the transitions i and j:

$$R_{ij} \equiv \frac{\int T_{\rm MB,i} dV}{\int T_{\rm MB,j} dV} = \frac{I(T_{\rm MB}, i)}{I(T_{\rm MB}, j)}; \tag{4.1}$$

where

$$T_{\rm MB} = \eta[J(T_{\rm ex}) - J(T_{\rm BG})](1 - {\rm e}^{-\tau}), \tag{4.2}$$

with

$$J(T) = \frac{h\nu}{k_B} \frac{1}{({\rm e}^{{\rm h}\nu/({\rm k_B T})} - 1)}. \tag{4.3}$$

To solve Eq. 4.1 for $T_{\rm ex}$ we neglected the background contribution $J(T_{\rm BG})$, and assumed that the emission is optically thin, and that it traces the same volume of gas for both transitions. From the latter assumption it follows that the filling factor η cancels out in the ratio, if the angular resolution is similar, and that the lines have equal profiles. For sub-sample S1 R_{ij}, and thus $T_{\rm ex}$, is obtained from $C^{17}O(3-2)$ and $C^{17}O(1-0)$, while for sub-sample S2 it is obtained from $C^{17}O(3-2)$ and $C^{18}O(2-1)$, assuming an isotopic ratio $[^{18}O]/[^{17}O] = 4$ (see Sect. 4.5.3) and correcting R_{ij} for the optical depth of $C^{18}O(2-1)$ (see Sect. 4.5.3). The derived $T_{\rm ex}$ range from ~ 5 to ~ 70 K and are listed in Tables C.10 and C.11, with their uncertainties for individual sources. Since we do not have maps, we cannot smooth molecular data to a common resolution to derive the temperature, removing the filling factor from the ratio. This is not a problem for sub-sample

S1, because $C^{17}O(3-2)$, observed with APEX, and $C^{17}O(1-0)$, observed with the 30-m, have similar angular resolutions ($19'' - 21''$), but it may be an issue for sub-sample S2 ($19'' - 28''$). As an example, if one assumes a source size of $70''$ and tries to account for the different angular resolutions using the correction factor $(\theta^2_{beam} + \theta^2_{source})/\theta^2_{source}$, the ratio R_{ij} varies by $\sim 10\%$. This implies a decrease in $T_{\rm ex}$ of $\lesssim 10\%$ for a $T_{\rm ex} \lesssim 20$ K and up to 25% for $T_{\rm ex} \sim 70$ K. For smaller sources the difference increases and reaches maximum for point sources. To this source of uncertainty, one has to add that the assumed value of the isotopic ratio $[^{18}O]/[^{17}O] = 4$ may not be appropriate for specific sources (cf. Fig. 4.5b). The highest excitation temperatures are found in S2, some of them possibly caused by the uncertainties discussed above. Equation 4.1 is implemented in JAGS[2] (Just Another Gibbs Sampler) to estimate $T_{\rm ex}$ and its uncertainty, directly from the measured quantities. In the procedure, we considered as physically plausible only temperatures up to ~ 100 K. This is also motivated by the transitions used, for which the method is increasingly insensitive above ~ 30 K.

For S3 we used the average values of $T_{\rm ex}$ from S1 and S2, listed in Table 4.2, for the appropriate group of sources to derive the $^{12}C^{17}O$ column density, and the mass from the sub-mm continuum.

4.5.3 Isotopic Abundance Variations in the Galaxy

To derive more accurate optical depths in Sect. 4.5.4 we start from a first estimate of the relative abundance of the different isotopes of C and O as a function of the Galactocentric distance D_{GC} in the range 2 kpc $\lesssim D_{GC} \lesssim$ 8 kpc. The isotopic gradients can then be used as *priors* for the procedure to derive τ. This can be achieved by comparing the column densities of different carbon monoxide isotopologues, for which we use the $(1-0)$ transition of $C^{18}O$, $C^{17}O$ and $^{13}C^{18}O$. If we assume that the transitions are optically thin, the integrated flux of a transition is proportional to the column density, and we can approximate the relative abundance of C or O isotopes with the ratio of the integrated fluxes of the lines, if we are using the same rotational transition (i.e. with similar excitation conditions, and likely tracing the same volume of gas). Using the same rotational transition thus implies that we do not need to know the actual value of $T_{\rm ex}$, which is the same for both isotopologues. The ratio of the fluxes was corrected for the small differences in the transition frequency (see Linke et al. 1977). Panel **(a)** in Figure 4.1 shows that we find no clear trend with D_{GC} for $[^{18}O]/[^{17}O]$, and our values of the ratio show

[2] `http://mcmc-jags.sourceforge.net/`

a large scatter. A constant value of this ratio in space and time is to be expected if ^{18}O is a secondary nucleosynthesis product (those that can be produced only in the presence of pre-existing seed nuclei, generated by previous stellar generations), like ^{17}O, and they both come from the same primary element, ^{16}O (Wilson & Rood 1994). On the other hand, Wouterloot et al. (2008) find that the [^{18}O]/[^{17}O] tends to increase in the outer Galaxy, out to $D_{GC} \sim 16$ kpc. For the fit, we selected sources with a small optical depth (< 0.3, i.e. a correction of $\sim 15\%$ in column density; see Eq. 4.5), derived from the detection equation alone, and fitted them with a linear relation. The fit gives a small negative slope, $\sim -0.1^{+0.1}_{-0.2}$. The slope is still consistent with zero and it is so small that the resulting values of [^{18}O]/[^{17}O] would change by only ~ 1 (25% of the assumed value of 4) over the whole range of D_{GC} of the S1 sample. This variation is of the order of intrinsic scatter of the fit ($\sim 1.0^{+0.2}_{-0.2}$). We note that a model with only one free parameter (the intrinsic scatter, and an [^{18}O]/[^{17}O] = 4 across the inner Galaxy) is to be favoured with respect to a model with three free parameters (the slope, the intercept and the intrinsic scatter): a Bayesian model comparison shows that the *odds ratio* (cf. e.g., Gregory 2005, and Sect. 2.2.3) is about 15 in favour of the first model. This thanks to the fact that more complex models are automatically penalised in the Bayesian approach, and are to be preferred only if the data justify the added complexity (Ockham's Razor). Therefore, we assume an average constant value for [^{18}O]/[^{17}O] = 4, independently of D_{GC}, with an intrinsic scatter as given by the fit; this value of the ratio is consistent with the measurements of Wouterloot et al. (2008) and Wilson & Rood (1994) for the same range of D_{GC}.

We also investigate the variation of the [^{12}C]/[^{13}C] ratio as a function of D_{GC}, derived from both I[^{12}C^{18}O]/I[^{13}C^{18}O] and I[^{12}C^{17}O]/I[^{13}C^{18}O]. The former gives a direct estimate of the [^{12}C]/[^{13}C] ratio, but it may be affected by optical depth issues, while the latter involves only optically thin transitions, but the ratio [^{18}O]/[^{17}O], despite not being dependent on the Galactocentric distance, may vary up to $\sim 50\%$ in different sources, thus increasing the scatter in the relation. The measured ratios and the results of fitting a straight line to the data points (using as priors the results reported by Milam et al. 2005, see below) are shown in Fig. 4.1b and c. From these panels, one can see that [^{12}C]/[^{13}C] increases with D_{GC}, in agreement with previous works (Langer & Penzias 1990; Wilson & Rood 1994), and expected for a primary/secondary product ratio (cf., Wilson & Rood 1994); in fact, primary elements are produced independently of the metallicity of the stars, while the production of secondary elements increases for higher metallicities. We find the relations [^{12}C]/[^{13}C] = $6.2^{+1.1}_{-2.1} D_{GC} + 9.0^{+9.9}_{-6.2}$ and ([^{12}C]/[^{13}C])/([^{18}O]/[^{17}O]) = $1.6^{+0.8}_{-0.3} D_{GC} + 1.1^{+1.9}_{-1.4}$, respec-

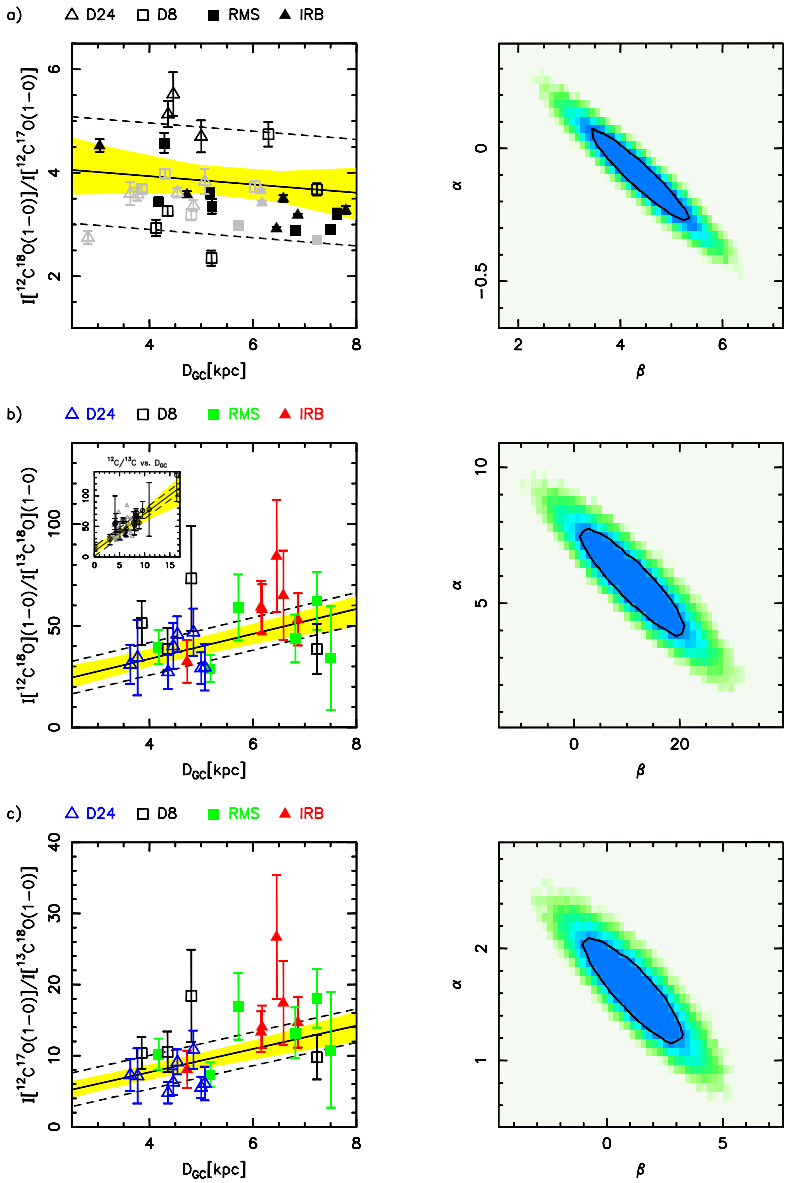

Figure 4.1: Ratio of integrated fluxes of different CO isotopologues as a function of Galactocentric radius. In the right panel of each row we show the joint probability distribution of the parameters of the fit ($y = \alpha x + \beta$); in black we indicate the 68% contour. In the left panel of each row, the black solid line is the best fit, the yellow shaded area shows the 68% uncertainty, and the dashed lines show the intrinsic scatter of the relation. (a) $\int {}^{12}\mathrm{C}^{18}\mathrm{O}(1-0)\,dV / \int {}^{12}\mathrm{C}^{17}\mathrm{O}(1-0)\,dV$, each group of sources is shown with a different symbol, as indicated above the left panel. Black points are those with an estimated ${}^{12}\mathrm{C}^{18}\mathrm{O}(1-0)$ optical depth less than 0.3 (only from the detection equation), grey points are those with $\tau > 0.3$. (b) $\int {}^{12}\mathrm{C}^{18}\mathrm{O}(1-0)\,dV / \int {}^{13}\mathrm{C}^{18}\mathrm{O}(1-0)\,dV$; each group of sources is shown with a different symbol and colour, as indicated. The small box in the top left corner shows the points from Milam et al. (2005) as black circles, and those from this work as grey triangles. (c) The same as (b) for $\int {}^{12}\mathrm{C}^{17}\mathrm{O}(1-0)\,dV / \int {}^{13}\mathrm{C}^{18}\mathrm{O}(1-0)\,dV$.

tively from $I[^{12}C^{18}O]/I[^{13}C^{18}O]$ and $I[^{12}C^{17}O]/I[^{13}C^{18}O]$. Note that the uncertainties reported in the relations are derived marginalising the probability distributions (cf. Sect. 2.2.2) shown in the right panels of Fig. 4.1b and c, but the values of the parameters of the fit α and β ($y = \alpha x + \beta$) are strongly correlated and the yellow-shaded area in the left panels of the figure, representing the fit uncertainty, takes this into account. The above fit results give a $[^{12}C]/[^{13}C]$ for the solar neighbourhood of $\sim$ 62 and $\sim$ 60 respectively, the latter derived with a fixed $[^{18}O]/[^{17}O]$ of 4. Also in this case source-to-source variations are found, resulting in an intrinsic scatter of $\sim 8^{+3}_{-4}$ ($\sim$ 15% of the $[^{12}C]/[^{13}C]$ at the position of the Sun), obtained from the fit procedure. The estimated scatter in isotopic ratios for sources at a given D_{GC} can be caused by a multiplicity of processes at work in the specific source (such as chemical fractionation and selective photodissociation) differently affecting the specific molecules, from our simple estimate of τ, or can be intrinsic if the metallicity and the star formation history are different or other processes have an important role in modifying the isotopic ratios (e.g., non-efficient mixing, radial mixing, cloud mergers). Milam et al. (2005) use three different molecular species, CN, CO, and H_2CO, to investigate the $[^{12}C]/[^{13}C]$ ratio across the Galaxy, finding that all species give consistent results. The authors use this result to show that photodissociation does not have systematic and strong effects on the isotopic ratios. In addition, they compare the data with the predictions from a simple model for chemical fractionation, showing that they are at odds, thus concluding that also this process does not play a fundamental role. In the small panel in Fig. 4.1b we also show the average values of $[^{12}C]/[^{13}C]$ reported by Milam et al. (2005) as black open circles, with the errorbars showing the range in the measured $[^{12}C]/[^{13}C]$ from the different species (or the given uncertainty where only one measurement is available), along with our points (grey open triangles). The comparison illustrates that the points are fully consistent with our measurements and fit. The fact that we find a smaller intercept is mainly due to the inclusion of Sgr B2 (D_{GC} = 0.1 pc) and WB189 (D_{GC} = 16.4 pc) in the work of Milam et al. (2005) and also to the unweighted fit that they use; the points with a high $[^{12}C]/[^{13}C]$ and a large uncertainty (cf. their Figure 2) could slightly increase the intercept.

4.5.4 Optical Depths and Column Densities

Assuming Local Thermodynamic Equilibrium (LTE), we can compute the column density of the molecules using the excitation temperature, according to:

$$N = C(\tau) f(T_{\rm ex}) \int T_{\rm MB} dV, \tag{4.4}$$

where τ is the optical depth of the transition, and $f(T_{\rm ex})$ is a term grouping together all the constants and the terms depending on $T_{\rm ex}$ (see e.g., Kramer & Winnewisser 1991). For a precise determination of the column density we have to estimate the optical depth τ of the lines. The correction factor $C(\tau)$ for Eq. 4.4 can be expressed in the form (for $\tau \lesssim 2$ Goldsmith & Langer 1999):

$$C(\tau) = \frac{\tau}{1 - \mathrm{e}^{-\tau}}. \tag{4.5}$$

Typically $C^{18}O$ and $C^{17}O$ have column densities so low that their emission is optically thin, meaning that the correction for τ is small and therefore the molecular column density is proportional to the integrated flux of the lines. However, it is worthwhile to check if the emission in environments of high column densities (as we expect for the clumps in the TOP100 sample) is indeed optically thin. The optical depth of a transition can be estimated by means of the detection equation or from the ratio of the integrated flux of the same transition, coming from different isotopologues, if the relative abundance is known (e.g., Hofner et al. 2000):

$$R_{ij} = \frac{\int T_{\rm MB,i} dV}{\int T_{\rm MB,j} dV} = \frac{1 - \mathrm{e}^{-\tau_{\rm i}}}{1 - \mathrm{e}^{-\varphi\tau_{\rm i}}}, \tag{4.6}$$

where φ is the relative abundance of the two isotopologues (X_j/X_i). To derive the optical depth we used different methods, depending on the data available.

Sub-sample S1: For these sources we have several CO isotopologues observed in the same transition, namely $^{12}C^{18}O$, $^{12}C^{17}O$ and $^{13}C^{18}O(1-0)$. We derive and make a fit to the probability distribution of the three line ratios by means of Monte Carlo Markov Chains. The results of the fits to the probabilities are used to describe the distribution out of which the measured ratios are extracted. The τ of the lines of the different isotopologues are interconnected by means of:

$$\tau_{^{12}C^{17}O} = \tau_{^{12}C^{18}O}/A; \tag{4.7}$$

$$\tau_{^{13}C^{18}O} = \tau_{^{12}C^{18}O}/B; \tag{4.8}$$

$$\tau_{^{13}C^{18}O} = \tau_{^{12}C^{17}O} A/B \equiv \tau_{^{12}C^{17}O}/C, \tag{4.9}$$

where A and B are the relative abundances of $[^{18}O]/[^{17}O]$ and $[^{12}C]/[^{13}C]$, respectively. The relations

$$\frac{\int T_{\mathrm{MB},^{12}\mathrm{C}^{18}\mathrm{O}} dV}{\int T_{\mathrm{MB},^{12}\mathrm{C}^{17}\mathrm{O}} dV} \equiv R_1 = \frac{1 - \mathrm{e}^{-\tau_{^{12}\mathrm{C}^{18}\mathrm{O}}}}{1 - \mathrm{e}^{-\tau_{^{12}\mathrm{C}^{18}\mathrm{O}}/\mathrm{A}}}; \tag{4.10}$$

$$\frac{\int T_{\mathrm{MB},^{12}\mathrm{C}^{18}\mathrm{O}} dV}{\int T_{\mathrm{MB},^{13}\mathrm{C}^{18}\mathrm{O}} dV} \equiv R_2 = \frac{1 - \mathrm{e}^{-\tau_{^{12}\mathrm{C}^{18}\mathrm{O}}}}{1 - \mathrm{e}^{-\tau_{^{12}\mathrm{C}^{18}\mathrm{O}}/\mathrm{B}}}; \tag{4.11}$$

$$\frac{\int T_{\mathrm{MB},^{12}\mathrm{C}^{17}\mathrm{O}} dV}{\int T_{\mathrm{MB},^{13}\mathrm{C}^{18}\mathrm{O}} dV} \equiv R_3 = \frac{1 - \mathrm{e}^{-\tau_{^{12}\mathrm{C}^{18}\mathrm{O}}/\mathrm{A}}}{1 - \mathrm{e}^{-\tau_{^{12}\mathrm{C}^{18}\mathrm{O}}/\mathrm{B}}}; \tag{4.12}$$

$$T_{\mathrm{MB},^{12}\mathrm{C}^{18}\mathrm{O}} = \eta[J(T_{\mathrm{ex}}) - J(T_{\mathrm{BG}})](1 - \mathrm{e}^{-\tau_{^{12}\mathrm{C}^{18}\mathrm{O}}}); \tag{4.13}$$

$$T_{\mathrm{MB},^{12}\mathrm{C}^{17}\mathrm{O}} = \eta[J(T_{\mathrm{ex}}) - J(T_{\mathrm{BG}})](1 - \mathrm{e}^{-\tau_{^{12}\mathrm{C}^{18}\mathrm{O}}/\mathrm{A}}); \tag{4.14}$$

were simultaneously solved with Monte Carlo Markov Chains in JAGS, thus combining the information from the detection equation and the line ratios for a more accurate determination of τ and of the isotopic ratios. Hofner et al. (2000) have maps in $C^{17}O(2-1)$ for a sample of similar sources at a comparable angular resolution, and find them to be extended; therefore, for simplicity we assume $\eta = 1$ for these calculations. The *priors* for A and B are Gaussian curves, centred on the value expected from the fit of the isotopic ratios as a function of D_{GC}, with a dispersion equal to the intrinsic scatter of the fit (see Sect. 4.5.3); the *prior* for τ comes from the fit of the hyperfine structure of the $C^{17}O(1-0)$ emission. This procedure returns $\tau_{^{12}\mathrm{C}^{18}\mathrm{O}}$, $\tau_{^{12}\mathrm{C}^{17}\mathrm{O}}$, A, B and C, and their respective uncertainties for each source in the sub-sample S1, refining our estimate of the isotopic ratios and of the optical depth. We use these values of the $[^{18}O]/[^{17}O]$ and $[^{12}C]/[^{13}C]$ isotopic ratios in Sect. 4.6.3 to derive a more accurate f_D, and in Sect. 4.6.2 to derive again the gradient of relative abundance as a function of D_{GC} (see Fig. 4.5). The results of this procedure for the refined estimate of the $[^{12}C]/[^{13}C]$ and $[^{18}O]/[^{17}O]$ ratios are discussed in Sect. 4.6.2 and summarised in Table C.12. We note that a significant fraction of the sources ($\sim 55\%$) shows an optical depth > 0.3 for $^{12}C^{18}O(1-0)$.

On the other hand, only one source has $\tau_{^{12}C^{17}O} > 0.3$, while $\tau \lesssim 0.2$ for the other sources; similar low values for the $^{12}C^{17}O$ opacity were obtained by Hofner et al. (2000).

Sub-sample S2: For this sub-sample we have observations of $^{13}C^{16}O$ and $^{12}C^{18}O(2-1)$. Thus, we derive τ from the ratio of these two transitions. To estimate the uncertainty in the optical depth, we calculate the probability distribution of the line ratio, considering the calibration uncertainty and the noise of the spectrum. This can be translated into a distribution of τ for $^{12}C^{18}O(2-1)$, using the appropriate value for $[^{12}C]/[^{13}C]$ and $[^{18}O]/[^{16}O]$ at the D_{GC} of the source. The results are listed in Table C.8.

Sub-sample S3: Finally, for the last sub-sample, the only measure for τ we have comes from the fit of the hyperfine structure of $^{12}C^{17}O(3-2)$. However, the satellites are too close to be spectrally resolved, meaning τ is highly uncertain. Thus, we assume that the emission is optically thin.

The column densities of the CO isotopologues are listed in Tables C.13, C.14 and C.15.

4.5.5 Column density of molecular hydrogen

The column density of molecular hydrogen $N(H_2)$ was calculated from the ATLAS-GAL peak flux, according to Schuller et al. (2009):

$$N(H_2) = \gamma \frac{F_p}{2.8\ m_p\ \Omega_B\ \kappa_{870}\ B_{870}(T_d)} \tag{4.15}$$

where F_p is the peak flux at 870 μm, the factor 2.8 accounts for the presence of helium ($\sim 10\%$ in number, e.g., Allen 1973), $\kappa_{870} = 1.8$ cm^2 g^{-1} is the dust opacity at 870 μm (derived from the numbers given in Ossenkopf & Henning 1994), m_p is the proton mass, Ω_B is the beam solid angle for a beam size of $\approx 19.2''$ (i.e. 9.81710^{-9}sr^2), $B_{870}(T_d)$ is the emission at 870 μm of a black-body with a dust temperature T_d and γ is the gas-to-dust ratio, assumed to be 100. To derive the column density of molecular hydrogen we assume that gas and dust are coupled, and that the molecules are in LTE, thus $T_d = T_K = T_{ex}$. For the sub-sample S3, we do not have a direct estimate of the temperature. Thus, we assign the typical temperature of the group to which the object belongs, with an uncertainty equal to the dispersion of that group (cf. Sect. 4.6 and Table 4.2).

Table 4.2: Mean and median values for $T_{\rm ex}$[K] for the four groups, with their dispersion.

Group	IRB	RMS	D8	D24
Mean	47	26	22	11
Median	47	24	16	10
σ	14	12	13	3

4.5.6 Masses

The clump mass is derived from the integrated 870 μm flux as given in the latest ATLASGAL catalogue (for details, see Csengeri et al., submitted to A&A), through:

$$M = \frac{\gamma S_{870} D^2}{\kappa_{870} B_{870}(T_{\rm d})}, \tag{4.16}$$

where S_{870} is the 870 μm integrated flux, and D is the distance. The objects are massive, ranging from $\sim 10^2$ to $\sim 3\times10^4$ $M_\odot$: we are dealing with extreme sources in the ATLASGAL survey, many of which are known sites of high-mass star formation. For sub-sample S3 the same assumptions for the temperature are made as for the determination of column densities. The masses are listed in Tables C.16 to C.18.

Kauffmann & Pillai (2010) derived a relation between mass and radius, to separate clumps with the potential of forming massive stars from those without. A similar threshold for high-mass star formation, with a constant surface density $\Sigma = 0.05$ g cm^{-2}, was derived by Urquhart et al. (2013a) for massive star forming clumps selected cross-correlating the ATLASGAL catalogues with the catalogue of the methanol multi-beam survey and the CORNISH survey. Figure 4.2 shows that all of the clumps in this sample are found above this empirical relations, implying that these clumps are potentially forming massive stars. In the figure, we used the $R_{\rm eff}$ definition from Rosolowsky et al. (2010) and the sizes of the two-dimensional Gaussian fitted to the emission in Csengeri et al. (subm.). With this definition, $R_{\rm eff}$ is approximately equal to the FWHM size of the clump.

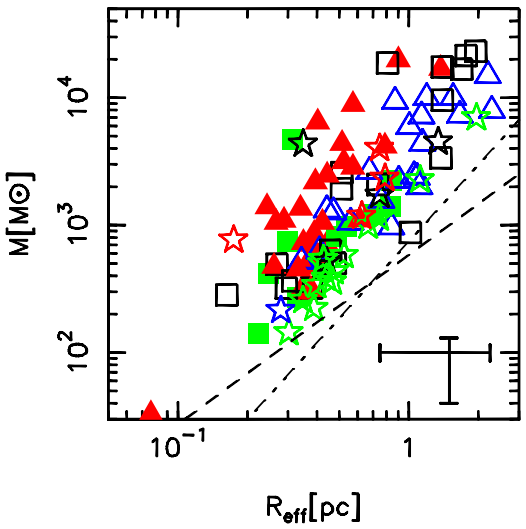

Figure 4.2: Mass-radius plot. $R_{\rm eff}$ is calculated according to Rosolowsky et al. (2010), using the sizes from Csengeri et al. (submitted to A&A), and it is approximately equal to the FWHM size of the clump. The Kauffmann & Pillai (2010) relation (dashed line) was rescaled to match our values of the dust opacity. The dash-dotted line indicates the threshold of Σ = 0.05 g cm^{-2} for massive clumps proposed by Urquhart et al. (2013a) for massive star formation to occur. All the sources are found above it, suggesting that they are potentially forming massive stars. A typical uncertainty for the mass (for sub-samples S1 and S2) is shown in the bottom right corner. We also indicate the effect of a change of a factor of 2 in $R_{\rm eff}$. The symbols (except open stars) and colours are the same as in Fig. 4.1. The stars refer to sources of sub-sample S3, while their colour still identifies the Group (red = IRB, green = RMS, black = D8, and blue = D24).

4.6 Discussion

4.6.1 Linewidths and Temperatures

Figure 4.3 shows that the typical linewidth of the $^{12}C^{17}O$ lines for IRB is much larger than that of the other groups. RMS and D8 sources show similar values of ΔV, slightly larger than those in D24. This may indicate that (proto)stars embedded in the molecular gas and dust deliver energy to the surrounding material, making it more turbulent than before their formation, which is reflected in the width of molecular lines. Alternatively, the IR-bright clumps may have been more turbulent from the start, and move much faster through the IR-dark phase, where we find

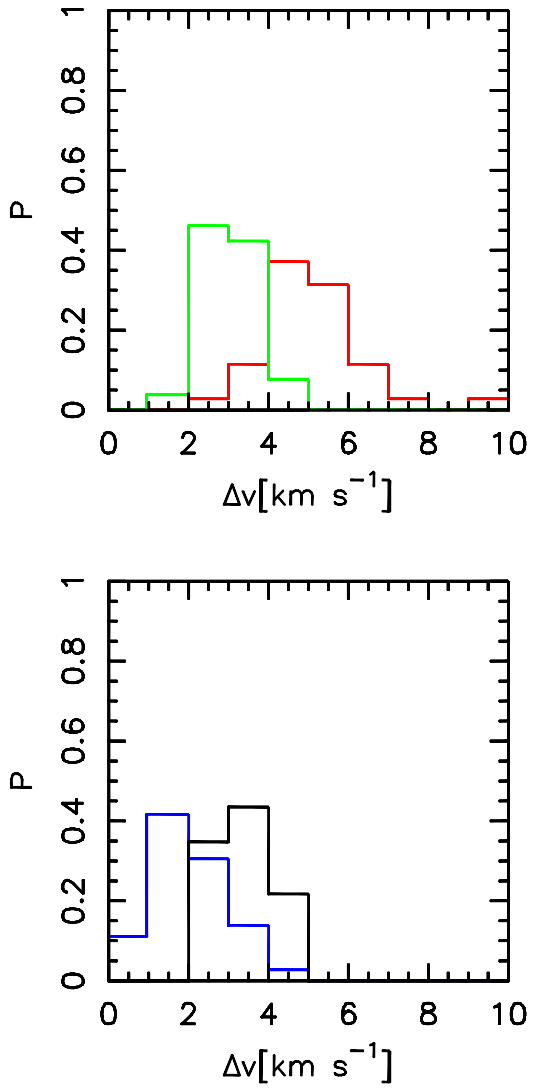

Figure 4.3: Normalised $^{12}C^{17}O(3-2)$ linewidth histogram for the IRB and RMS (upper panel), D8 and D24 (lower panel) sources. The colours are the same as in Fig. 4.2.

very few clumps with $\Delta V \gtrsim 4$ km s^{-1}.

Figure 4.4 shows that the four groups of objects have a different characteristic temperature, listed in Table 4.2. This indicates an increasing temperature as evolution proceeds. A similar result for gas and/or dust temperature is found in e.g., Rygl et al. (2010), Wienen et al. (2012) and Giannetti et al. (2013).

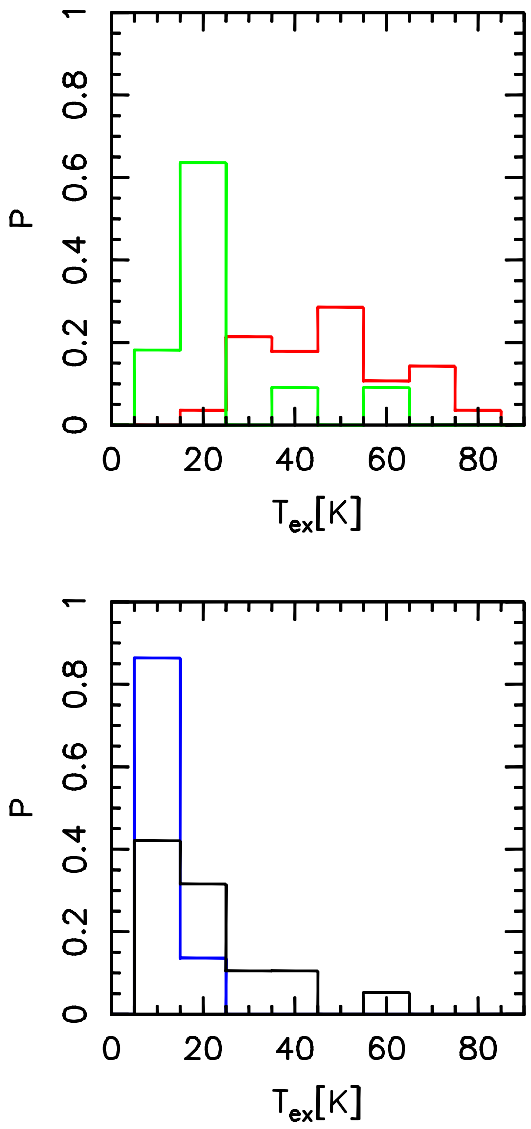

Figure 4.4: Normalised T_{ex} histogram for the IRB and RMS (upper panel), D8 and D24 sources (lower panel). The colours are the same as in Fig. 4.2.

4.6.2 Refined Estimate of the Isotopic Ratios

Figure 4.5 shows the refined estimate of the isotopic ratios for the sources in S1; we also included different velocity components observed in the spectra (indicated with crosses), with the appropriate estimate of the Galactocentric distance obtained with the rotation curve of Brand & Blitz (1993). First of all, both the isotopic ratios $[^{18}O]/[^{17}O]$ and $[^{12}C]/[^{13}C]$ show a large scatter for sources at similar D_{GC}, confirming the existence of source-to-source variations in the relative abundance of these isotopes at the same D_{GC}.

Here we derived the $[^{18}O]/[^{17}O]$ ratio in massive clumps and find it to be consistent with the current estimate of ~ 4 for 2 kpc $\lesssim D_{GC} \lesssim$ 8 kpc, albeit with a very large scatter that cannot be due to the uncertainty associated with the inferred values of the ratio. $[^{18}O]/[^{17}O]$ is found to range between ~ 2 and ~ 6, as can be seen in Fig. 4.5b. A few sources have $[^{18}O]/[^{17}O] \sim 5-6$, especially objects in groups D8 and D24, values similar to that found in pre-solar grains ($[^{18}O]/[^{17}O] \sim 5.5$, reported in e.g., Prantzos et al. 1996). Prantzos et al. (1996) discuss how ^{18}O poses a problem for models of chemical evolution of the Galaxy. Neither isotopic ratio $[^{18}O]/[^{16}O]$ nor $[^{18}O]/[^{17}O]$ can be reproduced by simple models describing the chemical evolution of the Milky Way. The former because it appears to be larger now in the Solar vicinity than it was at the time of the Sun's formation, whereas it is predicted to decrease with time, and the latter because it appears to be substantially larger in the pre-solar cloud than in the present-day ISM, while predicted to remain constant (e.g., Prantzos et al. 1996). The most probable solution to this discrepancy is the pollution of the pre-solar cloud by a previous generation of massive stars undergoing Type II Supernovae (SNe) events, as discussed in detail by Young et al. (2011) (for $[^{18}O]/[^{16}O]$ a role could also have been played by the position of the Sun at the time of its formation; see Wielen & Wilson 1997).

Young et al. (2011) show that values as high as those found in pre-solar grains can be reached if intermediate-mass Type II SNe events (from B stars) of a previous stellar generation pollute the surrounding medium, arguing that more massive progenitors are not able to produce similar values of the ratio $[^{18}O]/[^{17}O]$. It could be that the sources with a high $[^{18}O]/[^{17}O]$-ratio had an evolution similar to that of the Solar system in its earliest formation stages. Because several of these sources are near the inner molecular ring, many massive stars were formed in their vicinity, making this pollution scenario a reasonable one.

The procedure outlined in Sect. 4.5.4 also yields values of B (= $[^{12}C]/[^{13}C]$, see Eq. 4.8) for those sources without a $^{13}C^{18}O(1-0)$ detection (panel (c) of

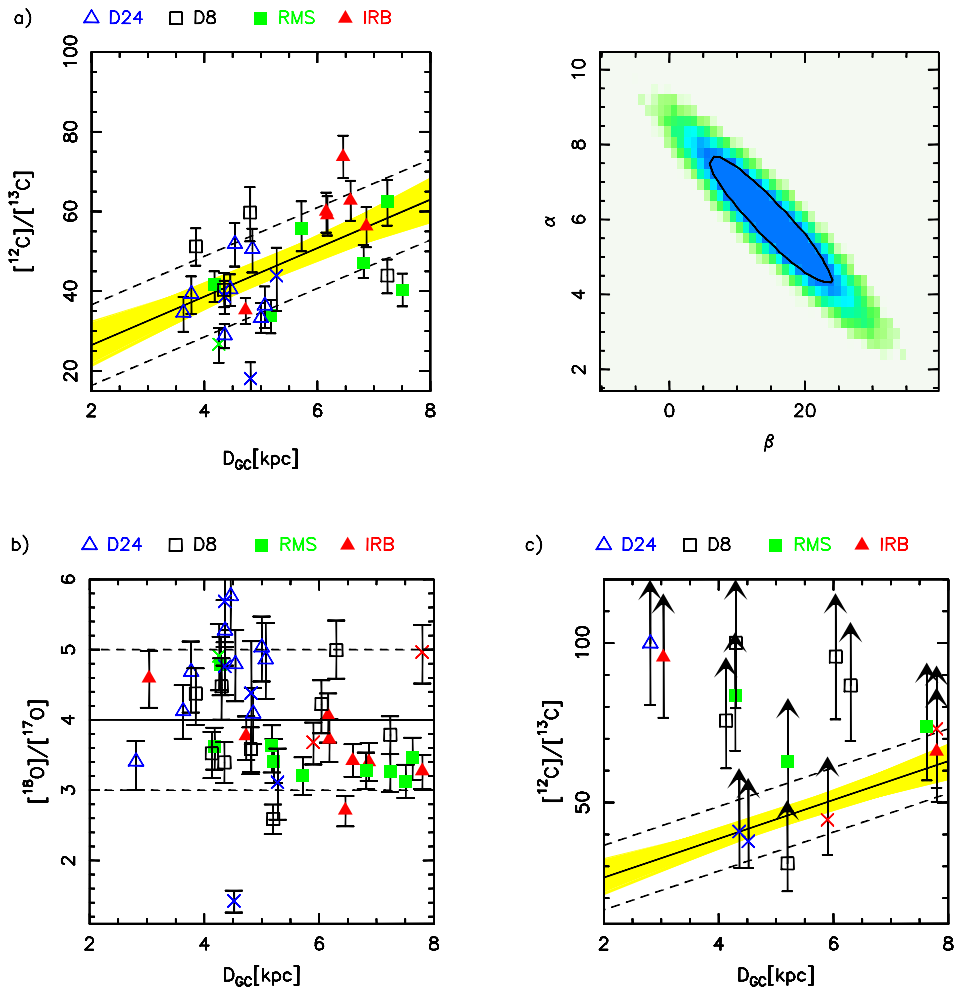

Figure 4.5: Ratio of different CO isotopologues as a function of Galactocentric radius, as determined from the procedure described in Sect. 4.5.4. Each group of sources is shown with a different symbol and colour, as indicated. Velocity components different from the main one are indicated with crosses; the colour of the cross refers to the main component classification. (a) $[^{12}C]/[^{13}C]$ for the sources detected in $^{13}C^{18}O(1-0)$. The black solid line is the best fit, the yellow-shaded area in the left panel indicates the 68% uncertainty, and the dashed lines show the intrinsic scatter of the relation; In the right panel we show the joint probability distribution of the parameters of the fit ($y = \alpha x + \beta$); in black we indicate the 68% contour. (b) the same as the left panel in (a), for $[^{18}O]/[^{17}O]$; (c) $[^{12}C]/[^{13}C]$ for the sources undetected in $^{13}C^{18}O(1-0)$ (see text). We show again the fit from the left panel in (a) for clarity.

Fig. 4.5): we used a flux for the undetected $^{13}C^{18}O$ transition equal to 1σ with σ derived from the spectrum as an input for the Monte Carlo calculations. Some of these sources have quite high values of $[^{12}C]/[^{13}C]$ given their D_{GC}, even if the uncertainties are large. Such large values of $[^{12}C]/[^{13}C]$ may be caused by simple dilution effects if the area of $^{13}C^{18}O(1-0)$ emission is substantially smaller than those of $^{12}C^{18}O(1-0)$ and $^{12}C^{17}O(1-0)$, or if not, it may be caused for instance by selective depletion of the heavier molecule. Excluding these non-detections and using the values for the carbon isotopic ratio from Sect. 4.5.4 we find a gradient of $[^{12}C]/[^{13}C] = 6.1^{+1.1}_{-1.8} D_{GC} + 14.3^{+7.7}_{-7.2}$, with an intrinsic scatter of $10.1^{+2.0}_{-2.5}$; this relation gives a most probable value for $[^{12}C]/[^{13}C]$ of $\sim 66 \pm 12$ for the Solar vicinity. The relation derived is consistent with that derived from simpler estimates, but each point has reduced uncertainties (cf. Figures 4.1b and 4.5), thanks to the better estimate of τ and the combination of all the line ratios. We note that the slope of the relation does not vary much, but the intercept has increased slightly, probably because of the correction for optical depth effects. This new estimate highlights even more the large scatter of the points.

No clear systematic difference in the isotopic ratios is found between the groups. This indicates that the isotopic ratios set by the complex interplay of the processes mentioned in Sect. 4.5.3 do not change appreciably on a large scale over the short time spanned by the first phases of high-mass star formation.

4.6.3 Depletion of CO

Figure 4.6 shows $N(H_2)$ as a function of $N(C^{18}O)$ and $N(C^{17}O)$ for the TOP100 sample. The dashed line indicates the canonical abundance of the CO isotopologue in the solar neighbourhood ($\sim 1.7 \times 10^{-7}$ for $C^{18}O$ and $\sim 4.2 \times 10^{-8}$ for $C^{17}O$). This is a first, simple approach for investigating CO depletion: in several sources there seems to be an abundance lower than the canonical one, suggesting that CO may indeed be frozen onto the surface of the dust grains. We observe that there appears to be a difference between groups D8 and D24 and groups IRB and RMS, with objects from the former two groups reaching markedly lower abundances.

Panels (a) and (b) of Fig. 4.7 show the CO depletion factor as a function of the excitation temperature. Here, the depletion factor is determined taking into account the CO abundance gradient with D_{GC}, deriving the expected $^{12}C^{18}O$ abundance according to Miettinen et al. (2011, and references therein):

$$X^{E}_{^{12}C^{18}O} = \frac{9.5 \times 10^{-5} e^{1.105 - 0.13 D_{GC}[\mathrm{kpc}]}}{58.8 D_{GC}[\mathrm{kpc}] + 37.1} \tag{4.17}$$

and the expected $^{12}C^{17}O$ was calculated with the $[^{18}O]/[^{17}O]$ derived as described above for the sub-samples S1 and S2 (see Sect. 4.5.4). Colder sources show larger CO depletion factors, suggesting that in less evolved sources CO in the gas phase is less abundant than in more evolved ones. Figure 4.8 shows that f_D (from $^{12}C^{17}O$, in this figure) also correlates with the peak column- and volume densities (as also found by Liu et al. 2013, with a lower angular resolution), increasing for higher densities. The peak volume density was calculated according to $n(H_2) = N(H_2)/(2R_{\rm eff})$. The average f_D decreases from the D24- to the IRB objects. Mean and median values for f_D for each group are listed in Table 4.3. The offset between the groups in Fig. 4.8 may be caused by the depletion- and evaporation timescales, that depend on density and temperature, which are different for each group. Denser objects are more prone to high-levels of molecular depletion, because the depletion timescale (i.e. the time after which depletion becomes important) decreases with increasing density, while for higher temperatures, molecules tend to evaporate more rapidly, as the evaporation timescale decreases for increasing temperatures. CO abundances lower than the canonical one are observed towards warm protostellar envelopes (e.g., Fuente et al. 2012, and references therein); the reason for this is yet unclear, and the authors suggest that conversion of CO in more complex molecules may happen on the grain surface and/or that the shocks and UV radiation illuminating the walls of the cavities produced by the protostellar outflow may be important factors in explaining the measured CO abundance.

That f_D decreases with age of the source is supported by Fig. 4.9, where we find an anti-correlation between the depletion factor and the L/M ratio, which we use as an indication for the time evolution of the source (e.g., Molinari et al. 2008; López-Sepulcre et al. 2011). In particular, using also the sources with upper- and lower limits (for a total of 79 sources) on the IR flux, we get a Pearson's correlation coefficient of -0.40, while if we exclude them 44 objects can be used, and we obtain a correlation coefficient of -0.34. This means that there is a probability of $\sim 1.1\%$ of getting similar results from an uncorrelated sample. The bolometric luminosities are extrapolated from the monochromatic luminosity, following Davies et al. (2011), based on the results of Mottram et al. (2011). The monochromatic luminosity was obtained from cross-matching our sources with the MSX (Egan et al. 2003) and WISE (Wright et al. 2010) point-source catalogues (see Csengeri et al. in prep. for details). The large scatter can be due to several reasons. The various distances to the targets imply that we probe different spatial scales, where the depletion factor may vary significantly, influencing the average value we derive. For sources in D8 and D24 the ratio between the depletion- and the free-fall timescales may differ in different sources, and some of the less evolved

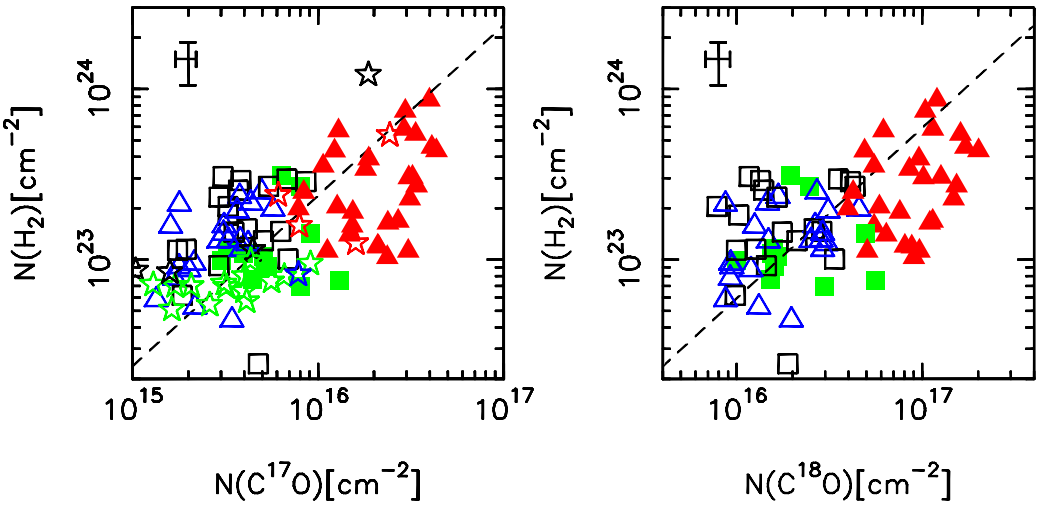

Figure 4.6: Comparison of $N(H_2)$ and the CO isotopologues column density. Symbols and colours are the same as in Fig. 4.2. A typical uncertainty (for subsamples S1 and S2) is shown in the top left corner of each panel.

ones may not have lived enough for the depletion to become important (see below), or have rather high temperatures ($\gtrsim$ 20 K) slowing- or impeding the process of sticking of molecules onto the grains (cf. Fig. 4.7). In addition, the luminosity estimate is uncertain due to the extrapolation from monochromatic- to bolometric luminosity.

The observed trends could be caused by the assumption of $T_{ex} = T_K = T_d$. In order to check if the trends are real, we performed two different tests. In the case of Fig. 4.7 we also used different dust temperatures for the groups: T_d = 10 K for group D24, T_d = 18 K for group D8, and T_d = 25 K for groups IRB and RMS (cf. e.g, Giannetti et al. 2013; Sánchez-Monge et al. 2013b). We obtain an average f_D of $\sim$ 6 for D24 and $\sim$ 2 – 3 for the IRB. Calculating the average f_D in bins of T_{ex} shows that the depletion factor decreases only slightly or stays constant for $T_{ex} \lesssim$ 25 K ($f_D \sim$ 7 – 5), while it decreases more rapidly for $T_{ex} \gtrsim$ 25 K (down to $\sim$ 2). On the other hand, to test the dependence of f_D on the density (Fig. 4.8), we selected the sources in a smaller range of T_{ex} (14 – 24 K, to remove extreme temperatures and have still $\sim$ 20 sources) and recomputed the densities and depletion factors assuming a constant T_d = 20 K. Panel (c) of Fig. 4.8 shows that the trends are still visible. The symbol sizes are proportional to the distance of the sources, showing that the trends are not due to distance effects.

In recent works (Wienen et al. 2012 and Wienen et al. in prep.) the ammonia

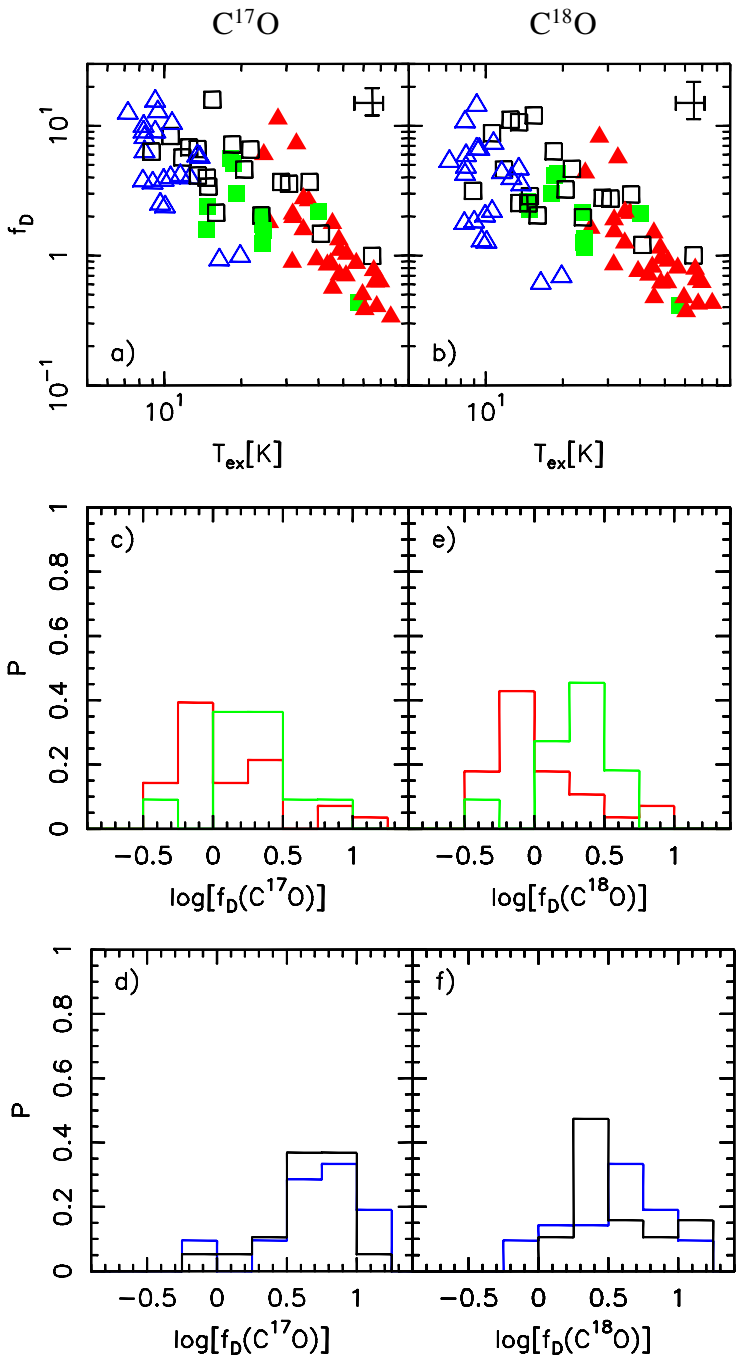

Figure 4.7: Panel **(a)** and **(b)** show CO depletion factors from $^{12}C^{18}O$ and $^{12}C^{17}O$ as a function of T_{ex}, respectively. A typical uncertainty is shown in the top right corner. The symbols and colours are the same as in Fig. 4.1. Panels **(c)** and **(d)** and **(e)** and **(f)** show the normalised histogram of depletion factor for the four groups, from $^{12}C^{17}O$ and $^{12}C^{18}O$, respectively; the colours are the same as in Fig. 4.2.

Table 4.3: Mean and median values for the depletion factor (f_D) for the four groups, with the dispersion of the points.

Group	IRB	RMS	D8	D24
Mean	2	2	5	6
Median	1	2	4	5
σ	2	1	3	3

(1,1), (2,2) and (3,3) inversion transitions were observed towards a sub-sample of sources in the TOP100 sample. The observations were carried out with Effelsberg- and MOPRA telescopes, thus sampling a larger scale than our observations, though with a typical filling factor of 0.1 (Wienen et al. 2012). The temperatures derived from ammonia are typically higher than those calculated in this work for sources in groups D8 and D24, especially for the latter, with typical values $\sim$ 20 K. We tried to reproduce the observed line intensities with RATRAN assuming a temperature of 20 K: the results are briefly discussed in Sect. 4.6.3.1.

For the sources in groups D8 and D24 we can derive the timescale for CO depletion τ_{dep}, using the expression given in Bergin & Tafalla (2007) (see Eq. 1.2, in Sect. 1.3.1.2) and the peak volume density of molecular hydrogen. We find that τ_{dep} is in the range 10^3 yr – 10^5 yr, of the same order of magnitude as the free-fall timescale, which is a rough measure of the clump lifetime. It is interesting to note that three out of four sources with $f_D < 2$ indeed have the largest τ_{dep}/τ_{ff} of the sample ($\gtrsim$ 1.5). Tackenberg et al. (2012) find that lifetimes of massive clumps are of the order of $10^4 - 10^5$ yr; we can compare this number with the timescale for depletion as a function of radius in clumps with a $n(H_2) \propto r^{-1.5}$ density profile (approximately the mean value for the clumps in the ATLASGAL survey). In practice, assuming a mass for the clump unequivocally sets the volume density of molecular hydrogen at all radii. Using again the equation of Bergin & Tafalla (2007), one can assign a characteristic timescale for CO depletion at each r, using the above-cited $n(H_2)$. We can thus derive an estimate of the size R_{dep} of the central depletion hole as the radius at which τ_{dep} matches the typical lifetime of massive starless clumps. This procedure yields values of R_{dep} in the interval $\sim 0.02 - 0.1$ pc for a clump with a mass within 1 pc of $\sim$ 550 $M_\odot$ and an age of 10^4 yr and 10^5 yr, respectively. The radius increases for larger masses.

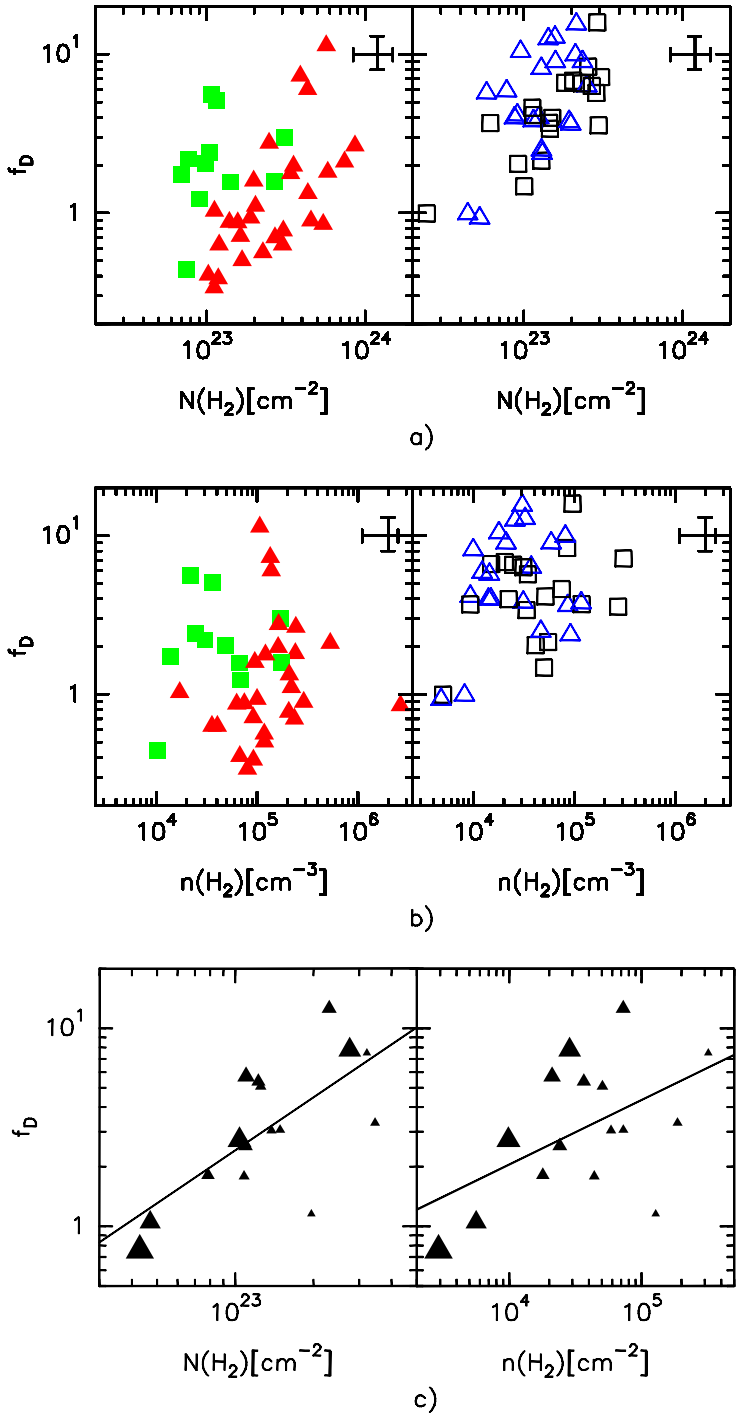

Figure 4.8: Panel **(a)** shows the CO depletion factor (from $^{12}C^{17}O$) as a function of $N(H_2)$. The symbols and colours in the panels are the same as in Fig. 4.1. Panel **(b)** is the same as (a), but for f_D as a function of $n(H_2)$. Panel **(c)** shows that removing the T_{ex}-dependence the trends are still visible (see text). The solid lines are unweigthed least-squares fits and symbol sizes are proportional to the distance of the source.

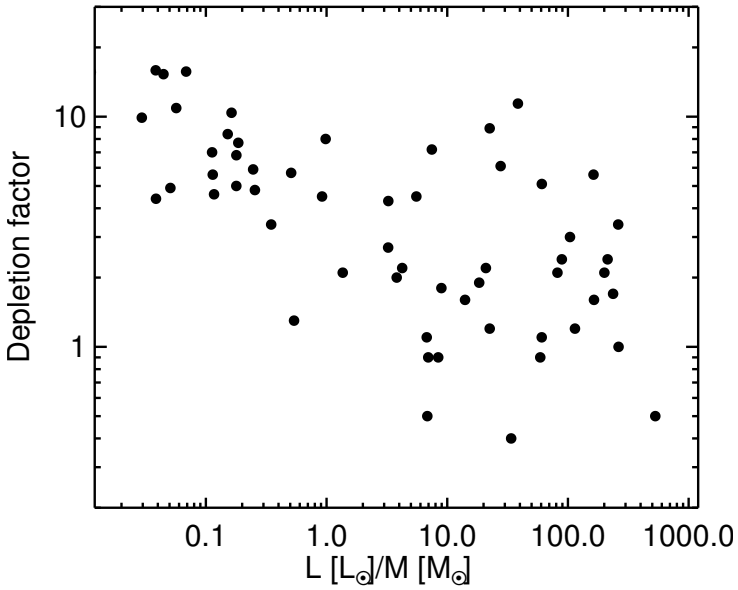

Figure 4.9: Depletion factor as a function of the L/M ratio.

4.6.3.1 RATRAN Modelling

The previous analysis assumes that molecules are in LTE. In order to have more solid results for CO abundances we used RATRAN[3] (Hogerheijde & van der Tak 2000) to build one-dimensional models of the clumps for typical parameters of the sample. To reproduce the observed CO line intensities and ratios, we build two grids of models, one set with a central heating source, the other with a constant temperature. For the former we vary the luminosity of the central source L (in 3 steps: 10^2 $L_\odot$, 5×10^3 $L_\odot$, 10^5 $L_\odot$, which is then translated in a power-law temperature profile; see Rowan-Robinson 1980; Wolfire & Cassinelli 1986) and the clump mass (from $\sim$ 200 $M_\odot$ to $\sim$ 45000 $M_\odot$ in 6 steps), while for the latter we vary the temperature (from 5 K to 15 K in 4 steps) and the mass (as in the other grid). The clump outer radius, the linewidth and the index α for the power law describing the density profile were fixed at 1 pc, 4 km s^{-1} and -1.5, respectively. We also assumed a typical distance of 4 kpc. The models were convolved with a Gaussian as large as the beam size for each wavelength, to simulate our observations.

Figure 4.10 and 4.11 show the two kinds of grid (centrally heated- and isothermal models, respectively) superimposed on the data points, with marker sizes

[3] www.sron.rug.nl/~vdtak/ratran/

proportional to the logarithm of the MSX flux in the E band. In both figures, panels **(a)**, **(b)** and **(c)** refer to sub-sample S1, where we compare $C^{17}O(3-2)$, $C^{17}O(1-0)$ and the sub-mm flux; on the other hand, panels **(d)**, **(e)** and **(f)** show the results for sub-sample S2, using $C^{17}O(3-2)$ and $C^{18}O(2-1)$. In each of the two figures we plot grids with three different depletion factors, as shown above the panels. For the models with a central heating source we use grains with thin ice mantles, while for the isothermal clumps we use grains with a thick ice coating, as suggested by their derived f_D. The thick ice mantle on the dust grains increases their opacities, thus reducing the column density of dust (and thus of molecular hydrogen, for a fixed gas-to-dust ratio) needed to obtain a given flux. The dotted lines indicate clumps with the same mass in both grids, while dashed lines indicate clumps with the same L or T, in Figures 4.10 and 4.11, respectively. The figures show that, for the sources with line ratios $^{12}C^{17}O(3-2)/^{12}C^{17}O(1-0) \gtrsim 1$ or $^{12}C^{17}O(3-2)/^{12}C^{18}O(2-1) \gtrsim 0.3$ and large sub-mm fluxes (corresponding also to sources with high MSX fluxes) are much better reproduced by a centrally heated clump, with only moderate depletion. On the other hand, sources with very low line ratios are consistent with cold, isothermal clumps, but need a larger depletion factor to reproduce the line fluxes. The fact that for sub-sample S2 the points are much more scattered around the model grid may be the result of having assumed the same $[^{18}O]/[^{17}O]$ for all sources, while, as observations have different angular resolutions, the geometry of the region and/or a different size of the source than the one assumed for the grid (1 pc) may have a larger impact on the measured ratios.

We tried to reproduce the observed line ratios using temperatures of the order of those suggested by ammonia. With the simple spherical models considered here, it is not possible to do so for the ratios $I[^{12}C^{17}O(3-2)]/I[^{12}C^{17}O(1-0)] \lesssim 1$ with a constant CO depletion. Even limiting the volume density of the clump to $1-3\times10^4$ cm^{-3} does not yield an acceptable combination of line intensities, ratios and peak fluxes in the sub-mm regime. A different approach is to use a drop profile for the CO abundance, i.e. to assume that the abundance is canonical when the density is below a given value, while all CO is locked onto grains for densities above this value. In this case, we constructed a grid of large clumps with a radius ~ 2 pc, to try to simulate the contribution from the external layers. We varied the mass in 10 steps (between $550-2900$ M$_\odot$ within 1 pc), the critical density defining the size of the central depletion hole (between 10^4-10^5 cm^{-3}) and the temperature of the depleted layers (in the range $8-15$ K). The temperature of the external layer was assumed to be constant and equal to 20 K. Figure 4.12 shows the results of these models, as a yellow-shaded area, compared with the peak fluxes and line intensities of S1. The spread in line intensities is due to the

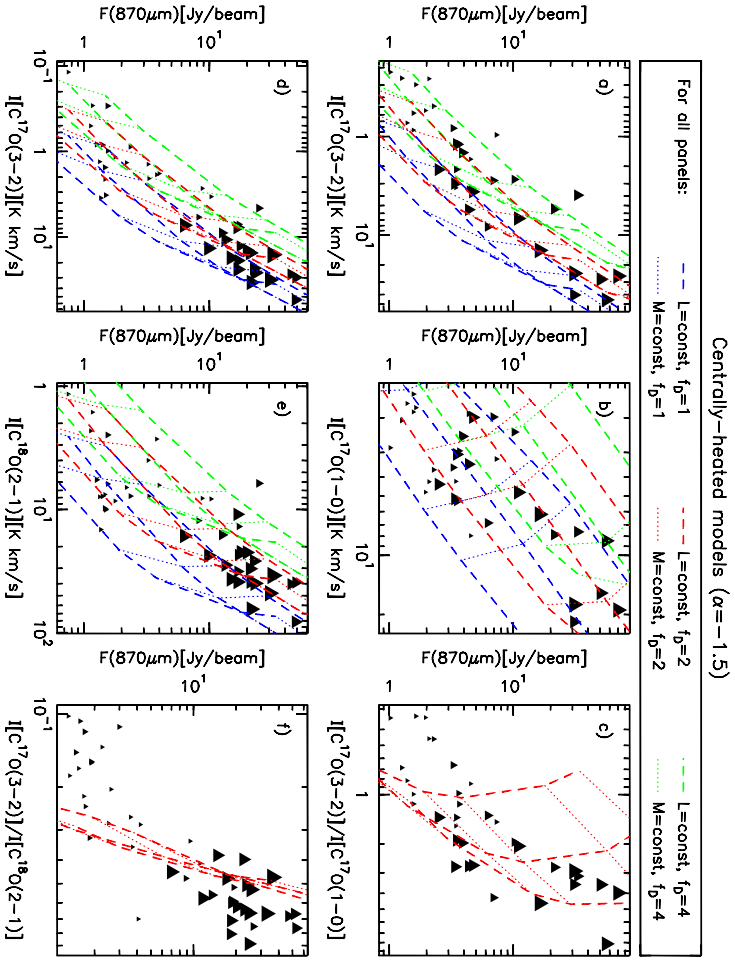

Figure 4.10: Line- and continuum fluxes of the sources, compared to grids of centrally heated models for typical sources parameters. The size of the symbol is proportional to the logarithm of MSX flux in band E. The grids include a central object heating the gas, and differ for depletion factors, indicated above the panels. The dashed line connects models with constant luminosity of the central object. The dotted line connects models with the same mass. Panels (a) to (c) refer to sub-sample S1, panels (d) to (f) to sub-sample S2.

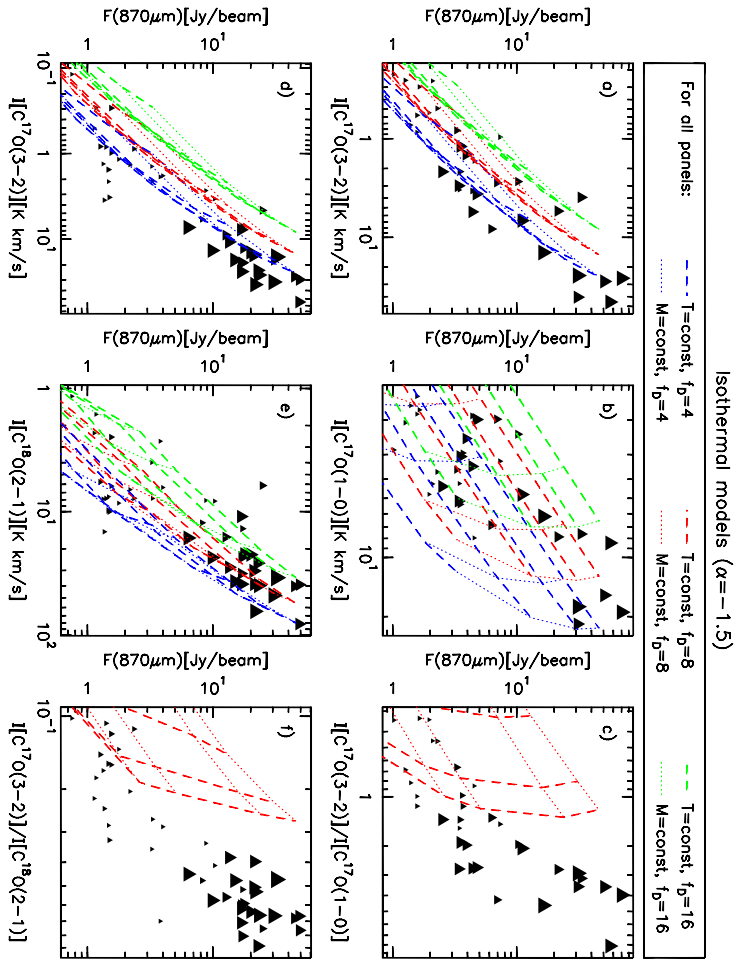

Figure 4.11: Same as Fig. 4.10, but for isothermal models. The dashed line connects models with constant temperature. Panels (a) to (c) refer to sub-sample S1, panels (d) to (f) to sub-sample S2.

different critical densities above which we assume that CO is completely depleted, while the range in sub-mm flux is mainly caused by the different masses of the clump; the temperature of the central regions has a minor impact for the low values considered. Despite the rather high temperature in the low-density external parts of the clumps, the observed molecular-line ratios can be reproduced with this kind of model.

In conclusion, both using a constant CO abundance throughout the clump and the temperature suggested by the CO line ratio or a drop-profile model we find

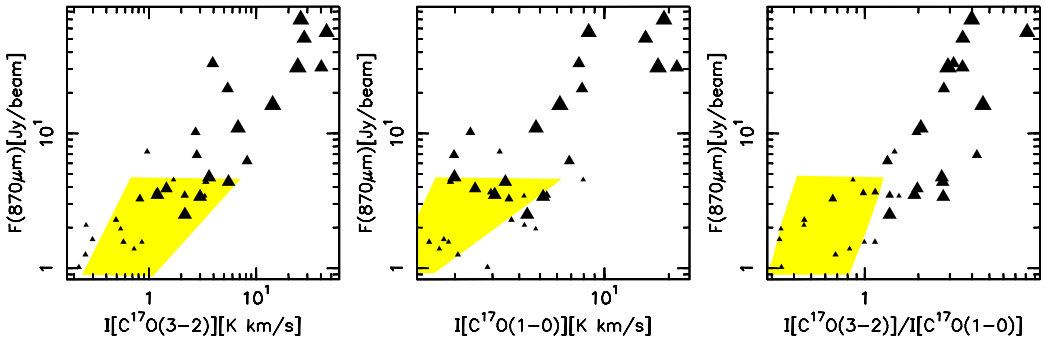

Figure 4.12: Same as panels (a), (b) and (c) in Fig. 4.10, but for models with a drop-profile in the $^{12}C^{17}O$ abundance (see text); the ranges in peak sub-mm fluxes, line- intensities and ratios spanned by the models are indicated as a yellow-shaded area.

indications that depletion is important for cold, massive clumps. On the one hand, we have a simple order-of-magnitude estimate of f_D, that can be even $10 - 20$ for cold sources, and on the other hand we can derive the rough size of the depletion hole, to be compared with that derived from the typical lifetimes of massive starless clumps (see Sect. 4.6.3). Both methods suggest depletion zones with radii $\lesssim 0.1$ pc, for a typical clump.

4.6.3.2 RATRAN Modelling of Individual Sources

A more detailed study is carried out for some individual sources in the sample, to properly take into account the source size, radial density distribution, linewidth, expected abundance and distance. The sources were selected from sub-sample S1 not to be extremely elongated from the 870 μm images. We selected more sources from among groups D8 and D24 objects to confirm and constrain better their large depletion factors. We build a grid of models with RATRAN, with 13 equally spaced steps in mass, and 11 in depletion factor. Depending on whether the clump is centrally heated or isothermal, 15 equal logarithmic steps in luminosity or 15 equal steps in temperature. The radius of the cloud was fixed at the value of $R_{\rm eff}$ as given in the ATLASGAL catalogue.

We compare the observed values of line- and peak 870 μm continuum fluxes with those predicted by the model, assigning a probability to each set of free

parameters of the model (M, L or T, f_D) according to:

$$P(M, L\,\mathrm{or}\,T, f_D|D, model) = \frac{1}{\psi}\, P(D|M, L\,\mathrm{or}\,T, f_D, model) \times P(M, L\,\mathrm{or}\,T, f_D|model), \tag{4.18}$$

where $P(D|M, L\,\mathrm{or}\,T, f_D, model)$ is the likelihood, evaluated following

$$P(D|M, L\,\mathrm{or}\,T, f_D, model) = \prod_{i=0}^{3} \mathrm{e}^{\frac{-(\mathrm{F_i}-\mathrm{F_{mod,i}})^2}{2\sigma^2_{\mathrm{F,i}}}}. \tag{4.19}$$

In Eq. 4.19 F_i are the observed integrated line flux and 870 μm peak fluxes, $F_{mod,i}$ are the same fluxes, predicted by the model and convolved with the beam of the observations and $\sigma_{F,i}$ are the flux uncertainties. ψ is a normalisation constant, so that

$$\int P(M, L\,\mathrm{or}\,T, f_D|D, model) dM (dL\,\mathrm{or}\,dT) df_D = 1. \tag{4.20}$$

Finally, $P(M, L\,\mathrm{or}\,T, f_D|model)$ is the *prior*, taken to be constant in the case of isothermal clumps, in the parameter range shown in Fig. 4.14. On the other hand, the luminosity derived in this way may not be well constrained, since it is derived only by the $^{12}C^{17}O(1-0)/(3-2)$ line ratio in the central regions probed by our single-pointing observations (i.e. representing the average T_{ex} along the line-of-sight), in the hypothesis of spherical symmetry. Therefore, using luminosities reported in literature, we set loosely informative Gaussian priors on L for the bright sources. Fazal et al. (2008), van der Tak et al. (2013) and Gaume et al. (1993) give a luminosity (scaled to the distance used here) of $\sim 8 \times 10^3$ $L_\odot$, $\sim 10^5$ $L_\odot$ and $\sim 6 \times 10^4$ $L_\odot$ for AGAL19.882-00.534, AGAL034.258+00.154 and AGAL049.489-00.389, respectively.

For sources in the first two groups we use models with a central heating source and thin ice mantles, while for groups D8 and D24 we use models with a constant temperature and thick ice mantles for the dust. Figure 4.14 shows the probability distributions for the modelled sources. The probability distribution as a function of mass and luminosity for the centrally heated sources, and mass and temperature for the isothermal objects is computed by integrating the probability cube along the depletion axis. Tables 4.4 and 4.5 show the parameters of the sources derived from RATRAN models and the width of their probability distribution, calculated integrating the probability cube along the other 2 axes. All regions include a large

Table 4.4: Parameters derived from RATRAN models for individual sources in groups IRB and RMS, assuming a constant abundance profile.

Source	$L(mean)$ $(10^3 \times L_\odot)$	$L(mode)$ $(10^3 \times L_\odot)$	68%int $(10^3 \times L_\odot)$	$M(mean)$ $(10^2 \times M_\odot)$	$M(mode)$ $(10^2 \times M_\odot)$	68%int $(10^2 \times M_\odot)$	$f_D(mean)$	$f_D(mode)$	68%int
AGAL019.882-00.534	20	16	5 – 43	5.4	5.3	3.3 – 7.0	2.4	2.1	1.3 – 3.3
AGAL034.258+00.154	16	8.9	4.0 – 24	12	12	8 – 15	1.2	1.3	0.7 – 1.8
AGAL049.489-00.389	56	38	17 – 100	130	124	82 – 167	2.2	2.0	1.2 – 3.0

Notes. The columns show the mean, mode and the shortest 68% interval of the derived luminosity, mass and depletion factor.

Table 4.5: Parameters derived from RATRAN models for individual sources in groups D8 and D24, assuming a constant abundance profile.

Source	$T_K(mean)$ (K)	$T_K(mode)$ (K)	68%int (K)	$M(mean)$ $(10^2 \times M_\odot)$	$M(mode)$ $(10^2 \times M_\odot)$	68%int $(10^2 \times M_\odot)$	$f_D(mean)$	$f_D(mode)$	68%int
AGAL008.684-00.367	12.7	12.5	11.0 – 14.0	215	205	151 – 266	5.0	5.0	4.0 – 6.0
AGAL010.444-00.017	8.8	8.5	7.9 – 9.6	157	145	104 – 202	14.4	14.5	10.7 – 17.6
AGAL013.178+00.059	13.9	13.6	11.9 – 15.6	29	28	21 – 36	11.7	11.1	8.7 – 14.4
AGAL014.492-00.139	8.9	8.8	8.0 – 9.8	34	31	24 – 43	9.3	8.7	6.8 – 11.7
AGAL018.606-00.074	16.3	15.0	11.8 – 18.0	44	37	24 – 57	3.1	3.0	1.9 – 4.0
AGAL028.564-00.236	8.3	8.3	7.3 – 9.1	99	95	66 – 127	7.2	6.7	5.4 – 8.8
AGAL034.411+00.234	16.1	15.5	14.2 – 17.7	5.4	5.1	3.9 – 6.6	9.5	9.1	7.2 – 11.5

Notes. The columns show the mean, mode and the shortest 68% interval of the derived temperature, mass and depletion factor.

quantity of gas and dust, and the temperatures for groups D8 and D24 are very low.

We note that groups IRB and RMS and groups D8 and D24 indeed show different depletion factors, with ranges between $1-3$ and $3-15$, respectively. These depletion factors are averaged along the line-of-sight and in the beam. Because groups D8 and D24 contain sources that are in an earlier stage of evolution than IRB and RMS objects, this result confirms that, as evolution proceeds, the molecules are evaporated from the dust grains in the gas phase, and thus the CO-depletion decreases in the environments around high-mass stars. Larger values of f_D are found by Fontani et al. (2012), for a separate sample of massive clumps (cf. Sect. 3.6.2.7). In that work the column density of molecular hydrogen is calculated with the expression of Beuther et al. (2005a), yielding column densities ~ 2.7 times larger than the expression used here, because a different dust opacity is used. Hernandez et al. (2011) study in detail depletion in a single IR-dark cloud, showing that a large mass of gas is affected by CO depletion. The large depletion factors found in this sample, together with those derived in Sect. 3.6.2.7 show that the freeze-out phenomenon is not only occurring also in high-mass clumps, but it involves large masses of gas (at least tens of $M_\odot$), as suggested by Hernandez et al. (2011).

It is reasonable to expect that the abundance profile is not constant within the clump, and that the depletion factors in the densest and coldest regions are larger than those derived; for example, in Zhang et al. (2009) it is claimed that depletion factors may reach values $\gtrsim 1000$ in the central regions of low mass cores. Our estimate may be, in fact, a lower limit for apparently starless objects, an average within an APEX beam along the line-of-sight, since we do not take into account such variable abundance profiles. A simple test performed with RATRAN shows that if we assume a depletion increasing with density, we find that the depletion factors in the inner regions may be much larger than those found with a constant profile, and, because the outer and less dense layers dominate the emission in this situation, one can use a larger gas and dust temperature to reproduce the observed line ratio, due to non-LTE excitation (similarly to the drop-profile models described in Sect. 4.6.3.1), thus decreasing the mass by up to a factor of ~ 3 for "cold" sources. However, without a map of molecular emission we do not have enough constraints for these more sophisticated models. Mapping of the clumps in molecular lines and at higher angular-resolution may unveil the actual mass of gas suffering from depletion and give indications on the abundance gradient, as well as a more accurate determination of temperature and mass.

On the other hand, Zinchenko et al. (2009) and Miettinen et al. (2011) report

determination of canonical abundance of CO towards massive clumps. In both works the sources show signs of active star formation, thus being similar to our more evolved sources. For these clumps with a central heating source the abundance may rise near to the (proto)star, due to the energy injected in the medium.

4.6.4 Stability of the Clumps

A simple analysis of the gravitational stability can be performed by comparing the virial mass with the mass calculated from the sub-mm emission by means of Eq. 4.16, assuming $T_{\rm d} = T_{\rm K} = T_{\rm ex}$ and that the clump is isothermal. We use again Eq. 3.2 to derive the virial mass, but in this case we assumed an average radial density profile $n(H_2) \propto r^{-1.5}$ (see Sect. 4.6.3.1), implying $k = 170$, $r = R_{\rm eff}$ (approximately the FWHM of the clump), and we use the $C^{17}O(3-2)$ line to derive ΔV, so that we use the same line for all sub-samples. Figure 4.13 shows this comparison, with the dashed- and dotted lines line indicating $M_{\rm vir} = M$ and $M_{\rm vir} = 2M$, respectively (see below): in the upper panel we show M *vs.* $M_{\rm vir}$ and in the lower one the virial parameter $\alpha = M_{\rm vir}/M$ as a function of M. Objects in groups IRB and RMS are mostly distributed around the virial equilibrium line, while the most massive ones in Groups 3 and 4 appear to be unstable, i.e. with $M_{\rm vir} \ll M$. The most massive sources in groups D8 and D24 have virial masses ~ 10 times lower than the mass derived from dust emission.

Here we try to understand if these massive sources do really have virial masses much lower than their actual mass, or if it is due to an observational effect. There is the possibility that the temperature we derive is underestimated and that the mass is consequently overestimated. The temperature of apparently starless clumps was previously measured by e.g., Rygl et al. (2010), Giannetti et al. (2013) and Sánchez-Monge et al. (2013b) making use of other temperature probes, typically NH_3. The characteristic $T_{\rm K}$ was found to be $\sim 10-15$ K, slightly larger than what we measure for group D24. However it is similar to that of group D8 and it is difficult to explain such a large difference in mass as being a consequence of this difference in temperature. The ammonia temperatures measured by Wienen et al. (2012) and Wienen et al. (in prep.) suggest temperatures of ~ 20 K for D8 and D24. Even allowing such temperature accounts for a change by only a factor $\lesssim 3$. On the other hand, the temperature we measure in IR-bright clumps may be relatively high and not representative of the whole clump, thus leading one to underestimate M. Again it is difficult to explain a difference of a factor of up to 20 in mass, because $T_{\rm K}$ from ammonia observations is typically around $20-40$ K for such sources. Depletion of CO may play a role in this: if the degree of depletion is

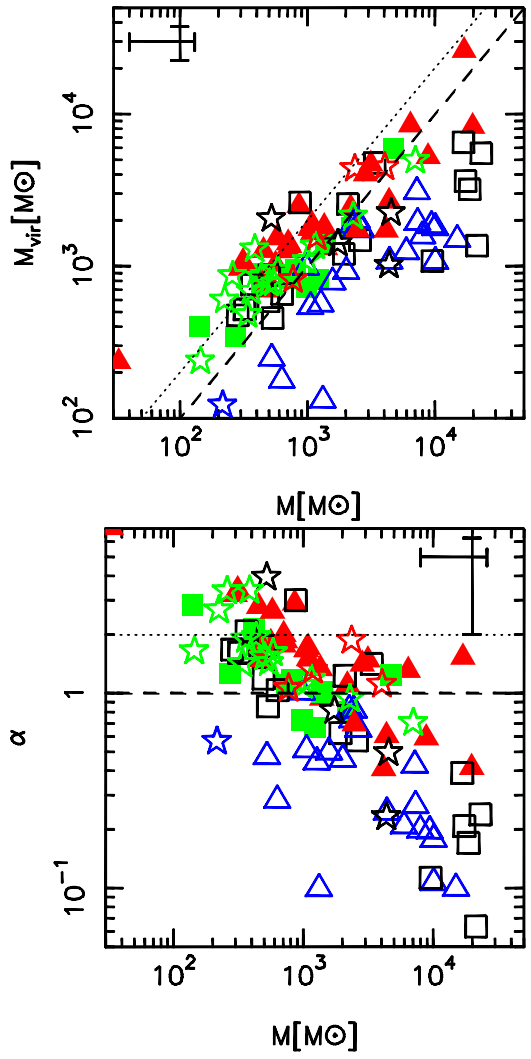

Figure 4.13: Comparison between the gas mass derived from ATLASGAL fluxes and the virial mass. In the upper panel we show M *vs.* $M_{\rm vir}$, in the lower one M *vs.* α ($= M_{\rm vir}/M$). The symbols and colours are the same as in Fig. 4.2. A typical uncertainty (for sub-samples S1 and S2) is shown in the top left or right corner. The dashed- and dotted lines line indicating $M_{\rm vir} = M$ and $M_{\rm vir} = 2M$, respectively (see text).

very high in the centre, we might not be able to probe the physical conditions of the gas there, where the density is very high. In this case we would be tracing only the gas in a more external layer (cf. also Sect. 4.6.3.1). If the source is starless, we do not expect the temperature in this external layer to be significantly lower than in the centre; on the contrary, in low-mass sources starless objects seem to have a small negative gradient (e.g., Bergin & Tafalla 2007), being colder in the centre, as fewer photons can penetrate the dense layers. On the other hand, we do not measure a large average depletion for star-forming sources (see 4.6.3). It is possible to have a larger effect on the mass if the density in the external layers is low, and the molecule is not in LTE. A simple test of the impact of this on the mass of the clump is described in Sect. 4.6.3.2. The presence of a thick ice coating on the dust grains changes the dust opacity; according to Ossenkopf & Henning (1994) it may increase by $\sim 30\%$ at these frequencies, with respect to a model with thin ice mantles. Using a model with thick mantles for "cold" clumps in groups D8 and D24 would decrease their masses, but not enough to significantly increase the derived $M_{\rm vir}/M$ ratios. Another source of uncertainty for α is the clump size. The ratio between the major- and minor axis of the source is typically between $1-2$. Therefore, this may cause an uncertainty on the virial mass of a factor of 2 for some clumps. The assumed gas-to-dust ratio of 100 may not be applicable to all sources in the sample, but we do not know enough about its variation to estimate its influence on the derived masses. The uncertainties described above do not seem to be able to account for the largest differences between the mass derived from dust emission and the virial mass.

A clump mass measured from the sub-mm emission larger than the virial mass was found also by Hofner et al. (2000) and Fontani et al. (2002). In the latter work, the authors use CH_3CCH as a temperature probe, which is a symmetric-top molecule. This molecule gives a reliable temperature estimate, thus reducing the uncertainties on the mass. In Chapter 3 (Giannetti et al. 2013) we have temperature determinations both from ammonia and SED fitting, and we find that the most massive clumps have $M > M_{\rm vir}$. In a recent work Kauffmann et al. (2013) study in detail the virial parameter in molecular clouds, for a large collection of objects, from entire clouds to cores. These authors find that in high-mass sources the virial mass can be much lower than the mass derived from observations of the dust. The authors consider $\alpha \sim 2$ as a limit for the gas motions alone to prevent collapse, to take into account a wide range of shapes and density gradients. However, our definition of $M_{\rm vir}$ already takes into account a density gradient ($n \propto r^{-1.5}$), implying values of α about 20% lower than theirs. They also discuss the observational uncertainties on α and conclude that the very low values of the virial parameter are

likely to be real. Kauffmann et al. (2013) fit a straight line to the $\log(M) - \log(\alpha)$ diagram for high-mass clumps, finding that the slope is ~ -0.5, and that $\alpha_{min} \sim 0.2$ from the fit, for high-mass sources. An analogous fit yields very similar results in both parameters for the clumps studied here, excluding the sources in groups IRB and RMS, to have a comparable sample. As shown in Kauffmann et al. (2013), despite the low values of the virial parameter, clumps with $M \gg M_{\rm vir}$ are not likely to be undergoing gravitational collapse. López-Sepulcre et al. (2010), on the other hand, find masses consistent with the virial mass, as discussed in Sect. 3.6.2.6. Thus, discordant claims on the virial stability of massive clumps exist in the literature. If these objects are really unstable, the magnetic field may play a significant role in opposing the collapse. For the most massive clumps, fields of the order of a mG are needed to halt the collapse. In particular, using the expression from Bertoldi & McKee (1992) for cold, magnetised clouds, the average critical magnetic field strength ranges between 0.3 – 3 mG. Magnetic fields of this order of magnitude have been measured in regions of high-mass star formation (e.g., Crutcher 2005; Girart et al. 2009).

4.7 Summary and Conclusions

We studied several CO isotopologues in 870 μm-bright clumps of the ATLASGAL survey, to investigate the depletion of carbon monoxide, and the $[^{12}C]/[^{13}C]$ and $[^{18}O]/[^{17}O]$ isotopic ratios in regions of (potential) massive star formation. This "TOP100" sample consists of 102 clumps.

The sample is selected to include the brightest sources in the sub-mm in different evolutionary stages, separated in four groups (from IR-bright to 24 μm-dark sources; Motte et al. 2007; Nguyen Luong et al. 2011, see Sect. 4.3).

From the ratio of different rotational transitions of the observed CO isotopologues we estimate an excitation temperature, with which we derive the molecular column density corrected for optical depth; in order to have a consistent estimate of the optical depth and a refined estimate of the isotopic ratios, we combined all available information from line intensities, ratios and hyperfine structure with a Bayesian approach, allowing the relative isotopic abundances to vary (see Sect. 4.5.4). Comparing the CO isotopologue-column densities with those of H_2, derived from the dust emission at 870 μm, we find that a significant fraction of the sources suffer from depletion, especially the ones with a low $T_{\rm ex}$.

The main result of this work is that we find that, just like for low-mass cores, depletion of CO is relevant also in massive sources during their early life, and

varies with evolution. Groups D8 (the brightest 8 μm-dark objects) and D24 (the brightest 24 μm-dark sources), typically show larger depletion factors and lower temperatures than the more evolved groups IRB and RMS (the brightest objects of the whole survey and the brightest among the remaining sources classified as MYSOs in the RMS survey, respectively; the clumps in both classes have mid-IR emission). The depletion factors f_D in the less evolved sources may be as large as ~ 20 (see Fig. 4.7 and Table 4.5; this corresponds to $f_D \sim 55$ using the dust opacities adopted in Fontani et al. 2012). These estimates are likely to be lower limits at least for starless sources, since they are averaged along the line-of-sight and derived with a constant abundance profile. On the other hand, the more evolved sources show a typical depletion $\sim 3-10$ times lower (cf. Sect. 4.6.3). The larger depletion found in groups D8 and D24 was confirmed with one-dimensional models made with RATRAN, to take into account possible non-LTE effects. Therefore, massive objects seem to follow an evolution of CO depletion similar to that of low-mass objects, where carbon monoxide is frozen onto grains, before the feedback from star formation evaporates the molecules back into the gas phase. The column- and volume densities are also found to correlate with the depletion factor: denser sources have a larger f_D, on average. However, among different groups the typical depletion at a given density decreases with increasing temperature, i.e. for more evolved sources. The dependence of the depletion factor on the temperature and density could be explained by the effect of these quantities on the evaporation- and freeze-out timescales.

An alternative possibility to reproduce the observations is to use models with a central drop in CO abundance. We used models where all CO is locked onto grains for densities above a critical value, whereas below this density, the abundance is canonical. Also in this case the observations can be qualitatively reproduced, again suggesting that CO depletion is important in the dense layers of massive clumps. Both these models and the comparison of typical lifetimes with the timescale for depletion as a function of radius suggest that the radius of the central depletion hole is roughly in the range $\sim 0.02-0.1$ pc (see Sect. 4.6.3).

A simple test for the stability of clumps is performed comparing the total mass M derived from dust continuum emission and the virial mass. The clumps are found to be near virial equilibrium for groups IRB and RMS. On the other hand, several sources of groups D8 and D24 seem to be gravitationally unstable, in the sense that $M_{\rm vir} \ll M$. We consider some sources of uncertainty and conclude that this is likely to be real, at least for the sources where $M_{\rm vir}/M$ is the smallest.

We also investigated the $[^{18}O]/[^{17}O]$ and $[^{12}C]/[^{13}C]$ isotopic ratios in the inner Galaxy. We find no significant gradient for $[^{18}O]/[^{17}O]$ as a function of D_{GC} for

2 kpc $\lesssim dgc \lesssim$ 8 kpc, and the ratios are consistent with ~ 4 with an intrinsic scatter of ~ 1. We find that a few sources with $D_{GC} \sim 4$ kpc have $[^{18}O]/[^{17}O]$ values of ~ 5.5, similar to the values measured for the pre-Solar cloud. $[^{12}C]/[^{13}C]$ is found to increase with D_{GC}, as predicted by the models of chemical evolution of the Galaxy (see e.g., Prantzos et al. 1996), with $[^{12}C]/[^{13}C] \sim 66 \pm 12$ in the Solar neighbourhood; however, the intrinsic scatter of the relation is as large as $\sim 7 - 13$. Milam et al. (2005) show that this large scatter is not likely due to processes such as chemical fraction of selective photodissociation, therefore leaving intrinsic differences (e.g., metallicity, star formation history) between sources, or other processes unaccounted for (such as cloud mergers, non-efficient- or radial gas mixing) to explain it.

Acknowledgements

This work was partly funded by the Marco Polo program (Università di Bologna), making it possible for AG to spend three months at the Max Planck Institute für Radioastronomie in Bonn. AG thanks the Max Planck Institute für Radioastronomie and FW for their hospitality and support. T.Cs.'s contribution was funded by the ERC Advanced investigator grant GLOSTAR (247078). This research made use of data products from the Midcourse Space Experiment. Processing of the data was funded by the Ballistic Missile Defense Organization with additional support from NASA Office of Space Science. This research has also made use of the NASA ADS, SIMBAD, CDS (Strasbourg) and NASA/IPAC Infrared Science Archive, which is operated by the Jet Propulsion Laboratory, California Institute of Technology, under contract with the National Aeronautics and Space Administration.

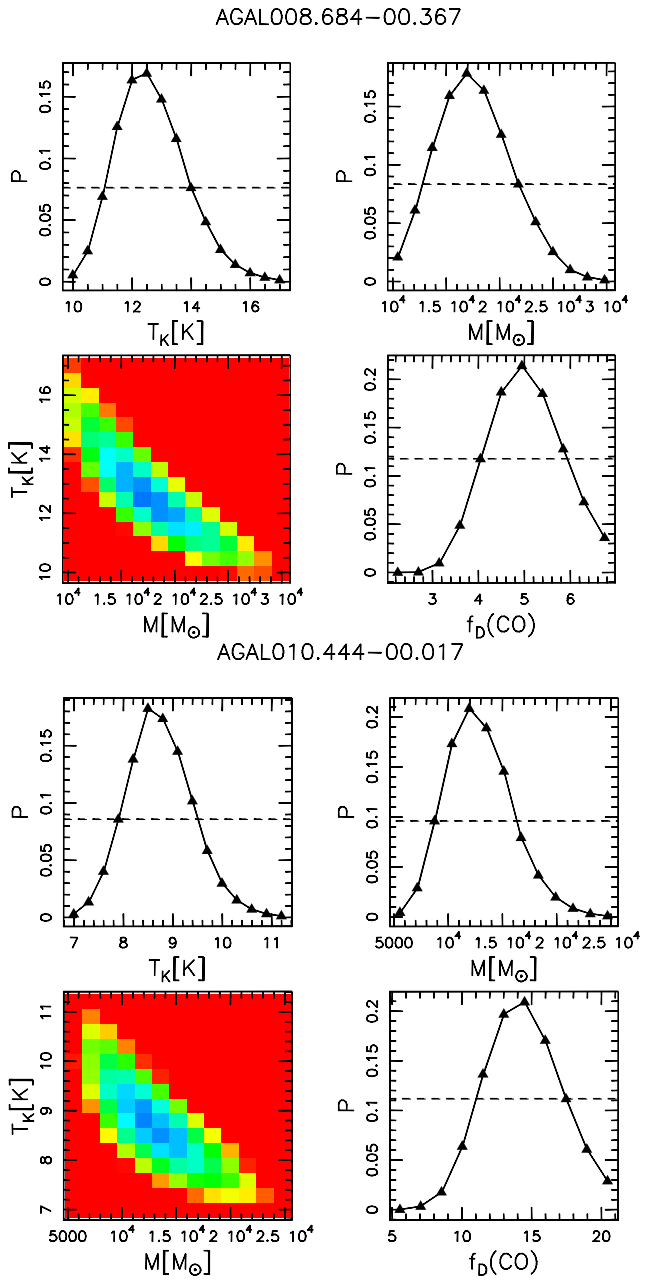

Figure 4.14: RATRAN results for individual sources. The panels show: (top left) probability distribution of the temperature/luminosity, depending on the source, (top right) probability distribution of the mass, (bottom left) 2D probability distribution of mass and T or L (depending on whether model is centrally heated or isothermal), (bottom right) probability distribution of the depletion factor.

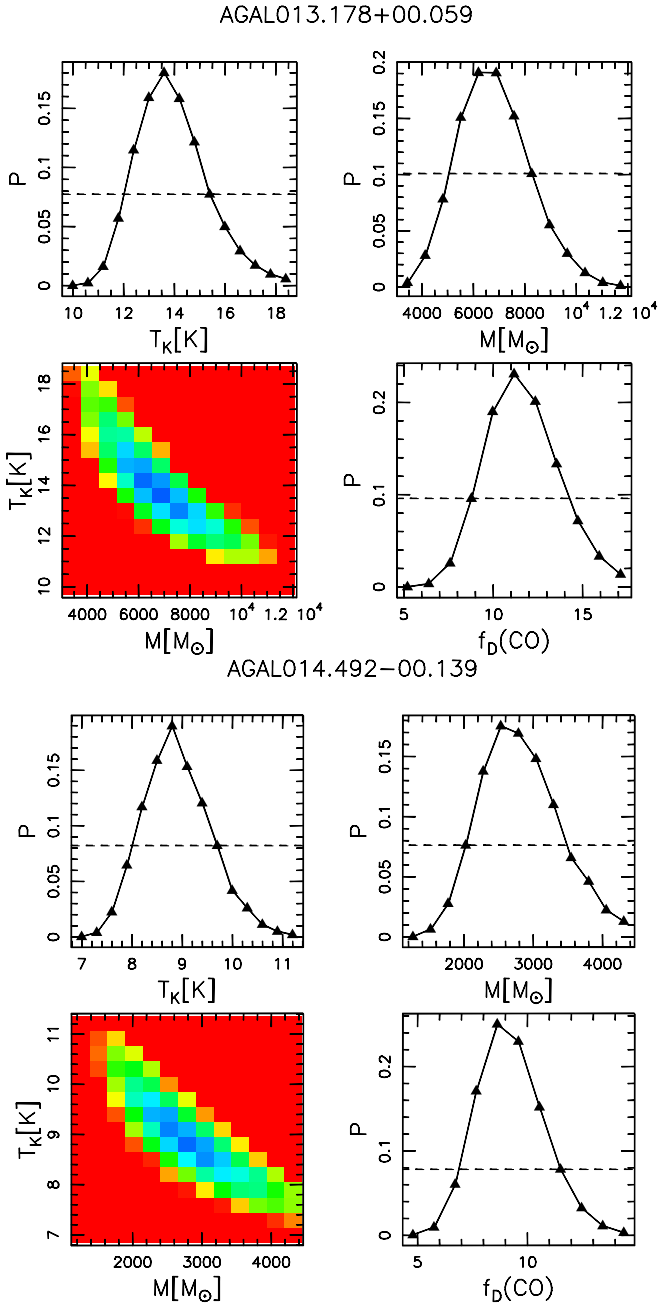

Figure 4.14: Continued.

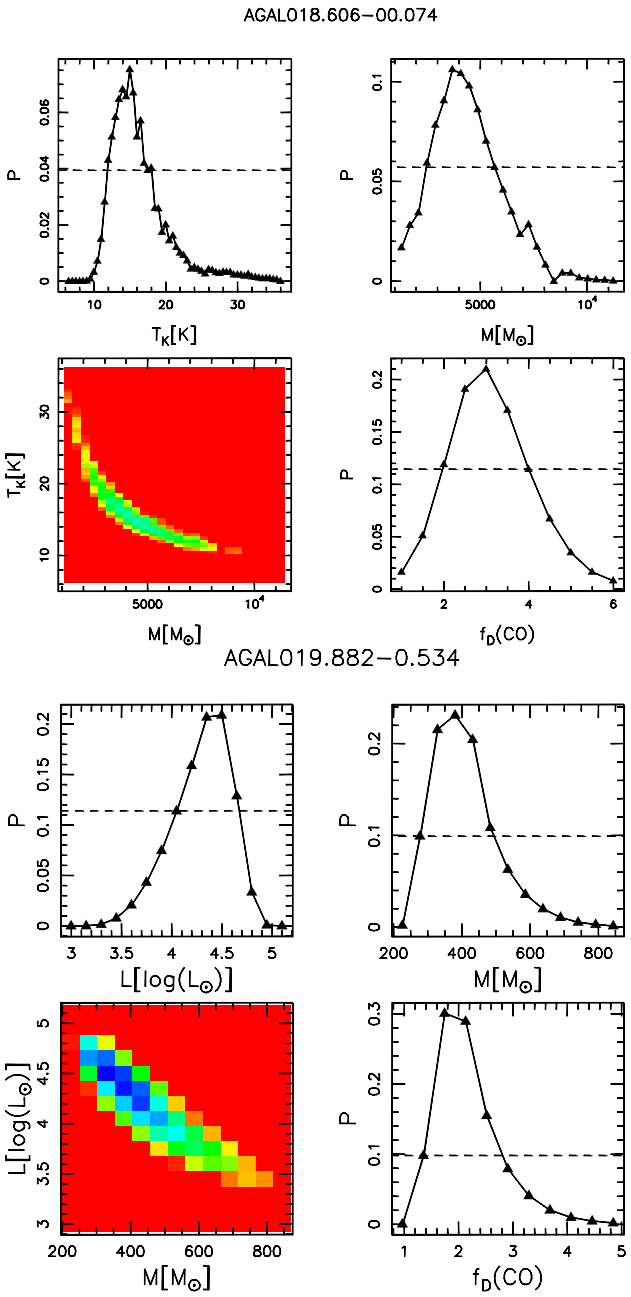

Figure 4.14: Continued.

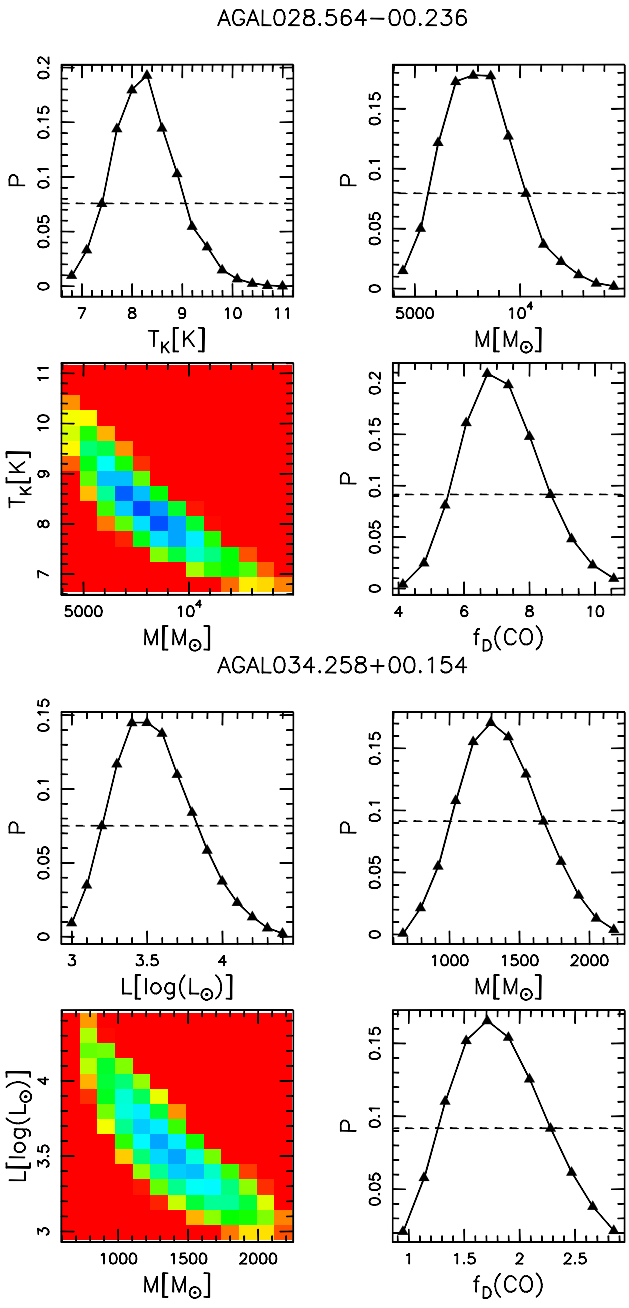

Figure 4.14: Continued.

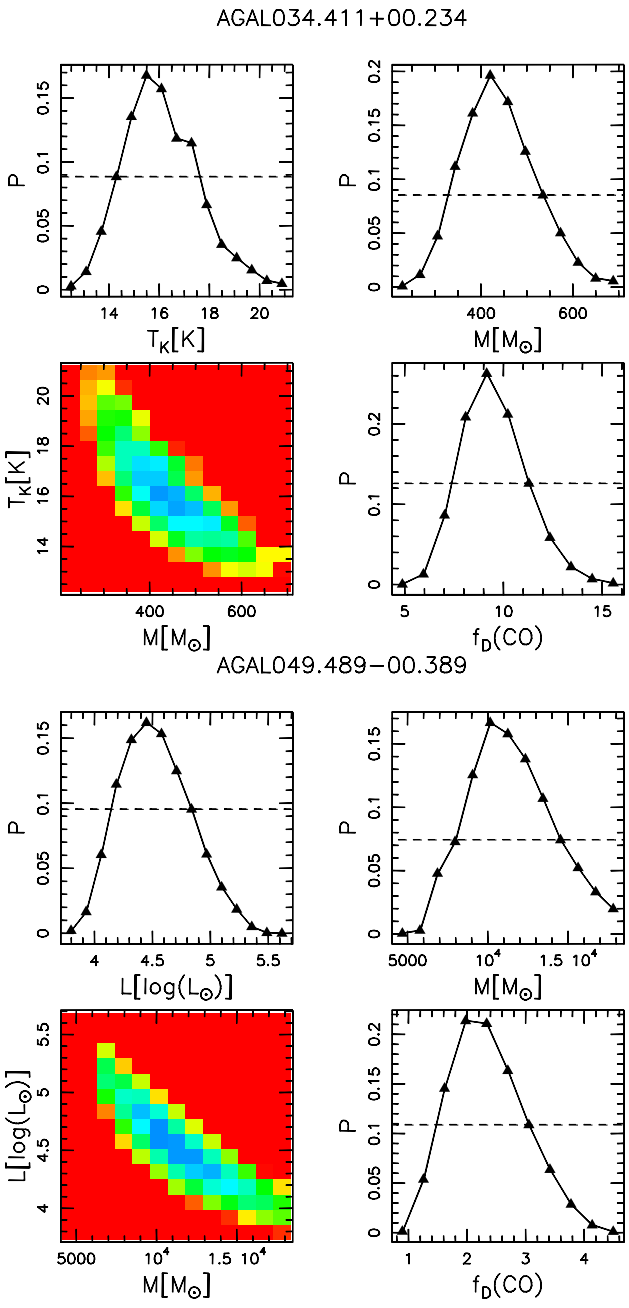

Figure 4.14: Continued.

Chapter 5

Later stages of massive star formation: the NGC 6357 complex

The first part of this chapter is from Giannetti, Brand, Massi, Tieftrunk and Beltrán, (2012, A&A, 538, A41); the second part is adapted from the preliminary results obtained in Massi, Giannetti, di Carlo, Brand, Beltrán and Marconi, in preparation.

5.1 Chapter summary

In the first part of the chapter (Sect. 5.2), we investigate the structure of the Galactic HII region G353.2+0.9, by analyzing (sub-)mm molecular-line and -continuum observations. This region is excited by the massive open cluster Pismis 24. We study the detailed morphology, distribution, and physical parameters (column- and volume densities, masses, temperatures and opacities) of the molecular gas and dust. We are also interested in the variation in these parameters across the photon-dominated region. We observed various molecules and transitions to derive the physical properties of the molecular gas through line ratios, and both LTE- and non-LTE analyses. The physical properties of the gas were derived with a Bayesian approach for the non-LTE analysis. Based on the ATLASGAL continuum data at 870 μm, we derived the column density of molecular hydrogen from the surface brightness and thus molecular abundances from the molecular column densities. We determined the mass of the dust from the integrated sub-mm flux. We also carried out the simplest possible analysis to identify the clump candidates for gravitational instability. The total mass of the gas in the region is $\sim$ 2000 $M_\odot$, while that of the dust is $\sim$ 21 $M_\odot$. The presence of a velocity gradient in the region, with clumps

with redder $V_{\rm LSR}$ nearer Pismis 24 suggests that the expansion of the ionised gas is pushing the molecular gas away from the observer. We unambiguously identify the ionisation front in G353.2+0.9, at the location of which we detect an increase in gas density and temperature. Its location and position angle is consistent with Pismis 24 being the main ionisation source. Almost no molecular gas is found south of the ionisation front, at the location of the intense, elongated continuum and atomic-line emission, strengthening the hypothesis that Pismis 24 is associated with G353.2+0.9. We find at least 14 clumps at different positions and LSR velocities, and we determine their physical conditions. The typical excitation temperatures are in the range of about $10 - 25$ K, while H_2 column densities are in the range $\sim 10^{20} - 10^{23}$ cm^{-2}. From the non-LTE analysis, we derive kinetic temperatures in the ranges $11 - 45$ K (CS) and $20 - 45$ K (CN). The H_2 number density is typically around $\sim 10^5$ cm^{-3} from CS and few $\times\, 10^5$ cm^{-3} from CN, with maxima above 10^6 cm^{-3}. The abundances of the molecules observed are found to vary across the region, and appear to be higher in regions further away from the ionisation front, except for CN.

In the second part of the chapter (Sect. 5.3), we address the star formation activity in NGC 6357, the age- and the initial mass function of Pismis 24, and we search for signs of triggered star formation in the region near to the cluster. We use Spitzer/IRAC data to identify intermediate- and high-mass YSOs in the whole complex, and through a stellar surface-density map we identify three clusters in the complex, and estimate that they host a comparable number of stars, between a few- and several thousands. Combining Spitzer/IRAC data with NTT/SofI (near-IR), HST/WFPC2 (optical) and Chandra/ACIS (X-ray) data, we investigate in detail the properties of the stellar population of Pismis 24 and of the nearby HII region G353.2+0.9. We construct colour-colour- and colour-magnitude diagrams to identify the YSOs and derive the fraction of young sources with a circumstellar disk. We use the X-ray- and near-IR data to select cluster members and derive the IMF of the cluster, after having constrained its age. We find that star formation is ongoing in NGC 6357, confirm that Pismis 24 is young ($\lesssim 3$ Myr), and that its IMF is consistent with those proposed by Kroupa et al. (1993) and Scalo (1998). Pismis 24 appears substructured in the near-IR frames. This indicates that it must be supervirial, as expected if it has experienced an early phase of gas expulsion, and thus must be able to retain a substructured morphology even after 5 Myr, instead of collapsing to a central concentration after 1 Myr, if it were subvirial (Parker & Meyer 2012). The star formation efficiency of the connected star formation event must have been $\gtrsim (2 - 6)\%$.

5.2 Molecular clouds under the influence of massive stars in the Galactic HII region G353.2+0.9

5.2.1 Introduction

NGC 6357 is a complex of HII regions and molecular clouds that form a very active star-forming region in the Sagittarius spiral arm. Optical, radio, and infrared (IR) images of NGC 6357 confirm that it contains a number of distinct HII regions in different stages of evolution (e.g., Felli et al. 1990; Massi et al. 1997). Figure 5.1 shows a large cavity or a collection of smaller, connected cavities in the region, delineated by ionised gas. Weak and diffuse Hα emission permeates this feature. G353.2+0.9 is the bright emission region north of the cavity, seen in Fig. 5.1. Just 55″ south of G353.2+0.9, lies the massive open cluster Pismis 24 (Pişmiş 1959). This cluster is thought to be the main source of ionisation of G353.2+0.9 (Massi et al. 1997; Bohigas et al. 2004). It contains at least $\sim$ 20 early-type (OB) stars, plus 24 O-type candidates (Wang et al. 2007) and includes three stars that are amongst the brightest and hottest known in the Galaxy, of spectral types O3.5 III(f*), O3.5 If*, and O4 III(f+) (Maíz Apellániz et al. 2007). Massey et al. (2001) derived a distance of 2.56 kpc and an age of $\sim$ 1 Myr for this cluster, and assuming that the molecular material is associated with Pismis 24, we consider NGC 6357 to be at the same distance. The large cavity is unlikely to have been formed by Pismis 24, because of its clearly off-centre position. The morphology and the size of the cavity seem to suggest that it was shaped by the winds and/or supernova events of one or more clusters (Wang et al. 2007) situated in the proximity of the centres of the smaller bubble-like structures.

Massi et al. (1997) performed a detailed study of the molecular emission associated with two of the HII regions in NGC 6357, to wit: G353.1+0.6, and G353.2+0.9 (cf. Fig. 5.12). The latter region is the younger one and exhibits signs of the presence of recently formed massive stars [e.g., ultra-compact HII regions (UCHII), embedded sources with infrared (IR)-excess].

Our study is focused on G353.2+0.9. Felli et al. (1990) observed it with the VLA at λ = 6 cm with an HPBW of 3.″5 (Fig. 7a of Felli et al. 1990). As is the case for the Hα emission, the high-resolution interferometric radio continuum observations reveal a very complex structure of the ionised gas, with a well-defined sharp boundary running east-west (the "Bar", in Figure 5.2). The emission is characterised by a strong intensity gradient to the south, while showing a more gentle decrease to the north (Fig. 8 in Felli et al. 1990). Felli et al. (1990) found

three UCHII (A, B, and C in Fig. 5.2).

The K_s band image in Fig. 5.2 shows that in the central part of the nebula there is an elephant trunk-like region of obscuration (clearly visible also in HST images; Hester & Desch 2005), with an UCHII region and IR source at its apex. This source shows a near-IR excess and X-ray emission: it was identified from HST observations to be in the evaporating gaseous globule (EGG) evolutionary phase (Hester et al. 1996), making it the first X-ray emitting EGG. This embedded object was classified as having a spectral type B0-B2 (Wang et al. 2007). The elephant trunk points toward Pismis 24 and is thought to be formed by the radiation and stellar winds from the OB stars in this cluster. The IR emission is brightest along the sides of the trunk and on the south-western side of G353.2+0.9, facing Pismis 24.

Massi et al. (1997) mapped G353.2+0.9 in CO($1-0$) and ^{13}CO($1-0$). These data were complemented with observations of other molecules and transitions along strips in the north-south direction, to determine variations in physical parameters across the photon-dominated region (PDR). Massi et al. (1997) found that G353.2+0.9 is a face-on, blister-type HII region, with most of the molecular material behind the HII region and to the north of it. Felli et al. (1990) suggested that G353.2+0.9 is not associated with Pismis 24, arguing that the southern sharp boundary (the "Bar") is produced by local ionisation caused by embedded sources, that are also responsible for the radio emission of G353.2+0.9. They also concluded that the nebula is ionisation-bounded to the south, implying that there are considerable quantities of molecular gas in the region south of the ionisation front. Molecular-line observations do not however support this claim: Massi et al. (1997) found very little molecular emission at the location of the "Bar".

Bohigas et al. (2004) found that this elongated structure has to have a considerable extent along the line-of-sight ($1-5$ pc, Bohigas et al. 2004). While this dimension is comparable to the extent in R.A., it is much larger than the extent in DEC. This suggests that the "Bar" is a layer of ionised matter seen edge-on. It could be caused by the interaction of the photoionised photoevaporative flow with the free wind of the Pismis 24 stars (Healy et al. 2004). This implies that the molecular gas in the region has already been swept by the stellar winds, i.e. the region south of the "Bar" should be nearly devoid of molecular material.

The present study follows up on the work described in Massi et al. (1997), which constitutes a first step in the study of the interface between the HII region and the molecular cloud. Our aim is to clarify the morphology of the region, by observing optically thin molecular lines (e.g. C^{18}O), and to confirm the absence of molecular material south of the main ionisation front, which is identified as

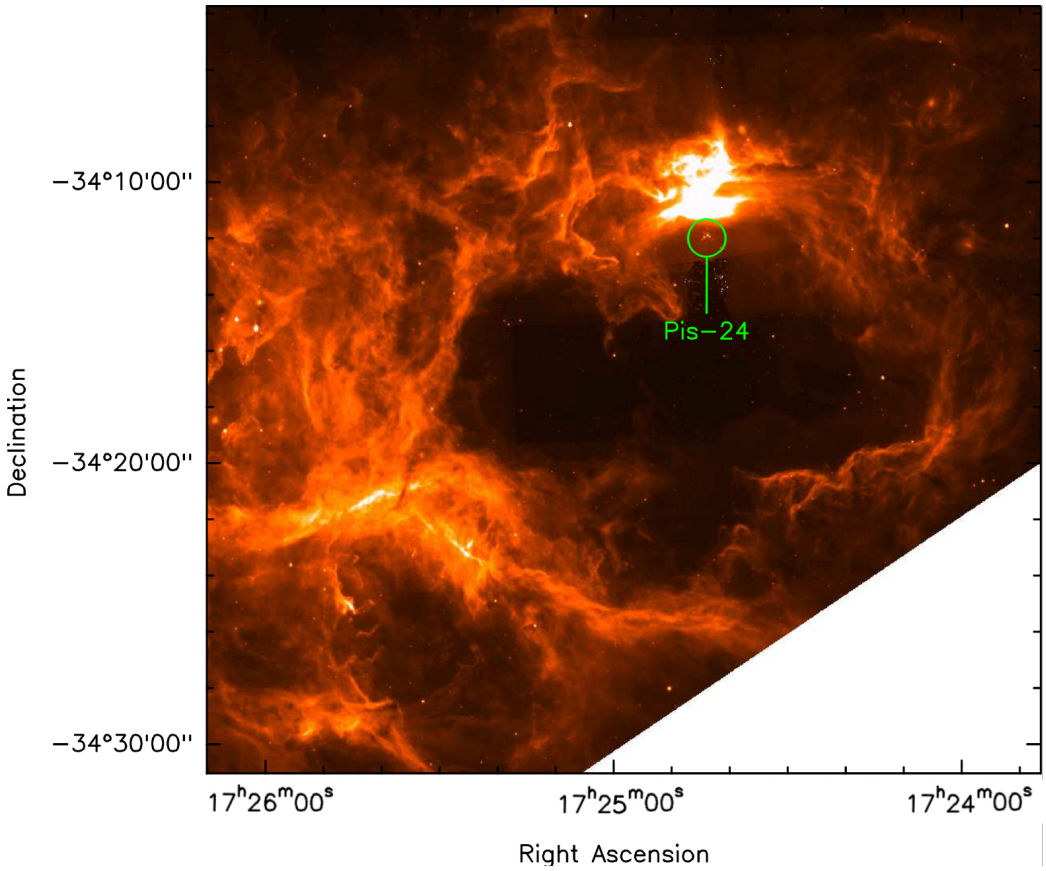

Figure 5.1: The 8 μm emission image of NGC 6357, taken from the GLIMPSE survey (`http://www.astro.wisc.edu/sirtf/`, Benjamin et al. 2003). The cavity is clearly visible at the centre of the image. G353.2+0.9 is the bright region at its northern border. The location of Pismis 24 is also shown in the figure. The coordinates are referred to the epoch J2000.

IF in Fig. 5.2 (see Sect. 5.2.3.11). This would strengthen the hypothesis of an association between G353.2+0.9 and Pismis 24. The physical conditions of the gas are derived by means of a non-LTE analysis for those molecules with several observed transitions or with hyperfine structure, while for the remaining molecules we assumed LTE (local thermodynamic equilibrium). The observation of the continuum at 870 μm allows us to infer the dust column density and mass, and thus to determine those of the gas, by assuming a gas-to-dust ratio. With the H_2 column densities determined in this way, we were able to calculate the abundance

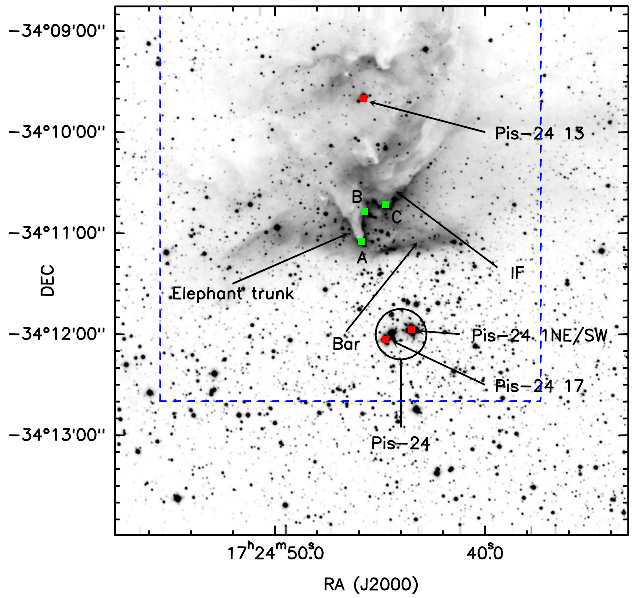

Figure 5.2: K_s-band image of G353.2+0.9 obtained with SofI (see Sect. 5.3). The actual ionisation front is indicated by "IF" (see text). The locations of the "Bar", Pismis 24, and the elephant trunk are indicated. The red and green squares mark the location of some early-type stars in Pismis 24 and the three UCHII regions identified by (Felli et al. 1990), respectively. The coordinates are referred to the epoch J2000.

for the observed molecules.

5.2.2 Observations and data reduction

The molecular-line observations were carried out between Sept. 1 and 9, 1999, with the 15-m Swedish-ESO Submillimeter Telescope (SEST; program 63.I-0189). This radio telescope was operational on La Silla in the period 1987-2004. The telescope was equipped with SIS receivers and a high-resolution acousto-optical spectrometer with a total bandwidth of 86 MHz, and a frequency resolution of about 42 kHz. The spectrometer was split into two parts, and we observed with two receivers simultaneously, one at a lower and the other at a higher frequency [e.g., $C^{18}O(1-0)$ and $C^{18}O(2-1)$]. Detailed information about the molecular transitions observed are reported in Table 5.1. The columns indicate the molecules and transitions observed, their rest frequency, resolution in frequency and velocity,

beam FWHM, main beam efficiency, spacing between points in the maps, and typical $T_{\rm MB}$ rms noise per channel of the spectra, respectively.

Most observations were made in frequency-switching mode, with a switch-interval in frequency sufficiently small to make the emission appear in both the signal and reference cycles, but large enough to avoid overlap between them.

The SiO(5 – 4), CN(1 – 0), CN(2 – 1), and $CH_3CCH(6-5)$ lines were observed with position switching. The emission of the last two molecules exhibits hyperfine structure, making it necessary to observe in position-switch mode. The telescope pointing was checked every three hours on the nearby SiO maser source AH Sco, and was found to be accurate to within 5″. The same source was also used as the off-position. The calibration was made using the standard chopper-wheel method described in Kutner & Ulich (1981). Our molecular-line maps are centred on $\alpha = 17^{\rm h}24^{\rm m}45.6^{\rm s}$, $\delta = -34^\circ11'20.7''$ (J2000), coinciding with the "Bar". The angular extent of the observed region is about $5' \times 5'$ for CS(2 – 1) and (3 – 2), while it is $\sim 3' \times 3'$ for the other molecules and transitions, with spacing between the raster point listed in Table 5.1 (Col. 7). The line intensities are expressed in terms of the main beam temperature, defined as $T_{\rm MB} = T_{\rm A}^*/\eta_{\rm MB}$. Data reduction and analysis for molecular-line data were performed with CLASS, part of the GILDAS (Grenoble Image and Line Data Analysis Software[1]) package.

The morphology and the distribution of the molecular gas can be investigated in greater detail by decomposing the emission profile into single Gaussian components at different $V_{\rm LSR}$. Given the limited number of velocity components, we decided to decompose the emission profiles at every position by fitting different Gaussian curves, starting from optically thin transitions (e.g. $C^{18}O$). The characteristics of the components identified in this way were then used as a template for the decomposition of the emission profiles of the other molecules and transitions.

CLASS offers the possibility to fit lines with hyperfine structure, such as those of CN, by specifying the relative intensity of the hyperfine components in the case of optically thin emission and assuming that their ratios have their LTE values. CLASS uses the optical depth as a free parameter of the fit, and gives it as output of the procedure.

We retrieved a map of G353.2+0.9 at 870 μm (345 GHz), taken with APEX from the ATLASGAL survey (Schuller et al. 2009). The rms noise in the map is $\sim$ 100 mJy beam^{-1}, determined in three regions free of emission around the HII region. These data were analysed with MOPSIC, the evolution of MOPSI (Map On-off Pointing Skydip Image), which was developed by R. Zylka (Obs. de

[1] `http://iram.fr/IRAMFR/GILDAS/`

Table 5.1: Molecular transitions observed.

Transition	ν (GHz)	$\Delta\nu$ (kHz)	ΔV ($10^{-2}\times$ km s^{-1})	$\theta_{\rm MB}$ ($''$)	$\eta_{\rm MB}$	Sp. ($''$)	rms (K)
$C^{18}O(1-0)$	109.7822	41.7	11.4	47	0.70	25	0.11
$C^{18}O(2-1)$	219.5603	41.7	5.70	24	0.50	25	0.20
$C^{34}S(2-1)$	96.4130	41.7	13.0	54	0.75	25	0.10
$CS(2-1)$	97.9810	41.7	12.8	53	0.75	50	0.10
$CS(3-2)$	146.9691	41.7	8.51	35	0.66	50	0.13
$CS(5-4)$	244.9356	41.7	5.11	21	0.50	25	0.25
$H_2CO(2_{1,2}\text{-}1_{1,1})$	140.8395	41.7	8.88	37	0.66	25	0.30
$CN(1-0)$	113.4910	41.7	11.0	46	0.70	25	0.11
$CN(2-1)$	226.8748	41.7	5.51	23	0.50	25	0.23
$CH_3CCH(6-5)$	102.5401	41.7	11.2	51	0.70	...(1)	0.17
$SiO(5-4)$	217.1049	41.7	5.76	24	0.50	...(1)	0.18

Notes. (1) Observed at selected positions only.

Grenoble).

5.2.3 Results and discussion

5.2.3.1 Morphology

Figure 5.3 shows the maps of integrated line-emission $\int T_{\rm MB}{\rm d}V$ towards G353.2+0.9. The molecular emission never extends significantly below $\Delta\delta = 0''$, confirming the lack of molecular material south of the "Bar" and ruling out the possibility that this feature is an ionisation front proceeding southward.

The molecular emission is concentrated between -10 and $+1$ km s^{-1} with, in some cases, strongly varying emission profiles between adjacent positions, as clearly visible in Fig. 5.4. In Fig. 5.3, it is possible to identify many different clumps. In higher-frequency transitions, such as $CS(5-4)$ and $CN(2-1)$, several clumps are resolved into two or more smaller clumps, or show an elongated appearance.

We find that the emission can be separated into 14 clumps in six velocity ranges (see Figure 5.5; all in units of km s^{-1}), i.e. $-7.3 \lesssim V_{\rm LSR} \lesssim -6.1$ (A and P), $-6.1 \lesssim V_{\rm LSR} \lesssim -4.7$ (B, C and L), $-4.7 \lesssim V_{\rm LSR} \lesssim -3.3$ (D and O), $-3.3 \lesssim V_{\rm LSR} \lesssim -1.9$ (E and F), $-1.9 \lesssim V_{\rm LSR} \lesssim -0.4$ (G and H), and $-0.4 \lesssim V_{\rm LSR} \lesssim +0.8$ (I,M and N). The names of the clumps do not correspond to those used in Massi et al. (1997), because of the higher spatial resolution in our present work and a different method

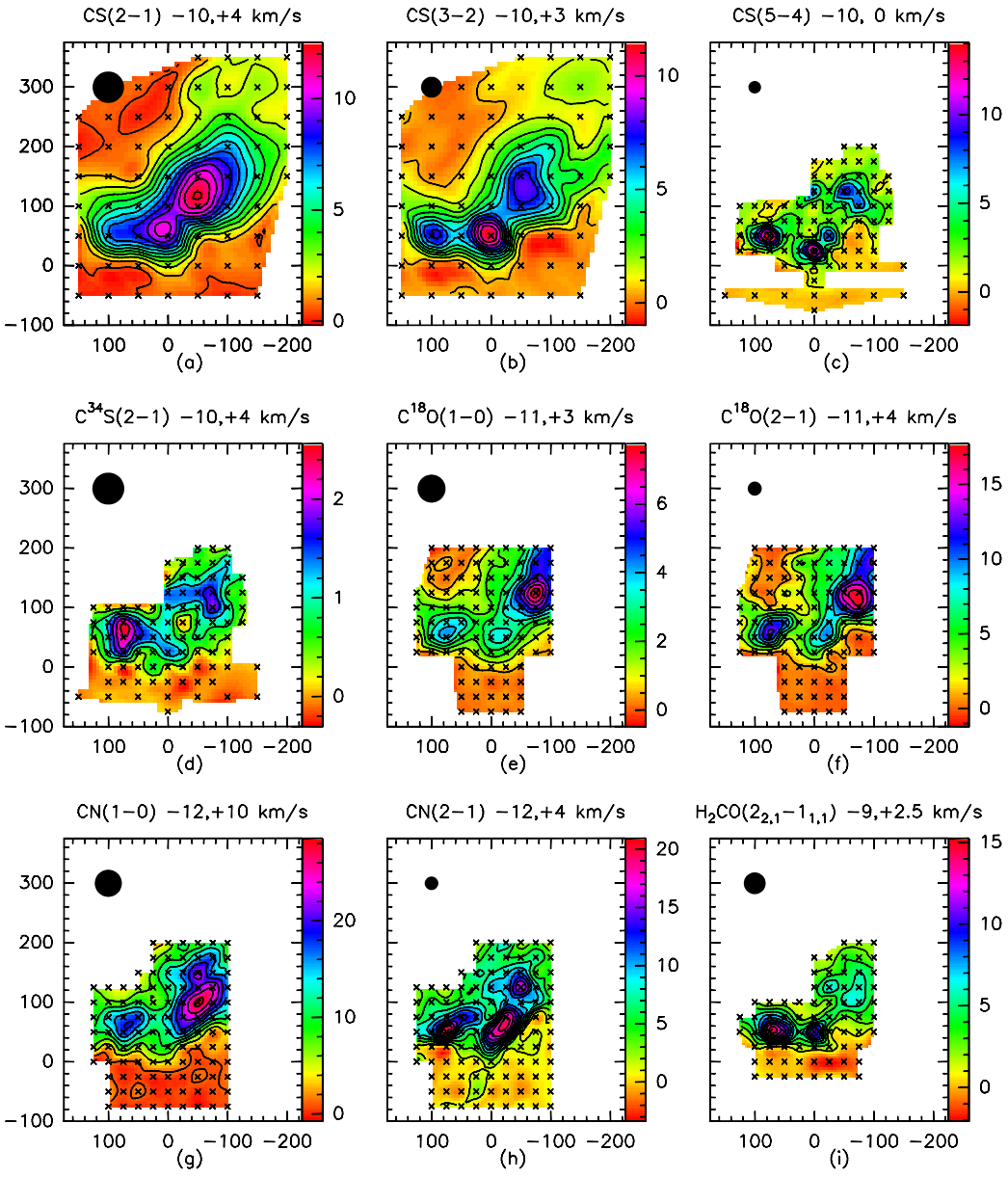

Figure 5.3: Maps of the integrated emission $\int T_{\rm MB} {\rm d}V$ of the different molecular species and transitions, within the whole velocity range of emission. The first contour is the 3σ level. Molecule, transition, and integration limits are indicated above each map. The beam size is indicated by the filled circle. The observed positions are marked with a cross. The contours levels (in units of K km s^{-1}) are, respectively (lowest (step) highest): (a) 0.41 (1.0) 12.41, (b) 0.51 (1.0) 11.51, (c) 0.89 (2.0) 12.89, (d) 0.4 (0.4) 2.4, (e) 0.47 (0.7) 7.47, (f) 0.81 (2.0) 16.81, (g) 0.98 (3.0) 27.98, (h) 1.25 (2.0) 19.25, (i) 0.92 (1.5) 15.92. Coordinates are offsets (arcsec) with respect to $17^{\rm h}24^{\rm m}45.6^{\rm s}$ $\delta = -34°11'20.7''$ (J2000).

of analysis (Gaussian decomposition versus integrated emission in velocity bins).

Figure 5.5 shows that the various clumps have slightly different position for different molecules and transitions, which could be the result of different excitation conditions, optical depth, chemical, or resolution effects. Furthermore, some clumps (such as P and O) are clearly visible only in high-density, high-frequency tracers. This is particularly clear in CS(5 − 4), which has the highest resolution. The emission of these tracers shows the presence of multiple high-density, small cores within a larger clump.

The clumps along the ionisation front tend to have redder velocities than the others. This is especially true for low-density tracers (cf. Fig. 5.5). Clumps N, H, and F, and D, B, and A exemplify this behaviour. This can be understood by taking into account the radiative and mechanical action of the stars of Pismis 24: when neutral gas is exposed to the intense energetic radiation of an early-type star, it becomes rapidly ionised near the surface of the cloud. This gas is heated to $T \sim 10000$ K (a factor of ~ 100 with respect to cold, neutral gas in the cloud), consequently causing a comparable increase in pressure, thus leading to a rapid expansion. However, the expansion towards the neutral gas is stopped by the presence of the dense material of the cloud. In the opposite direction, the low-density ionised gas cannot halt the expansion of this overpressurised gas. The ionised material moves predominantly away from the cloud, having an equal and opposite effect on the cloud.

Therefore, the molecular emission indeed suggests that the ionised, overpressurised gas in G353.2+0.9, observed by Bohigas et al. (2004), is expanding, thus pushing the molecular material away from the observer.

5.2.3.2 Temperatures

The first method used to derive the excitation temperatures uses the ratio of main beam temperatures of the (2 − 1) to (1 − 0) transitions of $C^{18}O$. We first resampled the spectra to the same velocity resolution, and then convolved the $C^{18}O(2-1)$ data with a Gaussian beam to match the spatial resolution of the (1 − 0) transition.

We calculated the ratio R_1 of $T_{\rm MB}(2-1)$ to $T_{\rm MB}(1-0)$ and determined $T_{\rm ex}$, assuming optically thin emission, from (Levreault 1988)

$$R_1 = 4\mathrm{e}^{-h\nu_{21}/kT_{\rm ex,21}} = 4\mathrm{e}^{-10.50/T_{\rm ex,21}}, \tag{5.1}$$

where $T_{\rm ex,21}$ is the excitation temperature of the $C^{18}O(2-1)$ transition. Assuming LTE, $T_{\rm ex}$ is the same for all levels. Since both transitions were observed simultaneously, the systematic calibration uncertainties should not affect the temperature

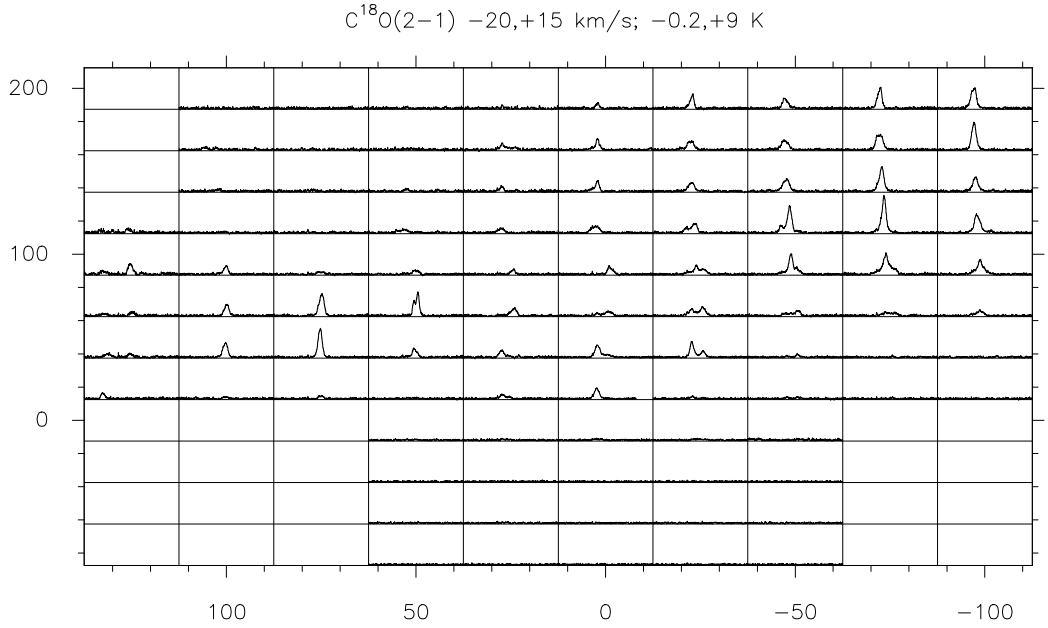

Figure 5.4: $T_{\rm MB}(C^{18}O(2-1))$ spectral map. Each frame corresponds to a single pointing with an offset in α and δ indicated in the figure. The x and y axes of each spectrum range from −20 to 15 km s^{-1} and from −0.2 to +9 K, respectively.

ratios, which are instead influenced by uncertainties in the Gaussian decomposition of the emission profile. Taking into account the uncertainties in the Gaussian fit performed with CLASS, we estimated that the uncertainties in $T_{\rm MB}$ should not exceed 5 − 15%, where both lines are detected above 3σ. Assuming a typical uncertainty in $T_{\rm MB}$ of 10%, the relative uncertainty in $T_{\rm ex}$ is $\sim$ 14%. We find that R_1 is always between $\sim$ 2 and $\sim$ 4, indicative of optically thin emission throughout the region. The $T_{\rm ex}(C^{18}O)$ (derived from Eq. 5.1) is fairly uniform, typically between $\sim$ 15 K and $\sim$ 25 K for all clumps. The higher values are found along the ionisation front, while for clump C, which is associated with the elephant trunk, we have $T_{\rm ex} \sim 20$ K.

Another temperature probe is methyl acetylene (CH_3CCH) (Bergin et al. 1994). This molecule has a high critical density, and its emission comes from high-density regions. Our observations are limited to four positions: (0″,50″) (clump C), (75″,75″) (clump E), (−75″,125″) (clump B), and (0″,−25″). We detected CH_3CCH only at (0″,50″) and (75″,75″), while the detection at (−75″,125″) is uncertain. Only at the first position were four components of the K-ladder visible, giving a reliable temperature estimate. The Boltzmann plot analysis (Fig. 5.6) gave

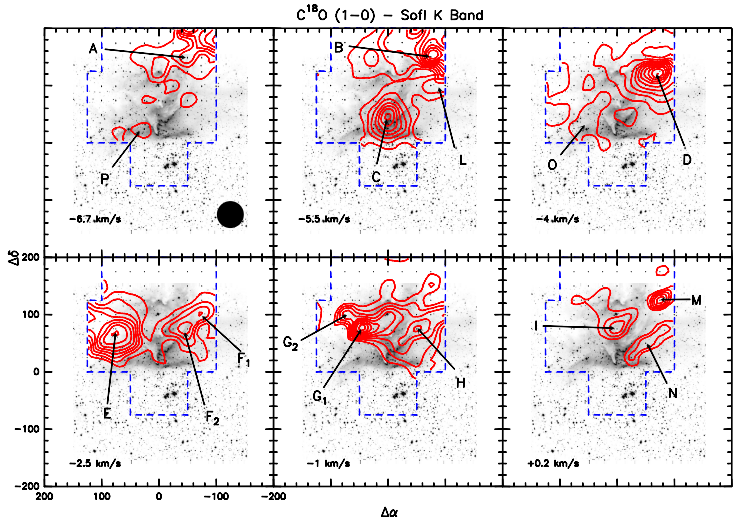

(a) $C^{18}O(1-0)$

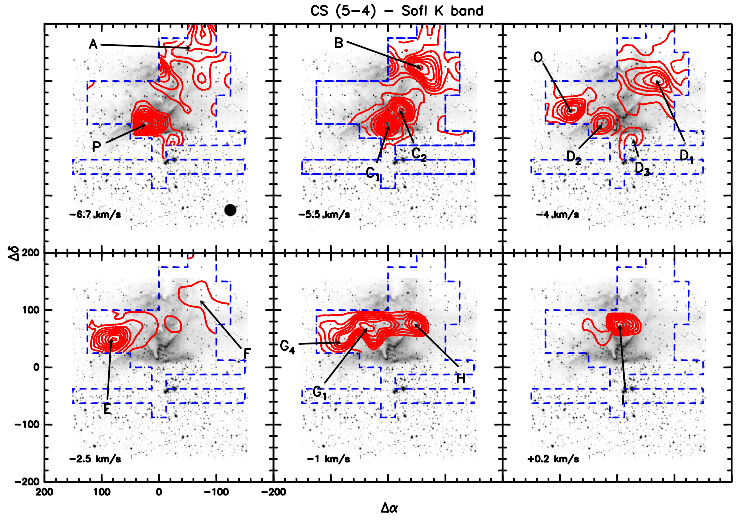

(b) $CS(5-4)$

Figure 5.5: **(a)** Integrated emission $\int T_{\rm MB} {\rm d}V$ of $C^{18}O(1-0)$ superimposed on the $K_{\rm s}$ image. Each plot corresponds to a different $V_{\rm LSR}$. The $V_{\rm LSR}$ of the clumps is indicated in the respective panel. The dashed (blue) lines indicate the observed area. The (red) contours show the integral under Gaussian components fitted to the line profiles. The beam of the transition is shown in the first panel. The first contour in each panel is the 3σ level. The integrated emission levels (in units of K km s^{-1}) are (lowest (step) highest): (−6.7 km s^{-1}) 0.17 (0.3) 2.27; (−5.5 km s^{-1}, C) 0.19 (0.3) 1.99; (−5.5 km s^{-1}, B) 0.20 (0.5) 4.70; (−4.0 km s^{-1}) 0.18 (0.7) 6.48; (−2.5 km s^{-1}) 0.19 (0.3) 2.89; (−1.0 km s^{-1}) 0.18 (0.2) 1.78; (+0.2 km s^{-1}) 0.15 (0.1) 0.65. **(b)** As **(a)**, but for $CS(5-4)$. The integrated emission levels (in units of K km s^{-1}) are (lowest (step) highest): (−6.7 km s^{-1}) 0.19 (0.3) 2.59; (−5.5 km s^{-1}, C) 0.20 (1.0) 10.20; (−5.5 km s^{-1}, B) 0.19 (0.5) 3.69; (−4.0 km s^{-1}) 0.19 (0.7) 4.39; (−2.5 km s^{-1}) 0.18 (1.0) 8.18; (−1.0 km s^{-1}) 0.17 (0.2) 1.37; (+0.2 km s^{-1}) 0.14 (0.1) 0.74. Note that names of the clumps do not correspond to those used in Massi et al. (1997).

a $T_{\rm ex} \sim 45$ K for clump C, which is higher than that derived from $C^{18}O$. At the other positions, we detected just two components, leading to very uncertain temperature estimates (22 K, clump E; 45 K, clump B) that, however, are roughly consistent with those determined from CS (see Sect. 5.2.3.8). This higher temperature could be due to the presence of internal heating sources in clumps B and C.

Although the excitation temperature is formally only a measure of the relative population of the energy levels in a transition, and therefore differs for different transitions, under the assumption of LTE, it provides a fair estimate of the kinetic temperature.

5.2.3.3 Column densities

Assuming LTE conditions, the total column density of the molecular gas can be obtained from observations of the J → J − 1 transition by means of the expression (Zielinsky 1999; Kramer & Winnewisser 1991)

$$\begin{aligned} N =& \frac{1}{\eta_c}\frac{3h}{8\pi^3\mu^2}\frac{Z}{\rm J}{\rm e}^{\frac{h\nu_{\rm J-1,0}}{kT_{\rm ex}}}\left[1-{\rm e}^{-\frac{h\nu_{\rm J,J-1}}{kT_{\rm ex}}}\right]^{-1}[J(T_{\rm ex})-J(T_{\rm BG}))]^{-1}\times \\ &\times\int T_{\rm MB}({\rm J},{\rm J}-1){\rm d}V \equiv f(T_{\rm ex})\int T_{\rm MB}({\rm J},{\rm J}-1){\rm d}V, \end{aligned} \tag{5.2}$$

where $J(T) = (h\nu_{\rm J,J-1}/k)({\rm e}^{h\nu_{\rm J,J-1}/kT}-1)^{-1}$, η_c is the efficiency with which the antenna couples to the source, μ is the dipole moment of the molecule, Z is the partition function, $T_{\rm BG}$ is the background temperature, and $T_{\rm MB}$ is the main beam temperature.

Equation (5.2) implies that there is a linear relation between the column density and the integrated line intensity at fixed $T_{\rm ex}$. This equation holds only in case of negligible optical depth (τ). However, from the detection equation

$$T_{\rm R}^{*} = \eta_c[J(T_{\rm ex})-J(T_{\rm BG})](1-{\rm e}^{-\tau}), \tag{5.3}$$

one can derive a correction factor $\tau/(1-{\rm e}^{-\tau})$, which makes it possible to calculate the column density while $\tau \lesssim 2$, with uncertainties less than 15% (Kramer 1988). In this expression, τ is the optical depth at the line centre (see Sect. 5.2.3.4 and 5.2.3.8).

In Table 5.2, we list the average value of the column density inside the 3σ contour of integrated intensity, derived from different molecules and transitions, for each distinct identified component. The derived excitation temperature is also listed, but we note that the column densities are computed assuming $T_{\rm ex} = 20$ K

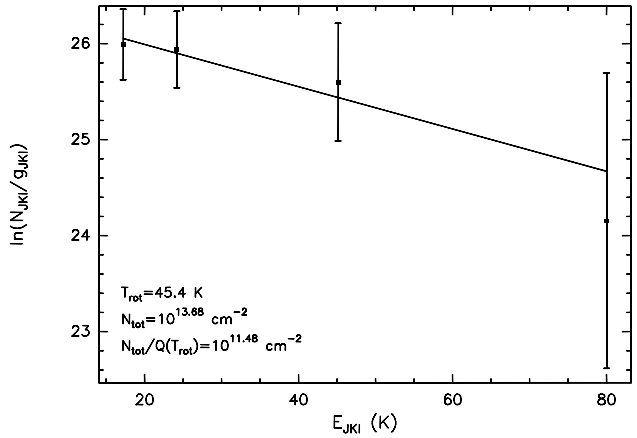

Figure 5.6: Boltzmann plot obtained from the CH_3CCH data at (0″,50″).

for all molecules and a τ derived according to Sect. 5.2.3.4. The assumption of a constant excitation temperature does not affect the results, because its range is small (15 – 25 K) and the variation in column density is only of the order of $\lesssim 15 - 20\%$.

5.2.3.4 Opacities and visual extinctions

We can derive the opacities of the transitions of $C^{18}O$, from the detection equation (5.3). The $C^{18}O$ lines are usually optically thin ($\tau \sim 10^{-2}$), although they reach $\tau \sim 0.1$ and $\tau \sim 0.2$, respectively for the transition (1 – 0) and (2 – 1) in clump E, in the elephant trunk and in some of the clumps aligned with the bright emission to the west of the trunk, i.e. the ionisation front. Assuming the standard value of ~ 8 for the abundance ratio $X(^{13}CO)/X(C^{18}O)$, one derives values of τ for the ^{13}CO of the order of 0.8 and 1.6, respectively, for the transition (1 – 0) and (2 – 1) at the same positions. This result confirms that the emission of ^{13}CO is marginally thick, as argued by Massi et al. (1997). The higher optical depth indicates that the molecular material has accumulated in these regions. Furthermore, non-negligible opacities could explain the slightly lower T_{ex} south of the clump C, with respect to those observed for the ionisation front.

An estimate of the visual extinction can be obtained from the H_2 column densities from the expression given by Bohlin et al. (1978). Typical values are 5 – 10 mag and 15 – 20 mag for $C^{18}O$ and H_2CO, respectively. The maximum values of A_V that we find, estimated from H_2CO, are those of clumps C and E ($\sim$ 50 mag).

Table 5.2: $V_{\rm LSR}$, position, mean LTE column density, excitation temperature ($C^{18}O$), FWHM of the lines, and diameter of the clumps.

Cl. ($V_{\rm LSR}$) (km s^{-1})	Offset ($''$)	$N(C^{18}O, 10)$ ($10^{14} \times$ cm^{-2})	$N(C^{18}O, 21)$ ($10^{14} \times$ cm^{-2})	$N(H_2CO, 21)$ ($10^{13} \times$ cm^{-2})	$T_{\rm ex}(C^{18}O)$ (K)	Line FWHM (km s^{-1})	FWHM size (pc)
A (-6.8)	(-45,180)	9.71	8.88	1.09	20	1.3	0.35
B (-5.6)	(-75,155)	18.50	18.36	2.09	20	1.8	0.55
C (-5.5)	(0,40)	8.14	10.10	3.79	21	2.0	0.35
D (-4.4)	(-70,120)	23.60	20.47	2.35	20	1.8	0.56
E (-2.3)	(80,60)	12.00	12.08	6.21	15	1.8	0.46
F (-2.1)	(-50,100)	7.43	5.54	...	17	1.2	0.40
G (-1.2)	(50,75)	10.50	10.87	3.32	13	1.3	0.27
H (-1.2)	(-50,75)	7.47	6.34	1.15	15	1.8	0.31
I (0.4)	(0,95)	2.81	3.12	1.14	15	1.4	0.30
L (-5.6)	(-75,95)	5.98	3.07	...	21	1.2	0.34
M (-0.3)	(-75,125)	2.86	...	...	...	...	...
N (-0.3)	(-50,50)	2.94	...	1.11	...	...	...
O (-3.4)	(50,70)	...	8.07	6.56	17	1.1	0.37
P (-5.9)	(25,25)[(1)]	...	...	1.20	...	...	...

Notes. The column density is determined by averaging the emission inside the 3σ contour in $\int T_{\rm MB} {\rm d}V$ of each molecule in each clump, assuming $T_{\rm ex} = 20$ K. In the first column, the mean $V_{\rm LSR}$ of the clump is also indicated. The notation $N(A, ij)$ means that the total column density of the molecule A is derived from the transition ij. [(1)] The position is derived from CS(5 – 4).

5.2.3.5 Dust

From the 870 μm image, kindly provided by the ATLASGAL project[2], we derived dust masses (and densities from these masses) from Eq. 3.1. We assumed that the dust temperature is 30 K throughout the region. However, the resulting masses and column densities do not depend strongly on temperature, for $T_{\rm d} = 20$ K and $T_{\rm d} = 50$ K the difference is a factor of three. The dust mass resulting from the total 870 μm flux is ~ 21 M$_\odot$. $\kappa_{870\mu{\rm m}}$ has an uncertainty of a factor of two, which implies an uncertainty in the dust mass of the same factor. Furthermore, the uncertainty due to the dust temperature is of the same order of magnitude.

The surface brightness F_ν at 870 μm also allows one to derive the gas column density, following Deharveng et al. (2009) and assuming a gas-to-dust ratio of 100. The contribution of the free-free emission, extrapolated from the radio data of Felli et al. (1990) assuming optically thin emission, is less than a few percent. The rms noise of the map (~ 100 mJy beam^{-1}) corresponds to a column density of

[2] `http://www.mpifr-bonn.mpg.de/div/atlasgal/`, Schuller et al. 2009

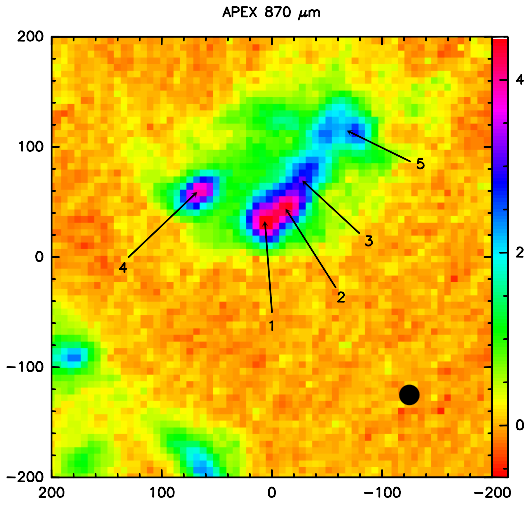

Figure 5.7: APEX image at 870 μm. The scale is expressed in Jy beam^{-1}. The APEX beam is shown as a filled circle. The locations of the main components identified are shown in the map. Component 5 was not fitted with a Gaussian, but was considered as a region of diffuse emission.

3.1×10^{21} cm^{-2} for $T = 20$ K, 1.9×10^{21} cm^{-2} for $T = 30$ K, and 1.0×10^{21} cm^{-2} for $T = 50$ K.

We decomposed the emission into four bi-dimensional Gaussian components with MOPSIC, plus three regions of diffuse emission: Fig. 5.7 shows the condensations identified.

The morphology of the emission at this wavelength is very similar to that of the integrated molecular emission and to that of the regions of obscuration visible at near-IR wavelengths. The maxima in the molecular-line emission do not always coincide with those of the dust. In particular, clump E shows a large displacement. We suggest that this could be an effect of a non-negligible τ.

To associate the dust components with molecular cores, we superimposed the map of the 870 μm emission on that of the molecular emission, as shown in Fig. 5.8. The masses of the components identified in the APEX image and their associated molecular clumps are listed in Table 5.3. The total mass indicated in this table is computed by integrating the total 870 μm flux. The H_2 column densities derived from the dust emission are on average in the range $3 - 7 \times 10^{22}$ cm^{-2}, while the maximum values are $\sim 10^{23}$ cm^{-2} (components 1, 2, and 4).

The visual extinctions corresponding to the maximum column densities are typically 100 mag. The average visual extinction lies between 15 and 40 mag,

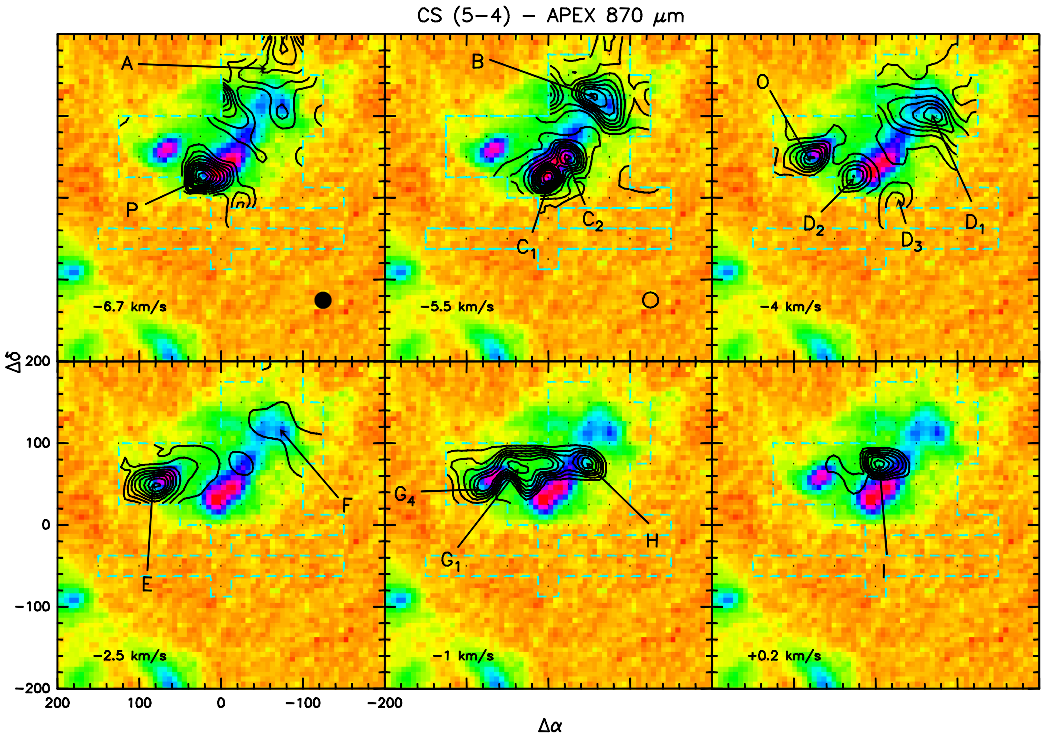

Figure 5.8: CS(5 − 4) emission (black and gray contours) superimposed on the 870 μm emission. The beam size of CS(5 − 4) is indicated by the filled circle, while the open circle indicates the APEX beam size. Each plot corresponds to a different $V_{\rm LSR}$. The $V_{\rm LSR}$ of the clumps is indicated in the respective panel. The contours (in units of K km s^{-1}) for each clump are (lowest (step) highest): (−6.7 km s^{-1}) 0.19 (0.3) 2.59; (−5.5 km s^{-1}, C) 0.20 (1.0) 10.20; (−5.5 km s^{-1}, B) 0.19 (0.5) 3.69; (−4.0 km s^{-1}) 0.19 (0.7) 4.39; (−2.5 km s^{-1}) 0.18 (1.0) 8.18; (−1.0 km s^{-1}) 0.17 (0.2) 1.37; and (+0.2 km s^{-1}) 0.14 (0.1) 0.74. The lowest contour corresponds to the 3σ level in $\int T_{\rm MB} {\rm d}V$.

depending on the component. The corresponding mean and maximum volume densities, calculated assuming spherical symmetry for the clumps, are $\sim 10^4$ cm^{-3} and $\sim 10^5$ cm^{-3}. These values are of the same order as those found from H_2CO, under the assumption of LTE. The low-density layers of the clumps are not visible in the 870 μm map owing to its high rms noise.

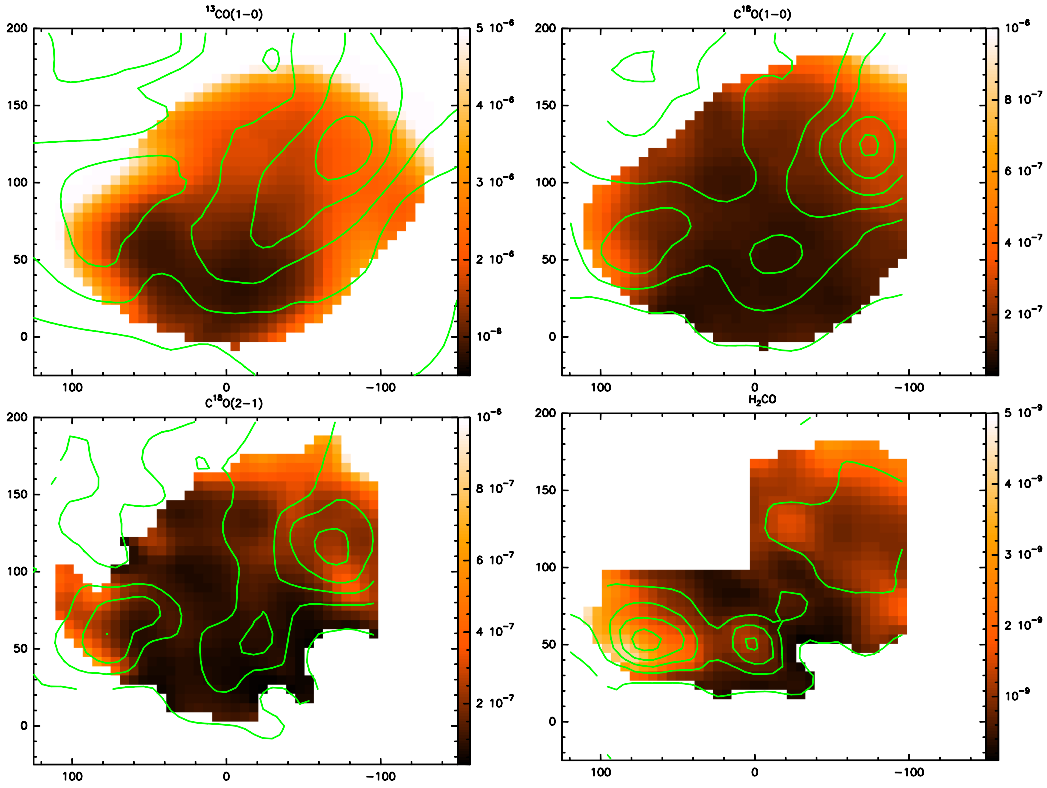

Figure 5.9: Maps of the abundance relative to H_2 of ^{13}CO, $C^{18}O$, and H_2CO, derived from $^{13}CO(1-0)$ (top left), $C^{18}O(1-0)$ (top right), $C^{18}O(2-1)$ (bottom left), and $H_2CO(2_{1,2}-1_{1,1})$ (bottom right). The green contours show the column density distribution of the molecules.

5.2.3.6 Molecular abundances

In Fig. 5.9, we show the abundances of ^{13}CO (not in the present dataset, taken from Massi et al. 1997), $C^{18}O$ and H_2CO as a function of position. To derive these maps, we smoothed the APEX image to match the resolution of the molecular transition considered and we divided pixel per pixel the molecular column density map by the H_2 column density map, obtained from the APEX image, using Eq. 4.15. We set a threshold of 3σ in both molecular and H_2 column densities. We can clearly see that the abundances vary in the region, in a similar way for the three molecules. The abundances are lower near the IF and the elephant trunk, while they appear to increase further away from IF, away from Pismis 24. The $C^{18}O$ abundance varies from $\sim 9.0 \times 10^{-8}$ in the region of the IF, to $\sim 1.9 \times 10^{-7}$ at the location of E, to

Table 5.3: Gas masses derived from dust emission.

Component	Mass ($M_\odot$)	Associated molecular clumps
1	370	C1
2	180	C2
3	210	H, F
4	340	E
5[(1)]	360	D, A, B
total[(2)]	2100	

Notes. The gas-to-dust ratio was assumed to be $\gamma = 100$. The total mass is computed by integrating the total 870μm flux. [(1)] Not a Gaussian fit, but a region that comprises all the emission at the corresponding location. [(2)] computed integrating the whole 870μ flux.

$\sim 2.3 \times 10^{-7}$ more to the north, at roughly the location of D. In the same three regions, the abundances of ^{13}CO and H_2CO are $\sim 1.0 \times 10^{-6}$, $\sim 1.5 \times 10^{-6}$, and $\sim 2.2 \times 10^{-6}$; and $\sim 6.0 \times 10^{-10}$, $\sim 1.5 \times 10^{-9}$, and $\sim 1.1 \times 10^{-9}$, respectively. We expect that this variation is at least partially due to an increase in T_K at the location of the ionisation front. A different T_K can modify the abundance through the H_2 column density, which was derived from the 870 μm emission.

5.2.3.7 LTE masses and volume densities

The masses of the clumps are listed in Table 5.4. They are derived averaging the emission inside the 3σ contour to determine the average column density and then integrating over the beam-corrected area of the emission. The abundances used are the average abundances derived in the previous paragraph, appropriate for the location of the clump. We also took into account the optical depth τ (determined from the detection equation) and a correction for helium, which contributes with a factor 1.36. The total mass of the complex is ~ 2000 $M_\odot$, in agreement with that found from the 870 μm continuum emission. This mass can be compared to the total mass of ionised hydrogen (290 $M_\odot$, Bohigas et al. 2004) and to the total dust mass (21 $M_\odot$, see Sect. 5.2.3.5). The masses of single clumps range from a few tens to several hundreds of $M_\odot$.

The volume density $n(H_2)$ is determined assuming that the extent of the clump along the line-of-sight is equal to its size in the plane of the sky. The ratio of

Table 5.4: Single-clump and total gas masses.

Cl.	$C^{18}O(1-0)$ ($M_\odot$)	$C^{18}O(2-1)$ ($M_\odot$)	$H_2CO(2_{1,2}-1_{1,1})$ ($M_\odot$)
A	130	160	170
B	320	310	330
C	270	270	350
D	570	400	300
E	210	240	300
F	70	50	140
G	130	90	60
H	180	170	250
I	20	30	60
L	20	40	...
M	< 10	...	...
N	20	...	20
O	...	50	90
P	...	...	90
Total	1950	1810	2090

Notes. The mass is computed integrating the column density within the 3σ contour in $\int T_{\rm MB} {\rm d}V$ for each clump. The transition from which we derived the mass is indicated in the top row. If the clump is divided into sub-clumps (indicated by numbers; cf. Fig. 5.5) the mass reported is the sum of all the sub-components.

volume densities determined from low- and high-density tracers may be up to a factor of ~ 100, e.g., the mean volume densities derived from $C^{18}O$ are typically $\sim 10^3$ cm^{-3}, while those of H_2CO are $\approx 10^4 - 10^5$ cm^{-3}. The volume densities derived in this way are always of the same order of magnitude of the critical density of the molecular transition used to determine it.

5.2.3.8 Non-LTE analysis

The three transitions of CS, plus $C^{34}S(2-1)$, allowed a non-LTE analysis at offsets where data points were available for all transitions. For this purpose, we used the

statistical equilibrium, radiative transfer code RADEX[3], for the approximation of a uniform sphere. The model requires as input the kinetic temperature, the H_2 number density, the molecular column density, and the FWHM of the line. We assumed the Solar value of 22.5 for the $^{32}S/^{34}S$ isotopic ratio. The model returns the brightness temperature of the lines, the opacity, and the excitation temperature. The FWHM of the CS line was determined by averaging those of the various observed lines, at one position. The brightness temperature of the line was estimated using

$$T_B = \frac{\vartheta_B^2 + \vartheta_S^2}{\vartheta_S^2} T_{MB}, \tag{5.4}$$

where ϑ_B is the beam size and ϑ_S is the source size. We assumed that all the transitions come from the same region, estimating the source size from the mean FWHM dimension of clumps in CS(5 − 4), that has the highest angular resolution. We varied the kinetic temperature between 10 K and 200 K, and the molecular hydrogen number density between 10^3 cm^{-3} and 10^7 cm^{-3}, both in 50 equally spaced logarithmic steps. The column density was varied between 5.2×10^{12} cm^{-2} and 5.5×10^{15} cm^{-2} for CS and between 2.3×10^{11} and 2.4×10^{14} cm^{-2} for $C^{34}S$, in 44 equal logarithmic steps.

To analyse the model results, we used a Bayesian approach. The Bayes theorem states that

$$P(T_K, N, n|D, model) = \frac{1}{\varphi} P(D|T_K, N, n, model)\, P(T_K, N, n|model), \tag{5.5}$$

where $P(T_K, N, n|D, model)$ is the probability of the parameters T_K, N, and n, given the data and the model, called *posterior*, $P(D|T_K, N, n, model)$ is the probability of the data given the model and its parameters, or *likelihood*, and $P(T_K, N, n|model)$ is the probability of the model parameters, which is called *prior* (see Chapter 2). The parameter φ is a normalisation constant given by the sum of the individual probability of each model, in order to have the posterior normalised to 1. We used a constant prior for the model parameters, thus giving equal weights to every value of the model parameters. The probability of measuring a certain value for the intensity of a line is assumed to be represented by a Gaussian curve centred on the value obtained from RADEX for specific physical conditions of the gas, and with a

[3] `http://www.strw.leidenuniv.nl/$\sim$moldata/radex.html`; van der Tak et al. 2007

σ given by the uncertainty in the measured value. Therefore, we multiplied four Gaussian curves, one for each transition, and the PDF for $\tau_{C^{34}S}$, computed with JAGS[4] assuming that CS(2 − 1) is optically thick, to obtain $P(D|T_K, N, n, model)$. The assumption of optical thickness for CS(2 − 1) is only used to derive the PDF for $\tau_{C^{34}S}$, but is not used further in the analysis of the model results. Explicitly, the expression for $P(D|T_K, N, n, model)$ is

$$P(D|T_K, N, n, model) = \frac{1}{\psi}\Big[\prod_{i=1}^{4}(e^{-(l_i-\mu_i)^2/(2\sigma_{l,i}^2)})\Big]P(\tau_{C^{34}S}), \tag{5.6}$$

where the index i runs over the three CS lines and $C^{34}S(2-1)$, l_i are the observed line intensities, μ_i are the modelled intensities, $\sigma_{l,i}$ takes into account the rms of the spectrum and a 15% calibration uncertainty, and ψ is a normalisation constant.

To determine the physical conditions of the gas, i.e. the single parameters of the model, we had to integrate over the other parameters (*marginalise*; see Sect. 2.2.2)

$$P(a|D, model) = \int P(a, b, c|D, model)\, db\, dc. \tag{5.7}$$

From the PDF of the parameters, we derived the expectation values and the 68% interval. The results for CS are summarised in Table 5.5. The columns show the offset of the spectrum used, the clump name, the kinetic temperature and its 68% interval, the number density of molecular hydrogen and its 68% interval, the column density and its 68% interval, the molecular abundance, the optical depth of CS(2 − 1), (3 − 2), (5 − 4) and $C^{34}S(2-1)$, and the excitation temperature of the same transitions, respectively.

From these analyses, we find that the volume density of molecular hydrogen ranges between several$\times 10^4$ and few$\times 10^6$ cm^{-3}, while T_K lies between $\sim$ 11 K and $\sim$ 45 K, for different clumps. The temperature derived from CH_3CCH for clump C is higher than the kinetic temperature obtained from this analysis for (0″,50″), while it is consistent with that at (0″,0″), most probably because the CH_3CCH beam takes in the emission from the region along the IF. However, CS(5 − 4) has its maxima at (0″,25″) and at (25″,50″) where we do not have data for CS(2 − 1) and (3 − 2), while at (0″,50″) the emission of CS(5 − 4) is weak.

There is a clear trend showing an increase in the densities towards the south, in the direction of Pismis 24 and in the clumps aligned with the IF (Fig. 5.2) west

[4] `http://mcmc-jags.sourceforge.net/`

of the elephant trunk. This region shows typical densities of few $\times 10^5$ cm^{-3} and $T_{\rm K} \sim 30 - 40$ K. The temperature for the point at (0″,0″) appears to be higher than the surrounding points, with $T_{\rm K} \sim 40$ K, while (0″,50″) has $T_{\rm K} \sim 18$ K. The column density ranges between $\sim 2 \times 10^{13}$ cm^{-2} and $\sim 2 \times 10^{14}$ cm^{-2}, implying CS abundances of between 7.0×10^{-10} and 4.0×10^{-8}, derived from the ratio with the H_2 column densities determined from the APEX data. The opacity of CS(2 − 1), CS(3 − 2) and CS(5 − 4) lies between 0.5 − 4, 0.8 − 6, and 0.1 − 2.7, respectively.

The derived $T_{\rm ex}$-values are around 7 − 16 K for CS(2 − 1), 6 − 11 K for CS(3 − 2), 5 − 9 K for CS(5 − 4) and 6 − 13 K for $C^{34}S(2-1)$. The ratios of $T_{\rm ex}$ for different transitions are always within a factor of two of each other.

A similar analysis was carried out for CN. In this case, $P(D|T_{\rm K}, N, n, model)$ was calculated by comparing total fluxes rather than line temperatures, due to hyperfine splitting, which is not included in the present model. Therefore we have

$$P(D|T_{\rm K}, N, n, model) = \frac{1}{\varphi}\Big[\prod_{i=1}^{2}(e^{-(F_i - F_{m,i})^2/(2\sigma^2_{F,i})})\Big] e^{-(\tau_{tot,(1-0)} - \tau_{m,(1-0)})/(2\sigma^2_{\tau})}, \quad (5.8)$$

where F_i is the measured flux, $F_{m,i}$ is the output of the model, $\tau_{tot,(1-0)}$ is the optical depth of the (1 − 0) transition as measured from the hyperfine satellite ratios, and $\tau_{m,(1-0)}$ is that predicted by the model. The uncertainty $\sigma_{F,i}$ takes into account the rms of the integral and a 15% calibration uncertainty, and σ_τ is the uncertainty in τ_{tot}, as given by CLASS. We used a Gaussian prior on $T_{\rm K}$, centred on 35 K, with a $\sigma_{T_K} = 30$ K, given the results of the analysis carried out for CS and the CO results in Massi et al. (1997). The parameter φ is the normalisation constant. Also in this case, the column and the number densities are constrained quite well, while the temperature is much more uncertain.

The results obtained from RADEX for CN are summarised in Table 5.6. The columns show the offset of the spectrum used, the clump name, the kinetic temperature and its 68% interval, the number density of molecular hydrogen and its 68% interval, the column density and its 68% interval, the molecular abundance, the optical depth of CN(1 − 0) and (2 − 1), and the excitation temperature of the same transitions, respectively. The values listed in Table 5.6 for τ_{10} are in very good agreement with those derived from the observations.

Owing to the poor constraints on $T_{\rm K}$, temperature maps are the most difficult to interpret. However, we obtain typical temperatures of between 25 K and 32 K for the whole region. The difference in $T_{\rm K}$ found with CS at (0″,50″) (18 K *vs.* 33 K) might be understood if one considers that CN is a good tracer of PDRs (Simon

Table 5.5: Summary of RADEX results from CS data, for selected offsets.

Offset ($''$)	Cl.	T_K (K)	68%int. (K)	$n(H_2)$ ($10^4 \times$ cm^{-3})	68%int. ($10^4 \times$ cm^{-3})	N(CS) ($10^{13} \times$ cm^{-2})	68%int. ($10^{13} \times$ cm^{-2})	[CS/H_2] (10^{-9})	τ_{21}	τ_{32}	τ_{54}	$\tau_{C^{34}S,21}$	$T_{ex,21}$ (K)	$T_{ex,32}$ (K)	$T_{ex,54}$ (K)	$T_{ex\ C^{34}S,21}$ (K)
(-100,200)	A	33	10 – 64	17	4.8 – 36	4.2	3.9 – 4.9	26	0.7	1.5	0.5	0.05	14	10	7	12
(-50,150)	B	25	11 – 35	18	8.3 – 30	7.4	6.1 – 7.7	5.2	1.4	2.5	1.2	0.09	13	10	6	11
(0,0)	C	40	10 – 72	5.3	1.9 – 8.3	4.3	3.1 – 6.1	9.5	1.2	1.4	0.1	0.08	8	6	6	6
(0,50)	C	18	11 – 20	25	14 – 52	21	14 – 52	2.7	2.4	4.1	2.2	0.17	13	11	6	10
(-50,100)	D	26	10 – 40	22	5.8 – 63	16	15 – 19	3.4	1.6	3.1	2.0	0.12	16	12	7	13
(100,50)	E	11	10 – 15	260	130 – 480	18	15 – 19	40	3.8	5.1	2.7	0.20	11	11	9	11
(-100,100)	F	29	10 – 40	14	5.8 – 25	2.1	1.6 – 2.5	0.7	0.5	0.8	0.1	0.03	11	7	6	10

Table 5.6: Summary of RADEX results from CN data, for selected offsets.

Offset ($''$)	Cl.	T_K (K)	68%int. (K)	$n(H_2)$ ($10^5 \times$ cm^{-3})	68%int. ($10^5 \times$ cm^{-3})	N(CN) ($10^{14} \times$ cm^{-2})	68%int. ($10^{14} \times$ cm^{-2})	τ_{10}	τ_{21}	$T_{ex,10}$ (K)	$T_{ex,21}$ (K)
(-50,150)	A	35	21 – 57	2.8	1.2 – 7.6	2.6	2.2 – 3.4	1.2	4.0	17	10
(-75,150)	B	25	11 – 35	2.3	0.8 – 7.6	0.7	0.6 – 0.9	0.9	1.6	9	6
(0,50)	C	33	26 – 40	18	11 – 28	2.3	1.9 – 3.0	0.2	1.6	67	18
(-50,100)	D	45	30 – 68	3.3	1.7 – 6.3	2.2	1.6 – 3.0	0.7	3.2	26	11
(75,50)	E	34	28 – 42	37	23 – 69	1.8	1.4 – 2.2	0.2	1.1	62	25
(50,75)	G	41	28 – 58	6.8	3.0 – 16	1.9	1.4 – 2.5	0.2	2.2	62	14
(-50,100)	H	33	21 – 57	2.5	1.0 – 6.3	1.7	1.4 – 2.2	1.2	3.5	15	8

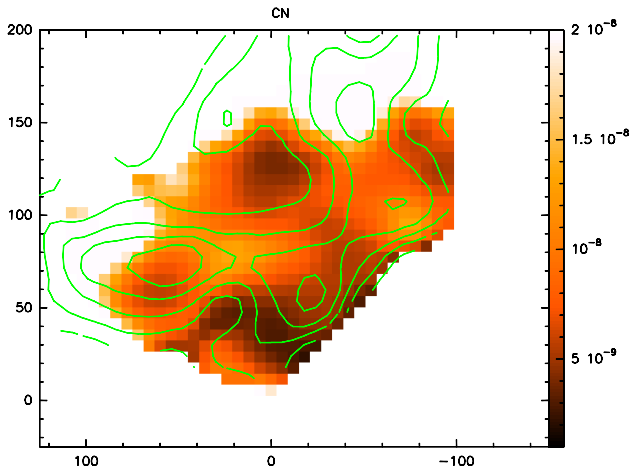

Figure 5.10: Map of molecular abundance relative to H_2, derived from CN data, through a non-LTE analysis. The green contours show representative values of the column density, to clarify the distribution of the molecule.

1997), thus the emission may come from the more external material, directly heated and shocked by the interaction with the early-type stars of Pismis 24. In all cases, these temperatures are usually within the 68% interval also found for E and at the edges of D and B, nearly facing Pismis 24.

In contrast, we derived a slightly lower temperature ($\sim$ 25 K) for C2 than for C1, which is nevertheless consistent with those cited above.

The clumps in the region have a typical number density in the range $\sim 1 - 6 \times 10^5$ cm^{-3}. The number density is highest along the IF (C1 and C2), in D and in E, with values up to a few $\times\, 10^6$ cm^{-3}. Clump E is particularly interesting, since it appears to have a resolved compressed layer facing Pismis 24. The H_2 number densities that we find are on average higher than those derived from CS, consistent with the idea that most of the emission comes from the high-density surface layers of the PDR.

The column density of single clumps lies between $\sim 5.0 \times 10^{13}$ cm^{-2} and $\sim 3.0 \times 10^{14}$ cm^{-2}.

After determining the column density for the various components, we were able to construct an integrated column density map, hence derive an abundance map similar to that of ^{13}CO, C^{18}O, and H_2CO, as given in Fig. 5.10. The emerging abundance pattern closely resembles that of the other three molecules, indicating once more that the region of the elephant trunk and the brightest part of the IF is where the influence of Pismis 24 is the strongest. The abundance of CN is

$\sim 5.0 \times 10^{-9}$ in the region of C, $\sim 8.0 \times 10^{-9}$ around D, and $\sim 7.9 \times 10^{-9}$ around E. We find that CN is enhanced with respect to other molecules around clump C and the IF, where the NIR emission is at its strongest and the ionising radiation more intense: this is suggested by a less pronounced variation in abundance than that found from different species. For CN, the column density peak of the gas and that of the dust for clump E coincide, showing that its displacement for the other molecules can be caused by optical depth effects (cf. Sect. 5.2.3.6) or that $C^{18}O$ and H_2CO are frozen onto grains at the centre of the clump (given also the very low temperature derived from CS). However, a displacement is observed for the peak in the region of clumps A and B, again toward Pismis 24. This and the temperatures comparable to those of C1 might indicate that the IF/PDR extends here, even though the brightness at NIR wavelengths is much lower than nearer Pismis 24.

5.2.3.9 Virial masses

The total mass of a spherical system in virial equilibrium is given by Eq. 3.2 (MacLaren et al. 1988). This expression neglects the influence of magnetic fields, rotation, and internal energy sources, which are usually non-negligible in molecular clouds.

To estimate R for Eq. 3.2, we used the "effective radius", i.e. the radius of a circle with the same area as the clump above the FWHM level, corrected for the beam size. When the FWHM is smaller than the beam size, we assumed as an upper limit to the angular size, half of the actually observed FWHM. As a consequence of the large beam, some individual clumps may be blended and appear as one. For example, C is resolved into two different clumps in CS(5 − 4), and less clearly also in $C^{18}O(2-1)$, while it appears to be unresolved in the other transitions.

Figure 5.11 shows the virial parameter $\alpha = M_{\rm vir}/M_{\rm LTE}$ as a function of $M_{\rm LTE}$, both determined from $C^{18}O(2-1)$, where we assumed that $q = 2$. The mass $M_{\rm LTE}$ was derived within the FWHM contour in $\int T_{\rm MB} {\rm d}V$. All clumps with masses above 50 $M_\odot$, and also two with lower masses ($M \sim 20$ $M_\odot$ G1 and O) have $\alpha \approx 1$, thus indicating that these clumps might be gravitationally bound.

5.2.3.10 Selective photodissociation

G353.2+0.9 is illuminated by several early-type stars. These stars deliver a huge quantity of energetic photons that dominate the chemistry and the heating of the gas in the PDR. The incident far-ultraviolet (FUV) flux is usually measured in

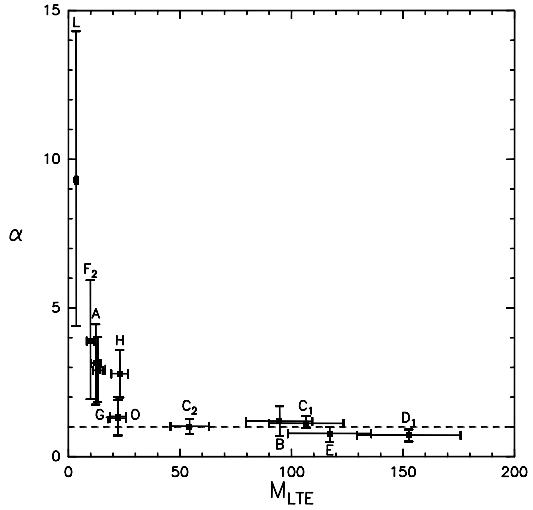

Figure 5.11: Virial parameter α as a function of $M_{\rm LTE}$. $M_{\rm vir}$ and $M_{\rm LTE}$ are both determined from $C^{18}O$. $M_{\rm LTE}$ is calculated within the FWHM contour in $\int T_{\rm MB} {\rm d}V$. The dashed line indicates $\alpha \sim 1$, i.e. $M_{\rm vir} = M_{\rm LTE}$.

terms of the ratio of the FUV flux in the region and the mean interstellar flux (the Habing Field, 1.6×10^{-3} erg cm^{-2} s^{-1}).

Considering the luminosities of the O3.5 If* [$\log(L/L_\odot) \sim 6$], of the O3.5 III(f*) [$\log(L/L_\odot) \sim 5.9$], and of the O4 III(f+) [$\log(L/L_\odot) \sim 5.8$] stars given by Weidner & Vink (2010), we can assume that these stars dominate the emission of energetic photons in the region. The fraction of luminosity emitted in the FUV band was estimated using a simple black-body law, between 912 Å and 2067 Å. We obtained a total FUV luminosity of

$$L_{\rm FUV,tot} = 1.2 \times 10^6 \, L_\odot, \tag{5.9}$$

and making use of

$$G_0 = \frac{1}{1.6 \times 10^{-3} \text{ erg cm}^{-2} \text{ s}^{-1}} \frac{L_{\rm tot}}{4\pi D^2}, \tag{5.10}$$

we find that $G_0 \sim 5.6 \times 10^4$, for a representative projected distance of the stars from the elephant trunk of 0.66 pc. On the other hand, for the ionisation front, we obtained $G_0 \sim 2.0 \times 10^4$, using a projected distance of 1.12 pc between the IF and the cluster.

The high FUV flux may influence the ratio of $C^{18}O$ and ^{13}CO, by means of selective photodissociation. This process tends to destroy the less abundant

isotopologue, owing to the lower optical depth, thus less effective self-shielding capability.

We obtained the ratio of the transitions of the two isotopologues (^{13}CO/C^{18}O) for both observed transitions, combining ^{13}CO and C^{18}O values measured in positions less than half a beam apart. We corrected for the effects of opacity of the ^{13}CO, evaluated through the detection equation (given in Eq. 5.3). The ratio of the $T_{\rm MB}$ of the lines should therefore be representative of the relative abundance of the two molecules. The ^{13}CO/C^{18}O ratio is everywhere consistent with the standard value of the relative abundance for the two isotopologues (~ 8), with three exceptions. The measured values of the ^{13}CO/C^{18}O ratio south of the ionisation front, are a factor of two higher than the standard value. South of the elephant trunk, we did not detect C^{18}O. However, assuming emission from C^{18}O at rms intensity we obtain a lower limit to the ratio of $7 - 10$. The model of Visser et al. (2009) shows that the relative increase in the ^{13}CO/C^{18}O ratio is about a factor 2-3, with the typical parameters of the region ($A_V \sim 5 - 10$ mag, $G_0 \sim 10^4 - 10^5$ and $n(\mathrm{H_2}) \sim 10^4 - 10^5$ cm^{-3}). The results reveal that selective photodissociation does indeed occur south of the ionisation front, and there is an indication that selective photodissociation is also taking place south of the elephant trunk.

At the position of the elephant trunk, at the IF and for clump E the ratio is smaller than the standard value. In this case, the ratio may still be influenced by optical depth effects (in particular an underestimated opacity for ^{13}CO, which was determined from Eq. 5.3, assuming optically thin emission).

5.2.3.11 Ionisation front and geometry of the region

Neither the present study nor that carried out by Massi et al. (1997) found significant quantities of molecular material around the "Bar" (see Fig. 5.2 and 5.5). This rules out the possibility that the "Bar" is an ionisation front eroding a molecular cloud. This also implies that we cannot exclude an association of G353.2+0.9 with Pismis 24 based on the position of this feature (as argued by Felli et al. 1990 prior to the availability of molecular line maps of the region). Energetic, spectral, and excitation analyses (e.g. Massi et al. 1997; Bohigas et al. 2004) indicate that Pismis 24 is indeed associated with G353.2+0.9 and that their proximity is not just a projection effect. The *actual* ionisation front in G353.2+0.9 lies along the IR-bright feature labelled IF in Fig. 5.2 and is possibly associated with the UCHII region C (Felli et al. 1990).

We find a significant number of molecular cores along this bright ridge of emission and its continuation to the north-west, where the NIR brightness strongly

diminishes. Furthermore, densities and temperatures are on average higher in this region. Our application of RADEX also revealed a slight increase in $T_{\rm K}$, volume density of H_2, and opacity here. There is intense radio continuum emission at 5 GHz (Felli et al. 1990) associated with this feature. This, together with the molecular gas distribution and physical conditions, confirm that IF is the main ionisation front in G353.2+0.9. Here, the ionising flux generated by the stars embedded in the region and by those of Pismis 24, erodes the molecular cloud and pushes its material towards the north. When the resolution is high enough, one can see that the clumps near the ionisation front, such as H, D, and C, are roughly parallel to it. High-density tracers are observed in rather small features at the edge of the ionisation front, indicating the regions where the gas was compressed by the shock front.

Molecular emission strongly decreases south of this ionisation front and no massive clumps are observed here, although some emission is visible, especially in low-density tracers (see Fig. 5.5). Bohigas et al. (2004) found that the region immediately surrounding the ionisation front is characterised by a thin layer (10^{-3} pc) of very dense ionised material, where a photoevaporative flow is generated.

We detect only very faint emission from CN(2 − 1) along the "Bar", which implies that there are very small clumps immersed in the PDR. These could be the remnants of the denser regions of a slab of gas, that has been photodissociated, the most massive part of which could be the tip of the elephant trunk. This is suggested by the presence of a small concentration of young stellar objects along the "Bar".

5.2.3.12 Comparison with massive clumps in early stages of evolution

In the previous chapters we investigated the properties of massive clumps in the earliest stages of the process of forming high-mass stars, while here we concentrate on those around an already formed young, massive cluster. These clumps are illuminated by an intense UV field from some of the hottest and most luminous stars known. Here I will briefly compare their respective properties.

- The temperatures measured in massive, quiescent clumps in Chapters 3 and 4 are lower than those measured in the UV-illuminated clumps which are found to be around 20 K from $C^{18}O$ and usually between 20 – 40 K from the other tracers (CS, CN and CH_3CCH). These temperatures are of the order of those found in star-forming sources; in addition to the external heating by the feedback of the OB stars in Pismis 24, in some of the clumps star formation may be ongoing as well, as suggested by the presence of a young

early B star at the tip of the elephant trunk (cf. Sect. 5.2.1) and by several lower-mass PMS stars in the HII region (see Sect. 5.3).

- The masses of the clumps in G353.2+0.9 are on average smaller than those of the objects investigated in the other chapters, and only some of them (e.g., C_1, C_2 and E) lie above the Kauffmann & Pillai (2010) relation discussed there.

- Another difference is found comparing the α-ratios, i.e. $M_{\rm vir}/M$. Keeping in mind that in the present Chapter I used $k = 126$ in Eq. 3.2, appropriate for a gradient $n(H_2) \propto r^{-2}$, the ratios shown in Fig. 5.11 must be increased by a factor 1.5 − 2.0. Observing the latter figure, and comparing it to Figures 3.7 and 4.13, the α of UV-illuminated clumps appears to be larger than that of massive clumps in an earlier stage of evolution and in a less violent environment. This is true for all clumps, both for those that appear gravitationally bound in Fig. 5.11 (and that remain so even after the rescaling to $k = 210$, according to the criteria of Kauffmann et al. 2013, used in Sect. 4.6.4), as for those that appear to be in the process of dispersion. The energetic feedback of massive stars may have played a role in this, as could be suggested also by the complex velocity field in the region.

- The molecular emission in G353.2+0.9 shows a large range in $V_{\rm LSR}$, from ~ -8 km s^{-1} to $\sim +1$ km s^{-1}, and a significant number of different velocity components, leading to the identification of 14 clumps in the above velocity range. This is possibly suggesting that the material is being fragmented, and stirred by the massive stars. An indication of fragmentation may also come from the region of the "Bar" where only faint CN emission is detected. This could be the result of the dissociation of the less dense layers of the gas, whereas the denser parts, such as the elephant trunk, resist better.

- Whereas in the first stages of high-mass star formation the molecular abundances are mainly influenced by adsorption of some species, especially CO, onto the surface of dust grains, with time feedback may take them back to about canonical levels, as we saw in Chapter 4 and in the clumps in G353.2+0.9, far from Pismis 24. In this region, the desorption of CO from the dust grains must be primarily because of the relatively elevated temperature, as the densities do not differ much from those in massive quiescent clumps. If the UV radiation is strong, as is the case around massive stars, selective photodissociation becomes important for the rarer species, that are

not as efficient in self-shielding themselves against the UV photons. This was directly observed for $C^{18}O$ in the region of the main ionisation front in G353.2+0.9, where the mean abundance of this molecule drops by a factor of ~ 2.

5.2.3.13 Pismis 24 13 (N36)

This star is located in the northern part of G353.2+0.9 (cf. Fig. 5.2) and is classified as a spectral type O6.5 V((f)) (Massey et al. 2001). Pismis 24 13 is worth noting because it seems to have produced its own HII region in the molecular gas (see e.g., Fig. 3 in Hester & Desch 2005). This is confirmed by the radio continuum and ion-line observations (Bohigas et al. 2004), which reveal free-free emission following very well the outer edge of the cavity and an increase in electron density in coincidence with this feature. This HII region appears to be in the foreground with respect to the elephant trunk and ionisation front.

Dense star clusters often produce runaway OB stars with high radial velocities through two different mechanisms (Zinnecker & Yorke 2007): asymmetric supernova explosions and dynamical three-body encounters. The radial velocities of these objects exceed 40 km s^{-1}. Gvaramadze et al. (2011) confirm that NGC 6357 is rich in OB runaway stars ejected from the clusters within the cavity. Pismis 24 13 could be one of these OB runaways, ejected from Pismis 24 in the direction of the molecular clouds, where its radiation and wind then created the observed HII region. To confirm this hypothesis we need a spectral measurement of the radial velocity of the star.

5.2.4 Summary and Conclusions

We have observed the Galactic HII region G353.2+0.9 in several molecular lines, which has allowed us to distinguish at least 14 clumps in its associated molecular cloud. We have determined temperatures, densities, and masses of each clump. We also identified the location of the real ionisation front in G353.2+0.9. There is a tendency for the clumps near to the ionisation front to have redder velocities than those further to the north. This is especially noticeable in low-density tracers (cf. Fig. 5.5), and is caused by the expansion of the ionised, overpressurised gas pushing the molecular material away from the observer. This may also be connected to the fact that, compared to the sources in the previous chapters, the spectra in this region can be much more structured, revealing the presence of several molecular

fragments, with typical masses lower than those of massive clumps in the early phases of high-mass star formation.

Excitation temperatures derived from the ratios of the line temperatures of the $C^{18}O(1-0)$ to the $(2-1)$ lines indicate that T_{ex} is in the range $15-25$ K, with the higher values being found along the IF. The temperatures derived from CH_3CCH, which is an effective tracer of kinetic temperature, are found to lie in the range of $\sim 22-45$ K.

The temperatures derived for these clumps are larger than those found for high-mass, quiescent clumps, and comparable to that of star-forming sources in Chapters 3 and 4.

Assuming LTE and a constant $T_{ex} = 20$ K, we derived the molecular column densities of ^{13}CO (from Massi et al. 1997), $C^{18}O$, and H_2CO, thus obtaining maps of molecular abundances, from their ratios with the H_2 column density, which we derived from the APEX 870 μm image, assuming $T_K = 30$ K and a gas-to-dust ratio $\gamma = 100$ (Fig. 5.9). The maps show similar features, with a decrease in the molecular abundance in the region of the elephant trunk and the IF with respect to other region of intense molecular emission [~(75″,75″), E; ~(-100″,125″), D, B]. The molecular abundances derived in this way are uncertain by at least a factor of two, owing to the variations in T_K across the region. Nevertheless, the region of lower molecular abundance outlines the IF, clearly showing the area where the influence of early-type stars is the strongest.

Column densities of molecular hydrogen derived from $C^{18}O$ and H_2CO, under the assumption of LTE and with the abundances calculated as described above, range between $10^{20} - 10^{23}$ cm^{-2}. The visual extinctions are proportional to the H_2 column density: typical values are in the range $5-30$ mag depending on the transition used, while the maximum values, estimated from H_2CO assuming LTE, are found in clumps C and E (~ 50 mag). The volume densities, determined assuming spherical geometry for the clumps, lie between $\sim 10^3$ cm^{-3} and $\sim 10^5$ cm^{-3}. The volume density derived in this way is of the same order of magnitude as the critical density of the transition used to determine it.

The total mass of gas in the region is ~ 2000 M$_\odot$. Single clumps have masses in the range 10 – several $\times\ 10^2$ M$_\odot$. The uncertainty in the mass for a given clump is dominated by the different physical conditions probed by the different transitions.

A simple virial analysis shows that all the clumps with masses above 50 M$_\odot$, in addition to two with lower masses ($M \sim 20$ M$_\odot$ G1 and O) have $\alpha \approx 1$, thus indicating that these clumps might be gravitationally bound. Comparing the values of α with those of massive clumps in an early phase in the process of forming high-mass stars, investigated in Chapters 3 and 4, we find that those of UV-illuminated

clumps are higher (cf. Sect. 5.2.3.12).

We performed a non-LTE analysis with RADEX, considering the four transitions of the two CS isotopologues in one case and the two transitions of CN in the other.

To analyse the model results, we used a Bayesian approach, evaluating the likelihood $P(D|T_K, N, n, model)$ based on Eqns. (5.6) and (5.8). We used a constant *prior* for all the parameters for CS and a Gaussian prior for T_K (μ = 35 K, σ = 30 K) for CN, according to our knowledge from CO, CH_3CCH, and the results from CS, to reduce the degeneration on this parameter.

For CS, we find $T_K \sim 11 - 45$ K, depending on the clump considered. The H_2 number density typically ranges from several $\times 10^4$ cm^{-3} to few $\times 10^5$ cm^{-3}, but exceeds 10^6 cm^{-3} for clump E, where $T_K \sim 11$ K. The CS column density lies between $\sim 2 \times 10^{13}$ cm^{-2} and $\sim 2 \times 10^{14}$ cm^{-2}. Making use of this result, we determined the abundance of CS, taking the ratio of the molecular column density to that of H_2 derived from the 870 μm emission. The abundances are found to lie between 7.0×10^{-10} and 4.0×10^{-8} (Table 5.5). These are lower limits because we do not know the column density of each velocity component, but just that of the strongest one. However, the results should not change by much, given that at a certain offset there is usually a single velocity component that dominates the emission.

For CN, we were able to construct maps for T_K, N, and n. We find that T_K lies typically in the range of 25 – 32 K, with a maximum of $\sim$ 45 K, but T_K is the most poorly constrained parameter, thus making the maps quite difficult to interpret. The H_2 number densities that we find are on average higher than those suggested by CS, in the range of $\sim 1 - 6 \times 10^5$ cm^{-3}, which is consistent with the idea that most of the emission comes from high-density surface layers of the PDR (Simon 1997). The temperature T_K shows a similar behaviour: the temperatures found from CN are usually slightly higher than those derived from CS or $C^{18}O$. In the region of the elephant trunk and the IF, the volume density is even higher, $\sim$ few $\times 10^6$ cm^{-3}, which is similar to the values also reached for E and D. The column density lies between $\sim 5.0 \times 10^{13}$ cm^{-2} and $\sim 3.0 \times 10^{14}$ cm^{-2}. Having a map of CN column density for each clump, we summed them at every position, obtaining an integrated N(CN) map, similar to those of $C^{18}O$, ^{13}CO, and H_2CO. This allowed us to obtain an abundance map (Fig. 5.10) that resembles those of the other molecules. The abundances found are in the range $5.0 - 7.9 \times 10^{-9}$ (Table 5.6). This map showed that CN is enhanced in the region of the trunk and along the IF, where the decrease in molecular abundance is less pronounced than for other molecules.

We did not find significant quantities of molecular material in the region near

the "Bar", which had been previously thought to be an ionisation front. This is consistent with the idea that the "Bar" appears to be a layer of ionised matter seen edge-on (Bohigas et al. 2004), the result of the free wind from the massive stars of Pismis 24 interacting with the photoevaporative flow generated at the true ionisation front (see Fig. 5.2). The presence of a very faint feature in CN($2-1$) along the "Bar" possibly suggests that the small quantity of molecular material in this region could be distributed in very small condensations inside the PDR, that could be the remnants of photodissociated gas in the region of the "Bar". The tip of the elephant trunk may be the densest part of this gas, that still resisted photodissociation.

The high incident FUV flux strongly influences the shape and the properties of G353.2+0.9. We investigated the presence of selective photodissociation of $C^{18}O$ making use of ^{13}CO data of Massi et al. (1997). The $^{13}CO/C^{18}O$ ratio is nearly everywhere consistent with the standard value of the relative abundance of the two isotopologues. We find that south of the ionisation front and the elephant trunk, $C^{18}O$ is underabundant with respect to ^{13}CO, being photodissociated by the strong, energetic radiation from Pismis 24 stars.

There seems to be a separate semispherical HII region in the northern part of G353.2+0.9, associated with the star Pismis 24 13 (N36), which is an O6.5 V((f)) (Massey et al. 2001). We propose that this star is a runaway O star, dissociating the molecular gas while making its way through it. Radial velocity measurements are needed to confirm this hypothesis.

Acknowledgements
We thank the ATLASGAL project for kindly providing the APEX data. This research made use of the NASA ADS, SIMBAD and CDS (Strasbourg) databases. At the time the observations discussed here were performed, Achim Tieftrunk was employed by the I. Physikalische Institut in Köln. We also thank Malcolm Walmsley and the anonymous referee for their useful comments, that greatly improved this work.

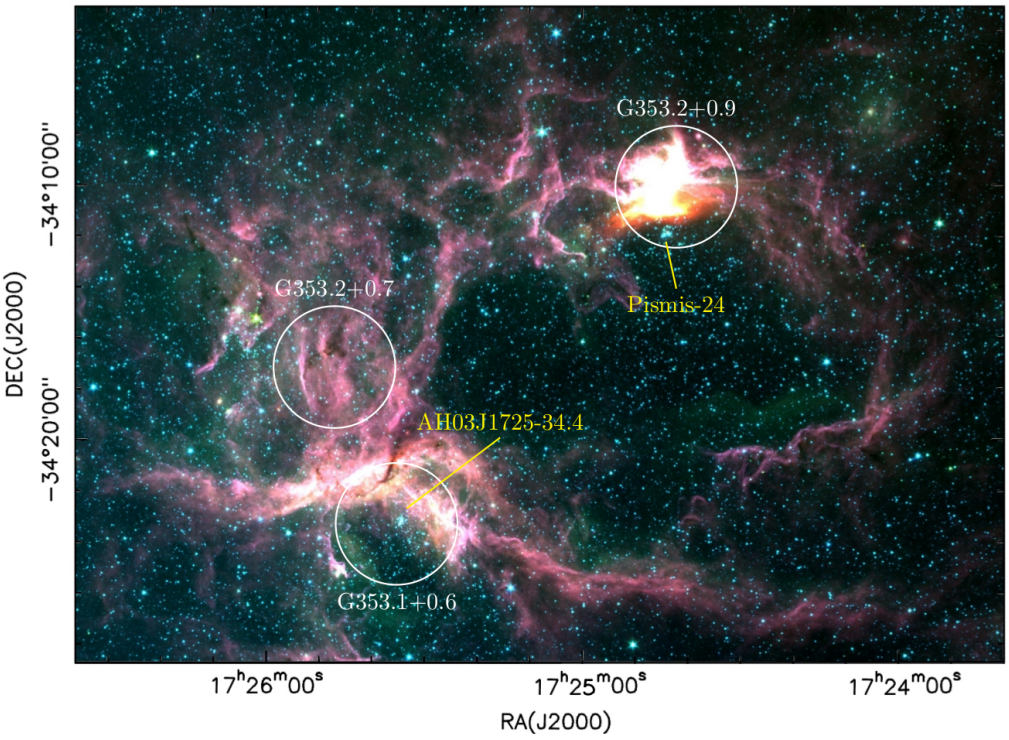

Figure 5.12: SPITZER/IRAC three-colour (blue=3.6 μm, green=4.5 μm red=8.0 μm) image of the NGC 6357 complex. The white circles mark the locations of the most prominent HII regions. The clusters Pismis 24 and AH03J1725-34.4 are also indicated.

5.3 Past and current star formation in NGC6357

The duration of star formation in a particular region and whether it occurs in a single- or in multiple bursts, or continuously are yet unsettled issues. In this section we investigate the star formation activity in the NGC 6357 complex (Fig. 5.12), where we find massive young clusters lying next to molecular gas. Our data offer the possibility to study the region both on the large- and on the small scale, focusing on the most prominent cluster, Pismis 24.

Young stars may be associated with large quantities of gas and dust, that may make them undetectable. The extinction caused by dust decreases with increasing wavelength, therefore IR observations have an important advantage over those

made in the optical regime to detect such objects, also because young stellar objects (YSOs) are relatively cool with respect to their MS counterparts, thus emitting a significant fraction of radiation in the IR. X-rays have similar advantages, because they can penetrate the interstellar medium, and because pre-MS stars are also much brighter at this wavelength than those in the MS phase.

We used deep archival Spitzer/IRAC data (from program #9091, PI J. Hester) to investigate the YSO population in the whole complex, and combined them with NTT/SofI near-IR-, Chandra X ray- (Wang et al. 2007), and archival HST/WFPC2 data to study the stellar population in Pismis 24 and the star formation activity in G353.2+0.9, where the vicinity of massive stars may have a dramatic influence on the birth of successive generations of stars, as discussed in Sect. 1.4.

IRAC is an instrument mounted on the Spitzer Space Telescope; it is equipped with four detectors working at different wavelengths, namely 3.6−, 4.5−, 5.6− and 8.0 μm. Each detector is an array of 256 pixel × 256 pixel, with a mean pixel scale of 1.22″, thus having a field of view of 5.2′ × 5.2′. The dithered observations allowed us to resample the images at a pixel scale about half the original one. The resolution of the IRAC observations is about 2″. With SofI at the 3.6 m ESO-NTT we observed the core of Pismis 24 and the nearby HII region G353.2+0.9 in the JHK_s-bands between $\approx 1-2$ μm. The field-of-view of the instrument is $\sim 5' \times 5'$, with a pixel size of 0.283″. The angular resolution of the images is $\sim 0.9''$. The HST archival observations were done in the F547M and F814W bands, that can be transformed into the *VI* Johnson-Cousins standard. The field-of-view of WFPC2 is divided over four detectors of 800 pixel × 800 pixel: three of them have pixels of $\sim 0.1''$, while the fourth has $\sim 0.046''$ per pixel. The field-of-view is enclosed in the SofI field, and includes part of the cluster core and G353.2+0.9. Finally, the ACIS data from the Chandra satellite have a total field of view of $\sim 16' \times 16'$, of which we use only the central part, corresponding to the near-IR JHK_s observations: thus the PSF is not significantly degraded, and the resolution is about 0.5″, limited by the pixel size.

5.3.1 IR photometry

The photometry of the three images in the JHK_s bands was performed with standard IRAF[5] tasks: the stars were retrieved with DAOFIND, and the results were inspected to remove false detections and add sources that were missed. Aperture photometry was carried out with PHOT, using an aperture comparable to the

[5]Image Reduction and Analysis Facility

FWHM of the point spread function (PSF), i.e. 3 pixel, and sky annuli of about ~ 2 times the FWHM both in radius and width. PSF-fit photometry was then performed with ALLSTAR, after constructing a model PSF from relatively isolated, bright stars. The results in the three bands were matched together with a radius of 3 pixel. The 3σ limiting magnitudes are found to be: $J \sim 19.7$ mag, $H \sim 19.0$ mag, $K_s \sim 18.5$ mag. A similar procedure was followed for the IRAC data, using an aperture of 4 pixel and a sky annulus of $4-12$ pixel, i.e. 2 and $2-6$ original pixels, respectively. The matching radius was chosen equal to 3 pixel of the final image, corresponding to $1.8''$, approximately the Spitzer resolution.

Plotting the number of stars in the field in small magnitude bins we obtain histograms like the ones in Fig. 5.13. The number of stars in each bin increases with increasing magnitude, up to a certain value, then it flattens and starts to fall off. This happens because, as the stars become increasingly faint, we are not able to recover all sources of that flux; our *completeness* is decreasing. Therefore, the turnover of the histogram may be used as a first estimate of the completeness limit for the band considered.

A more accurate estimate of the completeness limit may be obtained by adding artificial sources in the data, and check how many of them are retrieved by the procedure. The PSF is used to add sources with a range fluxes to the original image. For each flux, several runs are performed, to obtain a significant sample of artificial stars; the number of stars added per run is sufficiently small not to modify the field properties. Each image thus generated is processed with DAOFIND to retrieve the sources. The catalogue is finally compared with that of the artificial sources, to calculate the fraction of these that are found by the procedure; the magnitude for which this fraction has decreased to 80% is considered our completeness limit. The completeness limits of our images obtained in this way are listed in Table 5.7. The mass limits can be obtained if distance, average age and extinction of the stellar population are known. We can then compare the observed K_s and 3.6 μm magnitudes with the intrinsic ones in the K and L band, given a set of evolutionary tracks (e.g., Palla & Stahler 1999) for the appropriate age, after correcting for distance and reddening.

Figure 5.13 also shows that when asking for a good detection in multiple bands, the degree of completeness decreases with respect to that of the most sensitive band (cf. the dotted lines): for example K_s is more sensitive than J or H, and IRAC 3.6 and 4.5 μm are more sensitive than 5.6 and 8.0 μm.

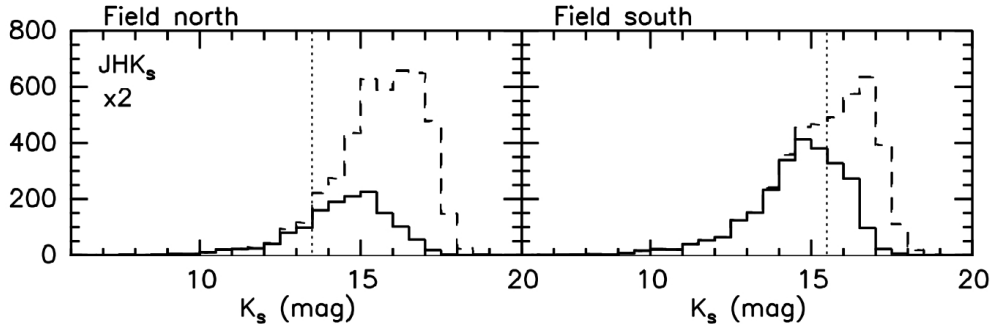

Figure 5.13: Example of histograms showing the number of stars as a function of K_s magnitude in bins of 0.5 mag. The dashed line indicates the histogram for sources with only a valid K_s detection, while the solid line shows that of sources with a valid detection also in J and H (multiplied by 2 for the northern field). The dotted line indicates the K_s magnitude for which we retrieve 80% of the sources, when requiring a valid detection also in the other bands.

5.3.2 Large scale distribution of IRAC sources

To identify the clusters in the region and study their morphology we mapped the surface density of stars. For this, we selected the sources detected in at least the 3.6 μm and 4.5 μm bands, and with a photometric uncertainty < 0.3 mag. The IRAC data are complete in mass down to $\sim 2-3$ M$_\odot$ for 1 Myr old PMS stars (using the PMS tracks from Palla & Stahler 1999), except towards the most extincted areas.

The surface density of the field was estimated by constructing a histogram of the number of squares with a given surface density of sources. This resembles a Poisson distribution, but with excess in the high-count wing, due to the non-random clustering of stars in the area. However, one can assume that the peak is mostly due to the random contribution, and the fit of a Poisson curve allows us to derive the average surface density of stars and its standard deviation. The contours in the left panel of Fig. 5.14 shows the surface density of stars (computed in squares of $1' \times 1'$, spaced by $30''$) above the mean field count plus 3σ. Three clusters are present in the region: Pismis 24, AH03J1725-34.4 (Dias et al. 2002; Gvaramadze et al. 2011), hereafter "A", and another one roughly at the location of G353.2+0.7, which we shall refer to as "B". All the clusters lie in areas of low/moderate extinction, bordering HII regions and molecular clouds. At $1'$ resolution the clusters appear substructured. The photometry in the IRAC bands allows us to identify YSOs

Table 5.7: Summary of the derived completeness limits for different bands and their combinations (second row). The visual extinction assumed to derive the mass completeness limit is indicated in the fourth row, where relevant.

Field	K_s	M	M	3.6 μm	M	M	K_s +(JH)	K_s +(JH4.5 μm)	K_s +(all IRAC bands)
	(mag)	($M_\odot$)	($M_\odot$)	(mag)	($M_\odot$)	($M_\odot$)	(mag)	(mag)	(mag)
A_V[mag]		10	20 – 40		5.5	10 – 20			
North	16.5	–	0.4 – 2	10.8	–	6 – 10	13.5	11.5	10.0
South	15.8	0.2	–	12.3	2	–	15.5	13.0	10.5

Notes. The columns show: the completeness limits in K_s magnitude, when requiring only a good detection in this band, and the corresponding mass limits for 2 different levels of visual extinction, for a distance of 1.7 kpc, and 1 Myr-old PMS stars from Palla & Stahler (1999). The 3.6 μm completeness limit, when requiring only a good detection in this band, and the corresponding mass limits for 2 different levels of visual extinction, derived from the ZAMS theoretical fluxes in the L band at 3.6 μm. The completeness limit in the K_s band, when requiring also a good detection in JH-, in JH4.5 μm- and in all IRAC bands, respectively.

through colour-colour plots, discarding most of the contaminants (broad line AGNs, star forming galaxies and unresolved knots of shock emission; Gutermuth et al. 2009) for sources detected in all four bands; however, the bands at 5.6 and 8.0 μm are less sensitive than those at 3.6 and 4.5 μm, and the completeness is therefore decreased (cf. Table 5.7). The positions of the YSOs are also indicated in the right panel of Fig. 5.14. Despite the fact that only the most massive and brightest YSOs are retrieved with IRAC photometry due to completeness issues, they appear to be concentrated towards the clusters. The diffuse population of Class II objects (cf. Sect. 1.3.1) visible in the figure may be strongly contaminated by evolved stars (AGBs), that can mimic the colours of YSOs (Robitaille et al. 2008). Class I sources seem to avoid the highest surface density peaks, clustering towards the molecular gas. Thus NGC 6357 seems to host ongoing star formation in the molecular gas near the clusters.

5.3.3 Stellar population of Pismis 24

Focusing on Pismis 24, a first diagnostic diagram to investigate the stellar population in this cluster and in the associated HII region G353.2+0.9 is the ($J - H$) vs. ($H - K_s$) colour-colour plot. Figure 5.15 shows this diagram for the northern-

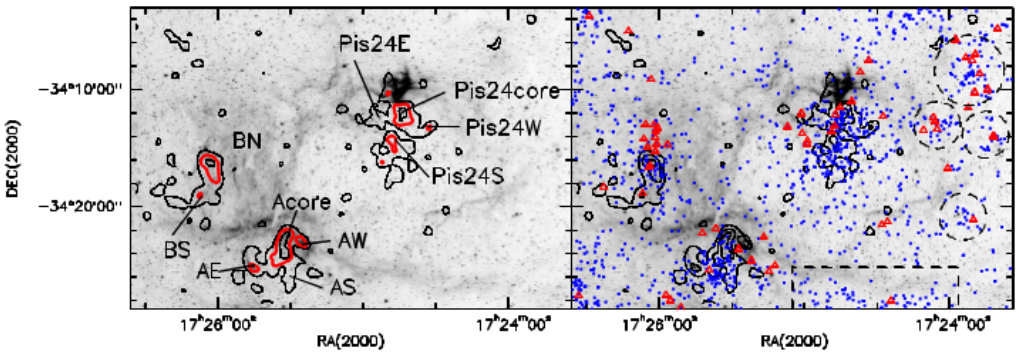

Figure 5.14: **Left:** Contours of the surface density of IRAC sources. Only sources detected in at least the two lowest IRAC bands, with photometric errors < 0.3 mag, and up to [3.6] = 12.25 are considered. The contours range in steps of 3σ from the estimated average surface density of field stars plus 3σ (14 + 11 = 25 stars arcmin^{-2}). Underlying (greyscale), the image at 3.6 μm. Also labelled, the tentatively identified subclusters (A stands for AH03J1725-34.4). **Right:** Same as left, but showing the positions of identified Class II sources (full blue squares) and Class I sources (open red triangles). Other YSO concentrations are enclosed in dashed-line circles and a rectangular box.

and southern parts of the SofI field (separated at DEC $\delta = -34°11'14''$, and characterised by the molecular gas and Pismis 24, respectively), including all sources with a photometric uncertainty < 0.3 mag and inside the completeness limit in the K_s band.

The black solid line shows the main sequence locus, while the dashed lines delineate the corresponding reddening band, following the Rieke & Lebofsky (1985) extinction law. The crosses on the dashed lines indicate intervals of A_V = 10 mag. A significant fraction of the sources are found below the reddening band, indicating the presence of a large population of YSOs in the region. There are, however, a large number of sources above the reddening band as well. This may point to a steeper extinction law; an anomalous reddening law for NGC 6357 is suggested by several authors (e.g., Chini & Krügel 1983; Bohigas et al. 2004; Russeil et al. 2012). Knowing the slope of the extinction law is fundamental to identify sources with an IR-excess (and hence a circumstellar disk; cf. Sect. 1.3.1), and thus their fraction with respect to the total stellar population, which can be used to constrain the age of the cluster. Checking the positions of the sources above the reddening band, we find that they are anti-correlated with the molecular gas and

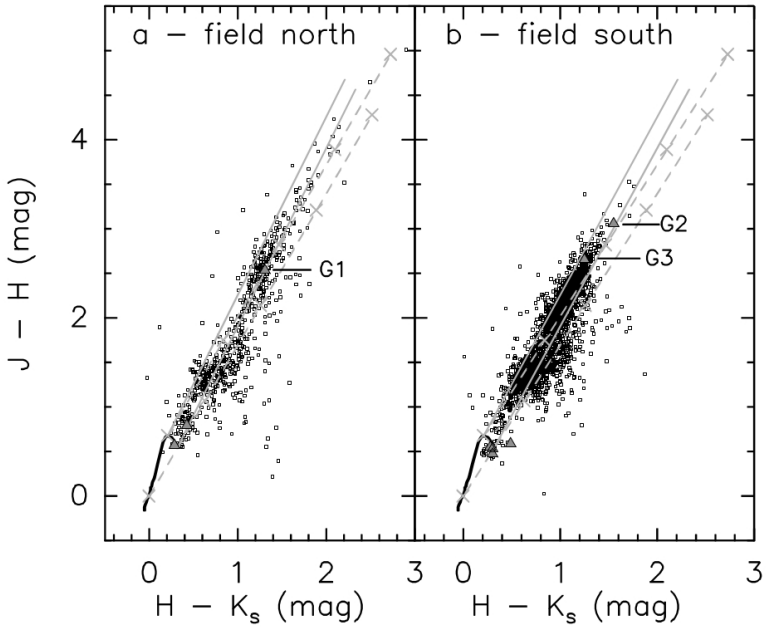

Figure 5.15: **a)** SofI $J - H$ vs. $H - K_s$ diagram for the northern field. **b)** SofI $J - H$ vs. $H - K_s$ diagram for the southern field. Only sources with $K_s < 16$ mag and photometric errors < 0.3 mag have been selected. The grey triangles mark the sources whose colours have been taken from 2MASS. Those labelled G1, G2, and G3 are candidate giant stars based on their brightness and extinction. The thick solid line is the main sequence locus (using the colours from Koornneef 1983). The dashed lines are reddening paths with crosses every $A_V = 10$ mag, following Rieke & Lebofsky (1985). Also shown as grey full lines, reddening vectors according to the extinction law derived by Straižys & Laugalys (2008).

with the cluster core, but are uniformly distributed elsewhere. This is consistent with the distribution expected for shielded background objects. We conclude that these are likely background giants, whose unreddened locus is found above that of the main sequence in a diagram like Fig. 5.15. We thus make the (conservative) choice of a Rieke & Lebofsky (1985) extinction law.

Figure 5.16 shows the colour-magnitude diagrams for the northern and southern fields. In agreement with Massey et al. (2001) and Fang et al. (2012), we find a typical extinction of $A_V \approx 5.7 - 7.6$ mag for the stars in Pismis 24. The extinction has the effect of moving the points along the reddening vector indicated in the figure, away from the ZAMS- or PMS tracks. Therefore, in principle, we can

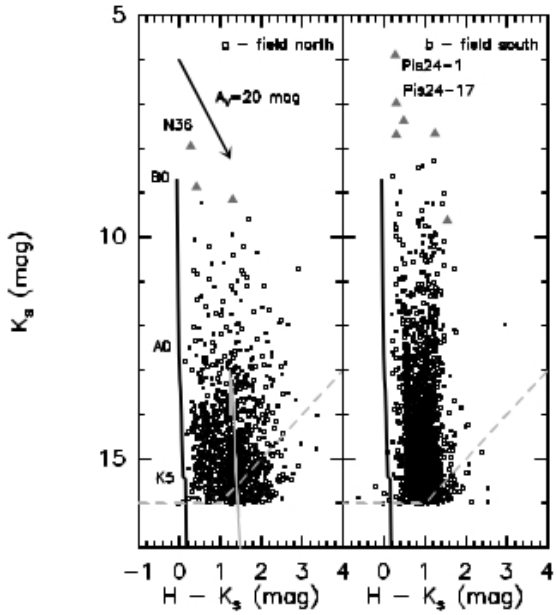

Figure 5.16: **a)** SofI K_s vs. $H - K_s$ diagram for the northern field. Also shown as a grey full line, the 1 Myr isochrone for PMS stars from the evolutionary tracks of Palla & Stahler (1999), for $A_V = 20$ mag, and masses in the $0.1 - 6$ $M_\odot$ range. **b)** SofI K_s vs. $H - K_s$ diagram for the southern field. In both panels, only sources with $K_s < 16$ mag and photometric errors < 0.3 mag have been included. The grey full triangles indicate the sources whose colours have been taken from 2MASS. Some of them, belonging to Pismis 24, are labelled. The thick solid vertical line marks the main sequence locus (using absolute magnitudes from Allen 1973 and colours from Koornneef 1983) for a distance of 1.7 kpc. The arrow indicates a reddening of $A_V = 20$ mag according to Rieke & Lebofsky (1985). Spectral types are labelled next to the ZAMS. The dashed grey line marks the completeness limit.

obtain the masses for each of the objects, tracing them back to the appropriate track, as described in Massi et al. (2006). This procedure does not take into account the IR-excess, thus leading to an overestimate in stellar mass. In the figure, the photometric depth of our image can be fully appreciated: converting the completeness limits into masses using the PMS tracks (1 Myr old objects) of Palla & Stahler (1999), we find that we are complete down to $M \sim 0.2$ $M_\odot$ with $A_V \sim 10$ mag for the southern field and $M \sim 0.4 - 2$ $M_\odot$ with $A_V \sim 20 - 40$ mag for the northern field.

The surface density of sources in the K_s field was computed in squares of $29'' \times 29''$ (100×100 pixel^2) spaced by half a cell, and is shown in contours in Fig. 5.17, above a level of 240 stars/arcmin^2 (180 + 60 stars/arcmin^2, mean field density plus 2σ). Pismis 24 appears substructured also in the central regions observed in the near-IR; all of the most massive members are found in the same subcluster, while the others host only low- and intermediate-mass stars. Parker & Meyer (2012) performed N-body simulations of clusters with 1000 members, and show that substructured distributions with radius of 1 pc collapse to central condensations after 1 Myr, if they are initially subvirial. On the other hand, if the cluster is initially supervirial, as expected in case they experience an early phase of fast gas removal, it still appears substructured after 5 Myr. Differential reddening may simulate the subclustering, but our data indicate that this is not the case. With the SofI near-IR data we are able to find more members than with IRAC data, due to the better angular resolution and mass completeness. However, the core appears smaller because of the small field covered by the K_s frame, implying that the field count estimate is contaminated by the halo of cluster members visible in X-ray data. With a larger frame we would be able to have a better determination of the field counts, and the number of cluster members would be even higher.

5.3.4 The K luminosity function and the initial mass function of Pismis 24

K luminosity functions (KLFs) are important tools to investigate the initial mass function (IMF) of young clusters (e.g., Lada & Lada 2003, and references therein); however, one has to remove the contamination by field stars. This is usually done statistically, using nearby fields devoid of cluster members. Because we lack a suitable comparison field for our K_s frame, we selected sources in a specific extinction interval, instead. Both the optical data of Fang et al. (2012) and our near-IR data show that in the interval $A_V \sim 3.2 - 7.8$ mag there is a dominant contribution of the cluster. X-ray data are very efficient in finding weak line T-Tauri stars, because they are much brighter in X-rays than main sequence stars of the same mass: therefore these observations offer an easy way to select young cluster members. Using the members selected from X-ray data we find that a more appropriate extinction interval would be $A_V \sim 3.2 - 15$ mag.

From the KLF constructed by including stars in these extinction intervals, we derived the dereddened KLF according to Massi et al. (2006). Figure 5.18 shows the dereddened KLF derived for the southern field, considering objects with

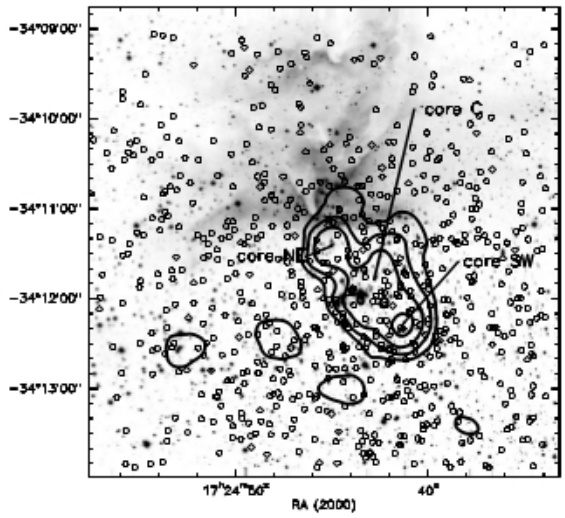

Figure 5.17: Contours of the surface density of near-IR sources overlaid with the K_s image of Pismis 24 and G353.2+0.9. Contours range from the average of field stars plus 2σ in steps of $\sim 1\sigma$. Only sources with $K_s < 16$ mag and photometric uncertainties in the JHK_s bands < 0.3 mag have been included. Also overlaid (open circles), the location of sources with a NIR excess.

3.2 mag $< A_V <$ 7.8 mag. Comparing the dereddened KLFs derived for sources in the extinction intervals 3.2 mag $< A_V <$ 7.8 mag and 3.2 mag $< A_V <$ 15 mag we find that they are statistically different. Thus, sources with 7.8 mag $< A_V <$ 15 mag give a significant contribution to the dereddened KLF.

Massi et al. (2006) show that knowing the age and star formation history of a cluster, it is possible to reconstruct the IMF from the dereddened KLF.

5.3.5 Age and initial mass function of Pismis 24

Massey et al. (2001) and Fang et al. (2012) derive an age < 2.7 Myr for Pismis 24. With the HST VI photometry we checked the age derivation of these authors. From the V vs. $V - I$ diagram shown in Fig. 5.20a we find that, if taken at face value, the sources seem to have ages between 1 and 10 Myr, with a median of ~ 3 Myr. To further investigate this age dispersion we compared the near-IR counterparts of the optical sources with the isochrones in a K_s vs. $H - K_s$ diagram (cf. Fig. 5.20b). The stars appear more massive in the IR, and trying to deredden them individually and correct the V vs. $V - I$ magnitudes accordingly moves the stars to the left

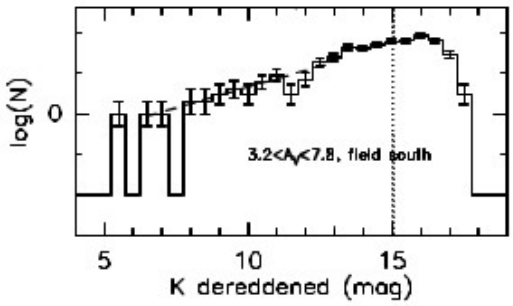

Figure 5.18: Example of dereddened KLF (see text) for sources in the $H - Ks$ colour interval corresponding to a reddening interval 3.2 mag $< A_V <$ 7.8 mag (see text), for the southern field. The dotted line indicates the completeness limit.

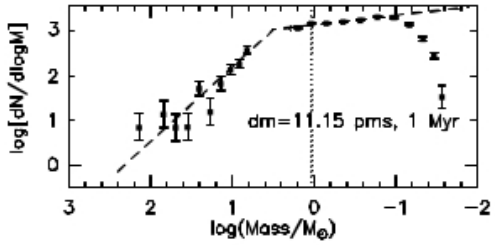

Figure 5.19: IMF derived from the dereddened KLF following Massi et al. (2006), for sources in the $H - Ks$ colour interval corresponding to a reddening interval 3.2 mag $< A_V <$ 7.8 mag (see text), for 1 Myr old PMS stars. The dotted line indicates the completeness limit.

of the ZAMS, indicating that the dispersion in the K_s vs. $H - K_s$ diagram is not only due to differential extinction, but also to an IR-excess which is not evident in a NIR colour-colour diagram, as shown in Fig. 5.20c. PMS stars of Solar and subsolar mass evolve in time contracting with an approximately constant effective temperature, thus decreasing in luminosity. Therefore, if the stars were 10 Myr old they would be fainter in the IR than younger PMS stars and the IR-excess would have to be even more prominent, and still not be evident in the colour-colour diagram, which is very unlikely. The age of the cluster can thus be constrained between 1 − 3 Myr and the dispersion in the V vs. $V - I$ is not real.

With the age constrained in this way, we used the isochrones by Palla & Stahler (1999) (for 1 and 3 Myr) to derive the IMF, following to the method discussed in Massi et al. (2006), and we find that there appears to be a change of slope around

$M \sim 2.5$ M$_\odot$ (cf. Fig. 5.19). The IMF is defined by:

$$\frac{dN}{d\log(M)} = kM^{\Gamma}. \tag{5.11}$$

We fitted the logarithm of the IMF with a two segment function, to derive the *index* Γ (Scalo 1998) in the two regimes. The IMF derived for 3.2 mag $< A_V <$ 7.8 mag and that constructed for 3.2 mag $< A_V <$ 15 mag are slightly different, and should represent a lower- and an upper limit for the IMF. This is because, limiting the colour, not only do we find fewer members, but we include just those with relatively small IR excesses: therefore the two colour ranges should encompass the *real* IMF slope. In addition, one has to keep in mind that because the IR excess is not taken into account in PMS tracks, we measure higher masses in the IR, thus leading to a measured Γ that may be steeper than the real one. We find that in the high-mass regime the IMF has a slope around -1.2 in the former case ~ -1.9 in the latter, while for $M \lesssim 2.5$ M$_\odot$ the IMF appears to flatten. The turnover mass is larger than the mass corresponding to the completeness limit for 3.2 mag $< A_V <$ 7.8 mag, while it is approximately equal to the mass completeness limit for 3.2 mag $< A_V <$ 15 mag. This flattening is consistent with a Scalo (1998)- or Kroupa et al. (1993) IMF.

Using the derived IMF, complemented with a Scalo's at the lowest masses (down to 0.1 M$_\odot$), to calculate the total number of cluster members, we estimate that Pismis 24 hosts $3600 - 11000$ stars (depending on the extinction interval used), consistent with the estimate of Wang et al. (2007) ($\sim$ 5000), for a distance of 1.7 kpc. This implies a stellar mass for the core of $(2 - 6) \times 10^3$ M$_\odot$.

On the basis of the previous discussion, we can try to infer the properties of the primordial environment out of which Pismis 24 was born.

First of all, we can expect that the properties of the gas are similar to those of massive quiescent clumps, therefore with average temperatures between $\sim 10 - 15$ K and possibly with a strong CO depletion.

Then, assuming that the HII region evolved in a medium of constant density with a radius equal to the distance between the massive clumps and the ionisation front (i.e. $\sim$ 1 pc), and using the age of the cluster ($\sim$ 1 Myr) as the age of this idealised HII region, we can derive its Strömgren radius ($\approx$ 0.02 pc) from Eq. 12-20 on Spitzer (1978). In turn, from the Strömgren radius we can derive the average density of the medium, resulting to be $n_{\rm H} \sim 10^6$ cm^{-3}. A single clump with a radius of $\sim$ 1 pc and a density of $\sim 10^6$ cm^{-3} has a total gas mass of $\approx 10^5$ M$_\odot$. Using the above estimate of the stellar mass in Pismis 24, we find that the star formation efficiency is $2\% - 6\%$. Such a large clump would encompass the whole

core of the cluster; however it would be much more massive than the brightest sources in the ATLASGAL survey. In order to reduce this mass, we can consider smaller clumps, still with a density of 10^6 cm^{-3}, but with a radius $R \sim 0.5$ pc, more than sufficient to include the single surface density peaks. The sizes of the clumps in the nearby HII region are similar to this, and several clumps with a similar radius were observed in Chapters 3 and 4. A clump with these properties would have a mass $\sim 10^4$ M$_\odot$; assuming that there were four of them, one for each peak in surface density of sources in the K_s frame, we get a total gas mass comparable to the most massive objects in Chapter 4. On the other hand, it is still much more massive than the clumps studied in Chapter 3, in agreement with our finding that those objects should not form stars more massive than late O stars. That there are very few sources like the one delineated here makes sense, because there are very few clusters like Pismis 24, hosting a large number of OB- and even O3 stars. The diameter size of the superposition of the four smaller clumps would be ~ 1.5 pc. In this case, the efficiency of star formation would range between $5 - 15\%$. Given that all the most massive stars in Pismis are in the same subcluster, there is the possibility that only one of the clumps was this massive, thus increasing the efficiency of star formation, or that some material from the low-density layers of nearby objects may have been focused onto the clump near to the bottom of the potential well, as suggested in the competitive accretion scenario. This material would increase the mass available for accretion, and could end up onto the most massive objects, in a situation similar to that shown in Smith et al. (2009).

The estimate of the density of the material is an upper limit, because part of the UV photons are absorbed by dust grains. This would decrease the average density (even by an order of magnitude), and the gas mass of the primordial material. Consequently the star formation efficiency would increase even more. Because the gas mass cannot be less than the stellar mass, we can interpret this result as proof that the average density of the clumps from which Pismis 24 was born, was very high.

Evolved regions like NGC 6357 show once more that massive stars form together with a significant number of lower mass stars, and that massive clumps do not host just a single massive star. In addition, from the situation observed in G353.2+0.9 we know that massive clumps may show signs of active star formation even if massive stars were not formed yet, if they are among the latest to be formed. In fact, as suggested by the observed substructure in Pismis 24, they may rapidly remove the gas in their immediate surroundings, thus inhibiting further star formation. The presence of low-mass PMS stars along with massive ZAMS objects is no proof against this, if the growth of high-mass stars towards the ZAMS is very

fast and takes only a minor fraction of the age of the cluster. Russeil et al. (2012) estimate the duration of the starless- and protostellar phases for the formation of high-mass stars in NGC 6357 to be 10^4 yr and 10^5 yr, respectively. This allows massive stars to accrete their mass and reach the MS while their low-mass counterparts are still contracting towards the ZAMS.

5.3.6 Star formation in Pismis 24 and in G353.2+0.9

Studying the fraction of stars with a circumstellar disk is another way of assessing the cluster age and investigating the star formation activity in the region, because, as a first approximation, we can assume that disks have lifetimes independent of the properties of the surrounding environment. We used JHK_s and 4.5 μm photometry to identify YSOs, as a large number of stars that have an IR-excess are missed using only JHK_s colours. Taking into account the completeness of the data we find a disk fraction of $0.3 - 0.6$ in the region, consistent with an age of $\sim 2 - 4$ Myr (Haisch et al. 2001). It must be kept in mind that due to the inclusion of IRAC data in the analysis, we are sampling stars with at least an intermediate mass, thus likely underestimating the fraction of sources with a disk, because it is believed that the lifetime of disks around intermediate-mass stars is shorter. A marginally higher value of the fraction of sources with an IR-excess is found towards the HII region, possibly indicating that the sources there are younger. Contrary to Fang et al. (2012) we do not find evidence of a decrease of objects with a disk towards the two most massive stars.

It is difficult to prove that the presence of massive stars triggered the formation of a successive generation of stars. However, Dale et al. (2012) find that the association of young stars with structures such as shells or pillars is a good indication that the formation of these stars has been triggered. This, in conjunction with the slightly higher fraction of stars with an IR-excess and the signs of external compression (see Sect. 5.2.3.8) constitutes circumstantial evidence that the high-mass stars in Pismis 24 are triggering the star formation in G353.2+0.9.

5.3.7 Summary

Our findings on the star formation activity in NGC 6357 may be summarised as follows:

- From the IRAC images we identify three clusters in the NGC 6357 complex, Pismis 24, AH03J1725-34.4, called A and another one towards G353.2+0.7,

referred to as B; all of them appear substructured at 1′ resolution in the IRAC stellar surface density maps, and lie in areas with a low/moderate extinction, bordering HII regions and molecular clouds.

- The $J - H$ vs. $H - K_s$ diagram suggests that the Rieke & Lebofsky (1985) extinction law is appropriate for the region, and that we are seeing a large number of background giants in the field.

- The *core* of Pismis 24 appears to be substructured in the near-IR images, indicating a young cluster and that it is supervirial, possibly due to an early event of fast gas expulsion. This allows the cluster to show substructure even after 5 Myr (Parker & Meyer 2012).

- We find that the age spread seemingly visible in optical data is not real, and we could constrain the age of Pismis 24 to be $\lesssim 3$ Myr. Assuming an age of 1 Myr and 3 Myr we convert the dereddened KLF in an IMF, finding it to be consistent with those proposed by Kroupa et al. (1993) and Scalo (1998).

- We estimate a star formation efficiency of $\gtrsim (2 - 6)\%$ for Pismis 24, in the case the cluster was formed from a single large clump with $R = 1$ pc, or $(5 - 15)\%$ for four clumps with $R = 0.5$ pc, one for each peak in surface density of K_s sources. We also find signs of star formation triggered by the massive stars.

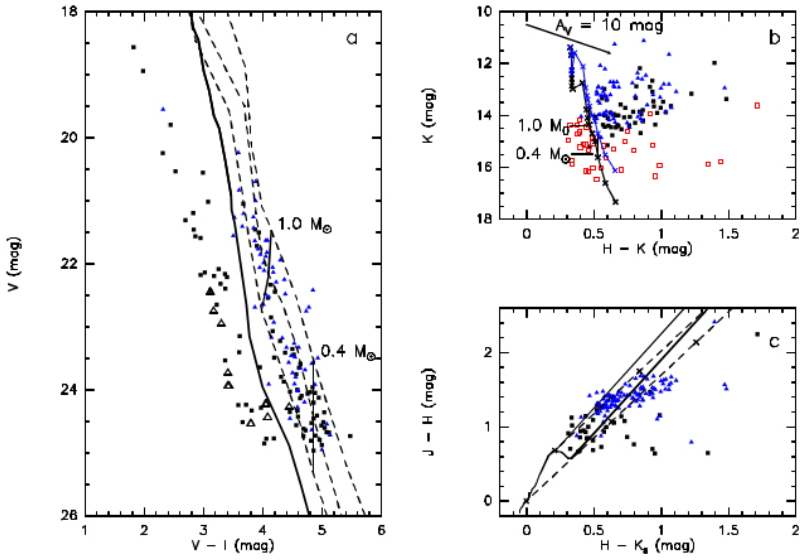

Figure 5.20: **(a)** V vs. $(V-I)$ diagram towards Pismis 24 from the HST/WFPC2 images. The full line indicates the ZAMS locus, while the dashed lines show the PMS tracks for stars 1, 3 and 10 Myr old (taken from Palla & Stahler 1999). All tracks have been reddened by $A_V = 5.5$ mag, and scaled to a distance of 1.7 kpc. Large open triangles show stars without a NIR counterpart, whereas the small blue triangles show stars with an X-ray detection. **(b)** K_s vs. $H-K_s$ for the NIR infrared counterparts of the optical stars (red open squares: stars on the left of the optical ZAMS; full squares: stars on the right of the optical ZAMS; blue full triangles: stars on the right of the optical ZAMS also detected in X-ray emission). The full lines are the isochrones for (from the right) 1 and 3 Myr old PMS stars obtained from the evolutionary tracks of Palla & Stahler (1999), for the same reddening and distance as above. The loci of 1 and 0.4 $M_\odot$ are labelled here as well. The arrow indicates a reddening of $A_V = 10$ mag according to Rieke & Lebofsky (1985). **(c)** $J-H$ vs. $H-K_s$ for the NIR infrared counterparts of the optical stars. The symbols are the same as in **(b)**, where stars on the left of the ZAMS were omitted. The solid line is the unreddened MS, the dashed lines are reddening paths with crosses every 10 mag of visual extinction, following Rieke & Lebofsky (1985). Also shown as solid lines, the reddening paths according to the extinction law derived by Straižys & Laugalys (2008).

Chapter 6

Final remarks

In this thesis two related arguments are investigated:

1. The first stages of the process of massive star formation, investigating the physical conditions and -properties of massive clumps in different evolutionary stages, and their CO depletion;

2. The influence that high-mass stars have on the nearby material and on the activity of star formation.

A sample of 46 massive clumps was selected from the catalogue of Beltrán et al. (2006), and observed with ATCA in NH_3(1,1) and (2,2), and in the $H_2O(6_{16} - 5_{23})$ maser line at 22 GHz. The selection criteria used were: (i) declination $< -30°$, (ii) comparable numbers of clumps dark- and bright in MSX images, (iii) angular distance greater than one SEST beam between IR-dark and bright sources, and (iv) $M \gtrsim 40$ $M_\odot$ in the Beltrán et al. (2006) catalogue. The Herschel/HiGAL-, MSX-, Spitzer/MIPS- (24 μm), Spitzer/IRAC- and SEST/SIMBA images for the observed fields were retrieved to construct the spectral energy distribution, for deriving the bolometric luminosity of the objects and estimating the dust temperature. From the ammonia inversion transitions, we derived the gas kinetic temperature. The dust- and kinetic temperatures are usually in good agreement (cf. Fig. 3.5), and indicate that the clumps are cold, ranging between $\sim 10 - 30$ K. With the temperature thus constrained, we could derive the mass of the clumps, and put our sample in a mass-luminosity diagram, to separate different evolutionary phases, as proposed by Molinari et al. (2008). Moreover, we searched for signposts of ongoing star formation in the clumps of our sample to refine the evolutionary classification. We

considered H_2O masers, 24 μm-, radio-continuum-, and extended 4.5 μm excess ("green fuzzies") emission. In this way, we could define three evolutionary classes, in order of increasing age:

- **QS:** Clumps without any signs of active star formation; the average luminosity is ~ 200 $L_\odot$, and $L/M \sim 1$ $L_\odot/M_\odot$. They are found below the ZAMS locus in the $M-L$ diagram (cf. Fig. 3.11). These clumps are likely starless or with (proto)stars too deeply embedded to be detected.

- **SFS-1:** Clumps with signs of ongoing star formation, but with luminosities usually well below 1000 $L_\odot$, and a $L/M \sim 2$ $L_\odot/M_\odot$. Therefore, they are still below the ZAMS, with a location similar to the QS in the $M-L$ diagram. These objects may host precursors of massive stars in an early stage of evolution, very extincted (proto)stars or lower-mass sources.

- **SFS-2:** Clumps with signs of ongoing star formation, and hosting luminous objects. Their typical L/M ratio is ~ 24 $L_\odot/M_\odot$ and they are found near the ZAMS locus in the $M-L$ diagram. These objects likely host high-mass ZAMS stars.

Sources more evolved than SFS-2 are called **Type 3**, according to Molinari et al. (2008). In these sources, the massive stars have already dispersed a significant fraction of the material from the parental clump. Due to our selection criteria, we have only one Type 3 source, and therefore we limit our analysis to the first three classes.

We investigated how the physical properties of the clumps change in these different phases. It is important to note that, according to the Kauffmann & Pillai (2010) criterion, essentially all of our clumps have the potential of forming massive stars. We find that the kinetic- and dust temperatures increase in more evolved sources; a similar behaviour is observed for column-, volume- and surface densities. However, in this case, the QS and the SFS-1 have peaks at similar locations for the distributions of these quantities. More evolved sources therefore seem to be more centrally condensed, and with steeper radial profiles of H_2 volume density. A similar behaviour is observed in the models of Smith et al. (2009), where all of the simulated clumps become more and more concentrated around the most massive sink particle as time proceeds.

A sub-sample of twenty-one sources among the QS and SFS-1, was observed with APEX in $C^{18}O(3-2)$, in $N_2H^+(3-2)$ and in $N_2D^+(4-3)$. We find surprisingly large CO depletion factors for these objects, between $5-78$ (using the expressions

in Beuther et al. 2005a). The CO depletion appears to be weakly correlated with the temperature. We also tentatively detect the $N_2D^+(4-3)$ transition for the first time in an IRDC.

Twenty-two clumps nearly equally distributed among the first three evolutionary stages listed above were also observed in several molecular lines with APEX. We find indications of the presence of Hot Cores in several SFS-2, and note that $SO(6_5-5_4)$ and $H_2CO(3_{2,1}-2_{2,0})$ become detectable shortly after the star formation process begins, also in SFS-1 sources with a rather low luminosity and L/M ratios. Thus, they could be used to easily select clumps in the earliest stages of the process of forming stars.

We investigated CO depletion and its evolution with time in ATLASGAL-selected massive clumps, making use of single pointing observations in several isotopologues of carbon monoxide, performed with APEX and the IRAM 30-m telescope. Objects in different evolutionary stages were selected from the ATLASGAL catalogue, on the basis of their sub-mm and IR properties (cf. Sect. 4.3).

The abundance of the CO isotopologues was derived comparing the column densities of these molecules with that of H_2, estimated from the dust continuum emission. Clumps in earlier evolutionary stages are found to be colder and to show larger depletion factors f_D up to $\sim$ 20 (corresponding to $\sim$ 55 using the Beuther et al. 2005a, expression for the dust column densities), with average values decreasing from $\sim$ 6 to $\sim$ 2 from the less evolved- to the more evolved objects. We find that the depletion is correlated with both the temperature and the density of the sources: it decreases for higher temperatures and increases for higher densities. RATRAN 1-D models with a constant abundance within the clump were used to confirm these large f_D.

A comparison of the depletion- and free-fall timescales for the clumps in an early evolutionary stage show that these quantities are of the same order of magnitude, and the objects with the lowest f_D indeed have the largest τ_{dep}/τ_{ff}.

Calculating the timescale for depletion as a function of radius in a "typical" clump with a density profile $\propto r^{-1.5}$, a mass within 1 pc of 550 $M_\odot$, and using a typical lifetime for massive starless clumps of $\sim 10^{4-5}$ yr, one can derive a rough estimate of the radius of the central depletion zone, which is found to lie in the interval $\approx 0.02 - 0.1$ pc. Similar numbers can also be derived from a general grid of RATRAN models with a drop profile in CO abundance (i.e. a canonical CO abundance is used up to a certain threshold in volume density; above this threshold, CO is completely frozen onto the dust grains).

Having defined an evolutionary sequence in terms of physical parameters one can now use already publicly available observations to arrange a larger sample of clumps on a timeline, and then use an instrument like ALMA to study objects in a certain evolutionary phase in great detail.

The influence that massive stars have on the nearby environment is investigated in the last part of the thesis.

Several molecular species were observed with the SEST towards G353.2+0.9, the brightest HII region in the NGC 6357 complex, near to the massive open cluster Pismis 24. At least 14 clumps were identified in the observed region (≈ 2.5 pc $\times$ 2.5 pc in $C^{18}O$); those with $M \gtrsim 50$ $M_\odot$ appear to be gravitationally bound. Through both LTE and non-LTE analyses, we find signs of external heating and compression in the gas associated with the main ionisation front. No relevant quantities of molecular gas are observed towards the "Bar" (cf. Sect. 5.2.3.11). Thus, we can confirm the association of the molecular gas and of the cluster.

We constructed maps of molecular abundance in the region, for ^{13}CO, $C^{18}O$, H_2CO and CN. The observed abundances of ^{13}CO and $C^{18}O$ are consistent with selective photodissociation in the region of the elephant trunk and of the ionisation front. On the other hand, CN appears enhanced in this region, confirming that this molecule is a good PDR tracer.

We studied the star formation in the whole NGC 6357 complex, through Spitzer/IRAC data. Three clusters are present in the region, Pismis 24, AH03J1725-34.4 and another one towards G353.2+0.7; all of them appear substructured at 1′ resolution of the IRAC stellar surface density maps. Colour-colour diagrams allowed us to identify several YSOs of Class I and II in the region, mostly distributed towards the molecular gas around the clusters, indicating that stars are being formed in NGC 6357.

Combining IRAC-, NTT/SofI-, HST/WFPC2- and Chandra/ACIS data, we could constrain the age and derive the IMF of Pismis 24. The cluster is young (1 − 3 Myr), and its IMF is consistent with those proposed by Kroupa et al. (1993) and Scalo (1998), with a highest mass of ~ 100 $M_\odot$ and a turnover somewhere around $M \sim 2.5$ $M_\odot$. The core of Pismis 24 appears substructured, again indicating young age and that it is supervirial, possibly due to an early event of fast gas expulsion. This, in fact, allows the cluster to appear substructured even after 5 Myr, while it would collapse to a central concentration in 1 Myr, if it were subvirial (Parker & Meyer 2012). The estimated star formation efficiency associated with the event that generated Pismis 24 is $\gtrsim (2 - 6)\%$ if the cluster was formed from a single large clump with $R = 1$ pc, or $(5 - 15)\%$ if the gas was divided into four

clumps with $R = 0.5$ pc, one for each peak in surface density of K_s sources. We also find signs of star formation triggered by the massive stars towards the HII region.

Bibliography

Adams, F. C. 1991, ApJ, 382, 544

Aikawa, Y., Herbst, E., Roberts, H., & Caselli, P. 2005, ApJ, 620, 330

Allen, C. W. 1973, Astrophysical quantities (London: University of London, Athlone Press, 3rd ed.)

Ambartsumian, V. A. 1947, Erevan: Acad. Sci. Armenian S. S. R.

Ambartsumian, V. A. 1949, AZh, 26, 3

Andreon, S. 2011, ArXiv e-prints; arXiv:1112.3652

Audit, E. & Hennebelle, P. 2008, in Numerical Modeling of Space Plasma Flows, eds. N. V. Pogorelov, E. Audit, & G. P. Zank, Vol. 385 of Astronomical Society of the Pacific Conference Series, p. 73

Bacmann, A., Lefloch, B., Ceccarelli, C., et al. 2002, A&A, 389, L6

Bacmann, A., Lefloch, B., Ceccarelli, C., et al. 2003, ApJ, 585, L55

Bally, J., Langer, W. D., Stark, A. A., & Wilson, R. W. 1987, ApJ, 312, L45

Barnard, E. E., Frost, E. B., & Calvert, M. R. 1927, in Carnegie institution of Washington, 1927., eds. E. E. Barnard, E. B. Frost, & M. R. Calvert

Beltrán, M. T., Brand, J., Cesaroni, R., et al. 2006, A&A, 447, 221

Beltrán, M. T., Codella, C., Viti, S., Neri, R., & Cesaroni, R. 2009, ApJ, 690, L93

Benjamin, R. A., Churchwell, E., Babler, B. L., et al. 2003, PASP, 115, 953

Bergin, E. A., Alves, J., Huard, T., & Lada, C. J. 2002, ApJ, 570, L101

Bergin, E. A., Goldsmith, P. F., Snell, R. L., & Ungerechts, H. 1994, ApJ, 431, 674

Bergin, E. A. & Tafalla, M. 2007, ARA&A, 45, 339

Bertin, E. & Arnouts, S. 1996, A&AS, 117, 393

Bertoldi, F. & McKee, C. F. 1992, ApJ, 395, 140

Beuther, H., Schilke, P., Menten, K. M., et al. 2002, ApJ, 566, 945

Beuther, H., Schilke, P., Menten, K. M., et al. 2005a, ApJ, 633, 535

Beuther, H., Sridharan, T. K., & Saito, M. 2005b, ApJ, 634, L185

Bisschop, S. E., Fraser, H. J., Öberg, K. I., van Dishoeck, E. F., & Schlemmer, S. 2006, A&A, 449, 1297

Blitz. 1993, in Protostars and Planets III, eds. E. H. Levy & J. I. Lunine

Blitz, L. & Williams, J. P. 1999, in NATO ASIC Proc. 540: The Origin of Stars and Planetary Systems, eds. C. J. Lada & N. D. Kylafis, p. 3

Bohigas, J., Tapia, M., Roth, M., & Ruiz, M. T. 2004, AJ, 127, 2826

Bohlin, R. C., Savage, B. D., & Drake, J. F. 1978, ApJ, 224, 132

Bolstad, W. M. 2007, Introduction to Bayesian Statistics (Wiley)

Bonnell, I. A., Bate, M. R., & Vine, S. G. 2003, MNRAS, 343, 413

Bonnell, I. A., Bate, M. R., & Zinnecker, H. 1998, MNRAS, 298, 93

Bonnell, I. A., Clarke, C. J., Bate, M. R., & Pringle, J. E. 2001, MNRAS, 324, 573

Bonnell, I. A., Larson, R. B., & Zinnecker, H. 2007, Protostars and Planets V, 149

Bourke, T. L., Crapsi, A., Myers, P. C., et al. 2005, ApJ, 633, L129

Brand, J. & Blitz, L. 1993, A&A, 275, 67

Brand, J., Cesaroni, R., Comoretto, G., et al. 2003, A&A, 407, 573

Brand, J., Cesaroni, R., Palla, F., & Molinari, S. 2001, A&A, 370, 230

Brand, J., Massi, F., Zavagno, A., Deharveng, L., & Lefloch, B. 2011, A&A, 527, A62

Brand, J. & Wouterloot, J. G. A. 1994, A&AS, 103, 503

Breen, S. L. & Ellingsen, S. P. 2011, MNRAS, 416, 178

Busquet, G., Palau, A., Estalella, R., et al. 2009, A&A, 506, 1183

Butler, M. J. & Tan, J. C. 2012, ApJ, 754, 5

Carey, S. J., Clark, F. O., Egan, M. P., et al. 1998, ApJ, 508, 721

Carey, S. J., Feldman, P. A., Redman, R. O., et al. 2000, ApJ, 543, L157

Carey, S. J., Noriega-Crespo, A., Mizuno, D. R., et al. 2009, PASP, 121, 76

Carpenter, J. M., Snell, R. L., Schloerb, F. P., & Skrutskie, M. F. 1993, ApJ, 407, 657

Caselli, P. 2011, in IAU Symposium, eds. J. Cernicharo & R. Bachiller, Vol. 280 of IAU Symposium, pp. 19–32

Caselli, P., Walmsley, C. M., Tafalla, M., Dore, L., & Myers, P. C. 1999, ApJ, 523, L165

Caselli, P., Walmsley, C. M., Zucconi, A., et al. 2002, ApJ, 565, 344

Caswell, J. L., Fuller, G. A., Green, J. A., et al. 2010, MNRAS, 404, 1029

Caswell, J. L., Fuller, G. A., Green, J. A., et al. 2011, MNRAS, 417, 1964

Cesaroni, R. 2005, in Massive Star Birth: A Crossroads of Astrophysics, eds. R. Cesaroni, M. Felli, E. Churchwell, & M. Walmsley, Vol. 227 of IAU Symposium, pp. 59–69

Chambers, E. T., Jackson, J. M., Rathborne, J. M., & Simon, R. 2009, ApJS, 181, 360

Chen, H.-R., Liu, S.-Y., Su, Y.-N., & Wang, M.-Y. 2011, ApJ, 743, 196

Chini, R. & Krügel, E. 1983, A&A, 117, 289

Churchwell, E., Babler, B. L., Meade, M. R., et al. 2009, PASP, 121, 213

Churchwell, E., Walmsley, C. M., & Cesaroni, R. 1990, A&AS, 83, 119

Commerçon, B., Hennebelle, P., & Henning, T. 2011, ApJ, 742, L9

Contreras, Y., Schuller, F., Urquhart, J. S., et al. 2013, A&A, 549, A45

Cox, R. T. 1946, American Journal of Physics, 14, 1

Crapsi, A., Caselli, P., Walmsley, C. M., et al. 2005, ApJ, 619, 379

Crutcher, R. M. 2005, in Massive Star Birth: A Crossroads of Astrophysics, eds. R. Cesaroni, M. Felli, E. Churchwell, & M. Walmsley, Vol. 227 of IAU Symposium, pp. 98–107

Cyganowski, C. J., Brogan, C. L., Hunter, T. R., & Churchwell, E. 2009, ApJ, 702, 1615

D'Agostini, G. 2003, Bayesian Reasoning in Data Analysis: A Critical Introduction (World Scientific)

Dale, J. E., Ercolano, B., & Bonnell, I. A. 2012, MNRAS, 427, 2852

Dale, J. E., Ercolano, B., & Bonnell, I. A. 2013, MNRAS, 431, 1062

Dame, T. M. & Thaddeus, P. 1994, ApJ, 436, L173

Dame, T. M., Ungerechts, H., Cohen, R. S., et al. 1987, ApJ, 322, 706

Davies, B., Hoare, M. G., Lumsden, S. L., et al. 2011, MNRAS, 416, 972

De Finetti, B. 1974, Theory of probability: a critical introductory treatment, Wiley series in probability and mathematical statistics. Probability and mathematical statistics (Wiley)

Deharveng, L. & Zavagno, A. 2011, in Computational Star Formation, eds. J. Alves, B. G. Elmegreen, J. M. Girart, & V. Trimble, Vol. 270 of IAU Symposium, pp. 239–246

Deharveng, L., Zavagno, A., & Caplan, J. 2005, A&A, 433, 565

Deharveng, L., Zavagno, A., Schuller, F., et al. 2009, A&A, 496, 177

Dias, W. S., Alessi, B. S., Moitinho, A., & Lépine, J. R. D. 2002, A&A, 389, 871

Draine, B. 2010, Physics of the Interstellar and Intergalactic Medium, Princeton Series in Astrophysics (Princeton University Press)

Egan, M. P., Price, S. D., Kraemer, K. E., et al. 2003, Air Force Research Laboratory Technical Report AFRL-VS-TR-2003-1589, 5114, 0

Egan, M. P., Shipman, R. F., Price, S. D., et al. 1998, ApJ, 494, L199

Elmegreen, B. G. 1998, in Origins, eds. C. E. Woodward, J. M. Shull, & H. A. Thronson, Jr., Vol. 148 of Astronomical Society of the Pacific Conference Series, p. 150

Elmegreen, B. G. & Lada, C. J. 1977, ApJ, 214, 725

Fang, M., van Boekel, R., King, R. R., et al. 2012, A&A, 539, A119

Fazal, F. M., Sridharan, T. K., Qiu, K., et al. 2008, ApJ, 688, L41

Feigelson, E. D. & Montmerle, T. 1999, ARA&A, 37, 363

Felli, M., Brand, J., Cesaroni, R., et al. 2007, A&A, 476, 373

Felli, M., Persi, P., Roth, M., et al. 1990, A&A, 232, 477

Flower, D. R., Pineau Des Forêts, G., & Walmsley, C. M. 2006, A&A, 456, 215

Fontani, F., Beltrán, M. T., Brand, J., et al. 2005, A&A, 432, 921

Fontani, F., Caselli, P., Crapsi, A., et al. 2006, A&A, 460, 709

Fontani, F., Cesaroni, R., Caselli, P., & Olmi, L. 2002, A&A, 389, 603

Fontani, F., Giannetti, A., Beltrán, M. T., et al. 2012, MNRAS, 423, 2342

Fuente, A., Caselli, P., McCoey, C., et al. 2012, A&A, 540, A75

Gaume, R. A., Johnston, K. J., & Wilson, T. L. 1993, ApJ, 417, 645

Gelfand, A. E. & Smith, A. F. M. 1990, Journal of the American Statistical Association, 85, 398

Geman, S. & Geman, D. 1984, IEEE Transactions on Pattern Analysis and Machine Intelligence, 6, 721

Giannetti, A., Brand, J., Sánchez-Monge, Á., et al. 2013, A&A, 556, A16

Girart, J. M., Beltrán, M. T., Zhang, Q., Rao, R., & Estalella, R. 2009, Science, 324, 1408

Glover, S. C. O. & Mac Low, M.-M. 2007, ApJ, 659, 1317

Goldsmith, P. F. & Langer, W. D. 1999, ApJ, 517, 209

Goodman, A. A., Benson, P. J., Fuller, G. A., & Myers, P. C. 1993, ApJ, 406, 528

Goodwin, S. P., Whitworth, A. P., & Ward-Thompson, D. 2004, A&A, 419, 543

Green, J. A., Caswell, J. L., Fuller, G. A., et al. 2009a, MNRAS, 392, 783

Green, J. A., Caswell, J. L., Fuller, G. A., et al. 2009b, MNRAS, 392, 783

Green, J. A., Caswell, J. L., Fuller, G. A., et al. 2012, MNRAS, 420, 3108

Green, J. A. & McClure-Griffiths, N. M. 2011, MNRAS, 417, 2500

Gregory, P. 2005, Bayesian Logical Data Analysis for the Physical Sciences: A Comparative Approach with Mathematica® Support (Cambridge University Press)

Griffin, M. J., Abergel, A., Abreu, A., et al. 2010, A&A, 518, L3

Güsten, R., Nyman, L. Å., Schilke, P., et al. 2006, A&A, 454, L13

Gutermuth, R. A., Megeath, S. T., Myers, P. C., et al. 2009, ApJS, 184, 18

Gvaramadze, V. V., Kniazev, A. Y., Kroupa, P., & Oh, S. 2011, A&A, 535, A29

Haisch, Jr., K. E., Lada, E. A., & Lada, C. J. 2001, ApJ, 553, L153

Healy, K. R., Hester, J. J., & Claussen, M. J. 2004, ApJ, 610, 835

Hennebelle, P. & Falgarone, E. 2012, A&A Rev., 20, 55

Herbst, E. & van Dishoeck, E. F. 2009, ARA&A, 47, 427

Hernandez, A. K., Tan, J. C., Caselli, P., et al. 2011, ApJ, 738, 11

Hester, J. J. & Desch, S. J. 2005, in Chondrites and the Protoplanetary Disk, eds. A. N. Krot, E. R. D. Scott, & B. Reipurth, Vol. 341 of Astronomical Society of the Pacific Conference Series, p. 107

Hester, J. J., Scowen, P. A., Sankrit, R., et al. 1996, AJ, 111, 2349

Heyminck, S., Kasemann, C., Güsten, R., de Lange, G., & Graf, U. U. 2006, A&A, 454, L21

Hildebrand, R. H. 1983, QJRAS, 24, 267

Hily-Blant, P., Walmsley, M., Pineau Des Forêts, G., & Flower, D. 2010, A&A, 513, A41+

Ho, P. T. P. & Townes, C. H. 1983, ARA&A, 21, 239

Hoare, M. G., Kurtz, S. E., Lizano, S., Keto, E., & Hofner, P. 2007, Protostars and Planets V, 181

Hoare, M. G., Purcell, C. R., Churchwell, E. B., et al. 2012, PASP, 124, 939

Hofner, P., Wyrowski, F., Walmsley, C. M., & Churchwell, E. 2000, ApJ, 536, 393

Hogerheijde, M. R. & van der Tak, F. F. S. 2000, A&A, 362, 697

Hollis, J. M., Lovas, F. J., & Jewell, P. R. 2000, ApJ, 540, L107

Isella, A. 2006, PhD thesis, Università degli studi di Milano

Jaynes, E. & Bretthorst, G. 2003, Probability Theory: The Logic of Science (Cambridge University Press)

Jørgensen, J. K., Schöier, F. L., & van Dishoeck, E. F. 2004, A&A, 416, 603

Kauffmann, J. & Pillai, T. 2010, ApJ, 723, L7

Kauffmann, J., Pillai, T., & Goldsmith, P. F. 2013, ApJ, 779, 185

Keto, E. 2007, ApJ, 666, 976

Kirk, J. M., Ward-Thompson, D., & André, P. 2005, MNRAS, 360, 1506

Koornneef, J. 1983, A&A, 128, 84

Kramer, C. 1988, Master's thesis, I. Phys. Inst., Köln

Kramer, C., Alves, J., Lada, C. J., et al. 1999, A&A, 342, 257

Kramer, C. & Winnewisser, G. 1991, A&AS, 89, 421

Kroupa, P., Tout, C. A., & Gilmore, G. 1993, MNRAS, 262, 545

Krumholz, M. R., Klein, R. I., McKee, C. F., Offner, S. S. R., & Cunningham, A. J. 2009, Science, 323, 754

Krumholz, M. R. & McKee, C. F. 2008, Nature, 451, 1082

Kurtz, S. 2002, in Hot Star Workshop III: The Earliest Phases of Massive Star Birth, ed. P. Crowther, Vol. 267 of Astronomical Society of the Pacific Conference Series, p. 81

Kutner, M. L. & Ulich, B. L. 1981, ApJ, 250, 341

Lada, C. J. 1987, in Star Forming Regions, eds. M. Peimbert & J. Jugaku, Vol. 115 of IAU Symposium, pp. 1–17

Lada, C. J. & Kylafis, N. D., eds. 1991, in: The physics of star formation and early stellar evolution

Lada, C. J. & Lada, E. A. 2003, ARA&A, 41, 57

Langer, W. D. & Penzias, A. A. 1990, ApJ, 357, 477

Langer, W. D., van Dishoeck, E. F., Bergin, E. A., et al. 2000, Protostars and Planets IV, 29

Levreault, R. M. 1988, ApJS, 67, 283

Linke, R. A., Goldsmith, P. F., Wannier, P. G., Wilson, R. W., & Penzias, A. A. 1977, ApJ, 214, 50

Lis, D. C., Roueff, E., Gerin, M., et al. 2002, ApJ, 571, L55

Liu, X.-L., Wang, J.-J., & Xu, J.-L. 2013, MNRAS, 431, 27

Loinard, L., Castets, A., Ceccarelli, C., Caux, E., & Tielens, A. G. G. M. 2001, ApJ, 552, L163

Loinard, L., Castets, A., Ceccarelli, C., et al. 2002, Planet. Space Sci., 50, 1205

López-Sepulcre, A., Cesaroni, R., & Walmsley, C. M. 2010, A&A, 517, A66

López-Sepulcre, A., Walmsley, C. M., Cesaroni, R., et al. 2011, A&A, 526, L2

Lynga, G. 1982, A&A, 109, 213

MacLaren, I., Richardson, K. M., & Wolfendale, A. W. 1988, ApJ, 333, 821

Maíz Apellániz, J., Walborn, N. R., Morrell, N. I., Niemela, V. S., & Nelan, E. P. 2007, ApJ, 660, 1480

Mangum, J. G., Wootten, A., & Mundy, L. G. 1992, ApJ, 388, 467

Marston, A. P., Reach, W. T., Noriega-Crespo, A., et al. 2004, ApJS, 154, 333

Mason, B. D., Gies, D. R., Hartkopf, W. I., et al. 1998, AJ, 115, 821

Massey, P., DeGioia-Eastwood, K., & Waterhouse, E. 2001, AJ, 121, 1050

Massi, F., Brand, J., & Felli, M. 1997, A&A, 320, 972

Massi, F., Lorenzetti, D., & Giannini, T. 2003, A&A, 399, 147

Massi, F., Testi, L., & Vanzi, L. 2006, A&A, 448, 1007

McKee, C. F. & Tan, J. C. 2003, ApJ, 585, 850

McKee, C. F., Zweibel, E. G., Goodman, A. A., & Heiles, C. 1993, in Protostars and Planets III, eds. E. H. Levy & J. I. Lunine, p. 327

Menten, K. M., Pillai, T., & Wyrowski, F. 2005, in Massive Star Birth: A Crossroads of Astrophysics, eds. R. Cesaroni, M. Felli, E. Churchwell, & M. Walmsley, Vol. 227 of IAU Symposium, pp. 23–34

Miettinen, O. 2013, ArXiv e-prints; arXiv:1311.4300

Miettinen, O., Hennemann, M., & Linz, H. 2011, A&A, 534, A134

Milam, S. N., Savage, C., Brewster, M. A., Ziurys, L. M., & Wyckoff, S. 2005, ApJ, 634, 1126

Millar, T. J., Bennett, A., & Herbst, E. 1989, ApJ, 340, 906

Mizuno, A., Onishi, T., Yonekura, Y., et al. 1995, ApJ, 445, L161

Molinari, S., Brand, J., Cesaroni, R., & Palla, F. 1996, A&A, 308, 573

Molinari, S., Brand, J., Cesaroni, R., Palla, F., & Palumbo, G. G. C. 1998a, A&A, 336, 339

Molinari, S., Pezzuto, S., Cesaroni, R., et al. 2008, A&A, 481, 345

Molinari, S., Swinyard, B., Bally, J., et al. 2010, PASP, 122, 314

Molinari, S., Testi, L., Brand, J., Cesaroni, R., & Palla, F. 1998b, ApJ, 505, L39

Morales Ortiz, J. L., Olmi, L., Burton, M., et al. 2012, A&A, 543, A65

Motte, F., Bontemps, S., Schilke, P., et al. 2007, A&A, 476, 1243

Mottram, J. C., Hoare, M. G., Urquhart, J. S., et al. 2011, A&A, 525, A149

Mueller, K. E., Shirley, Y. L., Evans, II, N. J., & Jacobson, H. R. 2002, ApJS, 143, 469

Nguyen Luong, Q., Motte, F., Hennemann, M., et al. 2011, A&A, 535, A76

Noriega-Crespo, A., Morris, P., Marleau, F. R., et al. 2004, ApJS, 154, 352

Öberg, K. I., van Broekhuizen, F., Fraser, H. J., et al. 2005, ApJ, 621, L33

Offner, S. S. R., Robitaille, T. P., Hansen, C. E., McKee, C. F., & Klein, R. I. 2012, ApJ, 753, 98

Olmi, L., Anglés-Alcázar, D., De Luca, M., et al. 2010, ApJ, 723, 1065

Ossenkopf, V. & Henning, T. 1994, A&A, 291, 943

Palla, F., Brand, J., Comoretto, G., Felli, M., & Cesaroni, R. 1991, A&A, 246, 249

Palla, F. & Stahler, S. W. 1999, ApJ, 525, 772

Panagia, N. & Walmsley, C. M. 1978, A&A, 70, 411

Parker, R. J. & Meyer, M. R. 2012, MNRAS, 427, 637

Perault, M., Omont, A., Simon, G., et al. 1996, A&A, 315, L165

Pişmiş, P. 1959, Boletin de los Observatorios Tonantzintla y Tacubaya, 2, 37

Pilbratt, G. L., Riedinger, J. R., Passvogel, T., et al. 2010, A&A, 518, L1

Pillai, T., Wyrowski, F., Carey, S. J., & Menten, K. M. 2006, A&A, 450, 569

Poglitsch, A., Waelkens, C., Geis, N., et al. 2010, A&A, 518, L2

Prantzos, N., Aubert, O., & Audouze, J. 1996, A&A, 309, 760

Price, S. D., Egan, M. P., Carey, S. J., Mizuno, D. R., & Kuchar, T. A. 2001, AJ, 121, 2819

Purcell, C. R., Hoare, M. G., Cotton, W. D., et al. 2013, ApJS, 205, 1

Rathborne, J. M., Jackson, J. M., Chambers, E. T., et al. 2005, ApJ, 630, L181

Rathborne, J. M., Jackson, J. M., & Simon, R. 2006, ApJ, 641, 389

Reid, M. J., Menten, K. M., Zheng, X. W., et al. 2009, ApJ, 700, 137

Rieke, G. H. & Lebofsky, M. J. 1985, ApJ, 288, 618

Robitaille, T. P., Meade, M. R., Babler, B. L., et al. 2008, AJ, 136, 2413

Robitaille, T. P., Whitney, B. A., Indebetouw, R., & Wood, K. 2007, ApJS, 169, 328

Robitaille, T. P., Whitney, B. A., Indebetouw, R., Wood, K., & Denzmore, P. 2006, ApJS, 167, 256

Rosolowsky, E., Dunham, M. K., Ginsburg, A., et al. 2010, ApJS, 188, 123

Roueff, E., Tiné, S., Coudert, L. H., et al. 2000, A&A, 354, L63

Rowan-Robinson, M. 1980, ApJS, 44, 403

Russeil, D., Zavagno, A., Adami, C., et al. 2012, A&A, 538, A142

Rygl, K. L. J., Wyrowski, F., Schuller, F., & Menten, K. M. 2010, A&A, 515, A42

Rygl, K. L. J., Wyrowski, F., Schuller, F., & Menten, K. M. 2013, A&A, 549, A5

Sánchez-Monge, Á., Beltrán, M. T., Cesaroni, R., et al. 2013a, A&A

Sánchez-Monge, Á., Palau, A., Fontani, F., et al. 2013b, MNRAS, 432, 3288

Saraceno, P., Andre, P., Ceccarelli, C., Griffin, M., & Molinari, S. 1996, A&A, 309, 827

Scalo, J. 1998, in The Stellar Initial Mass Function (38th Herstmonceux Conference), eds. G. Gilmore & D. Howell, Vol. 142 of Astronomical Society of the Pacific Conference Series, p. 201

Scheffler, H. 1982, in Landolt-Bornstein: Group 6: Astronomy, eds. P. Biermann, H. H. Fink, K. J. Fricke, W. Gliese, M. Grewing, W. K. Huchtmeier, B. F. Madore, H. Netzer, J. Rahe, H. Scheffler, L. D. Schmadel, J. Schmid-Burgk, G. A. Tammann, J. Trãmper, R. Wielen, A. Witzel, & G. Zech, p. 45

Schuller, F., Menten, K. M., Contreras, Y., et al. 2009, A&A, 504, 415

Shu, F. H., Adams, F. C., & Lizano, S. 1987, ARA&A, 25, 23

Simon, R. 1997, PhD thesis, University of Cologne

Smith, A. F. M. & Roberts, G. O. 1993, Journal Royal Statistical Society, Series B, 55, 2

Smith, R. J., Longmore, S., & Bonnell, I. 2009, MNRAS, 400, 1775

Snider, K. D., Hester, J. J., Desch, S. J., Healy, K. R., & Bally, J. 2009, ApJ, 700, 506

Spitzer, L. 1978, Physical processes in the interstellar medium, ed. John Wiley & Sons

Straižys, V. & Laugalys, V. 2008, Baltic Astronomy, 17, 143

Stutzki, J. & Güsten, R. 1990, ApJ, 356, 513

Swinyard, B. M., Ade, P., Baluteau, J.-P., et al. 2010, A&A, 518, L4

Tackenberg, J., Beuther, H., Henning, T., et al. 2012, A&A, 540, A113

Tafalla, M., Myers, P. C., Caselli, P., & Walmsley, C. M. 2004, A&A, 416, 191

Tafalla, M., Myers, P. C., Caselli, P., Walmsley, C. M., & Comito, C. 2002, ApJ, 569, 815

Testi, L., Felli, M., Persi, P., & Roth, M. 1998, A&AS, 129, 495

Thompson, R. I. 1984, ApJ, 283, 165

Tielens, A. G. G. M. & Hollenbach, D. 1985, ApJ, 291, 722

Urquhart, J. S., Hoare, M. G., Lumsden, S. L., Oudmaijer, R. D., & Moore, T. J. T. 2008, in Massive Star Formation: Observations Confront Theory, eds. H. Beuther, H. Linz, & T. Henning, Vol. 387 of Astronomical Society of the Pacific Conference Series, p. 381

Urquhart, J. S., Moore, T. J. T., Schuller, F., et al. 2013a, MNRAS, 431, 1752

Urquhart, J. S., Morgan, L. K., Figura, C. C., et al. 2011, MNRAS, 418, 1689

Urquhart, J. S., Thompson, M. A., Moore, T. J. T., et al. 2013b, MNRAS, 435, 400

van der Tak, F. F. S., Black, J. H., Schöier, F. L., Jansen, D. J., & van Dishoeck, E. F. 2007, A&A, 468, 627

van der Tak, F. F. S., Chavarría, L., Herpin, F., et al. 2013, A&A, 554, A83

van der Tak, F. F. S. & Menten, K. M. 2005, A&A, 437, 947

Vasyunina, T., Linz, H., Henning, T., et al. 2009, A&A, 499, 149

Vazquez-Semadeni, E. 2009, ArXiv e-prints; arXiv:0902.0820

Visser, R., van Dishoeck, E. F., & Black, J. H. 2009, A&A, 503, 323

Walborn, N. R. & Parker, J. W. 1992, ApJ, 399, L87

Walsh, B. 2004, retrieved from `http://web.mit.edu/~wingated/www/introductions/mcmc-gibbs-intro.pdf`

Wang, J., Townsley, L. K., Feigelson, E. D., et al. 2007, ApJS, 168, 100

Ward-Thompson, D., Scott, P. F., Hills, R. E., & Andre, P. 1994, MNRAS, 268, 276

Weidner, C. & Vink, J. S. 2010, A&A, 524, A98+

Wielen, R. & Wilson, T. L. 1997, A&A, 326, 139

Wienen, M., Wyrowski, F., Schuller, F., et al. 2012, A&A, 544, A146

Williams, J. P. & Cieza, L. A. 2011, ARA&A, 49, 67

Wilson, T. L., Rohlfs, K., & Huettermeister, S. 2005, Tools of Radio Astronomy, ed. Springer

Wilson, T. L. & Rood, R. 1994, ARA&A, 32, 191

Wolfire, M. G. & Cassinelli, J. P. 1986, ApJ, 310, 207

Wolfire, M. G. & Cassinelli, J. P. 1987, ApJ, 319, 850

Wouterloot, J. G. A., Henkel, C., Brand, J., & Davis, G. R. 2008, A&A, 487, 237

Wright, E. L., Eisenhardt, P. R. M., Mainzer, A. K., et al. 2010, AJ, 140, 1868

Wu, Y., Zhang, Q., Yu, W., et al. 2006, A&A, 450, 607

Young, E. D., Gounelle, M., Smith, R. L., Morris, M. R., & Pontoppidan, K. M. 2011, ApJ, 729, 43

Zavagno, A., Deharveng, L., Comerón, F., et al. 2006, A&A, 446, 171

Zhang, Q., Wang, Y., Pillai, T., & Rathborne, J. 2009, ApJ, 696, 268

Zielinsky, M. 1999, PhD thesis, Köln; `http://www.astro.uni-koeln.de/list/publications/year=1999&category=Astronomical/`

Zinchenko, I., Caselli, P., & Pirogov, L. 2009, MNRAS, 395, 2234

Zinnecker, H. & Yorke, H. W. 2007, ARA&A, 45, 481

Appendix A

Rules of probability

In this Appendix I give proof of the simple probability rules given in Sect. 2.2.1 (Equations from 2.4 to 2.8):

$$P(\mathrm{E}) = 1 - P(\overline{\mathrm{E}});$$

Demonstration:

The events E and its complement $\overline{\mathrm{E}}$ are disjoint

$$\mathrm{E} \cap \overline{\mathrm{E}} = \emptyset,$$

and their union is equal to U

$$\mathrm{E} \cup \overline{\mathrm{E}} = \mathrm{U}.$$

Using the second and third axioms of probability (see Sect. 2.2.1) we get:

$$P(\mathrm{E} \cup \overline{\mathrm{E}}) = P(\mathrm{E}) + P(\overline{\mathrm{E}}) = P(\mathrm{U}) = 1 \Rightarrow P(\mathrm{E}) = 1 - P(\overline{\mathrm{E}}).$$

$$P(\emptyset) = 0; \tag{A.1}$$

Demonstration:

The complement of U, $\overline{\mathrm{U}}$ is equal to the empty set

$$\overline{\mathrm{U}} = \emptyset,$$

and again, U and $\overline{\mathrm{U}}$ are disjoint, and their union is U

$$\mathrm{U} \cup \overline{\mathrm{U}} = \mathrm{U},$$

$$U \cap \overline{U} = \emptyset.$$

Therefore

$$P(U) = P(U) + P(\overline{U}) \Rightarrow P(\emptyset) = 0.$$

$$P(A \cup B) = P(A) + P(B) - P(A \cap B); \tag{A.2}$$

Demonstration:
We can write the union of A and B as:

$$A \cup B = A \cup (\overline{A} \cap B),$$

and B as:

$$B = (B \cap \overline{A}) \cup (A \cap B).$$

Because the events are disjoint, we can write, using the third axiom

$$P(A \cup B) = P(A) + P(\overline{A} \cap B)$$

and

$$P(B) = P(B \cap \overline{A}) + P(A \cap B).$$

Combining these expressions we get:

$$P(A \cup B) = P(A) + P(B) - P(A \cap B);$$

$$P(A \cup B) \geq P(A \cap B); \tag{A.3}$$

Demonstration:
Rewriting $A \cup B$

$$A \cup B = [(A \cap \overline{B}) \cup (\overline{A} \cap B)] \cup (A \cap B),$$

and using the third axiom

$$P(A \cup B) = P([(A \cap \overline{B}) \cup (\overline{A} \cap B)]) + P(A \cap B),$$

and finally, using the first axiom we get

$$P(\mathrm{A} \cup \mathrm{B}) \geq P(\mathrm{A} \cap \mathrm{B}),$$

When B is a subset of A, as in Fig. 2.1:

$$P(\mathrm{A}) \geq P(\mathrm{B}). \tag{A.4}$$

Demonstration:
We can simply rewrite A and B as:

$$\mathrm{A} = \mathrm{A} \cup \mathrm{B}$$

$$\mathrm{B} = \mathrm{A} \cap \mathrm{B}.$$

A can also be written in the following way:

$$\mathrm{A} = (\mathrm{A} \cap \overline{\mathrm{B}}) \cup (\mathrm{A} \cap \mathrm{B}).$$

Making use of the first and third axioms and substituting we obtain the result

$$P(\mathrm{A}) = P(\mathrm{A} \cap \overline{\mathrm{B}}) + P(\mathrm{A} \cap \mathrm{B}) \geq P(\mathrm{A} \cap \mathrm{B}) = P(\mathrm{B}).$$

Appendix B

Appendices to Chapter 3

B.1 Comments on individual sources

B.1.1 16061−5048c4 and 16435−4515c3

16061−5048c4 is included in the SFS due to the presence of a water maser. No clear mid-IR emission can be seen in the Spitzer images, suggesting that this is a clump in a very early stage of evolution or with a very high extinction.

For example, Breen & Ellingsen (2011) suggest that a maser is one of the first signs of active star formation to appear. This is because the maser is likely excited by the outflow, the onset of which happens in a phase where the mid-IR emission may still be too weak or too extincted to be detected. This seems to be consistent with the position of this source in the M-L plot. This is, in fact, one of the objects with the lowest kinetic temperature in the SFS and with a very low luminosity.

However, 16061−5048c4, in addition to the maser, shows a clear detection in the radio-continuum emission. Visual inspection of the radio image shows an elongated morphology of the emission at this wavelength, following closely the shape of the mm-clump, and displaced towards South-East. We conclude that this is not a compact HII region produced by the central YSO, but an ionisation front generated by a nearby massive star (most likely the corresponding IRAS source), rather than by the YSO.

A similar situation is observed in 16435−4515c3. This clump shows no signs of active star formation, apart from radio emission. It could be that also in this case this emission comes from an ionisation front outside the clump. In any case, this source was excluded from the analysis because the $NH_3(2,2)$ was not detected.

B.1.2 17355−3241c1

As evolution proceeds, the massive ZAMS star delivers huge quantities of ionising photons and energetic particles into the parent molecular cloud. This process disperses the clump, leaving only remnants of the original cloud, around an HII region.

17355−3241c1 is the most evolved source in our sample, as can be seen in the mass-luminosity plot. This is the only Type 3 source in our sample, with still a detectable 1.2 mm flux, but with dominant IR-emission.

The properties of this clump appear to confirm the evolutionary scenario: it has the lowest mass, column and surface density of the entire sample, and a high temperature and luminosity. In addition, the L/M ratio and the virial parameter α are the highest among all the observed clumps, above 120 $L_\odot\ M_\odot{}^{-1}$ and ~ 3.5, respectively. The high value of the virial parameter could be due to the destructive action of the central ZAMS star, dispersing the clump from which it was formed. On the other hand, this object does not show compact radio-continuum emission. The $M-L$ plot shows that the mass of the central ZAMS star should be $M \sim 6\ M_\odot$, corresponding to a B5 star, comparing its position in the $M-L$ plot with the evolutionary tracks. The output of Lyman continuum photons of such a star is low, and below the detection limit of the radio observations (cf. Thompson 1984; Sánchez-Monge et al. 2013a). However the uncertainty on the stellar mass is quite large. The SED fit with Robitaille models suggests a stellar mass of $\sim 8\ M_\odot$. Another possibility to explain the lack of radio continuum emission is that it is extended and filtered out by the interferometer. Finally, we remind that in both cases the stellar mass is an upper limit, under the assumption that the luminosity is dominated by the most massive object.

The SED of this object is different from that typical of the other objects with appreciable emission in the mid-IR, being almost flat in terms of energy up to 3.6 μm. Also the Robitaille model indicates that this is an older object.

B.1.3 Undetected sources

A number of sources do not have detections in ammonia, especially in the (2,2) transition. Among the SFS, they are weak also in (1,1), suggesting low beam-averaged NH_3 column densities. 16164−4929c2 and 14166−6118c1 have a clear detection at 1.2 mm, but no ammonia counterpart. NIR images show that these two objects contain a star cluster. The SED, the morphology of the IR emission and radio-continuum observations of these two clumps show that they host a

massive ZAMS star, that has already developed an HII region, different from the nearby clumps detected in ammonia. 13563−6109c1 also shows signs of the presence of a recognisable embedded cluster in NIR images, even if not as clear as 16164−4929c2 and 14166−6118c1.

On the other hand, four more sources with similar properties are found in the QS, but without clear signs of an embedded cluster. Two of these have quite strong NH_3(1,1) detections, indicating very low gas temperatures. These clumps might be just too cold to be detected in (2,2) or simply not massive enough to form stars with $M > 8$ $M_\odot$.

Finally, also 15454−5335c2 was not detected in ammonia. This source was identified at the edge of the SEST map. No IR source was found to be associated with it. The non-detection in NH_3 and visual inspection of the SEST map suggest that this might be just a noise spike in the SEST 1.2 mm continuum map.

B.2 SED fits

The modified black-body fit was done with a simple Bayesian approach, considering Gaussian uncertainties on the fluxes, taking into account the rms of the image and the calibration uncertainty at each wavelength (15% for SEST and SPIRE, 20% for PACS red and 10% for PACS blue fluxes: Beltrán et al. 2006; Swinyard et al. 2010; Poglitsch et al. 2010). We adopted a modified black-body as a model, comparing the observed and predicted fluxes at each wavelength, and multiplying the probability for each point, to obtain the total probability of the model. We took a constant *prior* on the mass, while we used a Gaussian *prior* on β, with mean value $\mu = 2$ and standard deviation $\sigma = 2$, and on the dust temperature T_d, with $\mu = 20$ K and $\sigma = 15$ K. In detail, the expression used is:

$$P(T_\mathrm{d}, M, \beta | D, model) = \frac{1}{\varphi} P(D|model, T_\mathrm{d}, M, \beta)\, P(T_\mathrm{d}, M, \beta|model), \qquad \text{(B.1)}$$

where φ is the usual normalisation constant, $P(T_\mathrm{d}, M, \beta|model)$ is the prior on the three parameters of the model, as described earlier, and $P(D|model, T_\mathrm{d}, M, \beta)$ is the likelihood, calculated according to the expression

$$P(D|model, T_\mathrm{d}, M, \beta) = \frac{1}{\psi} \prod_{6}^{i=1} (\mathrm{e}^{-(F_\mathrm{i} - F_\mathrm{mod,i})^2/(2\sigma^2_\mathrm{F,i})}). \qquad \text{(B.2)}$$

In Eq. B.2 ψ is the normalisation constant, F_i are the measured fluxes at the wavelengths observed with Herschel and SEST, $\sigma_{F,i}$ are the uncertainties associated with

each measurement, and $F_{mod,i}$ are the predicted fluxes. We considered temperatures between 5 and 50 K in 200 equal linear steps, masses between 10 and 10000 $M_\odot$ in 200 equal logarithmic steps, and β between 0.1 and 4, in 40 equal linear steps. Outside this range, the *prior* is set to 0. To test the dependence of the fit on the choice of *prior*, we also tried to use a constant *prior* on all the parameters of the fit. The results show that $T_{\rm d}$, M and β are not sensitive to this choice, within the uncertainties. To derive the probability distribution, and thus the uncertainty on the single parameters we integrated over the other two parameters.

B.3 Tables and figures

Table B.1: Properties of each clump, averaged within the FWHM contour. The columns show respectively: clump name, mass, volume- and column-density of H_2, mass surface density, with their 68% credibility interval, and the beam-corrected diameters of the clumps. The clumps above the horizontal line are those classified as star-forming, while the clumps below it are those classified as quiescent.

Clump	M	68% int.	$n(H_2)$	68% int.	$N(H_2)$	68% int.	Σ	68% int.	Diameter	Notes
	($10^2 \times M_\odot$)		($10^4 \times$ cm^{-3})		($10^{22} \times$ cm^{-2})		($10^{-1} \times$ g cm^{-2})		(pc)	
08477−4359c1	1.1	0.7 – 1.2	26.0	17.8 – 30.5	9.0	6.1 – 10.5	2.29	1.57 – 2.69	0.3	
12300−6119c1	1.4	1.1 – 1.7	10.5	7.9 – 12.4	5.4	4.1 – 6.4	1.39	1.04 – 1.64	0.5	
13560−6133c1	4.5	2.5 – 5.7	41.5	22.7 – 52.5	19.9	10.9 – 25.1	5.09	2.79 – 6.43	0.5	
15072−5855c1	0.6	0.3 – 0.8	10.8	5.5 – 13.5	4.2	2.1 – 5.3	1.07	0.54 – 1.35	0.4	
15278−5620c1	5.9	4.7 – 6.9	187.0	150.0 – 220.0	59.0	47.4 – 69.7	15.10	12.10 – 17.80	0.3	
15278−5620c2	1.7	1.3 – 2.0	5.1	4.0 – 6.1	3.5	2.8 – 4.2	0.90	0.71 – 1.08	0.7	
15470−5419c1	2.5	1.2 – 3.1	22.4	10.3 – 27.3	10.8	5.0 – 13.2	2.77	1.27 – 3.38	0.5	
15470−5419c3	5.0	4.1 – 5.8	4.0	3.3 – 4.6	4.3	3.6 – 5.0	1.11	0.91 – 1.28	1.1	
15557−5215c1	7.3	3.1 – 9.0	20.9	8.7 – 25.5	14.8	6.1 – 18.0	3.78	1.57 – 4.62	0.7	
15557−5215c2	3.7	2.9 – 4.4	13.0	10.1 – 15.5	8.5	6.7 – 10.2	2.19	1.70 – 2.61	0.7	
15579−5303c1	2.7	2.3 – 3.2	38.0	31.7 – 43.8	15.8	13.2 – 18.3	4.06	3.39 – 4.68	0.4	
16061−5048c1	2.1	1.6 – 2.6	36.5	26.7 – 44.5	14.2	10.4 – 17.3	3.63	2.66 – 4.43	0.4	
16061−5048c2	2.9	2.4 – 3.3	22.3	18.5 – 26.1	11.3	9.3 – 13.2	2.89	2.39 – 3.37	0.5	
16061−5048c4	3.6	2.9 – 4.3	5.6	4.6 – 6.6	4.9	4.0 – 5.8	1.25	1.01 – 1.47	0.9	
16093−5015c1	22.1	17.0 – 25.5	2.9	2.2 – 3.3	5.7	4.4 – 6.6	1.46	1.13 – 1.69	2.0	
16093−5128c1	5.6	4.5 – 6.6	13.5	10.8 – 15.9	10.1	8.0 – 11.8	2.58	2.06 – 3.03	0.8	
16093−5128c8	8.5	2.2 – 10.0	1.9	0.5 – 2.2	3.1	0.8 – 3.7	0.81	0.21 – 0.95	1.7	
16254−4844c1	1.3	0.9 – 1.7	43.2	30.9 – 55.8	13.6	9.7 – 17.5	3.47	2.49 – 4.49	0.3	(1)
16428−4109c1	1.9	1.5 – 2.2	13.8	10.9 – 15.6	7.2	5.6 – 8.1	1.83	1.44 – 2.07	0.5	
16428−4109c2	1.5	1.3 – 1.7	8.3	7.1 – 9.5	4.7	4.0 – 5.4	1.21	1.03 – 1.38	0.6	
16573−4214c2	1.1	0.8 – 1.3	174.0	128.0 – 208.0	32.2	23.6 – 38.4	8.25	6.04 – 9.84	0.2	(1)
17040−3959c1	0.4	0.3 – 0.5	47.5	38.0 – 56.0	9.7	7.7 – 11.4	2.47	1.98 – 2.91	0.2	(2)
17195−3811c1	2.3	1.1 – 2.7	10.9	5.1 – 13.2	6.5	3.0 – 7.8	1.65	0.78 – 2.00	0.6	
17195−3811c2	2.9	2.4 – 3.3	14.0	11.7 – 15.7	8.3	6.9 – 9.3	2.13	1.78 – 2.38	0.6	
17195−3811c3	3.7	3.0 – 4.2	5.0	4.0 – 5.7	4.5	3.7 – 5.2	1.15	0.94 – 1.33	0.9	
17355−3241c1	0.15	0.1 – 0.2	3.3	2.5 – 3.9	1.2	0.9 – 1.5	0.31	0.24 – 0.37	0.4	
13560−6133c2	4.5	1.4 – 5.5	20.1	6.4 – 24.8	12.2	3.9 – 15.1	3.13	1.00 – 3.86	0.6	
14166−6118c2	1.1	0.7 – 1.3	7.6	5.3 – 9.1	4.0	2.8 – 4.8	1.01	0.71 – 1.22	0.5	
14183−6050c3	4.2	1.8 – 4.7	5.2	2.2 – 5.9	4.9	2.1 – 5.5	1.25	0.53 – 1.40	1.0	
15038−5828c1	1.6	1.2 – 1.9	24.9	18.7 – 29.8	10.0	7.5 – 12.0	2.56	1.92 – 3.07	0.4	
15470−5419c4	4.8	2.6 – 6.1	4.3	2.4 – 5.4	4.5	2.5 – 5.7	1.14	0.63 – 1.45	1.1	
15557−5215c3	2.1	1.6 – 2.5	1.6	1.2 – 2.0	1.8	1.4 – 2.1	0.45	0.34 – 0.55	1.1	
15579−5303c3	5.1	2.9 – 6.3	10.2	5.8 – 12.7	8.1	4.6 – 10.1	2.08	1.18 – 2.57	1.1	
16093−5128c2	3.6	2.4 – 4.4	6.6	4.5 – 8.1	5.4	3.7 – 6.6	1.37	0.93 – 1.69	0.8	
16164−4929c3	3.2	2.1 – 4.0	7.3	4.7 – 9.1	5.6	3.6 – 6.9	1.43	0.92 – 1.78	0.8	
16482−4443c2	0.4	0.2 – 0.5	47.4	19.6 – 57.0	10.0	4.1 – 12.0	2.56	1.06 – 3.08	< 0.2	(3)

Notes. (1) Source with very poor uv-coverage in NH_3: spectrum extracted from non-cleaned maps.
(2) Lower limit for the mass and the derived quantities.
(3) Volume-, column- and surface-densities are lower limits, as the source is unresolved.

Table B.2: Properties of each clump, averaged within the 3σ contour. The columns show respectively: clump name, mass, volume- and column-density of H_2, mass surface density, with their 68% credibility interval, and the diameters of the clumps. The clumps above the horizontal line are those classified as star-forming, while the clumps below it are those classified as quiescent.

Clump	M	68% int.	$n(H_2)$	68% int.	$N(H_2)$	68% int.	Σ	68% int.	Diameter	Notes
	($10^2 \times M_\odot$)		($10^4 \times$ cm^{-3})		($10^{22} \times$ cm^{-2})		($10^{-1} \times$ g cm^{-2})		(pc)	
08477−4359c1	2.3	1.7 – 2.6	4.1	3.1 – 4.6	3.4	2.5 – 3.8	0.87	0.65 – 0.98	0.8	
12300−6119c1	2.7	2.0 – 3.2	1.8	1.4 – 2.1	2.1	1.6 – 2.5	0.53	0.40 – 0.63	1.2	
13560−6133c1	12.0	8.2 – 16.0	1.7	1.1 – 2.1	3.3	2.2 – 4.2	0.85	0.56 – 1.10	2.0	
15072−5855c1	1.4	0.8 – 1.8	2.0	1.0 – 2.5	1.8	0.9 – 2.3	0.46	0.24 – 0.58	0.9	
15278−5620c1	14.0	12.0 – 17.0	2.8	2.3 – 3.3	4.9	4.0 – 5.6	1.20	1.00 – 1.40	1.8	
15278−5620c2	3.0	2.6 – 3.3	1.6	1.4 – 1.8	2.0	1.8 – 2.2	0.51	0.45 – 0.57	1.3	
15470−5419c1	5.0	2.5 – 6.0	3.0	1.5 – 3.6	3.6	1.8 – 4.3	0.91	0.45 – 1.10	1.2	
15470−5419c3	11.0	10.0 – 11.0	1.0	1.0 – 1.1	2.2	2.2 – 2.4	0.57	0.55 – 0.61	2.2	
15557−5215c1	21.0	10.0 – 26.0	2.4	1.2 – 2.9	4.9	2.5 – 6.1	1.30	0.63 – 1.60	2.1	
15557−5215c2	8.4	7.5 – 9.5	1.4	1.2 – 1.6	2.5	2.3 – 2.9	0.65	0.58 – 0.73	1.9	
15579−5303c1	8.1	7.8 – 8.7	1.2	1.2 – 1.3	2.3	2.2 – 2.5	0.60	0.57 – 0.63	1.9	
16061−5048c1	5.2	4.3 – 6.2	1.7	1.4 – 2.0	2.5	2.1 – 3.0	0.64	0.53 – 0.76	1.5	
16061−5048c2	5.7	4.9 – 6.7	2.8	2.4 – 3.3	3.6	3.1 – 4.2	0.92	0.79 – 1.10	1.3	
16061−5048c4	6.3	5.7 – 6.7	1.9	1.7 – 2.0	2.8	2.5 – 3.0	0.71	0.65 – 0.77	1.5	
16093−5015c1	54.2	48.2 – 59.1	0.4	0.3 – 0.5	2.0	1.8 – 2.2	0.51	0.45 – 0.56	5.3	
16093−5128c1	12.0	11.0 – 14.0	2.1	1.9 – 2.3	3.8	3.4 – 4.2	0.97	0.86 – 1.10	1.9	
16093−5128c8	10.0	3.4 – 12.0	1.2	0.4 – 1.4	2.5	0.8 – 3.0	0.65	0.21 – 0.76	2.1	
16254−4844c1	2.3	1.9 – 3.0	2.3	1.9 – 3.0	2.3	1.9 – 3.0	0.60	0.48 – 0.77	1.0	(1)
16428−4109c1	8.1	6.6 – 9.3	1.1	0.9 – 1.2	2.1	1.7 – 2.4	0.53	0.43 – 0.62	2.0	
16428−4109c2	4.8	4.2 – 5.6	0.8	0.7 – 1.0	1.5	1.3 – 1.8	0.39	0.34 – 0.45	1.8	
16573−4214c2	1.7	1.4 – 2.0	8.8	7.2 – 10.0	5.1	4.2 – 6.0	1.30	1.10 – 1.50	0.6	(1)
17040−3959c1	0.6	0.6 – 0.7	6.3	5.7 – 6.9	3.0	2.6 – 3.2	0.75	0.68 – 0.83	0.5	(2)
17195−3811c1	6.5	3.6 – 7.8	1.6	0.9 – 1.9	2.6	1.4 – 3.1	0.66	0.36 – 0.80	1.6	
17195−3811c2	8.3	8.0 – 8.5	2.1	2.0 – 2.1	3.3	3.2 – 3.4	0.85	0.81 – 0.86	1.6	
17195−3811c3	6.3	5.5 – 6.8	1.8	1.6 – 2.0	2.8	2.4 – 3.0	0.71	0.63 – 0.77	1.5	
17355−3241c1	0.3	0.2 – 0.3	1.7	1.4 – 1.9	0.9	0.8 – 1.0	0.24	0.20 – 0.27	0.6	
13560−6133c2	8.1	2.9 – 9.1	3.5	1.2 – 3.9	4.6	1.7 – 5.2	1.20	0.43 – 1.30	1.4	
14166−6118c2	1.4	1.1 – 1.6	5.1	3.9 – 6.0	3.3	2.5 – 3.9	0.85	0.65 – 0.99	0.7	
14183−6050c3	5.4	2.3 – 5.9	3.2	1.4 – 3.6	3.9	1.6 – 4.2	0.99	0.41 – 1.10	1.2	
15038−5828c1	4.6	3.8 – 5.3	2.2	1.9 – 2.5	2.9	2.4 – 3.2	0.73	0.61 – 0.83	1.3	
15470−5419c4	6.2	3.7 – 7.7	2.6	1.6 – 3.2	3.5	2.1 – 4.3	0.89	0.53 – 1.10	1.4	
15557−5215c3	2.0	1.7 – 2.4	1.6	1.3 – 1.8	1.7	1.4 – 2.0	0.44	0.37 – 0.51	1.1	
15579−5303c3	10.0	6.1 – 12.0	1.4	0.9 – 1.7	2.8	1.7 – 3.3	0.71	0.42 – 0.86	2.0	
16093−5128c2	5.1	3.7 – 5.9	2.7	2.0 – 3.1	3.3	2.5 – 3.9	0.86	0.63 – 0.99	1.3	
16164−4929c3	5.4	3.4 – 6.8	2.5	1.6 – 3.2	3.3	2.0 – 4.1	0.84	0.52 – 1.05	1.3	
16482−4443c2	0.8	0.3 – 1.0	7.8	3.1 – 9.3	3.7	1.5 – 4.4	0.94	0.38 – 1.10	0.5	

Notes. (1) Source with very poor uv-coverage in NH_3: spectrum extracted from non-cleaned maps.
(2) Lower limit for the mass and the derived quantities.

Table B.3: Summary of star formation signposts for all the observed clumps. The clumps above the horizontal line are those classified as star-forming, while the clumps below it are those classified as quiescent. For the "green fuzzies", the notation Y+ indicates multiple "green fuzzies" associated with the clump. In the last column we show the Type of the source (see Chapter 3).

Clump	24 μm Emission	MSX Emission	GF	1.3 cm-Continuum	H_2O Maser	Type
08477−4359c1	Y	Y?	...	N	N	...
08589−4714c1	Y	Y	...	N	Y	...
12300−6119c1	...	Y	...	N	N	...
13039−6331c1	Y	Y	N	N	N	...
13560−6133c1	Y	N	N	Y	Y	2
13563−6109c1	Y	Y	N	Y?	N	...
14166−6118c1	Y	Y	N	Y	N	...
15072−5855c1	Y	Y	Y	N	N	2
15278−5620c1	Y	Y	Y	Y	Y	2
15278−5620c2	Y	N	Y+	N	N	1
15470−5419c1	N	N	Y	N	Y	1
15470−5419c3	Y	N	Y+	N	Y	1
15557−5215c1	Y	Y	Y	N	Y[c]	2
15557−5215c2	Y	N	Y	N	Y	1
15579−5303c1	Y	Y	Y+	Y	Y	2
16061−5048c1	Y	N	Y+	Y	Y	2
16061−5048c2	Y	Y	Y+	Y	Y[c]	2
16061−5048c4	N	N	N	Y	Y	1
16093−5015c1	Y	Y	Y+	N	N[d]	1
16093−5128c1	Y	Y	N	Y	N	2
16093−5128c8	N	N	Y[b]	N	N	1
16164−4929c2	Y	Y	N	Y	N	...
16254−4844c1	Y	N	Y	Y	N[d]	1
16428−4109c1	...	Y	...	Y	N	...
16428−4109c2	...	Y	...	Y	N	...
16573−4214c2	Y	N	Y	N	Y[a]	1
17040−3959c1	Y	N	N	N	N	1
17195−3811c1	Y	Y	Y	N	Y[a]	2
17195−3811c2	Y	N	Y	Y?	Y[a]	...
17195−3811c3	Y	N	N	N	Y[a]	...
17355−3241c1	Y	Y	N	N	N	3
10088−5730c2	...	N	...	N	N	...
13560−6133c2	N	N	N	N	N	1
14166−6118c2	N	N	N	N	N	1
14183−6050c3	N	N	N	N	N	1
15038−5828c1	N	N	N	N	N	1
15454−5335c2	N	N	N	...	N	...
15470−5419c4	N	N	N	N	N	1
15557−5215c3	N	N	N	...	N	1
15579−5303c3	N	N	N	...	N	1
16093−5128c2	N	N	N	N	N	1
16164−4929c3	N	N	N	N	N	1
16164−4929c6	N	N	N	...	N	...
16164−4837c2	...	N	N	...	N	...
16435−4515c3	N	N	N	Y?	N	...
16482−4443c2	N	N	N	...	N	1

Notes. [(a)] These sources have poor uv-coverage, thus a firm assignment to a clump in the region was not possible. [(b)] Visual inspection of the mid-IR images showed that this GF could be generated by the Spitzer PSF. However, we still consider the clump as star forming to be conservative, and because of the presence of a strong 24 μm source within the 3σ contour of the 1.2 mm continuum emission, at the location of the GF. [(c)] Source detected in our work, but not in that of Sánchez-Monge et al. (2013a). [(d)] Source detected in the work of Sánchez-Monge et al. (2013a), but not in our work.

Table B.4: Mean and median values for temperatures, luminosity, dust emissivity index β, L/M ratio, gas properties and diameters of the clumps in the QS and the SFS averaged within the FWHM contour of the 1.2 mm continuum emission. The pairs of columns show respectively: kinetic temperature, dust temperature, mass, diameter, column density, volume density, surface density, luminosity, dust emissivity index and L/M ratio.

Param.	T_K (K)		T_d (K)		M ($M_\odot$)		D (pc)		$N(H_2)$ ($10^{22} \times$ cm^{-2})		$n(H_2)$ ($10^5 \times$ cm^{-3})		Σ (g cm^{-2})		L ($10^2 \times L_\odot$)		β		L/M ($L_\odot/M_\odot$)	
	SFS	QS	SFS	QS	SFS	QS	SFS	QS	SFS	QS	SFS	QS	SFS	QS	SFS	QS	SFS	QS	SFS	QS
Mean	$19.5^{+1.5}_{-2.9}$	$14.1^{+1.8}_{-3.2}$	$19.6^{+1.4}_{-1.6}$	$11.8^{+1.7}_{-1.5}$	370^{+70}_{-120}	310^{+70}_{-140}	0.6	0.8	$11.2^{+2.2}_{-3.2}$	$5.8^{+1.3}_{-2.5}$	$3.0^{+0.6}_{-0.8}$	$0.9^{+0.2}_{-0.4}$	$0.29^{+0.06}_{-0.08}$	$0.15^{+0.03}_{-0.06}$	$53.6^{+7.9}_{-8.2}$	$2.3^{+0.6}_{-0.9}$	$1.9^{+0.2}_{-0.2}$	$2.4^{+0.3}_{-0.4}$	$18.9^{+13.4}_{-5.6}$	$0.9^{+1.0}_{-0.5}$
Median	18.7	14.0	19.9	11.1	260	340	0.5	0.8	8.4	4.9	1.4	0.7	0.22	0.13	15.2	2.3	1.9	2.6	6.5	0.8

Table B.5: Mean and median values for temperatures, luminosity, L/M ratio, gas properties and diameters averaged within the FWHM contour of the 1.2 mm continuum emission of the clumps in the SFS, divided in SFS-1 and SFS-2. The pairs of columns show respectively: kinetic temperature, dust temperature, diameter, column density, volume density, surface density, luminosity and L/M ratio.

Param.	T_K (K)		T_d (K)		D (pc)		$N(H_2)$ ($10^{22} \times$ cm^{-2})		$n(H_2)$ ($10^5 \times$ cm^{-3})		Σ (g cm^{-2})		L ($10^2 \times L_\odot$)		L/M ($L_\odot/M_\odot$)	
	SFS-2	SFS-1	SFS-2	SFS-1	SFS-2	SFS-1	SFS-2	SFS-1	SFS-2	SFS-1	SFS-2	SFS-1	SFS-2	SFS-1	SFS-2	SFS-1
Mean	$21.3^{+1.7}_{-3.8}$	$18.3^{+1.4}_{-3.0}$	$23.6^{+1.5}_{-1.6}$	$15.2^{+1.4}_{-1.5}$	0.7	0.7	$16.1^{+3.2}_{-4.6}$	$10.1^{+2.1}_{-3.0}$	$3.8^{+0.7}_{-1.0}$	$3.5^{+0.7}_{-1.0}$	$0.41^{+0.08}_{-0.12}$	$0.26^{+0.05}_{-0.08}$	$101.7^{+15.0}_{-15.0}$	$3.9^{+0.6}_{-0.8}$	$24.4^{+20.3}_{-7.8}$	$2.1^{+1.3}_{-0.7}$
Median	21.4	18.3	23.8	16.0	0.5	0.7	12.8	8.5	2.2	1.3	0.33	0.22	83.0	3.5	24.2	1.6

Table B.6: Parameters of the ammonia spectra averaged over the whole $NH_3(1,1)$ area of emission. The columns indicate the clump name, the peak flux of the (1,1) transition and the rms of the spectrum, the V_{LSR} of the emission, the ΔV of $NH_3(1,1)$, the peak flux of the (2,2) transition and the rms of the spectrum, and the ΔV of $NH_3(2,2)$, T_{rot}, T_K and ammonia column density, with their uncertainties. The clumps above the horizontal line are those classified as star-forming, while the clumps below it are those classified as quiescent (see Sect. 3.6). Note that, contrary to Table 3.2, we do not include clumps not detected in $NH_3(1,1)$.

Source	$F_{max}(1,1)$	rms	V_{LSR}	$\Delta V(1,1)$	$F_{max}(2,2)$	rms	$\Delta V(2,2)$	T_{rot}	68% int.	T_K	68% int.	$N(NH_3)$	68% int.
	(mJy)	(mJy)	(km s^{-1})	(km s^{-1})	(mJy)	(mJy)	(km s^{-1})	(K)	(K)	(K)	(K)	(10^{14} × cm^{-2})	(10^{14} × cm^{-2})
08477-4359c1	156.4	5.0	11.0	1.6	56.9	4.0	1.6	15.8	15.3 – 16.2	18.1	17.1 – 18.6	7.79	7.16 – 8.41
08589-4714c1	32.7	3.0	5.5	1.4	…	3.0	…	–	–	–	–	–	–
12300-6119c1	61.5	4.0	–42.3	1.4	22.9	4.0	1.4	17.3	16.0 – 18.5	20.5	17.9 – 21.9	2.36	1.49 – 3.12
13039-6331c1	21.0	6.0	27.8	0.7	…	7.0	…	–	–	–	–	–	–
13560-6133c1	143.0	7.0	–56.6	1.6	73.4	7.0	1.6	16.7	12.2 – 18.8	19.9	13.4 – 22.4	10.90	7.64 – 12.70
13563-6109c1	47.1	4.0	–53.2	1.1	…	5.0	…	–	–	–	–	–	–
15072-5855c1	28.0	5.0	–40.2	0.7	…	5.0	…	–	–	–	–	–	–
15278-5620c1	215.1	9.0	–48.8	1.5	97.2	8.0	1.5	13.3	11.5 – 14.9	14.7	12.1 – 16.8	14.90	12.10 – 17.00
15278-5620c2	224.1	7.0	–48.7	1.4	125.4	8.0	1.4	14.8	13.6 – 16.1	16.8	14.6 – 18.5	17.40	15.50 – 18.60
15470-5419c1	171.5	8.0	–60.8	2.4	81.2	8.0	2.4	14.6	13.8 – 15.9	16.4	14.8 – 18.1	20.00	17.70 – 21.80
15470-5419c3	198.5	4.0	–61.1	2.4	82.9	5.0	2.4	15.9	13.5 – 17.6	18.5	14.5 – 20.3	16.30	13.90 – 17.30
15557-5215c1	221.6	10.0	–67.8	1.3	104.4	9.0	1.3	15.8	14.9 – 16.3	18.1	17.1 – 18.6	11.40	10.30 – 12.40
15557-5215c2	186.0	7.0	–67.2	1.5	128.9	10.0	1.5	19.0	15.5 – 20.4	23.4	17.3 – 26.0	15.60	14.20 – 16.50
15579-5303c1	258.7	8.0	–48.9	2.5	194.1	9.0	2.5	23.2	19.9 – 25.3	31.1	24.4 – 35.1	14.40	13.60 – 15.10
16061-5048c1	282.2	7.0	–66.6	2.3	172.3	8.0	2.3	18.9	16.1 – 19.9	23.0	18.0 – 25.3	20.60	19.10 – 21.40
16061-5048c2	285.9	7.0	–67.0	2.0	188.9	6.0	2.0	17.9	15.8 – 19.4	21.4	17.5 – 23.0	26.40	24.50 – 27.70
16061-5048c4	174.3	6.0	–51.6	1.2	64.3	7.0	1.2	12.1	11.1 – 12.8	13.1	11.6 – 13.9	23.30	19.90 – 25.40
16093-5015c1	155.5	4.0	–42.4	1.4	41.5	4.0	1.4	15.8	15.4 – 16.3	18.0	17.1 – 18.7	2.51	2.00 – 2.77
16093-5128c1	193.4	8.0	–63.2	1.4	95.2	6.0	1.4	15.8	13.0 – 17.0	18.3	14.0 – 19.7	15.10	12.80 – 16.50
16093-5128c8	65.1	4.0	–96.0	1.1	23.1	4.0	1.1	13.4	9.0 – 15.9	15.2	8.9 – 17.6	9.58	5.11 – 18.10
16428-4109c1	103.1	5.0	–24.4	1.3	42.8	4.0	1.3	14.9	14.1 – 15.9	16.9	15.3 – 17.8	25.00	22.40 – 27.20
16428-4109c2	189.7	4.0	–25.2	1.1	83.7	4.0	1.1	15.1	14.5 – 15.8	17.1	16.3 – 17.8	7.24	6.80 – 7.66
17040-3959c1	112.9	4.0	–15.6	1.9	72.5	5.0	1.9	16.1	12.3 – 17.3	18.8	13.2 – 20.2	25.00	20.60 – 27.20
17195-3811c1	108.2	6.0	–25.6	1.2	48.0	6.0	1.2	16.5	11.8 – 18.4	19.7	12.4 – 22.0	5.22	3.74 – 6.55
17195-3811c2	159.7	4.0	–25.4	0.8	72.5	4.0	0.8	15.2	14.4 – 15.7	17.2	16.2 – 18.2	6.26	5.67 – 6.82
17195-3811c3	91.7	4.0	–25.3	0.7	46.8	4.0	0.7	13.6	12.7 – 13.8	15.0	14.0 – 15.7	10.80	9.65 – 11.80
17355-3241c1	78.7	4.0	–3.5	1.1	30.3	4.0	1.1	15.6	13.7 – 17.2	17.8	14.7 – 19.8	1.74	0.98 – 2.19
10088-5730c2	11.3	3.0	–4.6	0.9	…	4.0	…	–	–	–	–	–	–
13560-6133c2	79.3	9.0	–56.4	1.4	46.2	9.0	1.4	14.2	9.2 – 16.5	16.3	9.6 – 19.3	19.50	5.35 – 21.70
14166-6118c2	116.1	6.0	–39.5	1.1	35.2	6.0	1.1	12.6	11.5 – 14.0	13.8	12.0 – 15.6	6.21	4.75 – 7.32
14183-6050c3	44.9	6.0	–44.4	0.8	…	5.0	…	–	–	–	–	–	–
15038-5828c1	89.3	7.0	–68.8	1.9	27.5	7.0	1.9	12.7	11.3 – 13.5	13.8	12.3 – 15.0	12.40	9.78 – 14.20
15470-5419e4	151.0	5.0	–58.7	1.2	47.5	5.0	1.2	13.5	10.5 – 14.8	15.0	11.2 – 16.8	11.80	8.54 – 13.30
15557-5215c3	170.1	4.0	–68.4	1.4	64.3	4.0	1.4	14.3	13.7 – 14.5	15.9	15.3 – 16.3	12.80	12.10 – 13.50
15579-5303c3	69.5	6.0	–74.2	1.3	19.2	6.0	1.3	13.1	10.6 – 14.7	14.5	11.1 – 16.5	2.77	1.00 – 3.47
16093-5128c2	67.4	8.0	–97.2	1.8	…	8.0	…	–	–	–	–	–	–
16164-4929c3	143.6	5.0	–31.8	1.5	47.2	5.0	1.5	13.1	10.8 – 14.2	14.5	11.5 – 15.6	16.40	12.90 – 18.50
16164-4929e6	26.0	3.0	–32.6	0.8	…	3.0	…	–	–	–	–	–	–
16164-4837c2	48.1	3.0	–51.1	0.8	…	3.0	…	–	–	–	–	–	–
16435-4515c3	34.5	3.0	–51.8	1.1	…	3.0	…	–	–	–	–	–	–
16482-4443c2	89.9	6.0	–42.4	1.6	31.8	6.0	1.6	15.7	10.1 – 18.2	18.6	10.2 – 21.3	8.24	4.20 – 9.80

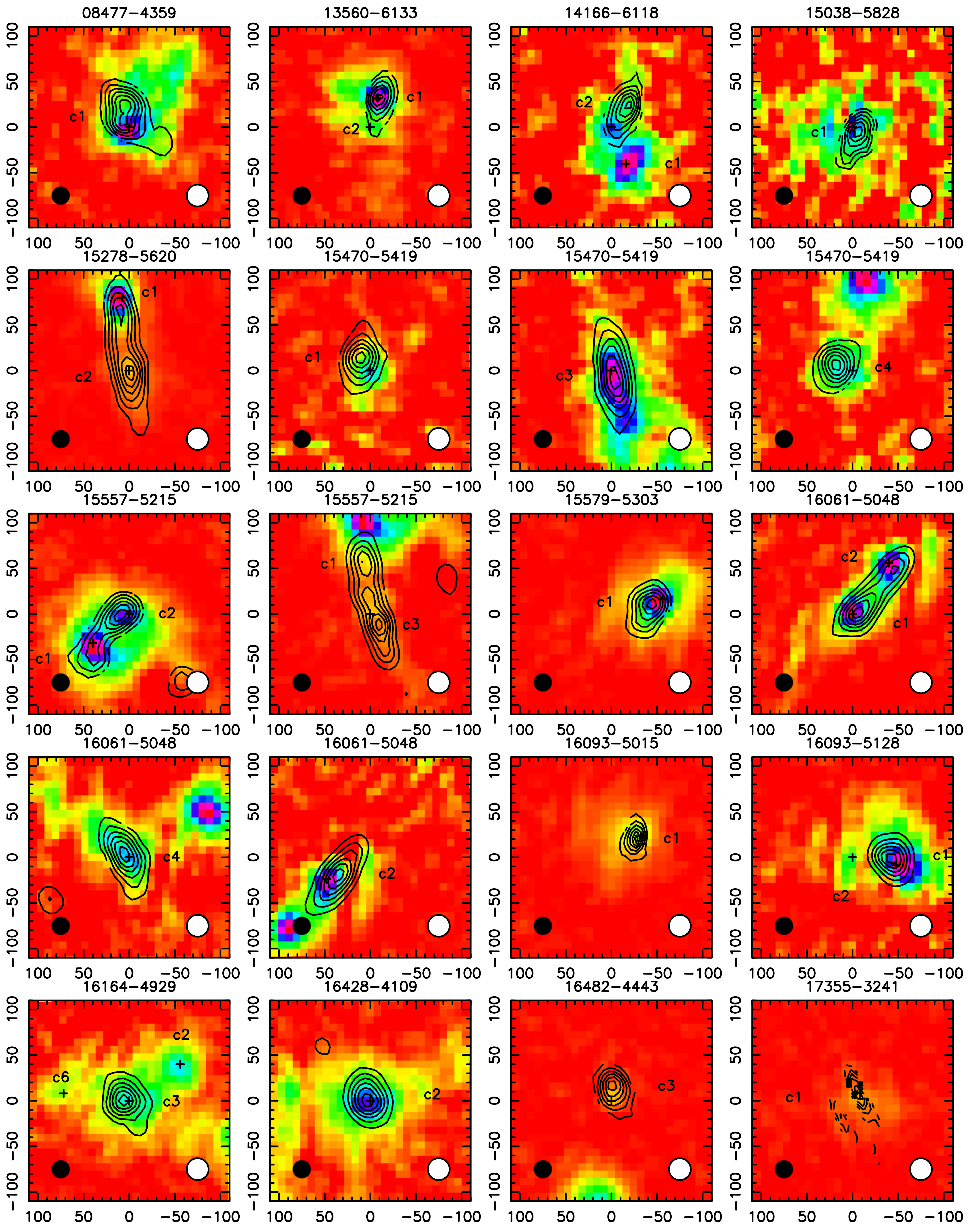

Figure B.1: **(a)**:Colourscale: SEST 1.2 mm; contours: NH_3(1,1) zeroth moment. The contours start from 15% of the peak, in step of 15% of the peak integrated emission. The peak flux and the ΔV of the line are given in Table 3.2. The position of each clump in our sample is indicated by a black cross. The SEST beam is indicated as a white circle, and the ATCA beam is shown as a black circle. The IRAS name is indicated above each panel, and the clump names are shown in the figures. The fields with poor uv-coverage (see Sect. 3.4) are not used to produce overlays, as the maps produced are not as reliable as the others.

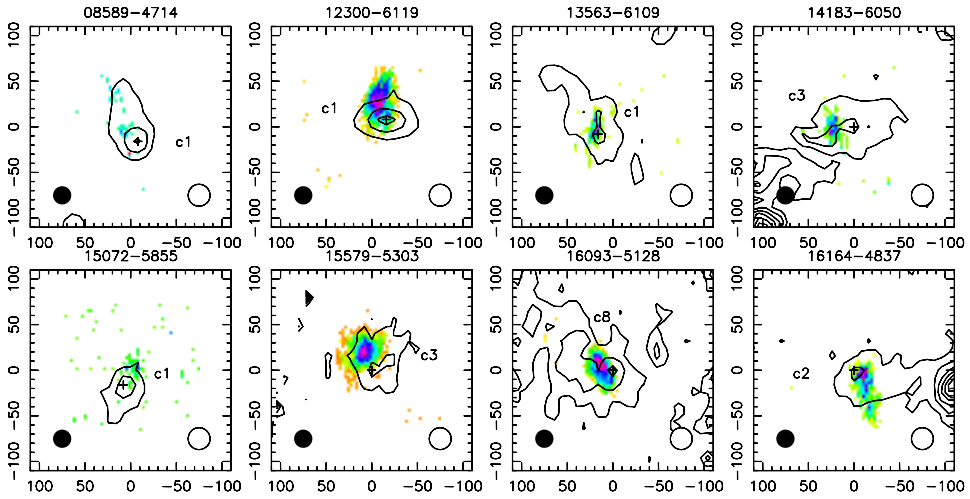

Figure B.1: **(b)**: Colourscale: $NH_3(1,1)$ zeroth moment; contours: SEST 1.2 mm. In this panel the colourscale and contours have been swapped in order to make the figure intelligible. The SEST contours are optimised to identify the clump. The position of each clump in our sample is indicated by a black cross. The SEST beam is indicated as a white circle, and the ATCA beam is shown as a black circle. The IRAS name is indicated above each panel, and the clump names are shown in the figures. The fields with poor uv-coverage (see Sect. 3.4) are not used to produce overlays, as the maps produced are not as reliable as the others.

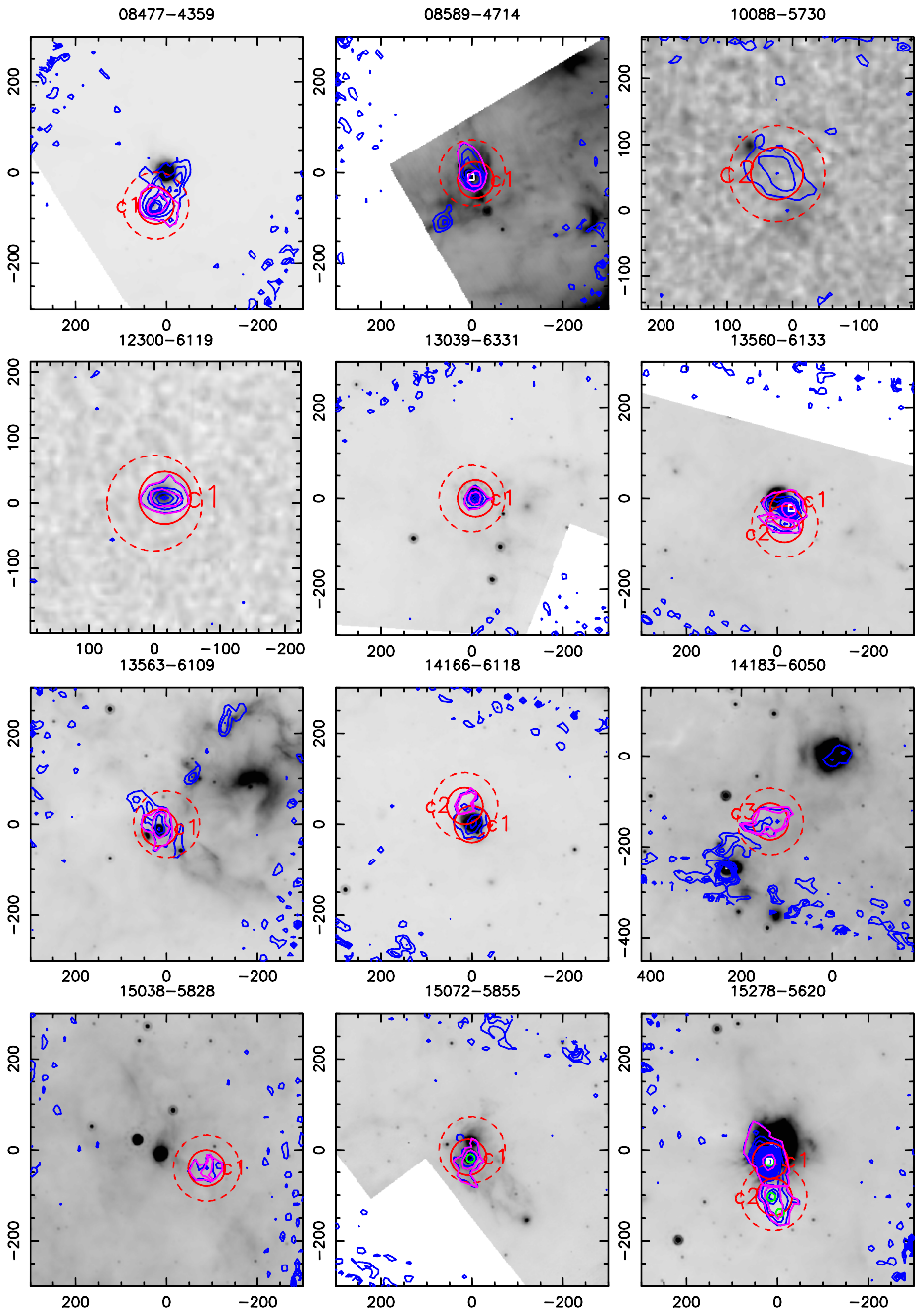

Figure B.2: SEST 1.2 mm emission (contours) superimposed on the Spitzer/MIPS 24 μm images. The IRAS name is indicated above each panel, and the clump names are shown in the figures. Dashed and solid red lines indicate the ATCA field and the observed clumps, respectively. H_2O maser spots are shown as white open squares, while "green fuzzies" are indicated as green open circles. In the last four panels the SEST emission is superimposed on MSX images. Purple lines indicate the 3σ and FWHM polygons used to extract fluxes from the SEST images.

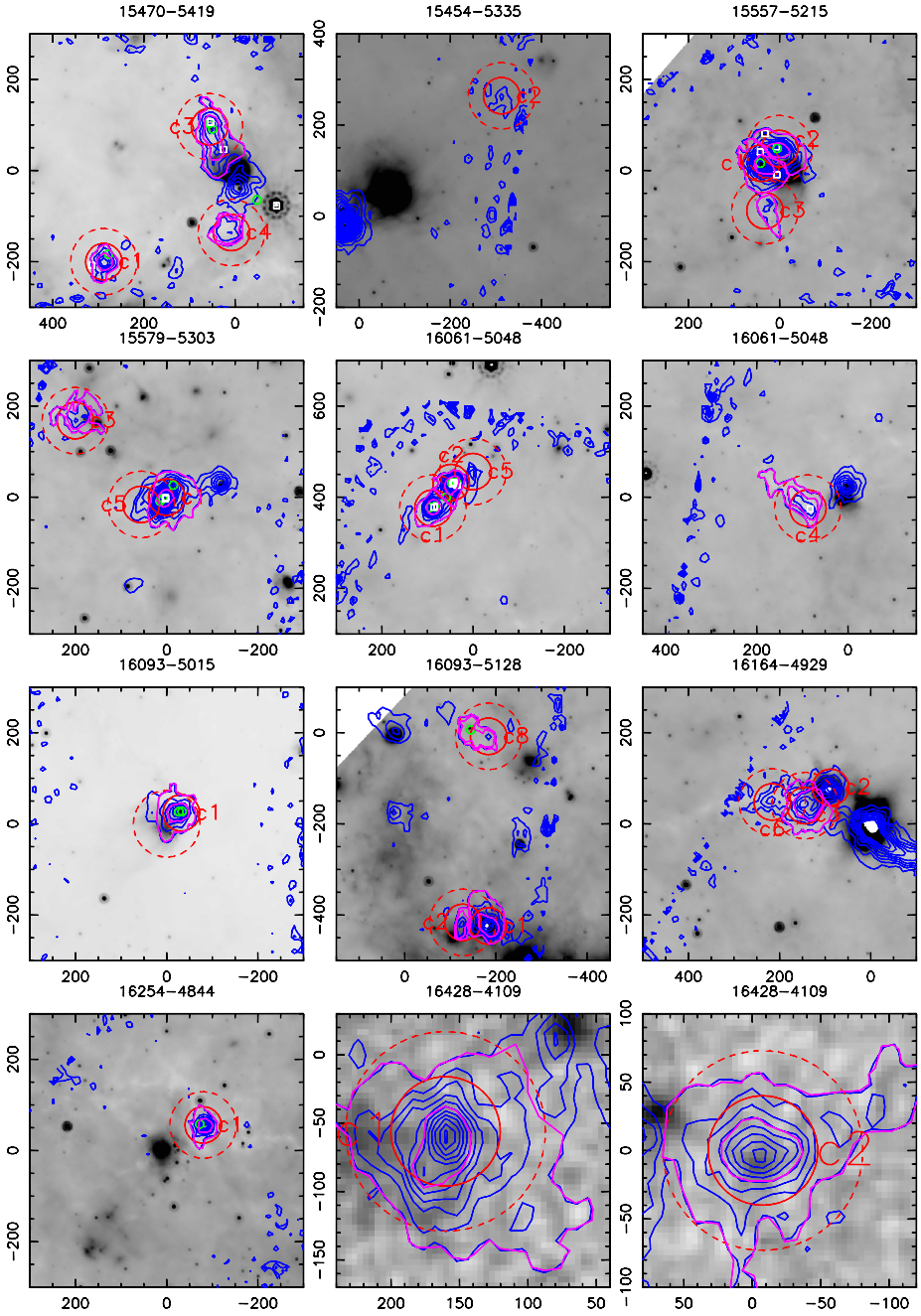

Figure B.2: Continued.

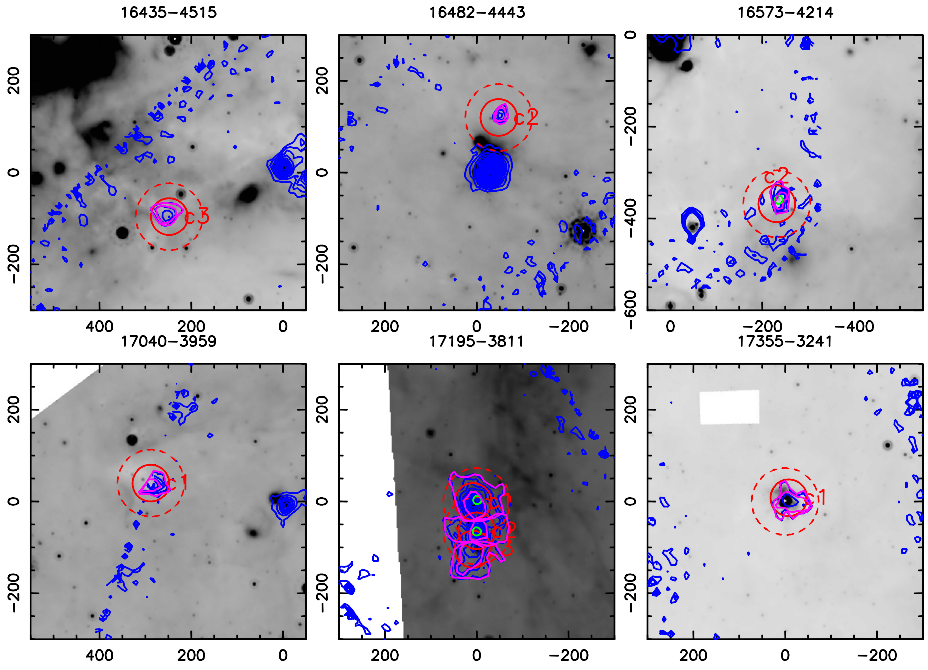

Figure B.2: Continued.

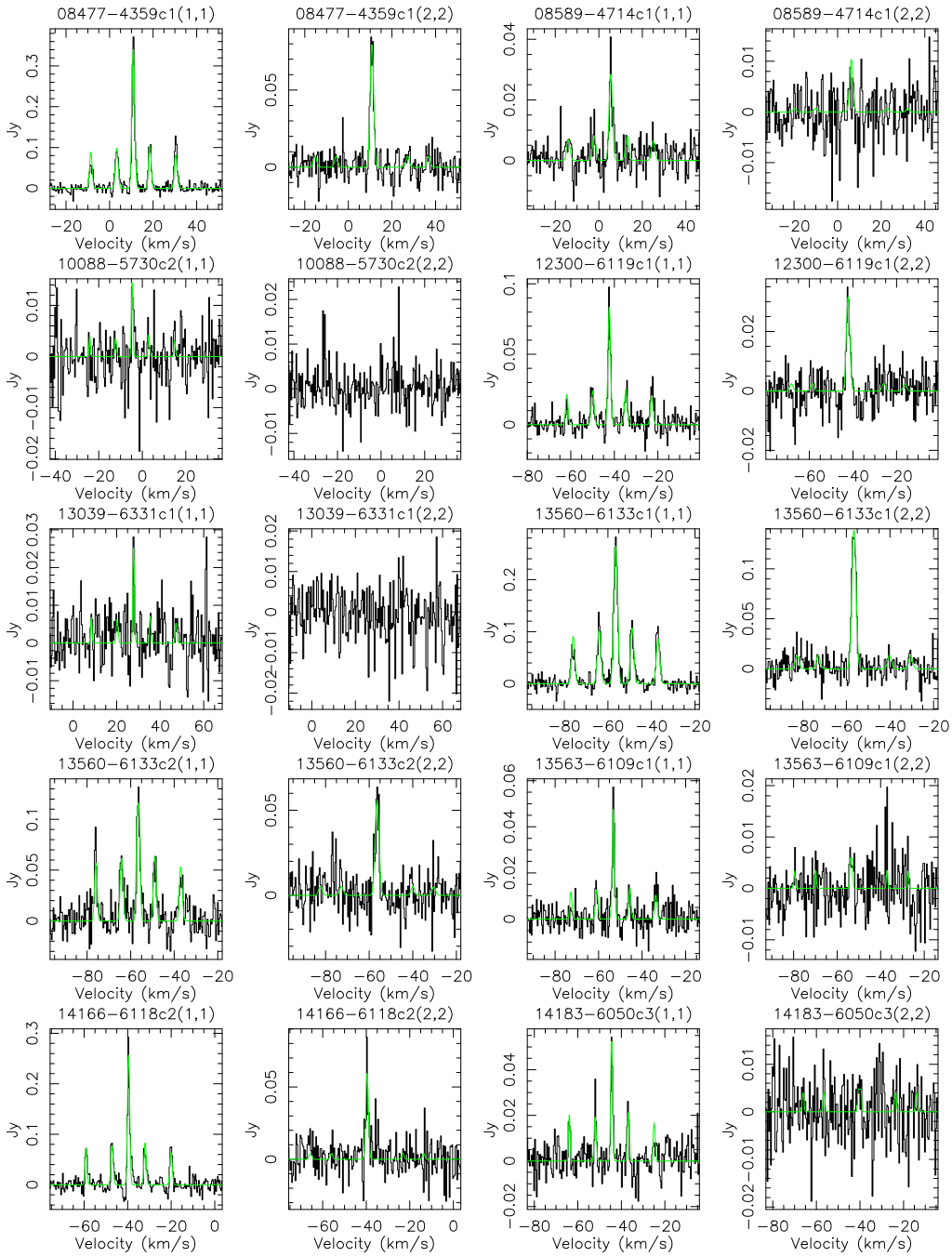

Figure B.3: NH_3(1,1) and (2,2) spectra extracted at the peak of NH3(1,1) emission for all clumps. The clump name and transition are indicated above each panel.

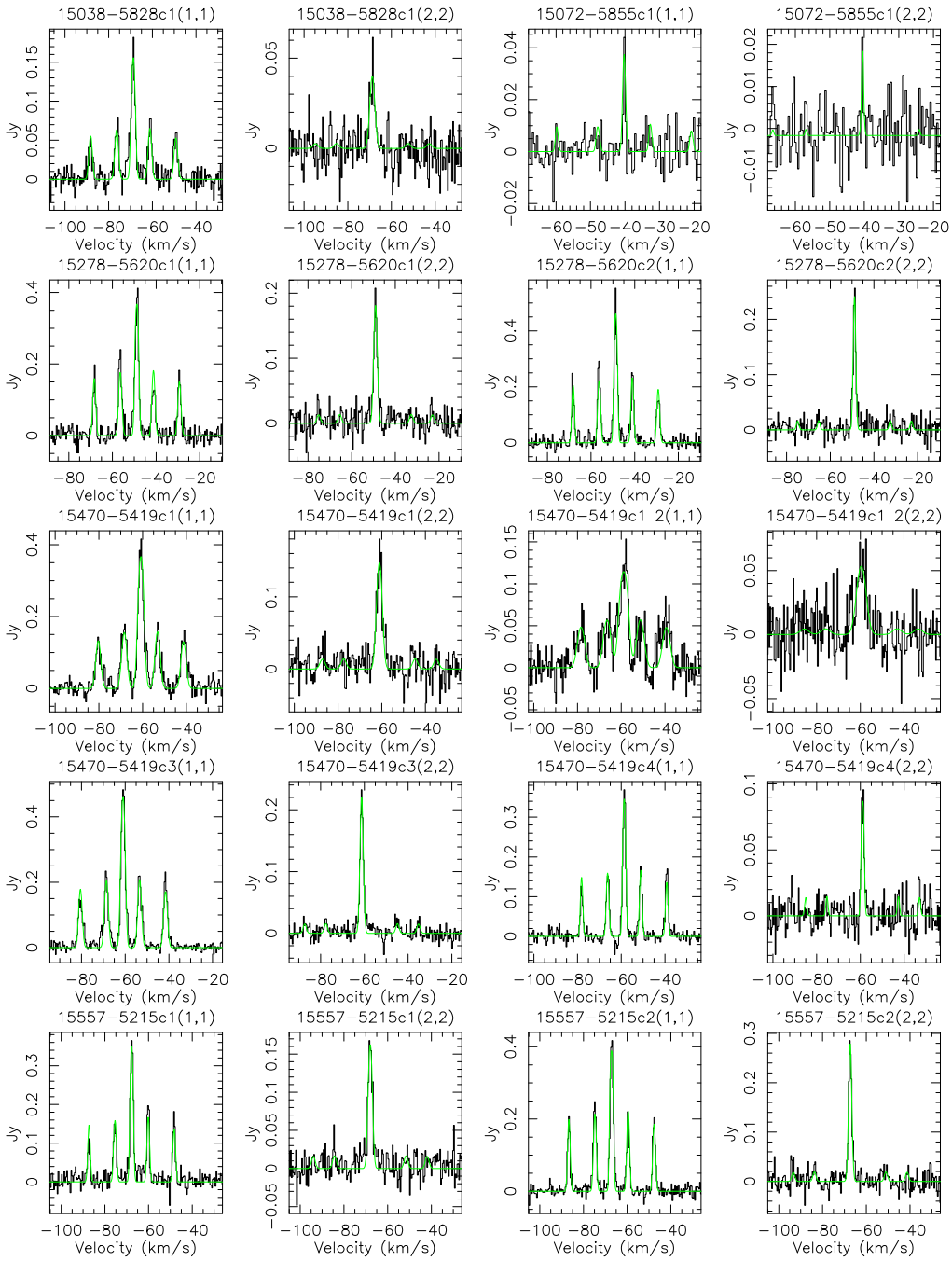

Figure B.3: Continued.

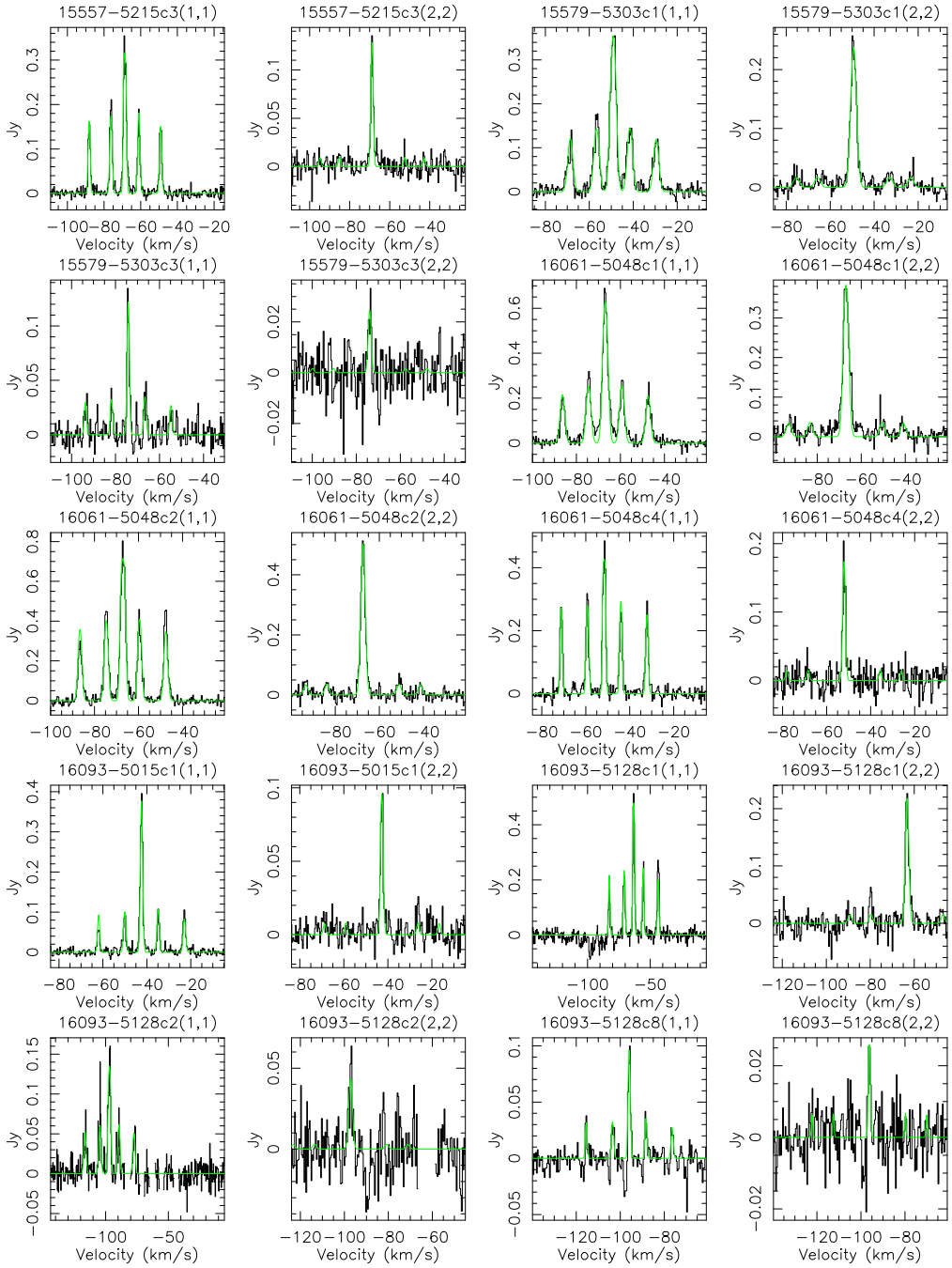

Figure B.3: Continued.

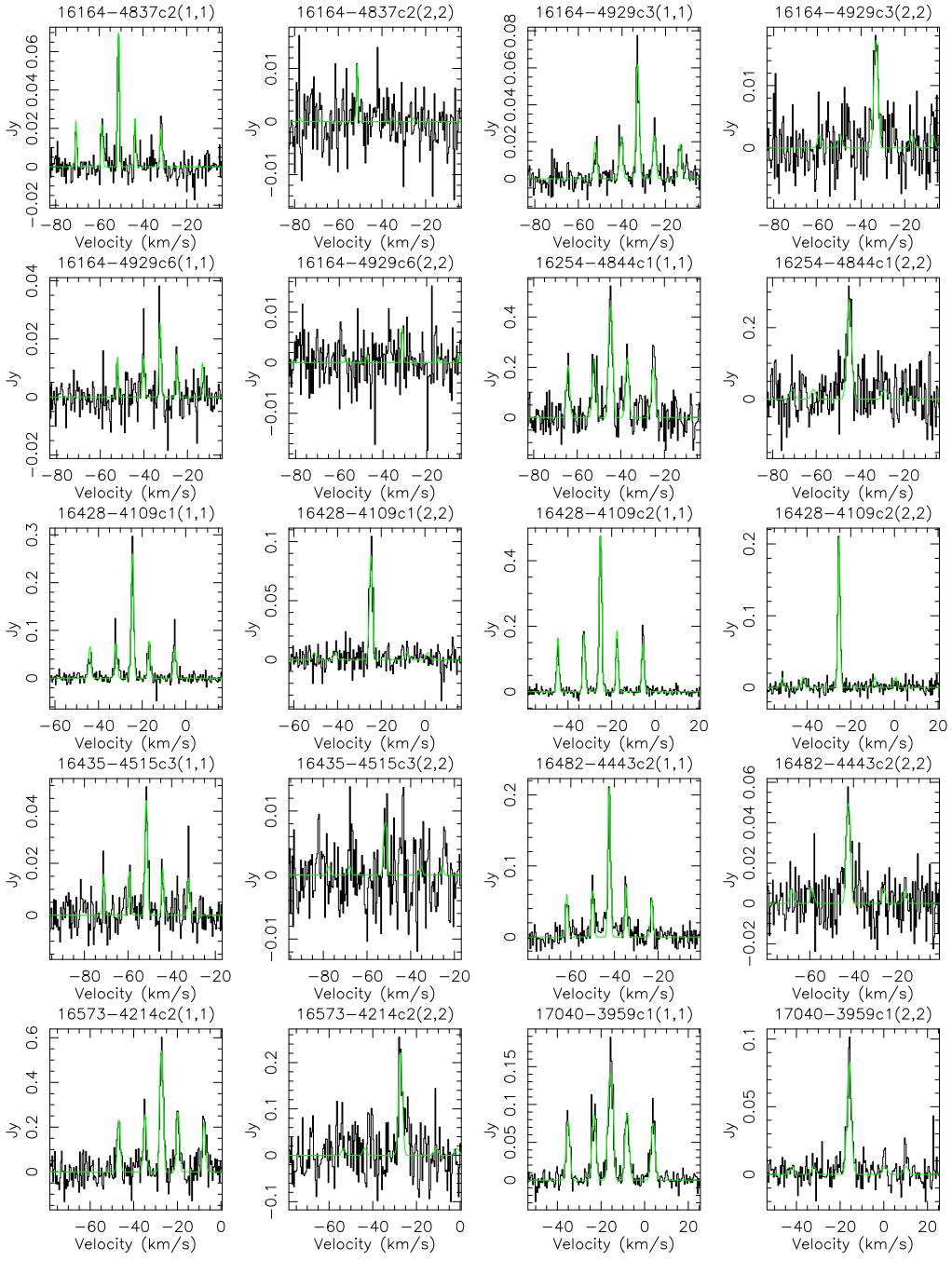

Figure B.3: Continued.

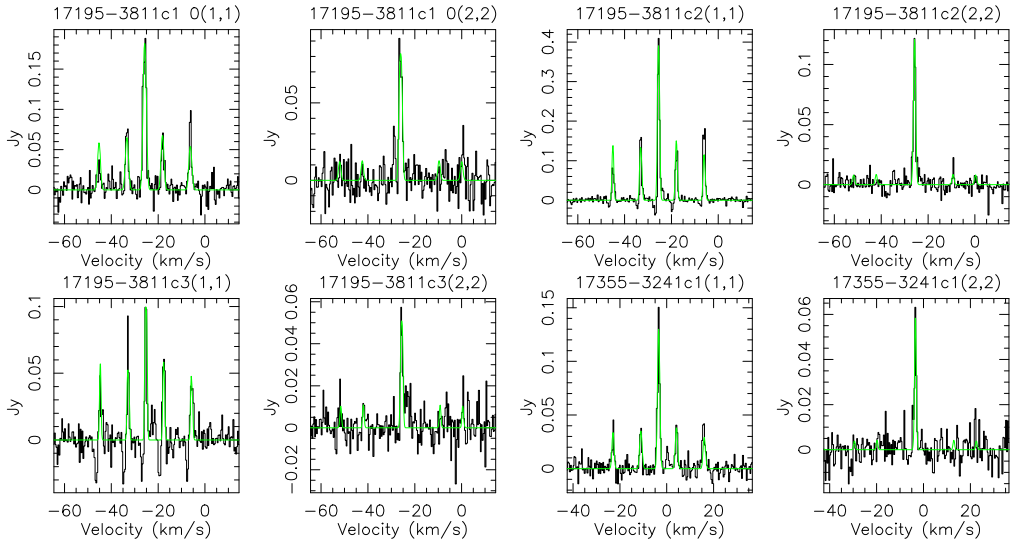

Figure B.3: Continued.

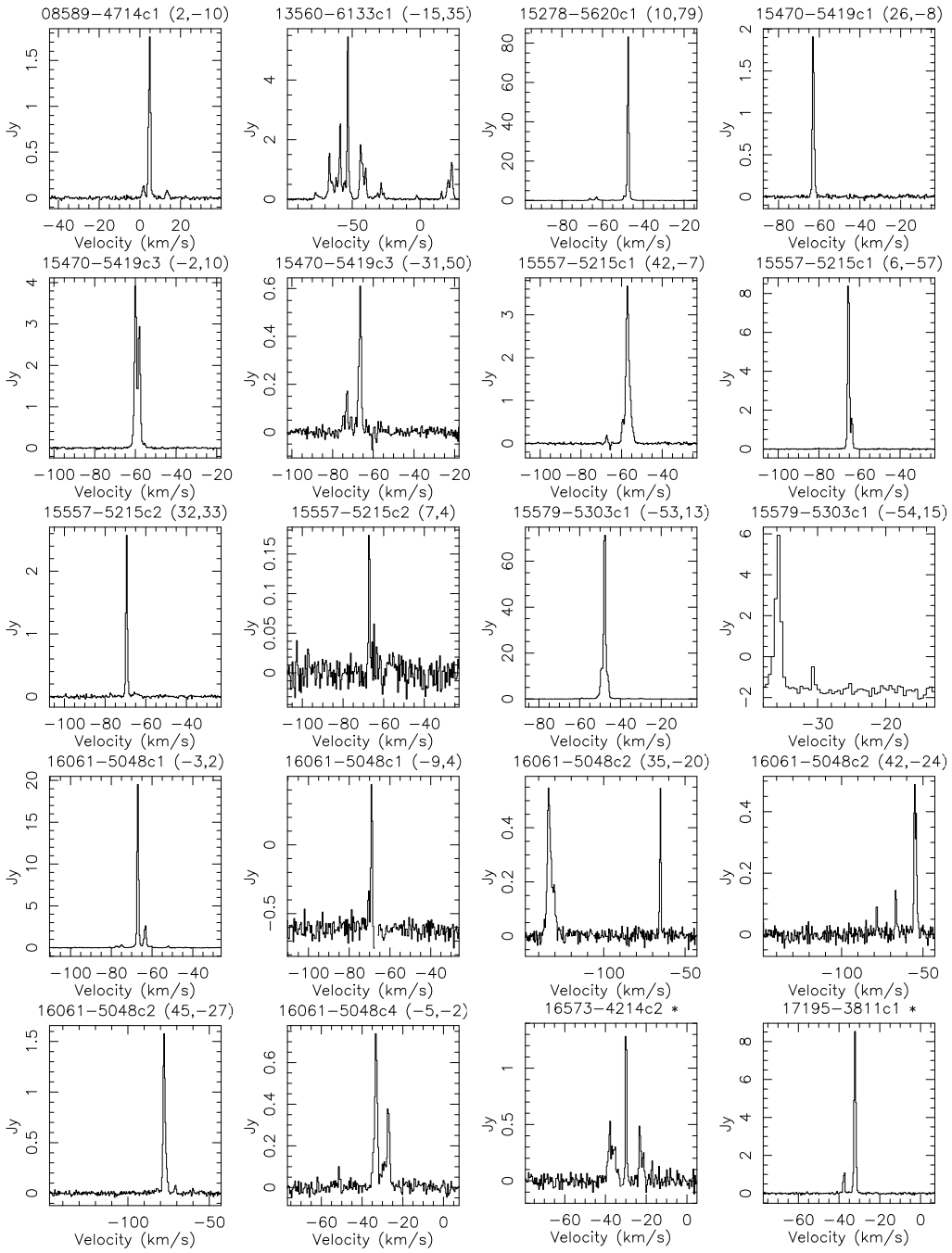

Figure B.4: H_2O maser spectra. The clump name and the offset of the maser w.r.t. the phase centre are indicated above each panel.

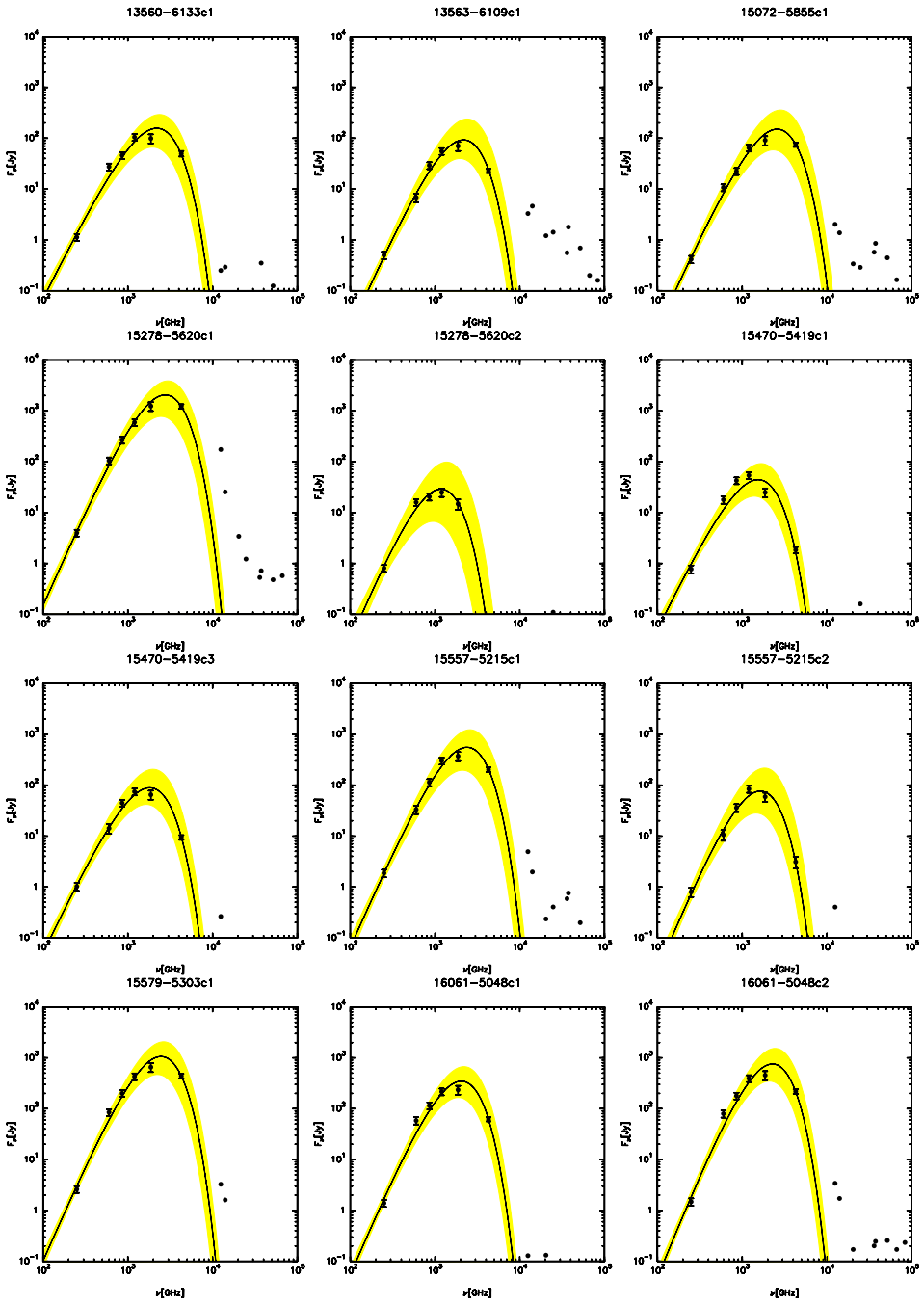

Figure B.5: Spectral energy distributions for the SFS. Uncertainties in the fluxes are indicated. The yellow-shaded area shows the region encompassed by the extreme values of the fit-derived parameters for the modified black-body.

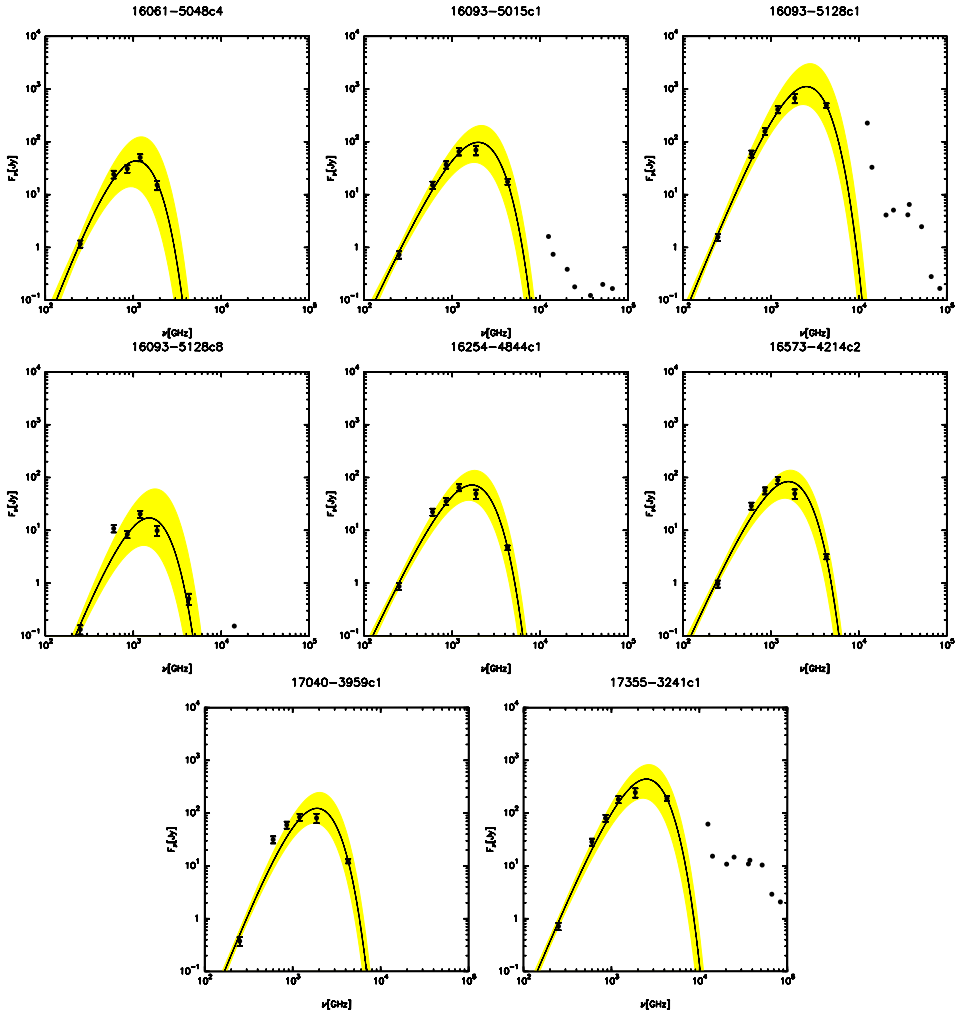

Figure B.5: Continued.

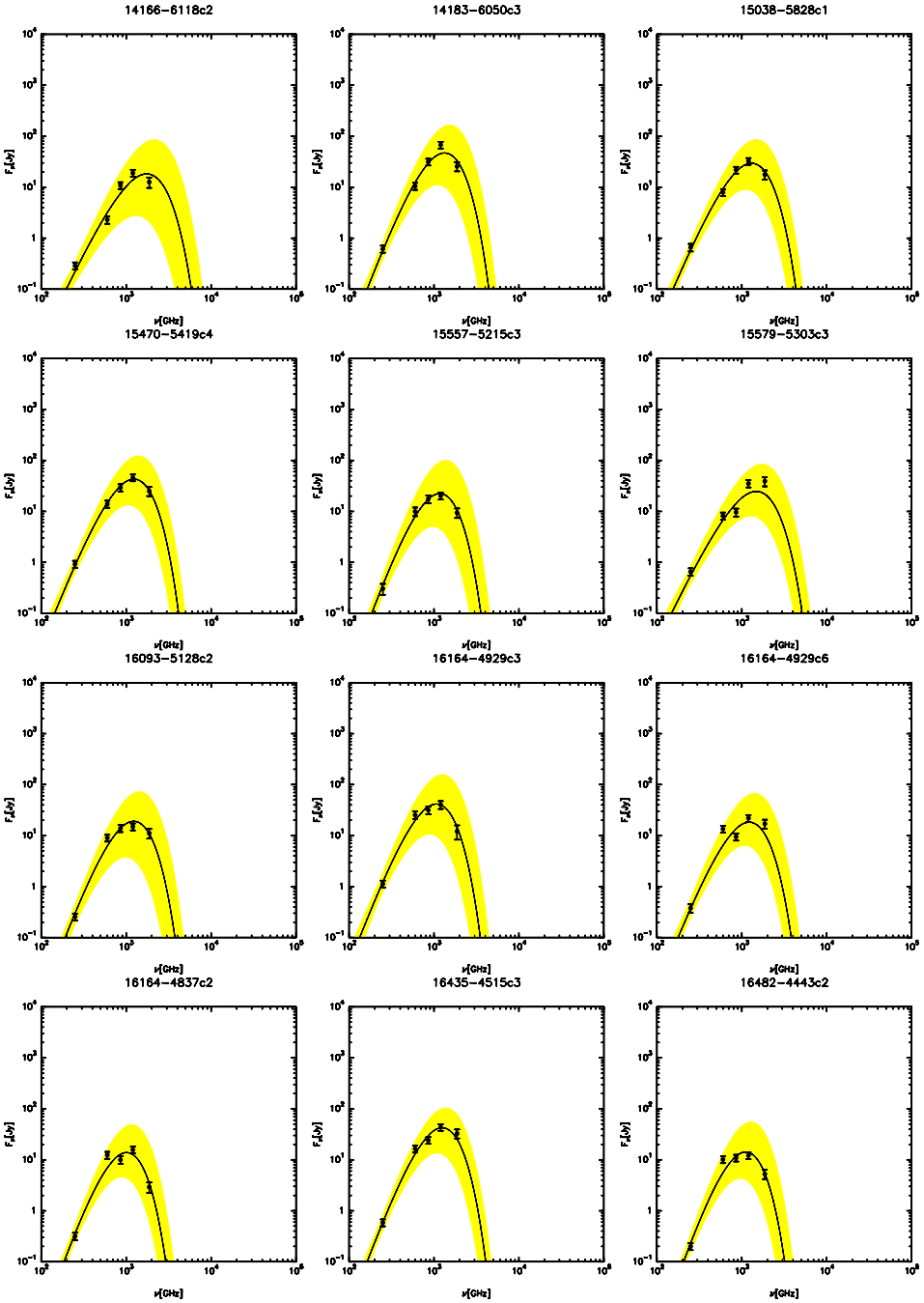

Figure B.6: Same as Fig. B.5, but for the QS.

Appendix C

Appendices to Chapter 4

In this Appendix we present the tables (C.1) and the spectra (C.2) pertaining to Chapter 4.

C.1 Tables

Table C.1: Distances and classification for sources in sub-sample S1, derived from $C^{17}O$(3-2).

Source	RA (HH:MM:SS)	DEC (DD:MM:SS)	V_{LSR} (km s^{-1})	D_{near} (kpc)	z_{near} (pc)	D_{far} (kpc)	z_{far} (pc)	HI[a]	D liter (kpc)	Method	Adopted D (kpc)	D_{GC} (kpc)	Group
AGAL008.684-00.367	18 : 06 : 23.35	−21 : 37 : 05.2	37.99	4.78	−30.60	12.03	−77.10	*F*	4.5[2]	*HI*	12.0	3.9	D8
AGAL008.706-00.414	18 : 06 : 36.72	−21 : 37 : 18.6	39.44	4.86	−35.00	11.95	−86.10	*F*	–	–	11.9	3.8	D24
AGAL010.444-00.017	18 : 08 : 44.59	−19 : 54 : 36.4	75.87	6.01	−1.80	10.71	−3.20	*F*	11.0[2]	*HI*	10.7	2.8	D24
AGAL010.472+00.027	18 : 08 : 38.24	−19 : 51 : 51.5	67.56	5.74	2.80	10.98	5.40	*F*	11.2[2]	*HI*	11.0	3.0	IRB
AGAL010.624-00.384	18 : 10 : 28.82	−19 : 55 : 48.4	−2.86	17.23	−115.20	–	–	*N*	2.4[4]	*SP*	2.4	6.2	IRB
AGAL012.804-00.199	18 : 14 : 13.34	−17 : 55 : 45.3	36.20	3.90	−13.50	12.67	−43.80	–	2.4[9]	*PA*	2.4	6.2	IRB
AGAL013.178+00.059	18 : 14 : 01.32	−17 : 28 : 38.6	50.42	4.64	5.00	11.92	12.90	*N*	4.8[12]	*HI*	4.6	4.1	D8
AGAL013.658-00.599	18 : 17 : 24.37	−17 : 22 : 08.0	48.37	4.47	−46.70	12.05	−125.80	*N*	12.3[2]	*HI*	4.5	4.3	RMS
AGAL014.114-00.574	18 : 18 : 13.14	−16 : 57 : 20.0	20.85	2.57	−25.70	13.92	−139.20	*N*	–	–	2.6	6.0	D8
AGAL014.194-00.194	18 : 16 : 58.77	−16 : 42 : 17.5	39.23	3.90	−13.10	12.58	−42.40	*N*	–	–	3.9	4.8	D8
AGAL014.492-00.139	18 : 17 : 22.09	−16 : 24 : 59.4	39.46	3.87	−9.40	12.58	−30.50	*N*	–	–	3.9	4.8	D24
AGAL014.632-00.577	18 : 19 : 15.22	−16 : 30 : 02.3	18.53	2.30	−23.10	14.15	−142.00	*N*	13.7[13]	*FR*	2.3	6.3	D8
AGAL015.029-00.669	18 : 20 : 22.37	−16 : 11 : 38.8	19.62	2.36	−27.60	14.06	−164.40	*N*	2.0[10]	*SP*	2.0	6.6	IRB
AGAL018.606-00.074	18 : 25 : 08.27	−12 : 45 : 22.8	46.63	3.85	−5.00	12.26	−15.80	*F*	–	–	12.3	5.0	D24
AGAL018.734-00.226	18 : 25 : 56.05	−12 : 42 : 50.8	42.61	3.62	−14.30	12.48	−49.20	*F*	13.0[2]	*HI*	12.5	5.2	D8
AGAL018.888-00.474	18 : 27 : 07.69	−12 : 41 : 36.4	66.06	4.74	−39.20	11.34	−93.60	*N*	3.4[2]	*HI*	4.7	4.3	D8
AGAL019.882-00.534	18 : 29 : 14.20	−11 : 50 : 28.4	44.97	3.66	−34.20	12.33	−115.10	*N*	3.3[2]	*HI*	3.7	5.2	RMS
AGAL022.376+00.447	18 : 30 : 24.26	−09 : 10 : 36.0	54.01	3.96	30.90	11.76	91.70	*N*	–	–	4.0	5.1	D24
AGAL023.206-00.377	18 : 34 : 54.99	−08 : 49 : 15.5	78.17	5.03	−33.10	10.60	−69.70	*N*	10.9[2]	*HI*	5.0	4.3	D8
AGAL024.629+00.172	18 : 35 : 35.61	−07 : 18 : 17.9	116.01	6.92	20.90	8.53	25.80	–	–	–	6.9	3.6	D24
AGAL028.564-00.236	18 : 44 : 18.04	−03 : 59 : 40.0	87.24	5.45	−22.40	9.48	−38.90	–	–	–	5.5	4.5	D24
AGAL028.861+00.066	18 : 43 : 46.06	−03 : 35 : 32.2	104.02	6.65	7.70	8.24	9.50	*N*	–	–	6.7	4.2	RMS
AGAL030.848-00.081	18 : 47 : 55.45	−01 : 53 : 29.5	94.35	7.21	−10.10	7.21	−10.10	*N*	–	–	7.2	4.4	D24
AGAL030.893+00.139	18 : 47 : 13.37	−01 : 45 : 04.0	97.26	6.39	15.40	8.20	19.70	*N*	–	–	6.4	4.5	D24
AGAL031.412+00.307	18 : 47 : 34.33	−01 : 12 : 45.5	98.15	6.67	35.70	7.84	42.00	*N*	5.6[4]	*SP*	5.6	4.7	IRB
AGAL034.258+00.154	18 : 53 : 18.52	01 : 15 : 01.5	58.52	3.96	10.60	10.09	27.10	*N*	2.1[4]	*SP*	2.1	6.9	IRB
AGAL034.401+00.226	18 : 53 : 18.79	01 : 24 : 37.8	57.44	3.89	15.40	10.13	40.10	–	1.6[11]	*PA*	1.6	7.2	RMS
AGAL034.411+00.234	18 : 53 : 18.18	01 : 25 : 23.0	58.01	3.93	16.00	10.10	41.20	–	1.6[11]	*PA*	1.6	7.2	D8
AGAL034.821+00.351	18 : 53 : 38.07	01 : 50 : 28.6	58.29	3.95	24.20	10.00	61.30	–	3.4[2]	*HI*	4.0	5.7	RMS
AGAL035.197-00.742	18 : 58 : 12.79	01 : 40 : 37.6	34.66	2.51	−32.50	11.39	−147.50	*N*	2.2[18]	*PA*	2.2	6.8	RMS
AGAL037.554+00.201	18 : 59 : 09.95	04 : 12 : 16.3	86.09	6.71	23.40	6.71	23.40	–	5.0[2]	*HI*	6.7	5.2	RMS
AGAL043.166+00.011	19 : 10 : 13.40	09 : 06 : 11.2	5.26	0.42	0.10	11.98	2.30	–	11.4[7]	*PA*	11.4	7.8	IRB
AGAL049.489-00.389	19 : 23 : 44.15	14 : 30 : 29.5	57.16	5.51	−37.50	5.51	−37.50	*T*	5.4[6]	*PA*	5.4	6.5	IRB
AGAL053.141+00.069	19 : 29 : 17.80	17 : 56 : 17.9	22.29	1.92	2.40	8.28	10.30	–	1.6[2]	*HI*	1.9	7.5	RMS
AGAL059.782+00.066	19 : 43 : 10.83	23 : 44 : 03.3	23.12	2.56	2.90	6.00	6.90	–	2.2[19]	*PA*	2.2	7.6	RMS

Notes. [(a)] From Wienen et al., in prep.
1: Caswell 1975, 2: Green & McClure-Griffith 2011, 3: Reid et al. 2009, 4: Moises et al. 2011, 5: Bik et al. 2005, 6: Sato et al. 2010, 7: Gwinn et al. 1992, 8: Blum et al. 2001, 9: Immer et al. 2012, 10: Xu et al. 2011, 11: Kurayama et al. 2011, 12: Pandian et al. 2008, 13: Sewilo et al. 2004, 14: Bica et al. 2004, 15: Busfield et al. 2006, 16: Urquhart et al. 2011, 17: Figueredo et al. 2005, 18: Zhang et al. 2009, 19: Xu et al. 2009.
Methods: PA = Direct parallax measurement; SP = Spectrophotometric measurement; HI = HI self-absorption; FR = Formaldehyde self-absorption.
In the "HI" column T, N and F indicate the tangent point, the near- and far distance, respectively.
The columns show the object's name, RA, DEC, $V_{\rm LSR}$, the near distance $D_{\rm near}$, the height above the Galactic plane for the near distance $z_{\rm near}$, the far distance $D_{\rm far}$, the height above the Galactic plane for the far distance $z_{\rm far}$, the distance ambiguity resolution according to Wienen et al., in prep., literature values for the distance and the method with which it was determined, the adopted distance and the resulting Galactocentric distance, and the source classification, according to Sect. 4.3.

Table C.2: Distances and classification for the sources in sub-sample S2, derived from $C^{17}O$(3-2).

Source	RA (HH:MM:SS)	DEC (DD:MM:SS)	V_{LSR} (km s^{-1})	D_{near} (kpc)	z_{near} (pc)	D_{far} (kpc)	z_{far} (pc)	HI	D liter (kpc)	Method	Adopted D (kpc)	D_{GC} (kpc)	Group
AGAL301.136-00.226	12 : 35 : 34.89	−63 : 02 : 32.8	−39.15	4.37	−17.50	4.37	−17.50	*F*	4.3[2]	*HI*	4.4	7.3	IRB
AGAL305.209+00.206	13 : 11 : 14.09	−62 : 34 : 41.5	−42.53	4.83	17.70	4.83	17.70	*F*	3.5[14]	*SP*	3.5	7.1	IRB
AGAL305.794-00.096	13 : 16 : 32.84	−62 : 49 : 41.3	−40.82	4.96	−8.70	4.96	−8.70	*F*	3.5[14]	*SP*	3.5	7.0	D24
AGAL317.867-00.151	14 : 53 : 16.60	−59 : 26 : 33.9	−40.19	2.95	−7.80	9.66	−25.50	*N*	–	–	3.0	6.6	D8
AGAL318.779-00.137	14 : 59 : 33.06	−59 : 00 : 33.5	−38.14	2.78	−6.70	10.01	−24.10	*N*	–	–	2.8	6.7	D8
AGAL320.881-00.397	15 : 14 : 33.18	−58 : 11 : 28.5	−45.30	3.22	−22.40	9.97	−69.40	*F*	–	–	10.0	6.3	D24
AGAL327.293-00.579	15 : 53 : 08.62	−54 : 37 : 06.2	−44.72	3.14	−31.70	11.17	−112.60	*N*	3.3[16]	*HI*	3.1	6.1	IRB
AGAL328.809+00.632	15 : 55 : 48.91	−52 : 43 : 07.9	−41.86	2.99	33.00	11.55	127.60	*N*	2.6[2]	*HI*	3.0	6.1	IRB
AGAL329.029-00.206	16 : 00 : 31.96	−53 : 12 : 54.0	−43.49	3.09	−10.80	11.49	−40.30	*F*	12.0[2]	*HI*	11.5	6.1	D8
AGAL330.879-00.367	16 : 10 : 20.12	−52 : 06 : 06.4	−62.48	4.16	−26.80	10.69	−68.90	*N*	3.4[1]	*HI*	4.2	5.3	IRB
AGAL330.954-00.182	16 : 09 : 52.67	−51 : 54 : 53.9	−91.16	5.70	−18.30	9.16	−29.40	*N*	4.7[2]	*HI*	5.7	4.5	IRB
AGAL331.709+00.582	16 : 10 : 06.79	−50 : 50 : 29.4	−67.76	4.44	45.40	10.53	107.70	*F*	–	–	10.5	5.0	D8
AGAL332.094-00.421	16 : 16 : 16.66	−51 : 18 : 25.3	−56.94	3.89	−28.60	11.13	−81.80	*N*	3.5[15]	*HI*	3.9	5.4	RMS
AGAL332.826-00.549	16 : 20 : 11.02	−50 : 53 : 14.5	−57.06	3.92	−37.70	11.21	−107.80	*N*	3.2[5]	*SP*	3.2	5.8	IRB
AGAL333.134-00.431	16 : 21 : 02.44	−50 : 35 : 12.2	−53.11	3.72	−28.00	11.45	−86.30	*N*	2.6[17]	*SP*	2.6	6.3	IRB
AGAL333.604-00.212	16 : 22 : 09.35	−50 : 05 : 58.8	−48.39	3.49	−13.10	11.74	−44.10	*N*	–	–	3.5	5.6	IRB
AGAL333.656+00.059	16 : 21 : 11.61	−49 : 52 : 16.3	−85.05	5.29	5.40	9.94	10.20	*N*	10.5[2]	*HI*	5.3	4.4	D24
AGAL335.789+00.174	16 : 29 : 47.34	−48 : 15 : 52.1	−50.11	3.67	11.20	11.84	36.20	*N*	3.2[2]	*HI*	3.7	5.4	D8
AGAL336.958-00.224	16 : 36 : 17.12	−47 : 40 : 44.3	−71.27	4.73	−18.50	10.91	−42.70	*F*	11.5[2]	*HI*	10.9	4.5	D24
AGAL337.176-00.032	16 : 36 : 18.78	−47 : 23 : 18.6	−67.77	4.59	−2.60	11.08	−6.20	*F*	4.0[2]	*HI*	11.1	4.6	D8
AGAL337.286+00.007	16 : 36 : 34.76	−47 : 16 : 51.2	−106.60	6.24	0.90	9.44	1.30	*F*	–	–	9.4	3.6	D24
AGAL337.406-00.402	16 : 38 : 50.89	−47 : 27 : 56.2	−41.01	3.26	−22.90	12.44	−87.50	*N*	2.7[2]	*HI*	3.3	5.6	IRB
AGAL337.704-00.054	16 : 38 : 29.57	−47 : 00 : 41.2	−47.41	3.63	−3.40	12.10	−11.20	*N*	12.2[15]	*HI*	3.6	5.3	IRB
AGAL337.916-00.477	16 : 41 : 10.60	−47 : 08 : 02.9	−39.55	3.20	−26.70	12.55	−104.70	*N*	2.7[1]	*HI*	3.2	5.7	IRB
AGAL338.066+00.044	16 : 39 : 28.60	−46 : 40 : 34.6	−69.17	4.69	3.60	11.08	8.50	*N*	–	–	4.7	4.5	D24
AGAL338.786+00.476	16 : 40 : 22.55	−45 : 51 : 04.1	−63.82	4.49	37.50	11.36	94.70	*N*	–	–	4.5	4.6	D24
AGAL340.374-00.391	16 : 50 : 02.47	−45 : 12 : 43.0	−43.55	3.60	−24.60	12.41	−84.70	*N*	–	–	3.6	5.3	D24
AGAL340.784-00.097	16 : 50 : 14.89	−44 : 42 : 31.6	−101.46	6.06	−10.50	9.99	−17.30	*F*	10.6[2]	*HI*	10.0	3.4	D8
AGAL342.484+00.182	16 : 55 : 02.53	−43 : 13 : 03.1	−41.49	3.66	11.80	12.55	40.30	*F*	12.9[2]	*HI*	12.6	5.1	D8
AGAL343.128-00.062	16 : 58 : 17.24	−42 : 52 : 02.0	−30.58	3.04	−3.30	13.23	−14.50	*N*	–	–	3.0	5.7	IRB
AGAL343.756-00.164	17 : 00 : 50.08	−42 : 26 : 11.9	−27.80	2.90	−8.30	13.42	−38.40	*N*	2.5[15]	*HI*	2.9	5.8	D8
AGAL344.227-00.569	17 : 04 : 07.75	−42 : 18 : 41.7	−22.26	2.52	−24.90	13.84	−137.20	*N*	2.1[2]	*HI*	2.5	6.1	D8
AGAL345.003-00.224	17 : 05 : 11.03	−41 : 29 : 07.2	−27.61	3.02	−11.90	13.40	−52.60	*N*	2.7[2]	*HI*	3.0	5.6	IRB
AGAL345.488+00.314	17 : 04 : 28.33	−40 : 46 : 24.6	−17.57	2.22	12.20	14.24	78.50	*N*	2.3[2]	*HI*	2.2	6.4	IRB
AGAL345.504+00.347	17 : 04 : 23.10	−40 : 44 : 26.7	−17.85	2.25	13.70	14.21	86.80	*N*	10.8[1]	*HI*	2.3	6.3	RMS
AGAL351.161+00.697	17 : 19 : 57.50	−35 : 57 : 50.8	−6.68	1.47	18.00	15.32	187.50	*N*	1.8[4]	*SP*	1.8	6.7	IRB
AGAL351.244+00.669	17 : 20 : 18.38	−35 : 54 : 43.4	−3.29	0.80	9.30	16.00	186.60	*N*	1.8[4]	*SP*	1.8	6.7	IRB
AGAL351.571+00.762	17 : 20 : 51.00	−35 : 35 : 25.8	−3.15	0.79	10.60	16.02	213.40	*N*	1.8[4]	*SP*	1.8	6.7	D24
AGAL351.581-00.352	17 : 25 : 24.90	−36 : 12 : 44.0	−95.91	6.81	−42.00	10.00	−61.60	*N*	5.1[2]	*HI*	6.8	2.0	IRB
AGAL351.774-00.537	17 : 26 : 42.59	−36 : 09 : 20.6	−2.75	0.72	−6.70	16.11	−151.30	*N*	0.4[2]	*HI*	0.7	7.8	IRB
AGAL353.066+00.452	17 : 26 : 13.50	−34 : 31 : 54.0	1.70	17.49	137.90	17.49	137.90	*N*	–	–	17.5	9.1	D24
AGAL353.409-00.361	17 : 30 : 26.26	−34 : 41 : 49.7	−16.05	3.44	−21.80	13.45	−85.20	*N*	–	–	3.4	5.1	IRB
AGAL353.417-00.079	17 : 29 : 18.94	−34 : 32 : 05.9	−54.43	6.06	−8.60	10.82	−15.30	*N*	–	–	6.1	2.6	D24
AGAL354.944-00.537	17 : 35 : 11.69	−33 : 30 : 23.8	−5.36	1.91	−18.00	15.02	−141.30	*N*	–	–	1.9	6.6	D24

Notes. As in Table C.1.

Table C.3: Distances and classification for the sources in sub-sample S3 derived from $C^{17}O$(3-2).

Source	RA (HH:MM:SS)	DEC (DD:MM:SS)	V_{LSR} (km s^{-1})	D_{near} (kpc)	z_{near} (pc)	D_{far} (kpc)	z_{far} (pc)	HI	D liter (kpc)	Method	Adopted D (kpc)	D_{GC} (kpc)	Group
AGAL030.818-00.056	18 : 47 : 46.82	−01 : 54 : 24.6	97.78	6.43	−6.20	8.17	−7.80	*N*	–	–	6.4	4.4	IRB
AGAL305.192-00.006	13 : 11 : 13.73	−62 : 47 : 27.1	−34.19	3.47	−0.40	6.33	−0.70	*F*	3.5[14]	*SP*	3.5	7.1	RMS
AGAL305.562+00.014	13 : 14 : 26.24	−62 : 44 : 24.9	−39.80	4.88	0.90	4.88	0.90	*F*	3.5[14]	*SP*	3.5	7.1	RMS
AGAL309.384-00.134	13 : 47 : 24.03	−62 : 18 : 09.5	−51.28	5.34	−12.10	5.34	−12.10	*N*	3.5[2]	*HI*	5.3	6.6	D8
AGAL310.014+00.387	13 : 51 : 38.36	−61 : 39 : 15.1	−41.31	3.61	24.40	7.32	49.40	*N*	–	–	3.6	6.8	RMS
AGAL313.576+00.324	14 : 20 : 08.34	−60 : 42 : 05.4	−46.94	3.78	21.40	7.94	44.90	–	3.0[2]	*HI*	3.8	6.5	RMS
AGAL316.641-00.087	14 : 44 : 18.77	−59 : 55 : 11.5	−17.66	1.35	−2.10	11.01	−16.90	*F*	–	–	11.0	7.6	RMS
AGAL326.661+00.519	15 : 45 : 02.97	−54 : 09 : 10.7	−39.79	2.84	25.70	11.36	102.90	*N*	–	–	2.8	6.3	RMS
AGAL326.987-00.032	15 : 49 : 08.16	−54 : 23 : 06.9	−58.63	3.95	−2.10	10.31	−5.60	*N*	–	–	4.0	5.6	D8
AGAL327.119+00.509	15 : 47 : 32.98	−53 : 52 : 45.0	−83.65	5.51	49.00	8.77	78.10	*N*	4.7[2]	*HI*	5.5	4.9	RMS
AGAL327.393+00.199	15 : 50 : 18.99	−53 : 57 : 04.5	−89.17	5.92	20.60	8.40	29.20	*N*	4.5[2]	*HI*	5.9	4.8	RMS
AGAL329.066-00.307	16 : 01 : 09.69	−53 : 16 : 01.6	−41.90	3.00	−16.10	11.58	−62.30	*F*	11.8[2]	*HI*	11.6	6.1	RMS
AGAL333.284-00.387	16 : 21 : 30.83	−50 : 26 : 58.9	−52.37	3.69	−24.80	11.50	−77.30	*N*	–	–	3.7	5.5	IRB
AGAL333.314+00.106	16 : 19 : 28.56	−50 : 04 : 42.1	−46.54	3.37	6.20	11.81	21.90	*N*	–	–	3.4	5.7	RMS
AGAL337.258-00.101	16 : 36 : 56.42	−47 : 22 : 27.0	−68.26	4.61	−8.10	11.07	−19.50	*F*	2.7[2]	*HI*	11.1	4.6	D8
AGAL338.926+00.554	16 : 40 : 34.36	−45 : 41 : 40.6	−61.57	4.40	42.40	11.47	110.70	*N*	3.9[1]	*HI*	4.4	4.7	IRB
AGAL339.623-00.122	16 : 46 : 06.58	−45 : 36 : 44.3	−34.58	3.01	−6.40	12.92	−27.50	*N*	2.6[2]	*HI*	3.0	5.8	RMS
AGAL340.746-01.001	16 : 54 : 03.66	−45 : 18 : 45.1	−29.42	2.76	−48.20	13.29	−232.50	*N*	–	–	2.8	6.0	RMS
AGAL341.217-00.212	16 : 52 : 17.75	−44 : 26 : 54.5	−43.55	3.67	−13.60	12.43	−46.00	*N*	3.1[2]	*HI*	3.7	5.2	RMS
AGAL345.718+00.817	17 : 03 : 06.46	−40 : 17 : 05.9	−11.19	1.56	22.30	14.91	212.90	*N*	–	–	1.6	7.0	RMS
AGAL351.131+00.771	17 : 19 : 34.42	−35 : 56 : 46.8	−5.34	1.22	16.40	15.58	209.70	*N*	1.8[4]	*SP*	1.8	6.7	D24
AGAL351.416+00.646	17 : 20 : 53.04	−35 : 47 : 02.3	−7.37	1.64	18.40	15.18	170.80	*N*	1.8[4]	*SP*	1.8	6.7	IRB
AGAL351.444+00.659	17 : 20 : 54.60	−35 : 45 : 12.8	−4.30	1.04	11.90	15.78	181.20	*N*	1.8[4]	*SP*	1.8	6.7	D8

Notes. As in Table C.1.

Table C.4: Line parameters for sub-sample S1.

Source	$C^{17}O(1-0)$							$C^{17}O(3-2)$						
	$\int T_{MB} dV$ (K km s^{-1})	T_{MB} (K)	rms (K)	V_{LSR} (km s^{-1})	$\sigma(V_{LSR})$ (km s^{-1})	ΔV (km s^{-1})	$\sigma(\Delta V)$ (km s^{-1})	$\int T_{MB} dV$ (K km s^{-1})	T_{MB} (K)	rms (K)	V_{LSR} (km s^{-1})	$\sigma(V_{LSR})$ (km s^{-1})	ΔV (km s^{-1})	$\sigma(\Delta V)$ (km s^{-1})
AGAL008.684-00.367	7.69	1.32	0.08	37.19	0.07	4.1	0.1	6.9	1.8	0.07	37.26	0.04	3.6	0.1
AGAL008.706-00.414	2.75	0.66	0.07	38.64	0.12	2.2	0.3	1.0	0.3	0.07	37.62	0.15	1.8	0.2
AGAL010.444-00.017	4.08	0.64	0.07	75.07	0.52	3.8	1.7	1.9	0.7	0.07	74.84	0.10	2.8	0.2
AGAL010.472+00.027	7.34	1.11	0.07	66.76	0.10	4.4	0.5	24.1	2.9	0.10	66.33	0.12	6.9	0.3
AGAL010.624-00.384	21.05	2.96	0.08	−3.02	0.00	5.8	0.1	77.6	11.8	0.08	−2.81	0.01	5.9	0.1
AGAL012.804-00.199	17.20	2.53	0.07	35.40	0.04	5.5	0.1	52.5	8.4	0.07	35.32	0.01	5.7	0.1
AGAL013.178+00.059	2.85	0.50	0.07	49.62	0.22	4.6	0.7	3.4	1.1	0.07	49.26	0.07	2.8	0.2
AGAL013.658-00.599	2.40	0.65	0.07	47.57	0.10	2.4	0.2	4.9	1.6	0.08	47.37	0.04	2.6	0.1
AGAL014.114-00.574	4.07	0.89	0.07	20.05	0.10	3.5	0.2	6.6	2.4	0.08	19.48	0.03	2.4	0.1
AGAL014.194-00.194	3.46	0.75	0.07	38.43	0.52	2.9	1.7	2.4	0.8	0.08	38.90	0.54	2.9	1.8
AGAL014.492-00.139	3.55	0.73	0.07	38.66	0.10	2.6	0.3	1.7	0.5	0.08	39.45	0.17	3.6	0.4
AGAL014.632-00.577	1.84	0.63	0.07	17.73	0.11	2.3	0.2	5.2	1.8	0.08	17.88	0.04	2.6	0.1
AGAL015.029-00.669-1	5.98	1.22	0.06	18.82	0.06	3.3	0.2	28.7	7.3	0.08	18.53	0.01	3.5	0.1
AGAL015.029-00.669-2	1.55	0.49	0.06	23.24	0.14	2.2	0.3	8.9	3.5	0.08	23.16	0.02	2.0	0.1
AGAL018.606-00.074	1.63	0.31	0.07	45.83	0.24	3.0	0.4	1.4	0.5	0.08	44.92	0.15	2.4	0.3
AGAL018.734-00.226	2.94	0.34	0.06	41.81	0.41	9.1	1.3	3.0	0.6	0.08	40.83	0.18	4.5	0.4
AGAL018.888-00.474	5.19	0.79	0.06	65.26	0.11	4.0	0.5	7.5	1.6	0.08	65.37	0.06	4.2	0.1
AGAL019.882-00.534	1.91	0.49	0.06	44.17	0.09	1.9	0.2	8.5	2.5	0.09	43.71	0.03	3.0	0.1
AGAL022.376+00.447-1	1.72	0.39	0.06	53.21	0.17	2.7	0.5	0.6	0.2	0.06	52.86	0.17	1.2	0.1
AGAL022.376+00.447-2	1.32	0.64	0.05	60.05	0.05	1.7	0.1	...	...	0.06	...	...	...	...
AGAL023.206-00.377	3.13	0.65	0.05	77.37	0.11	2.6	0.3	4.8	1.0	0.07	76.77	0.07	3.9	0.2
AGAL024.629+00.172-1	2.00	0.63	0.06	115.21	0.07	1.9	0.1	1.4	0.4	0.07	114.53	0.17	3.3	0.4
AGAL024.629+00.172-2	2.92	0.98	0.05	52.36	0.04	1.6	0.1	...	...	0.07	...	...	...	...
AGAL028.564-00.236	4.61	0.96	0.06	86.44	0.07	2.7	0.2	1.6	0.4	0.06	86.50	0.20	3.7	0.5
AGAL028.861+00.066-1	4.99	1.24	0.06	103.22	0.05	2.5	0.1	14.3	4.0	0.07	103.04	0.02	2.9	0.1
AGAL028.861+00.066-2	1.03	0.36	0.06	99.16	0.17	2.1	0.3	0.7	0.3	0.07	98.66	0.23	2.3	0.4
AGAL030.848-00.081-1	1.47	0.33	0.05	93.55	0.17	2.5	0.2	1.7	0.6	0.06	93.83	0.11	2.9	0.3
AGAL030.848-00.081-2	2.30	0.44	0.05	97.70	0.20	2.2	0.3	1.3	0.4	0.06	97.35	0.10	1.6	0.1
AGAL030.848-00.081-3	0.91	0.37	0.05	100.91	0.22	2.4	0.3	0.4	0.2	0.06	101.03	0.18	1.1	0.2
AGAL030.893+00.139-1	2.08	0.40	0.06	106.90	0.17	3.1	0.5	1.0	0.3	0.07	106.67	0.21	2.2	0.2
AGAL030.893+00.139-2	1.80	0.44	0.06	96.46	0.23	3.8	0.7	1.9	0.5	0.07	96.28	0.15	3.1	0.5
AGAL031.412+00.307	7.59	1.28	0.07	97.35	0.09	3.7	0.4	22.0	3.8	0.07	97.13	0.05	5.2	0.1
AGAL034.258+00.154	15.04	2.22	0.05	57.72	0.04	5.2	0.1	55.6	9.5	0.07	58.05	0.03	5.3	0.1
AGAL034.401+00.226	6.62	1.27	0.05	56.64	0.08	4.9	0.2	9.2	1.8	0.06	56.85	0.04	4.3	0.1
AGAL034.411+00.234	2.28	0.53	0.05	57.21	0.13	2.9	0.3	4.6	1.1	0.07	57.63	0.09	3.9	0.3
AGAL034.821+00.351	4.21	0.93	0.05	57.49	0.06	3.0	0.1	6.0	2.1	0.07	56.50	0.03	2.4	0.1
AGAL035.197-00.742	4.63	0.84	0.06	33.86	0.10	4.3	0.4	10.0	2.3	0.07	33.44	0.04	3.8	0.1
AGAL037.554+00.201	2.97	0.72	0.05	85.29	0.06	2.0	0.2	5.9	1.6	0.07	85.16	0.05	3.3	0.1
AGAL043.166+00.011-1	8.16	0.88	0.05	4.46	0.50	8.6	0.8	69.2	6.2	0.08	4.91	0.02	9.9	0.2
AGAL043.166+00.011-2	3.98	0.59	0.05	12.59	0.13	5.4	0.2	16.8	2.7	0.08	12.82	0.12	5.4	0.3
AGAL049.489-00.389	18.32	1.84	0.05	56.36	0.11	7.8	0.3	75.9	9.7	0.08	56.61	0.07	6.9	0.2
AGAL053.141+00.069	3.33	0.73	0.05	21.49	0.52	2.8	1.7	9.5	2.6	0.08	21.48	0.03	3.0	0.1
AGAL059.782+00.066	1.92	0.59	0.05	22.32	0.09	2.2	0.2	5.4	2.0	0.09	22.16	0.04	2.3	0.1

Notes. The columns show the integrated intensity, the main beam temperature, the rms of the spectrum, the V_{LSR}- and the width of the line, with their uncertainties for the molecular lines specified.

Table C.5: Line parameters $C^{18}O(1-0)$ for sub-sample S1.

Source	$\int T_{MB} dV$ (K km s^{-1})	T_{MB} (K)	rms (K)	V_{LSR} (km s^{-1})	$\sigma(V_{LSR})$ (km s^{-1})	ΔV (km s^{-1})	$\sigma(\Delta V)$ (km s^{-1})
AGAL008.684-00.367	26.42	5.22	0.08	37.27	0.02	4.9	0.1
AGAL008.706-00.414	9.22	3.12	0.07	38.70	0.02	2.9	0.1
AGAL010.444-00.017	10.49	2.55	0.06	75.59	0.07	4.1	0.2
AGAL010.472+00.027	30.71	4.61	0.08	66.80	0.06	6.2	0.1
AGAL010.624-00.384	71.13	11.33	0.07	−2.87	0.01	6.0	0.1
AGAL012.804-00.199	54.46	8.66	0.06	35.51	0.01	5.9	0.1
AGAL013.178+00.059	7.76	2.76	0.09	49.20	0.04	2.7	0.1
AGAL013.658-00.599	10.20	3.40	0.09	47.81	0.02	2.8	0.1
AGAL014.114-00.574	14.09	3.96	0.08	20.02	0.02	3.5	0.1
AGAL014.194-00.194	10.30	3.33	0.08	38.70	0.03	2.9	0.1
AGAL014.492-00.139	11.16	3.12	0.08	38.73	0.03	3.4	0.1
AGAL014.632-00.577	8.09	3.44	0.07	18.13	0.02	2.2	0.1
AGAL015.029-00.669-1	19.34	5.27	0.07	18.98	0.01	3.6	0.1
AGAL015.029-00.669-2	5.33	1.88	0.07	23.28	0.03	2.5	0.1
AGAL018.606-00.074	7.16	1.90	0.07	45.84	0.04	3.5	0.1
AGAL018.734-00.226	6.44	1.13	0.06	42.10	0.09	5.6	0.2
AGAL018.888-00.474	19.20	4.08	0.07	65.42	0.02	4.6	0.1
AGAL019.882-00.534	5.92	2.68	0.06	44.12	0.02	2.0	0.1
AGAL022.376+00.447-1	6.15	2.54	0.06	53.48	0.05	2.3	0.1
AGAL022.376+00.447-2	3.41	2.54	0.06	60.08	0.01	1.1	0.1
AGAL023.206-00.377	9.47	2.82	0.06	77.45	0.03	3.3	0.1
AGAL024.629+00.172-1	6.69	2.55	0.06	115.34	0.06	2.5	0.1
AGAL024.629+00.172-2	6.47	2.76	0.06	52.68	0.05	2.2	0.1
AGAL028.564-00.236	15.60	3.57	0.05	86.39	0.03	3.8	0.1
AGAL028.861+00.066-1	15.92	4.89	0.06	103.28	0.02	3.0	0.1
AGAL028.861+00.066-2	4.33	1.96	0.06	99.32	0.05	2.1	0.1
AGAL030.848-00.081-1	6.99	2.20	0.05	94.52	0.02	3.0	0.1
AGAL030.848-00.081-2	2.86	1.32	0.05	97.60	0.03	1.9	0.1
AGAL030.848-00.081-3	4.81	1.48	0.05	100.51	0.04	3.4	0.1
AGAL030.893+00.139-1	8.27	2.50	0.05	106.57	0.11	3.7	0.3
AGAL030.893+00.139-2	9.27	2.76	0.05	96.52	0.09	3.7	0.2
AGAL031.412+00.307	25.17	4.92	0.06	97.03	0.02	5.2	0.1
AGAL034.258+00.154	44.28	7.40	0.06	57.66	0.01	5.6	0.1
AGAL034.401+00.226	16.70	5.64	0.05	56.19	0.02	3.1	0.1
AGAL034.411+00.234	7.78	2.17	0.05	57.33	0.02	3.3	0.1
AGAL034.821+00.351	11.69	3.62	0.05	57.21	0.01	3.2	0.1
AGAL035.197-00.742	12.38	4.43	0.05	33.71	0.01	3.0	0.1
AGAL037.554+00.201	9.90	2.69	0.05	85.31	0.03	3.5	0.1
AGAL043.166+00.011-1	24.61	2.63	0.05	4.37	0.07	9.0	0.2
AGAL043.166+00.011-2	18.27	2.97	0.05	11.90	0.05	5.9	0.1
AGAL049.489-00.389	49.45	5.26	0.05	56.93	0.04	9.4	0.1
AGAL053.141+00.069	8.99	3.26	0.05	21.75	0.01	2.6	0.1
AGAL059.782+00.066	5.71	2.70	0.05	22.48	0.01	2.0	0.1

Notes. As in Table C.4.

Table C.6: Line parameters ^{13}CO(1 − 0) for sub-sample S1.

Source	$\int T_{\rm MB} dV$ (K km s^{-1})	$T_{\rm MB}$ (K)	rms (K)	$V_{\rm LSR}$ (km s^{-1})	$\sigma(V_{\rm LSR})$ (km s^{-1})	ΔV (km s^{-1})	$\sigma(\Delta V)$ (km s^{-1})
AGAL008.684-00.367	81.21	11.93	0.07	36.71	0.03	6.7	0.1
AGAL008.706-00.414	39.14	8.99	0.06	38.50	0.04	3.9	0.1
AGAL010.444-00.017	39.31	7.02	0.07	75.48	0.10	5.4	0.3
AGAL010.472+00.027	146.22	18.55	0.08	66.61	0.02	7.2	0.1
AGAL010.624-00.384	258.35	34.56	0.07	−3.03	0.01	7.0	0.1
AGAL012.804-00.199	176.77	23.40	0.07	35.33	0.02	7.4	0.1
AGAL013.178+00.059	42.80	12.89	0.10	49.24	0.04	3.2	0.1
AGAL013.658-00.599	45.41	12.52	0.08	48.11	0.02	3.5	0.1
AGAL014.114-00.574	53.34	17.98	0.08	19.50	0.02	3.2	0.1
AGAL014.194-00.194	49.71	13.73	0.09	38.72	0.02	3.4	0.1
AGAL014.492-00.139	42.52	7.85	0.09	39.22	0.05	6.0	0.1
AGAL014.632-00.577	42.36	13.88	0.10	17.80	0.02	2.7	0.1
AGAL015.029-00.669-1	147.30	31.61	0.08	18.97	0.00	4.5	0.1
AGAL015.029-00.669-2	46.34	14.93	0.08	23.30	0.01	2.9	0.1
AGAL018.606-00.074	29.45	8.97	0.06	45.48	0.04	3.3	0.1
AGAL018.734-00.226	39.77	6.71	0.07	41.78	0.05	6.0	0.1
AGAL018.888-00.474	102.73	17.32	0.07	65.33	0.03	5.8	0.1
AGAL019.882-00.534	44.36	15.68	0.06	44.16	0.02	2.7	0.1
AGAL022.376+00.447-1	21.26	7.78	0.06	53.22	0.03	2.5	0.1
AGAL022.376+00.447-2	19.21	4.62	0.06	60.52	0.11	4.8	0.3
AGAL023.206-00.377	27.89	5.33	0.06	77.92	0.09	5.1	0.2
AGAL024.629+00.172-1	25.44	7.82	0.06	115.20	0.04	3.0	0.1
AGAL024.629+00.172-2	14.05	4.08	0.06	53.05	0.08	3.3	0.2
AGAL028.564-00.236	39.51	6.89	0.06	86.36	0.09	5.1	0.2
AGAL028.861+00.066-1	52.71	12.45	0.06	103.65	0.06	4.2	0.1
AGAL028.861+00.066-2	13.85	3.95	0.06	98.44	0.18	3.4	0.5
AGAL030.848-00.081-1	31.35	9.60	0.05	94.48	0.03	3.0	0.1
AGAL030.848-00.081-2	18.67	6.99	0.05	97.58	0.04	2.5	0.1
AGAL030.848-00.081-3	26.84	6.34	0.05	100.92	0.06	3.9	0.1
AGAL030.893+00.139-1	39.69	8.37	0.05	106.67	0.03	4.2	0.1
AGAL030.893+00.139-2	38.55	6.04	0.05	96.57	0.12	6.6	0.3
AGAL031.412+00.307	65.62	8.43	0.07	97.36	0.04	8.2	0.1
AGAL034.258+00.154	106.52	25.98	0.10	56.32	0.02	3.8	0.1
AGAL034.401+00.226	61.16	12.77	0.05	56.78	0.05	6.1	0.1
AGAL034.411+00.234	32.69	7.68	0.05	57.68	0.05	5.1	0.1
AGAL034.821+00.351	38.39	9.31	0.06	57.35	0.03	4.0	0.1
AGAL035.197-00.742	71.34	13.45	0.05	33.71	0.01	5.0	0.1
AGAL037.554+00.201	32.26	5.71	0.05	85.31	0.05	7.0	0.1
AGAL043.166+00.011-1	193.67	19.09	0.06	4.19	0.01	9.8	0.1
AGAL043.166+00.011-2	112.41	16.83	0.06	12.01	0.00	6.2	0.1
AGAL049.489-00.389	310.33	29.66	0.07	56.76	0.00	9.8	0.1
AGAL053.141+00.069	42.35	13.62	0.05	21.61	0.01	3.0	0.1
AGAL059.782+00.066	49.46	16.49	0.05	22.58	0.01	2.9	0.1

Notes. As in Table C.4.

Table C.7: Line parameters $^{13}C^{18}O(1-0)$ for sub-sample S1.

Source	$\int T_{MB} dV$ (K km s^{-1})	T_{MB} (K)	rms (K)	V_{LSR} (km s^{-1})	$\sigma(V_{LSR})$ (km s^{-1})	ΔV (km s^{-1})	$\sigma(\Delta V)$ (km s^{-1})
AGAL008.684-00.367	0.67	0.11	0.02	37.06	0.44	5.6	1.0
AGAL008.706-00.414	0.35	0.09	0.02	38.38	0.97	3.8	2.4
AGAL010.444-00.017	...	...	0.03	...	...	...	...
AGAL010.472+00.027	...	...	0.04	...	...	...	...
AGAL010.624-00.384	1.40	0.26	0.03	−2.71	0.42	5.1	0.9
AGAL012.804-00.199	1.09	0.19	0.02	35.31	0.43	5.4	1.0
AGAL013.178+00.059	...	...	0.04	...	...	...	...
AGAL013.658-00.599	...	...	0.04	...	...	...	...
AGAL014.114-00.574	...	...	0.04	...	...	...	...
AGAL014.194-00.194	0.17	0.12	0.03	38.61	0.22	1.4	0.5
AGAL014.492-00.139	0.30	0.13	0.03	38.55	0.22	2.2	0.5
AGAL014.632-00.577	...	...	0.04	...	...	...	...
AGAL015.029-00.669-1	0.30	0.11	0.02	19.54	2.09	2.6	4.1
AGAL015.029-00.669-2	...	...	0.02	...	...	...	...
AGAL018.606-00.074	0.27	0.11	0.02	45.95	0.29	2.3	0.6
AGAL018.734-00.226	...	...	0.04	...	...	...	...
AGAL018.888-00.474	...	...	0.04	...	...	...	...
AGAL019.882-00.534	...	...	0.04	...	...	...	...
AGAL022.376+00.447-1	0.26	0.07	0.02	53.37	0.58	3.7	1.8
AGAL022.376+00.447-2	0.34	0.10	0.02	60.54	0.30	3.3	0.7
AGAL023.206-00.377	0.27	0.10	0.02	76.53	0.29	2.4	0.6
AGAL024.629+00.172-1	0.25	0.06	0.02	114.34	0.59	4.1	1.1
AGAL024.629+00.172-2	0.24	0.16	0.02	52.61	0.13	1.4	0.3
AGAL028.564-00.236	0.46	0.18	0.03	85.95	0.17	2.4	0.3
AGAL028.861+00.066-1	0.43	0.16	0.02	103.08	0.19	2.6	0.5
AGAL028.861+00.066-2	0.23	0.11	0.03	99.53	0.23	1.9	0.4
AGAL030.848-00.081-1	0.28	0.07	0.02	95.87	0.47	3.7	1.3
AGAL030.848-00.081-2	...	...	0.02	...	...	...	...
AGAL030.848-00.081-3	...	...	0.02	...	...	...	...
AGAL030.893+00.139-1	0.27	0.12	0.02	106.47	0.25	2.1	0.6
AGAL030.893+00.139-2	0.26	0.11	0.02	96.17	0.27	2.3	0.6
AGAL031.412+00.307	0.84	0.19	0.03	97.33	0.57	4.2	1.7
AGAL034.258+00.154	0.91	0.15	0.03	57.19	0.58	5.8	1.3
AGAL034.401+00.226	0.33	0.14	0.03	55.90	0.19	2.2	0.5
AGAL034.411+00.234	0.21	0.10	0.02	57.52	0.29	2.1	0.7
AGAL034.821+00.351	0.22	0.13	0.03	57.37	0.22	1.7	0.5
AGAL035.197-00.742	0.31	0.07	0.01	33.62	0.93	4.3	1.3
AGAL037.554+00.201	0.36	0.12	0.04	85.70	0.26	2.7	0.5
AGAL043.166+00.011-1	...	...	0.04	...	...	...	...
AGAL043.166+00.011-2	...	...	0.04	...	...	...	...
AGAL049.489-00.389	0.61	0.09	0.02	56.63	0.97	6.5	2.2
AGAL053.141+00.069	0.27	0.06	0.02	21.03	1.75	4.1	3.1
AGAL059.782+00.066	...	...	0.04	...	...	...	...

Notes. As in Table C.4.

Table C.8: Line parameters for sub-sample S2.

Source	$C^{18}O(2-1)$									$C^{17}O(3-2)$								
	$\int T_{MB} dV$ (K km s^{-1})	T_{MB} (K)	rms (K)	V_{LSR} (km s^{-1})	$\sigma(V_{LSR})$ (km s^{-1})	ΔV (km s^{-1})	$\sigma(\Delta V)$ (km s^{-1})	τ	68%int.	$\int T_{MB} dV$ (K km s^{-1})	T_{MB} (K)	rms (K)	V_{LSR} (km s^{-1})	$\sigma(V_{LSR})$ (km s^{-1})	ΔV (km s^{-1})	$\sigma(\Delta V)$ (km s^{-1})	τ	$\sigma(\tau)$
AGAL301.136-00.226	54.90	33.94	0.09	−39.15	0.01	4.7	0.1	0.4	0.3 – 0.6	21.88	3.93	0.10	−39.28	0.02	4.7	0.1	0.1	0.1
AGAL305.209+00.206	42.23	21.22	0.08	−42.53	0.02	6.2	0.1	0.3	0.2 – 0.3	16.19	2.40	0.08	−42.15	0.05	4.9	0.2	0.9	0.1
AGAL305.794-00.096	11.87	11.32	0.08	−40.82	0.03	3.1	0.1	1.1	0.7 – 1.6	1.99	0.69	0.09	−40.91	0.14	2.3	0.4	0.7	0.6
AGAL317.867-00.151	10.73	8.21	0.11	−40.19	0.04	3.6	0.1	0.4	0.2 – 0.5	3.07	0.76	0.08	−40.61	0.12	3.7	0.5	0.1	5.5
AGAL318.779-00.137	11.03	7.55	0.11	−38.14	0.04	4.1	0.1	0.5	0.3 – 0.6	2.26	0.72	0.09	−39.36	0.11	2.8	0.3	0.1	0.4
AGAL320.881-00.397	18.26	17.70	0.08	−45.30	0.01	3.2	0.1	0.7	0.5 – 0.9	5.93	2.42	0.09	−45.96	0.03	2.1	0.1	0.1	0.1
AGAL327.293-00.579	76.06	36.48	0.06	−44.72	0.02	5.9	0.1	0.8	0.6 – 1.1	58.18	7.47	0.07	−44.89	0.11	5.9	0.3	0.1	0.1
AGAL328.809+00.632	76.43	50.75	0.13	−41.86	0.01	4.4	0.1	0.7	0.5 – 0.9	50.72	9.16	0.10	−41.87	0.02	5.0	0.1	0.1	0.1
AGAL329.029-00.206	15.91	9.26	0.12	−43.49	0.05	5.0	0.1	0.6	0.4 – 0.8	5.33	1.18	0.08	−43.17	0.09	4.0	0.2	0.1	0.1
AGAL330.879-00.367	78.49	46.94	0.07	−62.48	0.01	4.9	0.1	0.8	0.6 – 1.1	47.32	9.51	0.09	−62.58	0.02	4.4	0.1	0.1	0.1
AGAL330.954-00.182	127.05	50.43	0.08	−91.16	0.01	7.8	0.1	1.1	0.8 – 1.5	86.66	9.85	0.09	−92.02	0.01	8.0	0.1	0.1	0.1
AGAL331.709+00.582	10.52	7.49	0.08	−67.76	0.03	4.3	0.1	0.3	0.2 – 0.5	3.72	0.81	0.08	−67.29	0.13	4.4	0.4	0.1	0.1
AGAL332.094-00.421	39.15	29.88	0.11	−56.94	0.01	4.1	0.1	1.1	0.7 – 1.5	17.56	4.09	0.08	−57.49	0.01	3.5	0.1	0.2	0.1
AGAL332.826-00.549	99.99	41.87	0.17	−57.06	0.01	6.8	0.1	1.0	0.7 – 1.3	66.59	10.80	0.11	−57.39	0.01	5.4	0.1	0.1	0.1
AGAL333.134-00.431	118.73	54.55	0.17	−53.11	0.01	6.0	0.1	0.6	0.5 – 0.8	62.99	9.17	0.10	−53.50	0.01	6.1	0.1	0.1	0.1
AGAL333.604-00.212	77.21	24.17	0.18	−48.39	0.02	10.1	0.1	0.4	0.3 – 0.5	36.45	5.25	0.09	−47.10	0.03	6.4	0.1	0.1	0.1
AGAL333.656+00.059	19.85	15.64	0.08	−85.05	0.03	3.5	0.1	0.7	0.5 – 0.8	3.16	1.18	0.08	−85.24	0.07	2.5	0.2	0.1	0.1
AGAL335.789+00.174	29.52	23.22	0.11	−50.11	0.01	3.5	0.1	0.5	0.4 – 0.7	14.08	3.41	0.08	−50.56	0.02	3.4	0.1	0.1	0.1
AGAL336.958-00.224	7.71	7.39	0.09	−71.27	0.03	3.0	0.1	0.4	0.3 – 0.6	0.91	0.30	0.09	−71.31	0.21	1.8	1.7	2.3	1.6
AGAL337.176-00.032	23.43	12.69	0.13	−67.77	0.05	5.9	0.1	0.5	0.4 – 0.7	2.65	0.78	0.08	−68.16	0.09	2.1	0.3	1.4	0.8
AGAL337.286+00.007-1	6.81	5.52	0.07	−106.60	0.08	3.8	0.2	2.1	1.2 – 0.7	1.23	0.39	0.09	−107.45	0.19	1.9	0.5	1.1	1.0
AGAL337.286+00.007-2	3.81	4.03	0.07	−74.28	0.13	2.8	0.3	0.5	0.3 – 0.6	…	…	0.09	…	…	…	…	…	…
AGAL337.406-00.402	51.98	35.84	0.18	−41.01	0.02	4.5	0.1	0.9	0.6 – 1.1	42.04	8.61	0.09	−40.85	0.02	4.3	0.1	0.1	0.1
AGAL337.704-00.054	39.31	18.71	0.11	−47.41	0.02	6.0	0.1	0.6	0.4 – 0.7	21.96	3.10	0.07	−47.35	0.03	6.0	0.1	0.1	0.1
AGAL337.916-00.477	57.65	37.43	0.18	−39.55	0.01	4.5	0.1	0.6	0.5 – 0.7	51.17	10.30	0.09	−39.45	0.01	4.3	0.1	0.1	0.1
AGAL338.066+00.044-1	7.20	5.07	0.08	−69.17	0.06	4.3	0.2	0.6	0.4 – 0.8	1.58	0.72	0.09	−70.08	0.15	2.5	0.4	0.1	0.3
AGAL338.066+00.044-2	14.90	7.07	0.08	−40.03	0.05	6.0	0.1	0.5	0.4 – 0.7	1.14	0.20	0.06	−39.99	0.67	4.6	2.8	0.1	1.2
AGAL338.786+00.476	17.44	10.88	0.08	−63.82	0.02	4.6	0.1	0.7	0.5 – 0.9	2.52	0.67	0.09	−63.97	0.11	2.4	0.3	1.0	0.5
AGAL340.374-00.391	21.23	12.62	0.07	−43.55	0.03	5.0	0.1	0.9	0.6 – 1.2	2.91	0.64	0.09	−43.37	0.12	2.6	0.1	2.1	0.1
AGAL340.784-00.097	12.27	11.51	0.18	−101.46	0.04	3.2	0.1	0.7	0.5 – 0.8	8.60	2.06	0.09	−101.73	0.05	3.7	0.1	0.1	0.1
AGAL342.484+00.182	20.16	24.45	0.15	−41.49	0.01	2.4	0.1	0.9	0.6 – 1.1	5.38	2.21	0.10	−41.55	0.03	2.1	0.1	0.1	0.6
AGAL343.128-00.062	47.57	31.18	0.16	−30.58	0.02	4.5	0.1	0.6	0.4 – 0.7	28.22	5.25	0.09	−30.34	0.02	4.8	0.1	0.1	0.1
AGAL343.756-00.164	17.51	12.37	0.16	−27.80	0.04	4.5	0.1	0.4	0.3 – 0.5	7.24	1.84	0.11	−28.15	0.07	3.4	0.2	0.1	0.1
AGAL344.227-00.569	26.64	19.09	0.17	−22.26	0.02	4.0	0.1	1.1	0.7 – 1.5	13.84	3.07	0.11	−22.30	0.04	3.9	0.1	0.1	0.1
AGAL345.003-00.224-1	24.25	13.67	0.18	−27.61	0.08	6.0	0.2	1.7	1.0 – 3.1	17.26	3.10	0.10	−26.86	0.04	5.0	0.1	0.1	0.1
AGAL345.003-00.224-2	6.08	8.88	0.18	−85.22	0.13	2.3	0.4	2.3	1.4 – 3.1	…	…	0.10	…	…	…	…	…	…
AGAL345.488+00.314	66.29	41.87	0.18	−17.57	0.01	5.2	0.1	0.6	0.4 – 0.7	31.63	6.56	0.09	−17.73	0.02	4.6	0.1	0.1	0.1
AGAL345.504+00.347	42.84	26.10	0.19	−17.85	0.02	4.8	0.1	0.5	0.4 – 0.6	24.68	4.45	0.10	−17.79	0.03	4.7	0.1	0.1	0.1
AGAL351.161+00.697	49.61	34.57	0.07	−6.68	0.03	4.2	0.1	0.5	0.3 – 0.6	25.24	5.43	0.10	−6.50	0.03	4.2	0.1	0.1	0.1
AGAL351.244+00.669	63.45	56.46	0.15	−3.29	0.01	3.4	0.1	0.5	0.4 – 0.7	39.47	11.20	0.10	−3.39	0.01	3.1	0.1	0.1	0.1
AGAL351.571+00.762	16.09	22.80	0.08	−3.15	0.01	2.0	0.1	0.8	0.6 – 1.1	2.53	1.52	0.10	−3.36	0.04	1.5	0.1	0.1	0.2
AGAL351.581-00.352	51.25	31.31	0.09	−95.91	0.01	5.3	0.1	2.0	1.2 – 3.2	38.59	7.18	0.11	−95.43	0.02	4.1	0.1	0.4	0.1
AGAL351.774-00.537	101.78	48.21	0.13	−2.75	0.02	6.1	0.1	1.2	0.8 – 1.7	68.01	9.68	0.13	−2.80	0.04	5.6	0.1	0.1	0.1
AGAL353.066+00.452-1	13.23	14.37	0.10	1.70	0.02	2.7	0.1	0.4	0.3 – 0.5	3.19	1.28	0.12	1.50	0.07	1.9	0.3	0.4	0.4
AGAL353.066+00.452-2	3.28	4.15	0.10	−2.06	0.05	2.4	0.1	0.1	0.0 – 0.1	…	…	0.12	…	…	…	…	…	…
AGAL353.409-00.361	58.29	30.89	0.14	−16.05	0.01	5.7	0.1	0.4	0.3 – 0.5	37.39	8.62	0.12	−15.77	0.01	3.8	0.1	0.1	0.1
AGAL353.417-00.079-1	7.47	7.58	0.09	−54.43	0.03	2.8	0.1	1.3	0.8 – 2.0	0.76	0.50	0.12	−54.90	0.54	1.1	1.8	0.3	0.1
AGAL353.417-00.079-2	5.70	8.69	0.09	−16.82	0.02	1.9	0.1	1.7	1.0 – 3.2	1.07	1.01	0.12	−17.10	0.06	0.9	0.1	0.1	0.2
AGAL353.417-00.079-3	5.81	3.13	0.09	−49.20	0.09	3.8	0.2	0.3	0.1 – 0.5	…	…	0.12	…	…	…	…	…	…
AGAL353.417-00.079-4	2.42	2.99	0.09	−81.79	0.08	2.5	0.2	0.3	0.2 – 0.5	…	…	0.12	…	…	…	…	…	…
AGAL354.944-00.537	13.26	14.11	0.10	−5.36	0.02	2.7	0.1	0.8	0.6 – 1.0	1.42	0.62	0.13	−5.58	0.18	2.0	0.5	0.9	0.8

Notes. The columns show the integrated intensity, the main beam temperature, the rms of the spectrum, the V_{LSR}-, the width- and the opacity of the line, with their uncertainties for the molecular lines specified.

Table C.9: Line parameters $C^{17}O(3-2)$ for sub-sample S3.

Source	$\int T_{MB} dV$ (K km s^{-1})	T_{MB} (K)	rms (K)	V_{LSR} (km s^{-1})	$\sigma(V_{LSR})$ (km s^{-1})	ΔV (km s^{-1})	$\sigma(\Delta V)$ (km s^{-1})	τ	$\sigma(\tau)$
AGAL030.818-00.056	12.15	1.98	0.07	97.78	0.05	5.5	0.1	2.0	0.1
AGAL305.192-00.006	3.16	0.86	0.07	−34.19	0.09	3.0	0.3	0.9	0.1
AGAL305.562+00.014	16.84	4.79	0.09	−39.80	0.02	3.0	0.1	4.8	0.1
AGAL309.384-00.134	6.25	1.76	0.09	−51.28	0.06	3.1	0.1	1.8	0.1
AGAL310.014+00.387	7.55	2.02	0.09	−41.31	0.04	3.0	0.1	2.0	0.1
AGAL313.576+00.324	7.69	1.65	0.09	−46.94	0.05	3.5	0.3	1.6	0.2
AGAL316.641-00.087	3.04	0.78	0.09	−17.66	0.10	3.1	0.2	0.8	0.5
AGAL326.661+00.519	12.25	4.38	0.08	−39.79	0.02	2.4	0.1	4.4	0.1
AGAL326.987-00.032	1.46	0.32	0.08	−58.63	0.34	4.8	0.9	0.3	0.3
AGAL327.119+00.509	10.41	3.21	0.08	−83.65	0.02	2.8	0.1	3.2	0.1
AGAL327.393+00.199	3.86	1.01	0.08	−89.17	0.07	3.0	0.2	1.0	0.1
AGAL329.066-00.307	2.39	0.57	0.09	−41.90	0.16	3.6	0.4	0.6	0.3
AGAL333.284-00.387	31.82	8.02	0.10	−52.37	0.01	3.5	0.1	8.0	0.1
AGAL333.314+00.106	5.85	1.35	0.09	−46.54	0.07	3.9	0.2	1.4	0.3
AGAL337.258-00.101	2.24	0.64	0.10	−68.26	0.15	2.9	0.4	0.6	0.3
AGAL338.926+00.554	15.84	3.02	0.11	−61.57	0.05	5.3	0.1	3.0	0.1
AGAL339.623-00.122	7.49	2.34	0.09	−34.58	0.04	2.7	0.1	2.3	0.1
AGAL340.746-01.001	4.86	1.72	0.09	−29.42	0.05	2.8	0.1	1.7	0.1
AGAL341.217-00.212	8.06	2.31	0.09	−43.55	0.04	3.0	0.1	2.3	0.1
AGAL345.718+00.817	5.97	2.15	0.09	−11.19	0.03	1.9	0.1	2.1	0.2
AGAL351.131+00.771	6.13	3.37	0.10	−5.34	0.02	1.4	0.1	3.4	0.1
AGAL351.416+00.646	48.48	8.72	0.08	−7.37	0.07	4.8	0.2	8.7	0.1
AGAL351.444+00.659	26.20	5.96	0.11	−4.30	0.02	3.8	0.1	6.0	0.1

Notes. As in Table C.8.

Table C.10: Excitation temperature for sub-sample S1.

Source	T_{ex} (K)	68%int. (K)	Group
AGAL008.684-00.367	11.8	10.6 – 12.6	D8
AGAL008.706-00.414	8.4	7.7 – 8.9	D24
AGAL010.444-00.017	9.2	8.5 – 9.8	D24
AGAL010.472+00.027	27.9	20.4 – 32.5	IRB
AGAL010.624-00.384	31.7	22.6 – 37.2	IRB
AGAL012.804-00.199	25.8	18.8 – 29.7	IRB
AGAL013.178+00.059	13.5	11.9 – 14.7	D8
AGAL013.658-00.599	18.6	15.2 – 20.9	RMS
AGAL014.114-00.574	15.9	13.7 – 17.6	D8
AGAL014.194-00.194	10.6	9.5 – 11.4	D8
AGAL014.492-00.139	9.2	8.4 – 9.8	D24
AGAL014.632-00.577	23.9	18.8 – 28.0	D8
AGAL015.029-00.669-1	44.9	29.9 – 54.3	IRB
AGAL015.029-00.669-2	56.0	45.9 – 49.3	(IRB)
AGAL018.606-00.074	11.6	10.2 – 12.5	D24
AGAL018.734-00.226	12.5	11.1 – 13.7	D8
AGAL018.888-00.474	14.9	12.8 – 16.3	D8
AGAL019.882-00.534	40.1	26.7 – 46.7	RMS
AGAL022.376+00.447-1	8.3	7.6 – 8.8	D24
AGAL022.376+00.447-2	4.8	4.0 – 5.4	(D24)
AGAL023.206-00.377	15.4	13.2 – 17.1	D8
AGAL024.629+00.172-1	10.7	9.6 – 11.6	D24
AGAL024.629+00.172-2	4.5	3.7 – 5.1	(D24)
AGAL028.564-00.236	8.4	7.8 – 8.9	D24
AGAL028.861+00.066-1	24.3	19.2 – 28.4	RMS
AGAL028.861+00.066-2	10.5	9.3 – 11.5	(RMS)
AGAL030.848-00.081-1	13.5	11.7 – 14.8	D24
AGAL030.848-00.081-2	9.7	8.9 – 10.4	(D24)
AGAL030.848-00.081-3	9.0	8.1 – 9.7	(D24)
AGAL030.893+00.139-1	9.2	8.4 – 9.9	(D24)
AGAL030.893+00.139-2	12.6	11.1 – 13.9	D24
AGAL031.412+00.307	24.6	19.0 – 28.9	IRB
AGAL034.258+00.154	31.8	22.1 – 36.9	IRB
AGAL034.401+00.226	14.6	12.7 – 15.8	RMS
AGAL034.411+00.234	18.4	15.4 – 20.7	D8
AGAL034.821+00.351	14.8	12.8 – 16.2	RMS
AGAL035.197-00.742	19.1	15.5 – 21.3	RMS
AGAL037.554+00.201	18.1	15.4 – 20.4	RMS
AGAL043.166+00.011-1	70.0	54.0 – 73.0	IRB
AGAL043.166+00.011-2	37.8	25.7 – 44.1	(IRB)
AGAL049.489-00.389	36.7	24.9 – 42.1	IRB
AGAL053.141+00.069	24.2	18.4 – 27.8	RMS
AGAL059.782+00.066	23.9	18.2 – 27.1	RMS

Notes. In the Group column the identifiers between parentheses are the classifications of the main component.

Table C.11: Excitation temperature for sub-sample S2.

Source	T_{ex} (K)	68%int. (K)	Group
AGAL301.136-00.226	31.9	18.4 – 35.2	IRB
AGAL305.209+00.206	35.0	19.2 – 40.6	IRB
AGAL305.794-00.096	9.6	8.2 – 10.3	D24
AGAL317.867-00.151	20.5	14.6 – 22.4	D8
AGAL318.779-00.137	13.5	10.6 – 14.5	D8
AGAL320.881-00.397	19.8	14.7 – 22.2	D24
AGAL327.293-00.579	65.9	58.1 – 86.7	IRB
AGAL328.809+00.632	59.6	42.4 – 86.7	IRB
AGAL329.029-00.206	21.7	15.4 – 24.4	D8
AGAL330.879-00.367	48.5	26.3 – 66.6	IRB
AGAL330.954-00.182	48.2	26.4 – 59.5	IRB
AGAL331.709+00.582	28.6	16.8 – 30.7	D8
AGAL332.094-00.421	24.5	16.1 – 26.1	RMS
AGAL332.826-00.549	51.4	27.6 – 66.1	IRB
AGAL333.134-00.431	45.6	24.3 – 56.9	IRB
AGAL333.604-00.212	45.5	24.8 – 58.6	IRB
AGAL333.656+00.059	10.6	9.1 – 11.4	D24
AGAL335.789+00.174	40.9	21.6 – 47.8	D8
AGAL336.958-00.224	9.4	8.0 – 10.2	D24
AGAL337.176-00.032	8.9	7.8 – 9.6	D8
AGAL337.286+00.007-1	8.3	7.3 – 9.0	D24
AGAL337.286+00.007-2	4.5	3.4 – 5.2	(D24)
AGAL337.406-00.402	67.7	61.0 – 86.7	IRB
AGAL337.704-00.054	51.7	29.4 – 65.1	IRB
AGAL337.916-00.477	76.9	73.4 – 86.8	IRB
AGAL338.066+00.044-1	13.8	10.8 – 15.1	D24
AGAL338.066+00.044-2	7.4	6.5 – 7.9	(D24)
AGAL338.786+00.476	9.9	8.6 – 10.7	D24
AGAL340.374-00.391	9.0	7.8 – 9.6	D24
AGAL340.784-00.097	64.8	55.2 – 86.7	D8
AGAL342.484+00.182	14.7	11.7 – 16.0	D8
AGAL343.128-00.062	56.3	34.4 – 86.7	IRB
AGAL343.756-00.164	36.9	19.4 – 42.8	D8
AGAL344.227-00.569	30.7	18.4 – 34.5	D8
AGAL345.003-00.224-1	35.1	19.3 – 39.8	IRB
AGAL345.003-00.224-2	3.8	3.1 – 4.5	(IRB)
AGAL345.488+00.314	39.5	20.9 – 46.0	IRB
AGAL345.504+00.347	57.3	36.2 – 77.4	RMS
AGAL351.161+00.697	48.7	25.2 – 65.9	IRB
AGAL351.244+00.669	60.8	46.8 – 86.7	IRB
AGAL351.571+00.762	10.1	8.8 – 10.9	D24
AGAL351.581-00.352	32.9	19.6 – 37.3	IRB
AGAL351.774-00.537	43.5	22.5 – 51.2	IRB
AGAL353.066+00.452-1	16.4	12.5 – 18.1	D24
AGAL353.066+00.452-2	5.5	3.7 – 6.5	(D24)
AGAL353.409-00.361	66.8	59.8 – 86.8	IRB
AGAL353.417-00.079-1	7.2	6.3 – 7.8	D24
AGAL353.417-00.079-2	9.1	7.9 – 10.0	(D24)
AGAL353.417-00.079-3	4.0	3.1 – 4.6	(D24)
AGAL353.417-00.079-4	5.2	3.5 – 5.7	(D24)
AGAL354.944-00.537	8.2	7.2 – 8.9	D24

Notes. As in Table C.10

Table C.12: Optical depths and isotopic ratios for sub-sample S1.

Source	$\tau(C^{18}O(1-0))$	68%int.	$\tau(C^{17}O(1-0))$	68%int.	$\frac{[^{18}O]}{[^{17}O]}$	68%int.	$\frac{[^{12}C]}{[^{13}C]}$	68%int.	$\frac{[^{12}C^{17}O]}{[^{13}C^{18}O]}$	68%int.
AGAL008.684-00.367	0.77	0.61 – 0.91	0.17	0.15 – 0.20	4.4	3.9 – 4.7	51.2	46.4 – 55.8	11.7	10.7 – 12.6
AGAL008.706-00.414	1.00	0.73 – 1.21	0.21	0.17 – 0.25	4.7	4.1 – 5.1	39.3	34.3 – 43.7	8.4	7.6 – 9.2
AGAL010.444-00.017	0.67	0.50 – 0.80	0.20	0.16 – 0.23	3.4	3.0 – 3.7	100.0	80.6 – 116.9	29.4	23.4 – 34.1
AGAL010.472+00.027	0.26	0.17 – 0.32	< 0.10	...	4.6	4.2 – 5.0	95.7	76.6 – 110.1	20.9	16.6 – 24.3
AGAL010.624-00.384	0.43	0.30 – 0.53	0.11	0.08 – 0.13	4.1	3.7 – 4.4	60.1	54.7 – 64.7	14.8	13.6 – 15.8
AGAL012.804-00.199	0.46	0.33 – 0.56	0.12	0.09 – 0.15	3.7	3.4 – 4.0	59.2	54.0 – 63.8	15.9	14.7 – 17.1
AGAL013.178+00.059	0.29	0.20 – 0.36	< 0.10	...	3.5	3.2 – 3.8	75.7	60.7 – 90.3	21.6	16.9 – 25.2
AGAL013.658-00.599	0.28	0.19 – 0.33	< 0.10	...	4.8	4.4 – 5.2	83.5	66.2 – 100.5	17.4	13.5 – 20.6
AGAL014.114-00.574	0.38	0.27 – 0.46	< 0.10	...	4.2	3.8 – 4.6	95.8	76.1 – 111.3	22.7	18.3 – 26.3
AGAL014.194-00.194	0.54	0.41 – 0.63	0.15	0.12 – 0.18	3.6	3.2 – 3.9	59.7	52.5 – 66.1	16.7	14.6 – 18.6
AGAL014.492-00.139	0.82	0.61 – 0.97	0.20	0.16 – 0.23	4.1	3.7 – 4.5	50.6	44.7 – 55.7	12.4	11.2 – 13.5
AGAL014.632-00.577	0.20	0.12 – 0.24	< 0.10	...	5.0	4.6 – 5.4	86.7	69.3 – 100.5	17.4	13.7 – 20.3
AGAL015.029-00.669-1	0.13	0.07 – 0.15	< 0.10	...	3.4	3.2 – 3.7	62.8	57.7 – 67.7	18.4	16.8 – 19.9
AGAL015.029-00.669-2	< 0.10	...	< 0.10	...	3.7	3.4 – 4.0	44.6	33.6 – 53.7	12.1	9.1 – 14.5
AGAL018.606-00.074	0.40	0.23 – 0.50	< 0.10	...	5.0	4.5 – 5.5	33.3	29.6 – 37.0	6.6	6.0 – 7.4
AGAL018.734-00.226	0.12	0.09 – 0.14	< 0.10	...	2.6	2.4 – 2.8	30.9	22.2 – 38.1	12.0	8.5 – 14.5
AGAL018.888-00.474	0.47	0.33 – 0.55	0.10	0.08 – 0.12	4.5	4.0 – 4.9	100.1	79.6 – 118.3	22.4	17.9 – 26.4
AGAL019.882-00.534	< 0.10	...	< 0.10	...	3.4	3.1 – 3.7	62.9	47.3 – 74.1	18.4	14.1 – 22.1
AGAL022.376+00.447-1	0.70	0.50 – 0.83	0.14	0.11 – 0.17	4.9	4.3 – 5.4	36.4	30.8 – 41.2	7.5	6.4 – 8.4
AGAL022.376+00.447-2	1.19	0.47 – 1.68	0.26	0.17 – 0.36	4.4	3.3 – 5.1	18.1	13.0 – 22.1	4.1	3.6 – 4.5
AGAL023.206-00.377	0.31	0.21 – 0.37	< 0.10	...	3.4	3.1 – 3.7	40.4	36.0 – 44.6	11.9	10.5 – 13.1
AGAL024.629+00.172-1	0.58	0.39 – 0.69	0.14	0.11 – 0.16	4.1	3.7 – 4.5	34.7	29.8 – 38.6	8.4	7.3 – 9.3
AGAL024.629+00.172-2	1.11	0.59 – 1.57	0.35	0.26 – 0.48	3.1	2.6 – 3.6	43.9	35.1 – 50.9	14.1	12.6 – 15.6
AGAL028.564-00.236	1.19	0.93 – 1.38	0.25	0.21 – 0.28	4.8	4.3 – 5.3	51.9	46.2 – 57.1	10.8	9.7 – 11.8
AGAL028.861+00.066-1	0.31	0.22 – 0.38	< 0.10	...	3.6	3.3 – 3.9	41.7	37.3 – 45.0	11.5	10.6 – 12.5
AGAL028.861+00.066-2	0.34	0.22 – 0.42	< 0.10	...	4.9	4.4 – 5.4	26.7	22.0 – 30.8	5.5	4.6 – 6.4
AGAL030.848-00.081-1	0.29	0.20 – 0.35	< 0.10	...	5.3	4.8 – 5.7	29.0	25.7 – 31.8	5.5	4.9 – 6.0
AGAL030.848-00.081-2	0.26	0.18 – 0.31	0.18	0.13 – 0.21	1.4	1.3 – 1.6	37.8	29.5 – 45.8	26.6	20.9 – 31.5
AGAL030.848-00.081-3	0.29	0.19 – 0.35	< 0.10	...	5.7	5.0 – 6.2	40.9	29.5 – 51.1	7.2	5.1 – 8.9
AGAL030.893+00.139-1	0.48	0.35 – 0.57	0.10	0.08 – 0.12	4.8	4.4 – 5.1	38.7	34.3 – 42.6	8.1	7.2 – 9.0
AGAL030.893+00.139-2	0.29	0.21 – 0.34	< 0.10	...	5.8	5.3 – 6.2	40.5	36.3 – 44.2	7.0	6.2 – 7.7
AGAL031.412+00.307	0.38	0.23 – 0.47	0.10	0.07 – 0.12	3.8	3.4 – 4.0	35.3	31.8 – 38.3	9.4	8.7 – 10.1
AGAL034.258+00.154	0.36	0.22 – 0.46	0.11	0.07 – 0.13	3.4	3.1 – 3.7	56.4	51.0 – 61.1	16.6	15.1 – 17.8
AGAL034.401+00.226	0.48	0.35 – 0.58	0.14	0.11 – 0.17	3.3	3.0 – 3.5	62.6	56.4 – 67.9	19.2	17.4 – 21.1
AGAL034.411+00.234	0.19	0.13 – 0.22	< 0.10	...	3.8	3.5 – 4.1	43.9	39.5 – 47.9	11.6	10.5 – 12.9
AGAL034.821+00.351	0.36	0.25 – 0.44	0.11	0.08 – 0.14	3.2	2.9 – 3.5	55.9	50.0 – 62.5	17.4	15.2 – 19.4
AGAL035.197-00.742	0.28	0.18 – 0.34	< 0.10	...	3.3	3.0 – 3.5	47.2	43.3 – 51.5	14.4	13.1 – 15.6
AGAL037.554+00.201	0.31	0.20 – 0.39	< 0.10	...	3.6	3.3 – 3.9	34.0	29.4 – 37.8	9.4	8.3 – 10.5
AGAL043.166+00.011-1	< 0.10	...	< 0.10	...	3.3	3.0 – 3.5	66.2	50.2 – 80.2	20.2	15.6 – 24.3
AGAL043.166+00.011-2	0.11	0.05 – 0.13	< 0.10	...	5.0	4.5 – 5.4	73.1	54.6 – 86.3	14.8	11.1 – 17.7
AGAL049.489-00.389	0.15	0.09 – 0.19	< 0.10	...	2.7	2.5 – 2.9	73.8	68.4 – 79.0	27.2	24.7 – 29.5
AGAL053.141+00.069	0.20	0.13 – 0.24	< 0.10	...	3.1	2.9 – 3.4	40.4	36.2 – 44.4	12.9	11.5 – 14.2
AGAL059.782+00.066	0.15	0.10 – 0.18	< 0.10	...	3.5	3.1 – 3.7	74.0	56.9 – 86.7	21.4	16.8 – 25.6

Notes. The columns show the opacity for $C^{18}O(1-0)$, $C^{17}O(1-0)$, the $[^{18}O]/[^{17}O]$, the $[^{12}C]/[^{13}C]$ and $([^{12}C]/[^{13}C])/([^{18}O]/[^{17}O])$, with their respective uncertainties for sub-sample S1. Where the derived τ is less than 0.10, we indicate $\tau < 0.10$, to show that the emission is optically thin.

Table C.13: Molecular column densities for sub-sample S1.

Source	$N(^{12}C^{18}O)$ $(10^{16} \times cm^{-2})$	68%int. $(10^{16} \times cm^{-2})$	$N(^{12}C^{17}O, 1-0)$ $(10^{15} \times cm^{-2})$	68%int. $(10^{15} \times cm^{-2})$	$N(^{12}C^{17}O, 3-2)$ $(10^{15} \times cm^{-2})$	68%int. $(10^{15} \times cm^{-2})$	$N(^{13}C^{18}O)$ $(10^{13} \times cm^{-2})$	68%int. $(10^{13} \times cm^{-2})$	$N(H_2)$ $(10^{23} \times cm^{-2})$	68%int. $(10^{23} \times cm^{-2})$	Group
AGAL008.684-00.367	4.1	3.5 – 4.7	8.6	7.6 – 9.5	7.0	6.1 – 8.0	74.8	61.5 – 86.9	2.9	2.1 – 3.5	D8
AGAL008.706-00.414	1.5	1.2 – 1.7	2.9	2.5 – 3.3	2.2	1.9 – 2.6	36.5	29.6 – 42.0	1.3	0.9 – 1.6	D24
AGAL010.444-00.017	1.5	1.2 – 1.7	4.3	3.8 – 4.9	3.4	2.9 – 3.9	< 3.6	...	2.1	1.6 – 2.6	D24
AGAL010.472+00.027	6.2	4.8 – 7.4	12.9	11.0 – 14.6	11.4	10.2 – 12.5	< 20.8	...	5.7	3.6 – 7.3	IRB
AGAL010.624-00.384	17.2	12.6 – 20.3	41.2	34.4 – 46.8	36.3	31.9 – 40.3	286.4	209.1 – 333.4	4.6	2.8 – 6.0	IRB
AGAL012.804-00.199	11.5	8.7 – 13.2	29.2	25.2 – 32.8	25.4	22.9 – 28.0	191.4	146.3 – 231.9	5.9	3.7 – 7.3	IRB
AGAL013.178+00.059	1.0	0.9 – 1.2	3.3	2.9 – 3.6	2.8	2.4 – 3.1	< 5.4	...	1.8	1.3 – 2.2	D8
AGAL013.658-00.599	1.6	1.3 – 1.8	3.3	2.9 – 3.6	2.8	2.5 – 3.1	< 9.0	...	1.2	0.8 – 1.4	RMS
AGAL014.114-00.574	2.1	1.8 – 2.4	5.1	4.6 – 5.6	4.3	3.8 – 4.8	< 9.4	...	1.3	0.9 – 1.6	D8
AGAL014.194-00.194	1.4	1.2 – 1.6	3.7	3.2 – 4.1	3.0	2.6 – 3.5	18.4	13.5 – 23.2	2.6	1.9 – 3.1	D8
AGAL014.492-00.139	1.7	1.4 – 1.9	3.8	3.3 – 4.3	3.0	2.5 – 3.5	31.3	25.4 – 37.8	2.3	1.8 – 2.9	D24
AGAL014.632-00.577	1.4	1.1 – 1.7	2.9	2.5 – 3.2	2.6	2.3 – 2.8	< 8.2	...	0.9	0.6 – 1.2	D8
AGAL015.029-00.669-1	5.5	3.8 – 6.7	15.4	11.5 – 17.6	13.9	11.3 – 15.8	82.5	49.1 – 102.5	1.6	0.8 – 2.0	IRB
AGAL015.029-00.669-2	1.8	1.3 – 2.2	4.8	3.9 – 5.7	4.6	3.7 – 5.5	< 20.9	...	...	...	(IRB)
AGAL018.606-00.074	0.9	0.8 – 1.1	1.8	1.6 – 2.0	1.5	1.3 – 1.7	29.7	24.4 – 34.2	0.9	0.7 – 1.2	D24
AGAL018.734-00.226	0.8	0.7 – 0.9	3.3	2.9 – 3.6	2.8	2.3 – 3.1	< 8.0	...	2.1	1.5 – 2.5	D8
AGAL018.888-00.474	2.9	2.4 – 3.3	6.3	5.6 – 6.9	5.3	4.6 – 5.9	< 10.1	...	1.5	1.0 – 1.8	D8
AGAL019.882-00.534	1.5	1.0 – 1.8	4.5	3.5 – 5.2	4.0	3.4 – 4.5	< 17.5	...	0.8	0.4 – 1.1	RMS
AGAL022.376+00.447-1	0.9	0.7 – 1.0	1.8	1.6 – 2.0	1.4	1.2 – 1.6	26.8	20.2 – 33.6	2.1	1.5 – 2.6	D24
AGAL022.376+00.447-2	0.8	0.5 – 1.0	1.9	1.4 – 2.3	< 1.4	...	45.7	32.3 – 56.6	...	...	(D24)
AGAL023.206-00.377	1.3	1.1 – 1.5	3.8	3.4 – 4.2	3.3	2.9 – 3.6	33.7	25.8 – 41.5	2.9	2.0 – 3.6	D8
AGAL024.629+00.172-1	0.9	0.8 – 1.1	2.1	1.9 – 2.4	1.8	1.5 – 2.0	27.0	20.2 – 34.0	1.0	0.7 – 1.2	D24
AGAL024.629+00.172-2	1.6	0.9 – 2.1	4.9	3.2 – 6.0	< 3.4	...	35.7	23.7 – 43.0	...	...	(D24)
AGAL028.564-00.236	2.7	2.2 – 3.1	5.0	4.3 – 5.5	3.8	3.2 – 4.4	48.0	40.2 – 55.2	2.5	1.9 – 3.1	D24
AGAL028.861+00.066-1	3.0	2.4 – 3.5	8.1	7.0 – 8.9	7.1	6.4 – 7.8	72.8	54.9 – 85.5	0.7	0.4 – 0.9	RMS
AGAL028.861+00.066-2	0.5	0.5 – 0.6	1.1	1.0 – 1.2	0.9	0.7 – 1.0	24.5	19.4 – 29.9	...	...	(RMS)
AGAL030.848-00.081-1	0.9	0.8 – 1.1	1.7	1.5 – 1.9	1.4	1.2 – 1.6	32.8	24.4 – 41.7	0.8	0.5 – 1.0	D24
AGAL030.848-00.081-2	0.3	0.3 – 0.4	2.5	2.1 – 2.7	2.0	1.6 – 2.2	< 6.5	...	...	...	(D24)
AGAL030.848-00.081-3	0.6	0.5 – 0.6	0.9	0.8 – 1.1	0.8	0.6 – 0.9	< 7.5	...	...	...	(D24)
AGAL030.893+00.139-1	1.1	0.9 – 1.2	2.2	1.9 – 2.4	1.7	1.5 – 2.0	28.0	22.4 – 33.4	...	...	(D24)
AGAL030.893+00.139-2	1.2	1.0 – 1.4	2.0	1.8 – 2.2	1.7	1.4 – 1.9	29.8	23.3 – 36.0	0.9	0.6 – 1.1	D24
AGAL031.412+00.307	4.9	3.9 – 5.9	12.3	10.7 – 13.9	10.8	9.8 – 11.9	141.4	109.1 – 166.3	4.4	2.8 – 5.5	IRB
AGAL034.258+00.154	10.4	7.4 – 12.2	29.6	23.8 – 32.8	26.0	22.9 – 28.7	187.1	139.2 – 223.9	7.5	4.7 – 9.7	IRB
AGAL034.401+00.226	2.5	2.1 – 2.8	8.0	7.2 – 8.9	6.8	5.8 – 7.5	40.5	32.6 – 48.3	2.7	2.0 – 3.4	RMS
AGAL034.411+00.234	1.2	1.0 – 1.3	3.1	2.7 – 3.4	2.7	2.4 – 3.0	29.2	22.5 – 34.8	3.1	2.2 – 3.8	D8
AGAL034.821+00.351	1.7	1.4 – 1.9	5.1	4.6 – 5.6	4.3	3.8 – 4.8	27.8	22.0 – 33.7	1.0	0.7 – 1.3	RMS
AGAL035.197-00.742	2.0	1.6 – 2.2	6.4	5.6 – 7.0	5.6	5.0 – 6.1	45.0	36.5 – 52.0	3.1	2.2 – 3.9	RMS
AGAL037.554+00.201	1.5	1.3 – 1.8	4.0	3.6 – 4.4	3.4	3.1 – 3.8	50.2	40.0 – 62.8	1.1	0.8 – 1.4	RMS
AGAL043.166+00.011-1	10.2	8.8 – 11.7	30.9	26.9 – 34.4	39.4	34.0 – 44.6	< 13.8	...	3.0	2.3 – 3.6	IRB
AGAL043.166+00.011-2	4.5	3.1 – 5.3	8.9	7.0 – 10.2	7.9	6.7 – 8.9	< 8.1	...	...	...	(IRB)
AGAL049.489-00.389	12.1	8.6 – 14.3	40.0	31.7 – 46.5	35.6	30.2 – 39.9	140.4	91.0 – 168.2	8.7	5.2 – 11.4	IRB
AGAL053.141+00.069	1.6	1.3 – 1.8	5.3	4.5 – 5.9	4.7	4.2 – 5.1	45.7	32.2 – 58.8	0.9	0.6 – 1.1	RMS
AGAL059.782+00.066	1.0	0.8 – 1.2	3.0	2.6 – 3.4	2.7	2.4 – 2.9	< 18.9	...	1.0	0.7 – 1.3	RMS

Notes. As in Table C.10

Table C.14: Molecular column densities for sub-sample S2.

Source	$N(^{12}C^{18}O)$ $(10^{16} \times cm^{-2})$	68%int. $(10^{16} \times cm^{-2})$	$N(^{12}C^{17}O)$ $(10^{15} \times cm^{-2})$	68%int. $(10^{15} \times cm^{-2})$	$N(H_2)$ $(10^{23} \times cm^{-2})$	68%int. $(10^{23} \times cm^{-2})$	Group
AGAL301.136-00.226	5.5	4.7 – 6.0	10.7	9.4 – 11.6	3.6	1.4 – 4.6	IRB
AGAL305.209+00.206	4.0	3.4 – 4.3	7.9	6.8 – 8.6	2.0	0.7 – 2.8	IRB
AGAL305.794-00.096	2.5	1.7 – 3.0	3.3	2.2 – 4.0	1.3	0.9 – 1.6	D24
AGAL317.867-00.151	1.0	0.8 – 1.1	1.8	1.4 – 1.9	1.1	0.6 – 1.5	D8
AGAL318.779-00.137	1.3	1.0 – 1.5	1.9	1.4 – 2.3	1.1	0.7 – 1.5	D8
AGAL320.881-00.397	2.0	1.7 – 2.2	3.4	2.8 – 3.8	0.4	0.2 – 0.6	D24
AGAL327.293-00.579	12.7	10.5 – 14.5	32.4	26.4 – 38.9	3.1	1.6 – 3.6	IRB
AGAL328.809+00.632	11.4	9.2 – 13.2	27.2	21.2 – 32.8	1.7	0.8 – 2.0	IRB
AGAL329.029-00.206	1.6	1.4 – 1.8	2.9	2.4 – 3.3	2.3	1.2 – 3.0	D8
AGAL330.879-00.367	11.0	8.7 – 12.1	23.9	18.9 – 26.5	1.6	0.6 – 2.0	IRB
AGAL330.954-00.182	20.2	15.9 – 22.1	43.6	34.5 – 48.9	4.4	1.8 – 5.4	IRB
AGAL331.709+00.582	1.0	0.8 – 1.1	1.9	1.6 – 2.0	0.6	0.3 – 0.8	D8
AGAL332.094-00.421	5.0	4.3 – 5.5	9.1	7.8 – 10.0	1.4	0.7 – 1.9	RMS
AGAL332.826-00.549	15.4	12.1 – 17.3	34.1	27.0 – 39.5	2.7	1.1 – 3.3	IRB
AGAL333.134-00.431	14.8	11.9 – 16.2	31.4	25.1 – 34.5	2.3	0.9 – 2.9	IRB
AGAL333.604-00.212	8.6	6.8 – 9.5	18.1	14.7 – 19.9	3.4	1.3 – 4.5	IRB
AGAL333.656+00.059	3.0	2.2 – 3.6	4.2	2.9 – 5.0	1.2	0.8 – 1.6	D24
AGAL335.789+00.174	3.4	2.8 – 3.7	6.9	5.7 – 7.4	1.0	0.4 – 1.3	D8
AGAL336.958-00.224	1.2	0.8 – 1.5	1.6	1.0 – 2.0	1.6	0.9 – 1.9	D24
AGAL337.176-00.032	4.3	3.2 – 5.2	5.4	3.9 – 6.6	2.7	1.8 – 3.4	D8
AGAL337.286+00.007-1	2.6	1.7 – 3.2	3.1	1.9 – 3.8	1.6	0.9 – 1.9	D24
AGAL337.286+00.007-2	2.0	1.5 – 2.5	< 1.3	...	...	...	(D24)
AGAL337.406-00.402	9.1	7.6 – 10.3	23.7	19.0 – 28.0	1.0	0.6 – 1.2	IRB
AGAL337.704-00.054	5.1	4.0 – 5.7	11.3	8.6 – 13.0	1.1	0.5 – 1.4	IRB
AGAL337.916-00.477	9.7	8.5 – 10.8	30.7	26.5 – 35.5	1.1	0.8 – 1.3	IRB
AGAL338.066+00.044-1	0.9	0.6 – 1.0	1.3	1.0 – 1.6	0.6	0.3 – 0.7	D24
AGAL338.066+00.044-2	3.8	2.5 – 4.6	4.1	2.6 – 5.1	...	...	(D24)
AGAL338.786+00.476	2.9	2.1 – 3.4	3.9	2.6 – 4.6	1.2	0.7 – 1.4	D24
AGAL340.374-00.391	4.6	3.2 – 5.4	5.7	3.9 – 6.8	2.0	1.2 – 2.5	D24
AGAL340.784-00.097	1.9	1.5 – 2.2	4.8	3.8 – 5.6	0.2	0.1 – 0.3	D8
AGAL342.484+00.182	2.6	2.0 – 3.0	4.1	3.2 – 4.8	1.5	0.9 – 1.9	D8
AGAL343.128-00.062	6.4	5.1 – 7.3	14.8	11.4 – 16.9	1.4	0.6 – 1.7	IRB
AGAL343.756-00.164	1.8	1.5 – 1.9	3.5	3.0 – 3.8	1.4	0.6 – 1.9	D8
AGAL344.227-00.569	3.5	3.1 – 3.8	6.8	6.0 – 7.5	3.0	1.3 – 3.9	D8
AGAL345.003-00.224-1	4.3	3.6 – 4.6	8.4	7.2 – 9.1	2.5	0.9 – 3.2	IRB
AGAL345.003-00.224-2	6.5	5.3 – 8.0	< 2.3	...	...	...	(IRB)
AGAL345.488+00.314	7.6	6.2 – 8.2	15.5	12.8 – 16.7	1.9	0.6 – 2.4	IRB
AGAL345.504+00.347	5.6	4.5 – 6.5	13.1	10.2 – 15.3	0.8	0.4 – 0.9	RMS
AGAL351.161+00.697	5.9	4.6 – 6.5	12.8	10.0 – 14.2	2.0	0.8 – 2.6	IRB
AGAL351.244+00.669	8.8	7.2 – 10.1	21.3	16.6 – 24.6	1.2	0.6 – 1.4	IRB
AGAL351.571+00.762	2.8	2.0 – 3.4	3.8	2.7 – 4.7	1.3	0.8 – 1.6	D24
AGAL351.581-00.352	9.7	8.2 – 10.4	18.8	16.3 – 20.4	3.9	1.6 – 5.4	IRB
AGAL351.774-00.537	16.1	13.1 – 17.8	33.7	27.0 – 36.6	5.5	2.0 – 6.9	IRB
AGAL353.066+00.452-1	1.3	1.1 – 1.5	2.2	1.7 – 2.5	0.5	0.3 – 0.7	D24
AGAL353.066+00.452-2	1.2	0.6 – 1.8	< 1.1	...	...	...	(D24)
AGAL353.409-00.361	8.1	6.6 – 9.2	21.0	16.7 – 24.9	1.2	0.7 – 1.4	IRB
AGAL353.417-00.079-1	2.9	1.7 – 3.7	3.1	1.9 – 3.8	1.4	0.9 – 1.8	D24
AGAL353.417-00.079-2	1.6	1.0 – 2.0	2.1	1.3 – 2.5	...	...	(D24)
AGAL353.417-00.079-3	2.9	2.4 – 3.5	< 1.3	...	...	...	(D24)
AGAL353.417-00.079-4	1.1	0.6 – 1.6	< 0.9	...	...	...	(D24)
AGAL354.944-00.537	3.1	2.1 – 3.7	3.7	2.4 – 4.4	1.9	1.3 – 2.4	D24

Notes. As in Table C.10

Table C.15: Molecular column densities for sub-sample S3.

Source	$N(^{12}C^{17}O)$ $(10^{15} \times cm^{-2})$	68%int. $(10^{15} \times cm^{-2})$	$N(H_2)$ $(10^{23} \times cm^{-2})$	68%int. $(10^{23} \times cm^{-2})$	Group
AGAL030.818-00.056	6.1	4.5 – 7.5	2.4	0.9 – 3.5	IRB
AGAL305.192-00.006	1.7	1.2 – 1.8	0.7	0.2 – 0.9	RMS
AGAL305.562+00.014	9.1	6.4 – 10.4	1.0	0.3 – 1.2	RMS
AGAL309.384-00.134	4.4	2.0 – 4.9	1.1	0.2 – 1.4	D8
AGAL310.014+00.387	4.0	2.9 – 4.6	0.8	0.2 – 1.0	RMS
AGAL313.576+00.324	4.1	2.7 – 4.6	0.6	0.2 – 0.7	RMS
AGAL316.641-00.087	1.6	1.2 – 1.8	0.5	0.2 – 0.7	RMS
AGAL326.661+00.519	6.6	4.7 – 7.4	0.8	0.3 – 1.0	RMS
AGAL326.987-00.032	1.0	0.5 – 1.2	0.9	0.2 – 1.0	D8
AGAL327.119+00.509	5.6	4.0 – 6.3	0.7	0.2 – 0.9	RMS
AGAL327.393+00.199	2.1	1.4 – 2.2	0.7	0.2 – 0.9	RMS
AGAL329.066-00.307	1.3	0.9 – 1.4	0.7	0.2 – 0.9	RMS
AGAL333.284-00.387	16.0	12.4 – 19.5	1.3	0.4 – 2.0	IRB
AGAL333.314+00.106	3.1	2.1 – 3.5	0.7	0.3 – 1.0	RMS
AGAL337.258-00.101	1.6	0.7 – 1.7	0.8	0.2 – 1.1	D8
AGAL338.926+00.554	7.9	6.1 – 10.3	1.6	0.6 – 2.4	IRB
AGAL339.623-00.122	4.0	2.8 – 4.5	0.7	0.2 – 0.8	RMS
AGAL340.746-01.001	2.6	1.8 – 2.9	0.5	0.2 – 0.7	RMS
AGAL341.217-00.212	4.3	3.2 – 4.8	1.0	0.3 – 1.2	RMS
AGAL345.718+00.817	3.2	2.2 – 3.6	0.7	0.2 – 0.9	RMS
AGAL351.131+00.771	7.8	3.6 – 10.1	0.8	0.4 – 1.1	D24
AGAL351.416+00.646	24.4	18.8 – 31.3	5.4	2.0 – 7.8	IRB
AGAL351.444+00.659	18.7	9.7 – 20.9	12.2	2.6 – 15.5	D8

Table C.16: Masses from 870 μm dust emission and virial masses for sub-sample S1.

Source	M ($10^3 \times M_\odot$)	68%int. ($10^3 \times M_\odot$)	M_{vir} ($10^3 \times M_\odot$)	68%int. ($10^3 \times M_\odot$)	Group
AGAL008.684-00.367	17.40	7.46 – 24.78	3.62	2.77 – 4.52	D8
AGAL008.706-00.414	14.97	5.83 – 20.39	1.50	0.96 – 1.96	D24
AGAL010.444-00.017	10.09	3.51 – 13.94	1.80	1.19 – 2.30	D24
AGAL010.472+00.027	19.99	6.07 – 27.62	8.35	6.02 – 10.36	IRB
AGAL010.624-00.384	1.06	0.37 – 1.52	1.78	1.32 – 2.21	IRB
AGAL012.804-00.199	2.21	1.29 – 3.02	2.44	2.19 – 2.67	IRB
AGAL013.178+00.059	18.76	5.91 – 26.07	3.20	2.32 – 4.07	D8
AGAL013.658-00.599	0.99	0.37 – 1.41	0.73	0.51 – 0.91	RMS
AGAL014.114-00.574	0.53	0.20 – 0.75	0.46	0.35 – 0.57	D8
AGAL014.194-00.194	1.93	0.73 – 2.63	1.20	0.12 – 1.75	D8
AGAL014.492-00.139	2.65	1.07 – 3.71	1.74	1.10 – 2.31	D24
AGAL014.632-00.577	0.32	0.13 – 0.46	0.52	0.39 – 0.65	D8
AGAL015.029-00.669-1	0.57	0.25 – 0.74	1.04	0.94 – 1.14	IRB
AGAL018.606-00.074	7.31	2.83 – 9.87	1.95	1.03 – 2.56	D24
AGAL018.734-00.226	16.75	7.16 – 23.56	6.52	4.30 – 8.53	D8
AGAL018.888-00.474	2.08	0.82 – 2.94	2.56	1.98 – 3.21	D8
AGAL019.882-00.534	0.44	0.10 – 0.62	0.78	0.57 – 0.95	RMS
AGAL022.376+00.447-1	1.32	0.52 – 1.84	0.13	0.08 – 0.17	D24
AGAL023.206-00.377	2.58	0.99 – 3.56	1.48	1.11 – 1.84	D8
AGAL024.629+00.172-1	2.26	0.87 – 3.04	1.86	1.15 – 2.47	D24
AGAL028.564-00.236	7.22	3.07 – 10.29	3.10	1.80 – 4.22	D24
AGAL028.861+00.066-1	1.41	0.48 – 2.00	1.44	1.08 – 1.77	RMS
AGAL030.848-00.081-1	2.39	0.88 – 3.34	1.75	1.09 – 2.20	D24
AGAL030.893+00.139-2	2.44	0.99 – 3.41	2.01	0.96 – 2.67	D24
AGAL031.412+00.307	4.41	2.21 – 5.95	2.69	2.27 – 3.15	IRB
AGAL034.258+00.154	1.40	0.36 – 2.02	1.33	0.96 – 1.75	IRB
AGAL034.401+00.226	0.42	0.27 – 0.53	0.90	0.81 – 0.99	RMS
AGAL034.411+00.234	0.28	0.18 – 0.37	0.47	0.39 – 0.55	D8
AGAL034.821+00.351	1.23	0.45 – 1.70	0.82	0.61 – 1.01	RMS
AGAL035.197-00.742	0.75	0.45 – 0.98	0.83	0.73 – 0.93	RMS
AGAL037.554+00.201	2.24	0.81 – 3.15	1.81	1.34 – 2.23	RMS
AGAL043.166+00.011-1	17.09	11.08 – 22.12	26.31	22.36 – 29.62	IRB
AGAL049.489-00.389	8.93	4.93 – 11.72	5.29	4.75 – 5.68	IRB
AGAL053.141+00.069	0.14	0.06 – 0.20	0.41	0.30 – 0.51	RMS
AGAL059.782+00.066	0.27	0.18 – 0.35	0.35	0.32 – 0.39	RMS

Table C.17: Masses from 870 μm dust emission and virial masses for sub-sample S2.

Source	M ($10^3 \times M_\odot$)	68%int. ($10^3 \times M_\odot$)	$M_{\rm vir}$ ($10^3 \times M_\odot$)	68%int. ($10^3 \times M_\odot$)	Group
AGAL301.136-00.226	2.49	0.58 – 3.22	1.74	1.34 – 2.10	IRB
AGAL305.209+00.206	1.06	0.32 – 1.48	1.78	1.45 – 2.07	IRB
AGAL305.794-00.096	1.06	0.53 – 1.35	0.54	0.30 – 0.70	D24
AGAL317.867-00.151	0.36	0.09 – 0.47	0.76	0.43 – 0.96	D8
AGAL318.779-00.137	0.63	0.21 – 0.85	0.66	0.42 – 0.80	D8
AGAL320.881-00.397	2.01	0.67 – 2.72	0.93	0.71 – 1.14	D24
AGAL327.293-00.579	1.10	0.37 – 1.39	1.89	1.42 – 2.30	IRB
AGAL328.809+00.632	0.46	0.13 – 0.59	1.28	0.99 – 1.56	IRB
AGAL329.029-00.206	23.11	5.86 – 30.30	5.52	4.01 – 6.80	D8
AGAL330.879-00.367	0.71	0.18 – 0.91	1.27	1.00 – 1.55	IRB
AGAL330.954-00.182	3.17	0.84 – 4.26	4.72	3.65 – 5.68	IRB
AGAL331.709+00.582	3.37	0.80 – 4.47	4.77	3.25 – 5.88	D8
AGAL332.094-00.421	0.82	0.21 – 1.14	0.95	0.75 – 1.16	RMS
AGAL332.826-00.549	1.36	0.12 – 1.75	1.83	0.85 – 2.73	IRB
AGAL333.134-00.431	0.86	0.25 – 1.16	2.52	2.10 – 2.93	IRB
AGAL333.604-00.212	2.87	0.51 – 3.74	4.06	3.18 – 4.91	IRB
AGAL333.656+00.059	9.41	3.57 – 12.61	1.85	1.34 – 2.28	D24
AGAL335.789+00.174	0.50	0.09 – 0.63	0.87	0.69 – 1.06	D8
AGAL336.958-00.224	5.97	2.18 – 8.11	1.25	0.11 – 1.62	D24
AGAL337.176-00.032	21.44	8.52 – 28.09	1.36	0.84 – 1.74	D8
AGAL337.286+00.007-1	10.09	3.97 – 13.24	1.08	0.33 – 1.55	D24
AGAL337.406-00.402	0.32	0.11 – 0.41	1.08	0.85 – 1.31	IRB
AGAL337.704-00.054	6.48	1.47 – 8.26	8.51	6.67 – 10.35	IRB
AGAL337.916-00.477	0.30	0.12 – 0.38	0.97	0.76 – 1.18	IRB
AGAL338.066+00.044-1	0.97	0.30 – 1.27	0.99	0.58 – 1.31	D24
AGAL338.786+00.476	1.57	0.50 – 2.08	0.79	0.47 – 1.04	D24
AGAL340.374-00.391	1.27	0.47 – 1.68	0.57	0.41 – 0.68	D24
AGAL340.784-00.097	0.87	0.30 – 1.18	2.62	2.03 – 3.20	D8
AGAL342.484+00.182	9.57	2.65 – 12.84	1.08	0.82 – 1.31	D8
AGAL343.128-00.062	0.58	0.11 – 0.71	1.54	1.19 – 1.85	IRB
AGAL343.756-00.164	0.32	0.07 – 0.41	0.52	0.38 – 0.63	D8
AGAL344.227-00.569	0.49	0.11 – 0.64	0.59	0.44 – 0.70	D8
AGAL345.003-00.224-1	0.73	0.13 – 0.94	1.37	1.05 – 1.67	IRB
AGAL345.488+00.314	0.71	0.17 – 0.94	1.43	1.12 – 1.75	IRB
AGAL345.504+00.347	4.78	1.39 – 6.39	5.93	4.53 – 7.26	RMS
AGAL351.161+00.697	0.48	0.04 – 0.63	0.85	0.33 – 1.26	IRB
AGAL351.244+00.669	0.47	0.04 – 0.62	0.70	0.32 – 1.09	IRB
AGAL351.571+00.762	0.63	0.03 – 0.81	0.18	0.06 – 0.26	D24
AGAL351.581-00.352	4.19	0.94 – 5.50	1.73	1.33 – 2.07	IRB
AGAL351.774-00.537	0.03	0.01 – 0.04	0.24	0.18 – 0.29	IRB
AGAL353.066+00.452-1	7.97	2.55 – 10.70	1.59	0.83 – 2.08	D24
AGAL353.409-00.361	1.11	0.38 – 1.53	1.67	1.28 – 1.98	IRB
AGAL353.417-00.079-1	4.40	1.50 – 5.64	1.08	0.11 – 1.28	D24
AGAL354.944-00.537	0.52	0.19 – 0.68	0.25	0.09 – 0.33	D24

Table C.18: Masses from 870 μm dust emission and virial masses for sub-sample S3.

Source	M ($10^3 \times M_\odot$)	68%int. ($10^3 \times M_\odot$)	M_{vir} ($10^3 \times M_\odot$)	68%int. ($10^3 \times M_\odot$)	Group
AGAL030.818-00.056	4.04	0.93 – 6.78	4.51	3.51 – 5.63	IRB
AGAL305.192-00.006	0.43	0.08 – 0.58	0.85	0.59 – 1.06	RMS
AGAL305.562+00.014	0.50	0.08 – 0.65	0.77	0.64 – 0.91	RMS
AGAL309.384-00.134	1.74	0.18 – 2.45	1.42	1.06 – 1.80	D8
AGAL310.014+00.387	0.58	0.10 – 0.89	0.95	0.69 – 1.17	RMS
AGAL313.576+00.324	0.26	0.03 – 0.36	0.87	0.60 – 1.12	RMS
AGAL316.641-00.087	2.29	0.22 – 3.29	2.15	1.46 – 2.70	RMS
AGAL326.661+00.519	0.34	0.04 – 0.52	0.48	0.36 – 0.59	RMS
AGAL326.987-00.032	0.52	0.05 – 0.83	2.06	0.85 – 2.73	D8
AGAL327.119+00.509	0.99	0.12 – 1.44	1.09	0.81 – 1.34	RMS
AGAL327.393+00.199	1.15	0.15 – 1.74	1.36	0.92 – 1.69	RMS
AGAL329.066-00.307	7.03	0.95 – 11.38	4.99	2.95 – 6.51	RMS
AGAL333.284-00.387	1.19	0.38 – 2.14	1.56	1.19 – 1.94	IRB
AGAL333.314+00.106	0.39	0.05 – 0.55	1.31	0.96 – 1.63	RMS
AGAL337.258-00.101	4.54	0.55 – 7.11	2.26	1.25 – 2.98	D8
AGAL338.926+00.554	2.35	0.54 – 4.22	4.41	3.25 – 5.52	IRB
AGAL339.623-00.122	0.36	0.05 – 0.55	0.69	0.52 – 0.85	RMS
AGAL340.746-01.001	0.22	0.03 – 0.32	0.60	0.44 – 0.76	RMS
AGAL341.217-00.212	0.54	0.07 – 0.77	0.78	0.61 – 0.98	RMS
AGAL345.718+00.817	0.14	0.02 – 0.21	0.24	0.17 – 0.30	RMS
AGAL351.131+00.771	0.22	0.02 – 0.32	0.12	0.05 – 0.19	D24
AGAL351.416+00.646	0.77	0.28 – 1.93	0.82	0.25 – 1.21	IRB
AGAL351.444+00.659	4.37	0.82 – 7.35	1.02	0.25 – 1.50	D8

C.2 Spectra

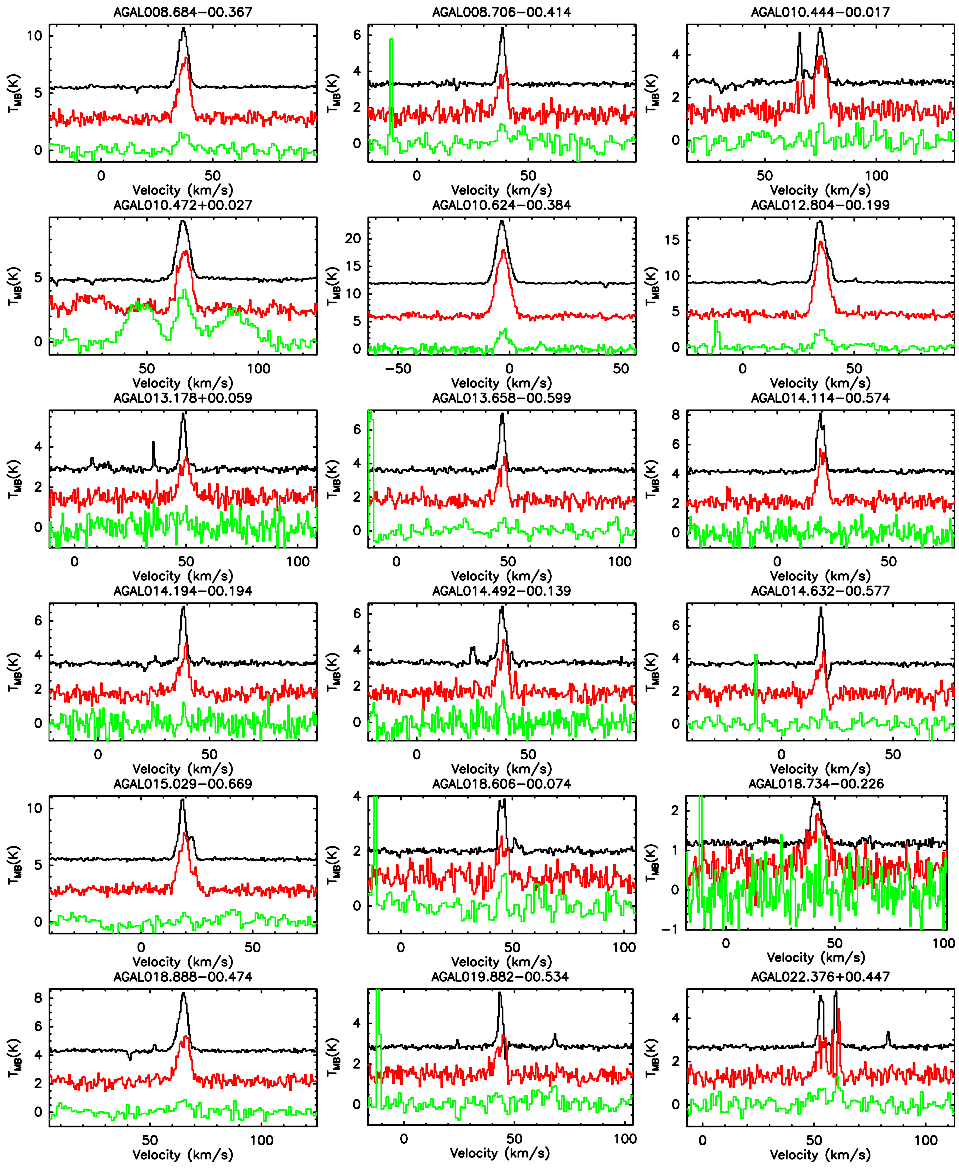

Figure C.1: $^{13}C^{18}O(1-0)$ (10x,green), $C^{17}O(1-0)$ (red) and $C^{18}O(1-0)$ (black). The spectra are displaced for clarity.

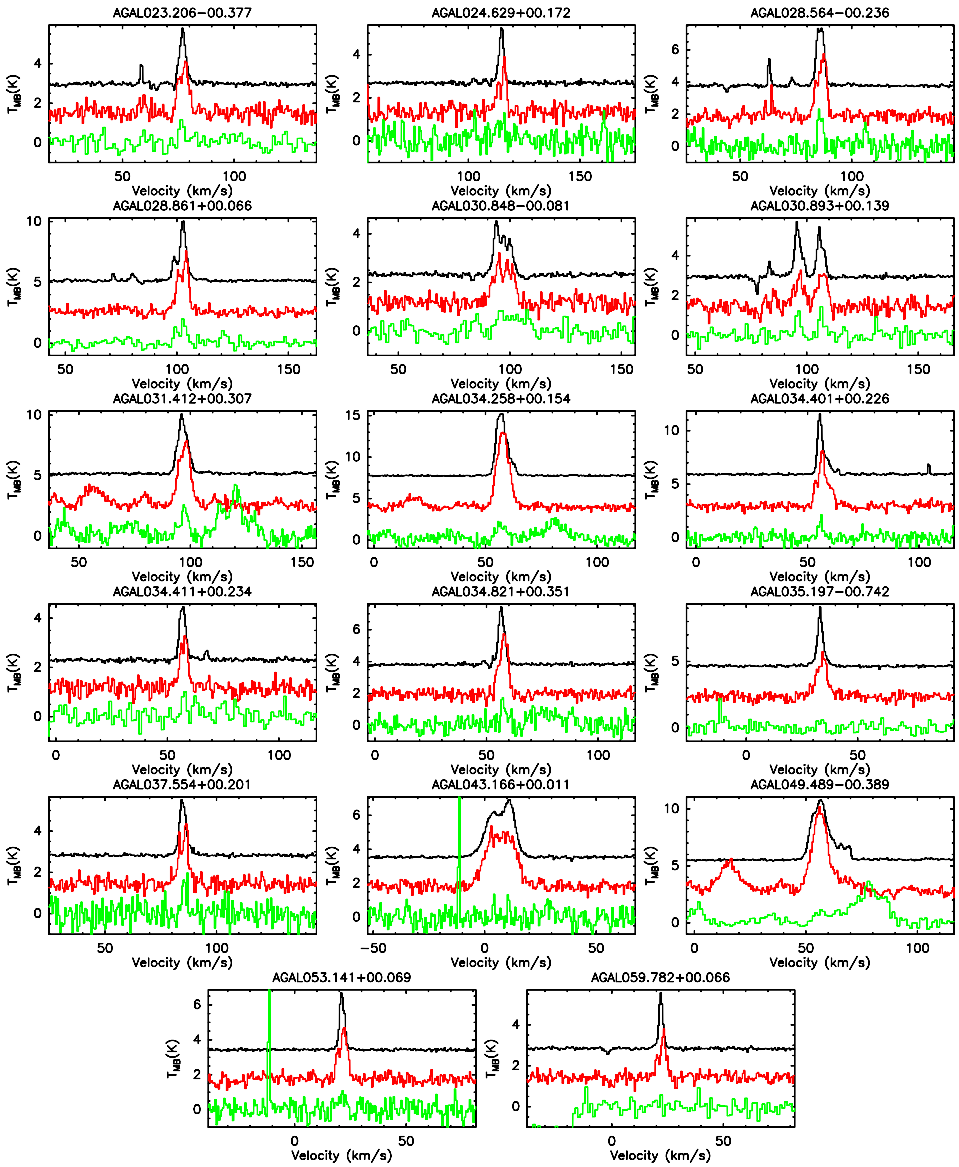

Figure C.1: Continued.

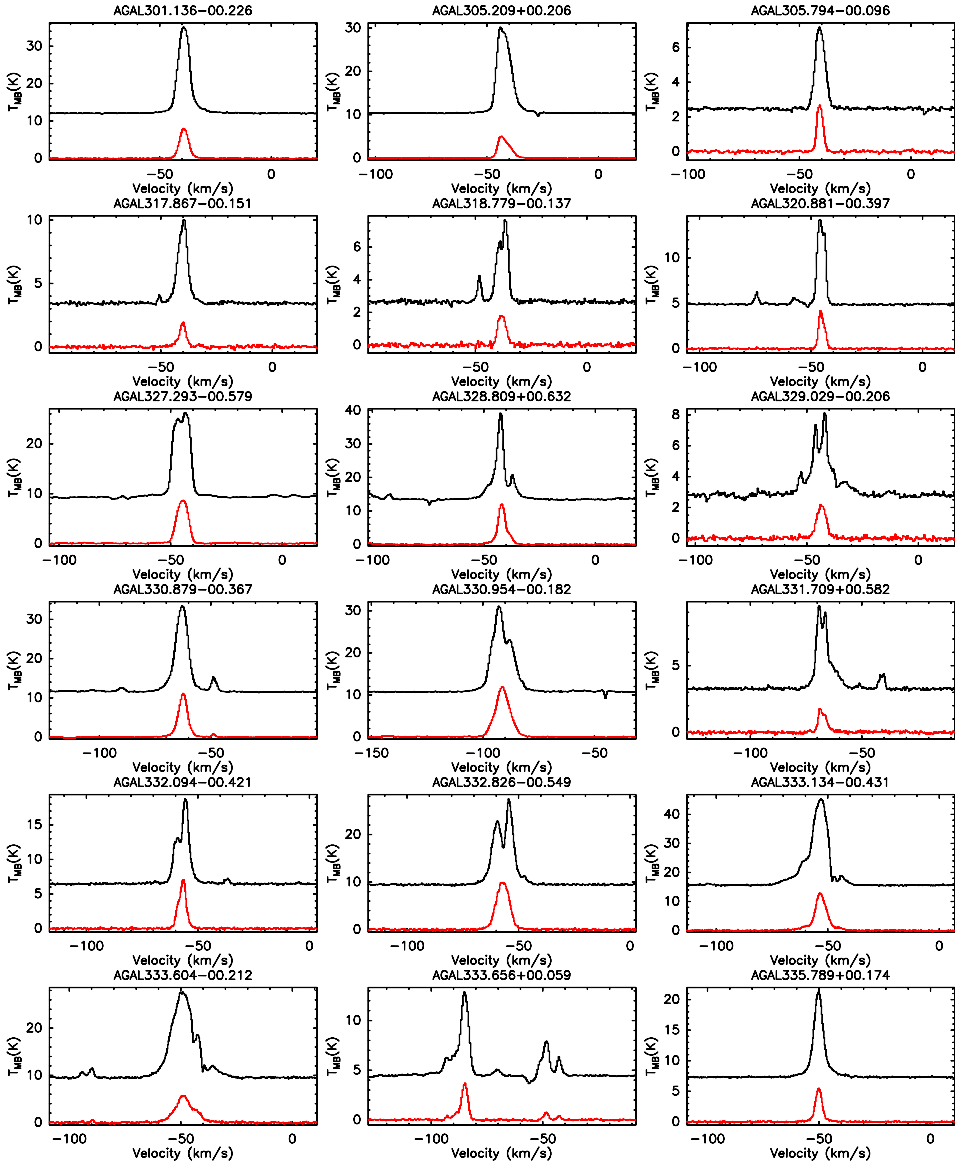

Figure C.2: $C^{18}O(2-1)$ (red) and $^{13}CO(2-1)$ (black). The spectra are displaced for clarity.

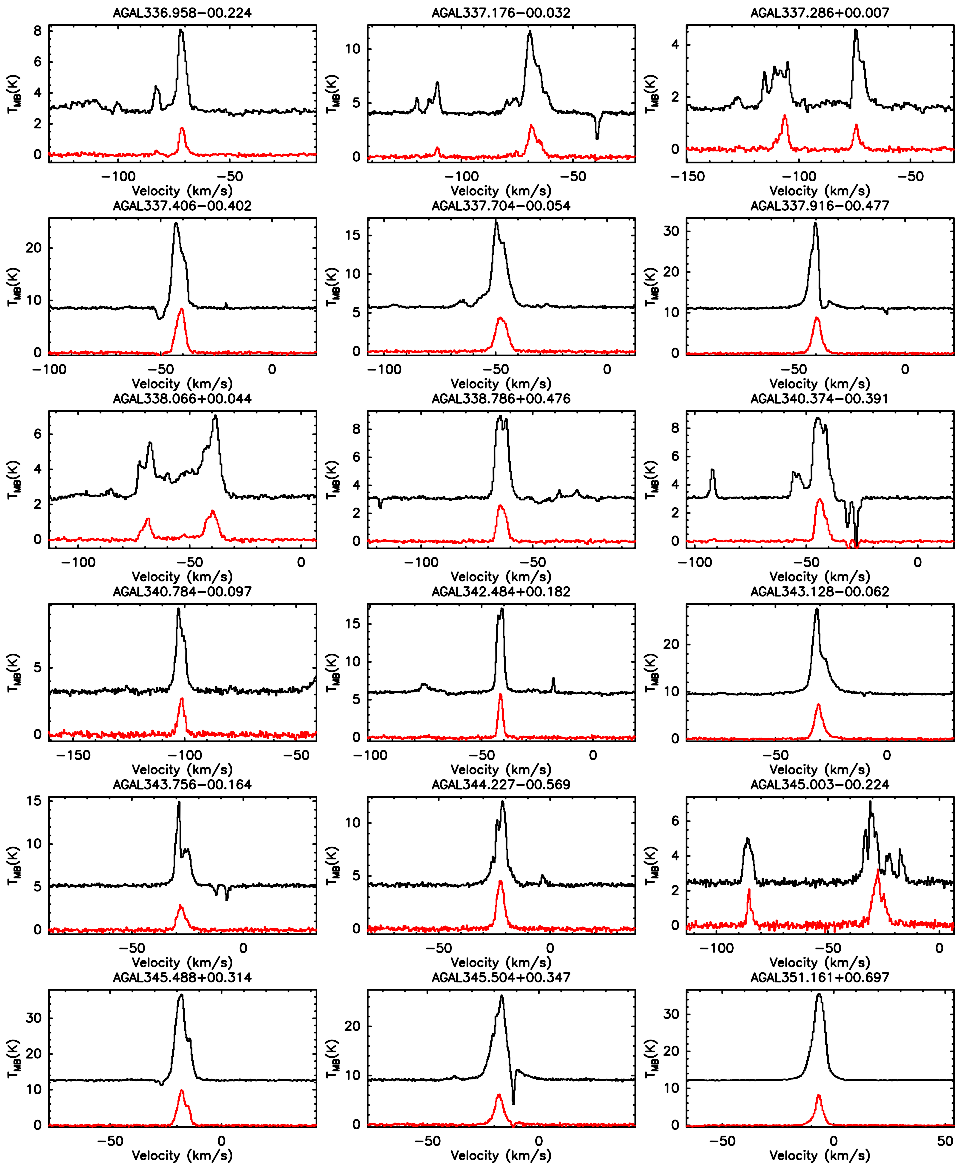

Figure C.2: Continued.

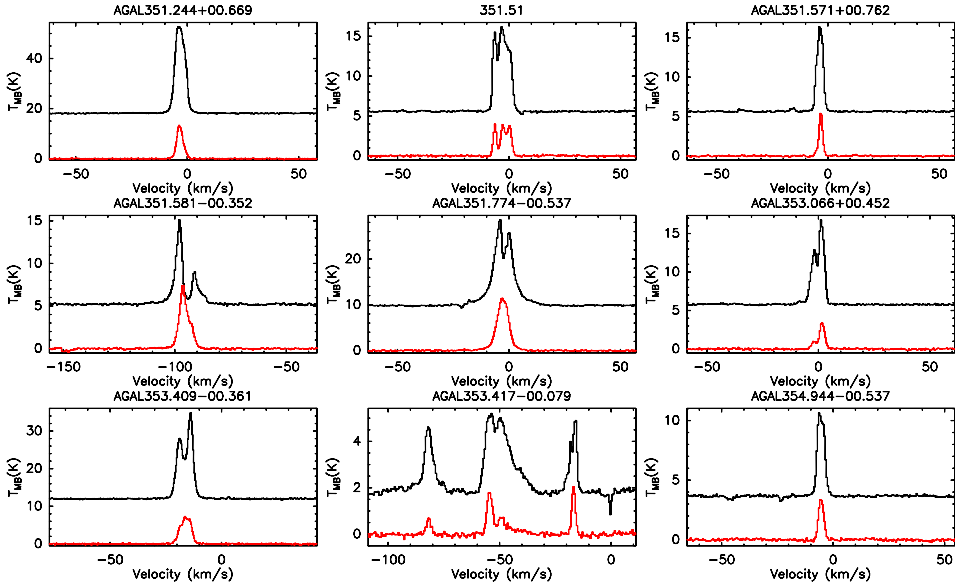

Figure C.2: Continued.

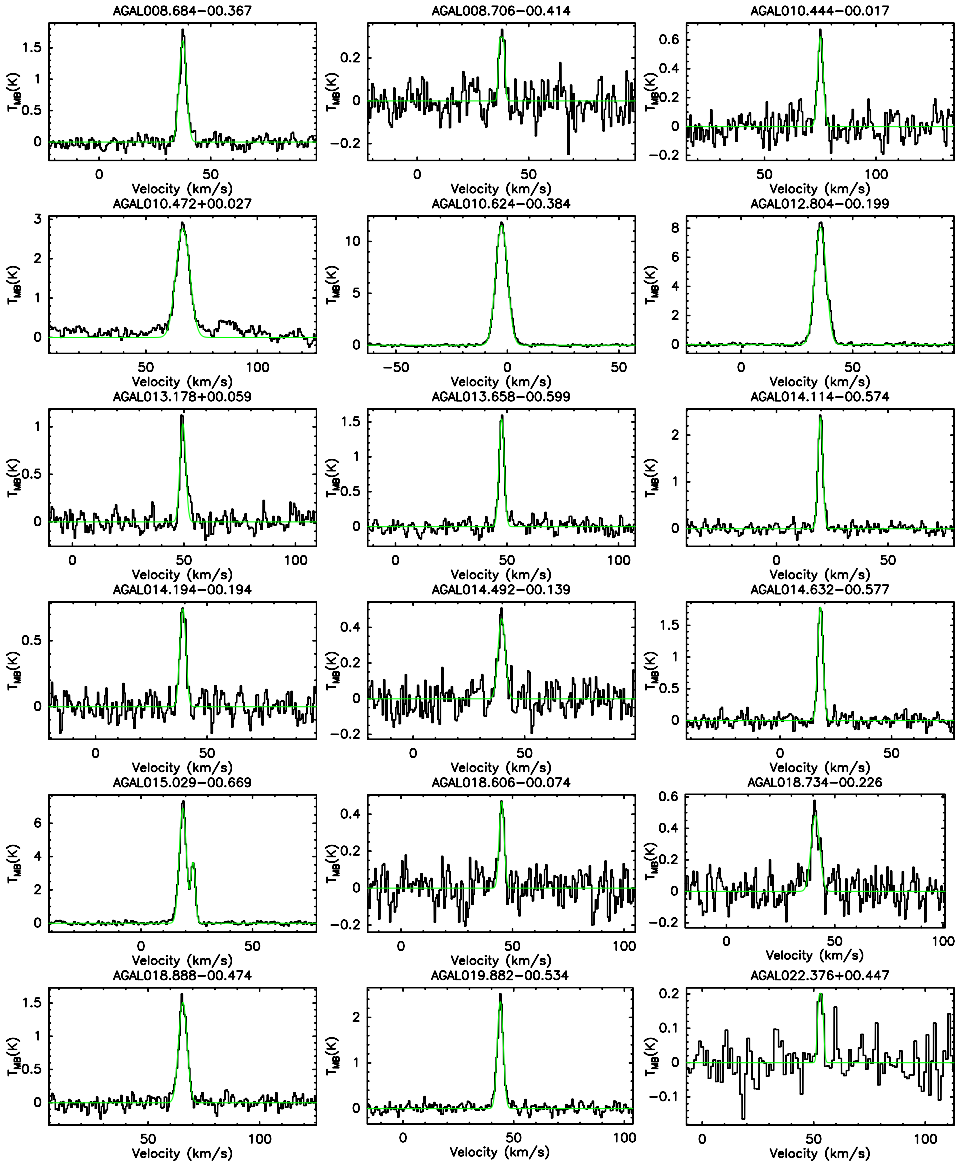

Figure C.3: $C^{17}O(3-2)$ for sub-sample S1. The fit is shown in green.

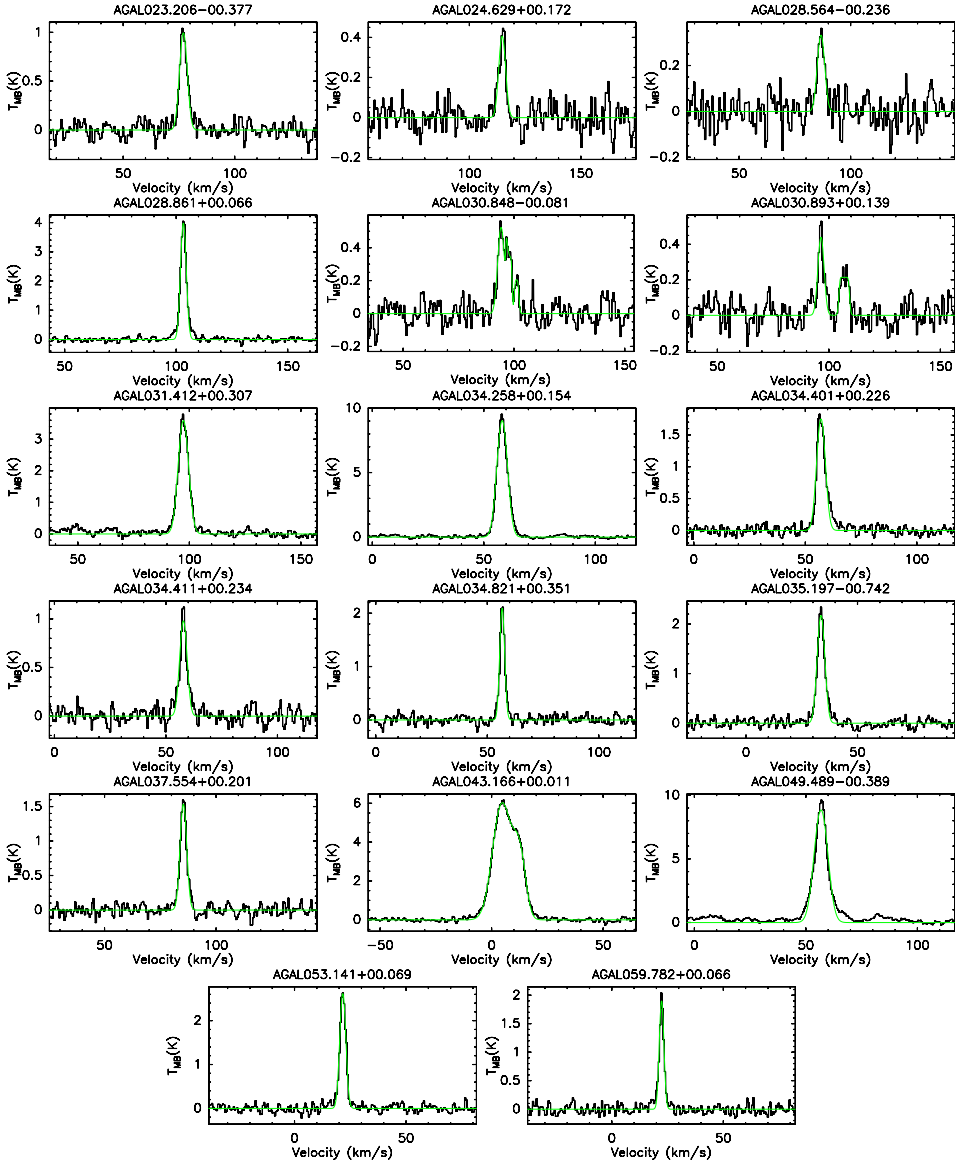

Figure C.3: Continued.

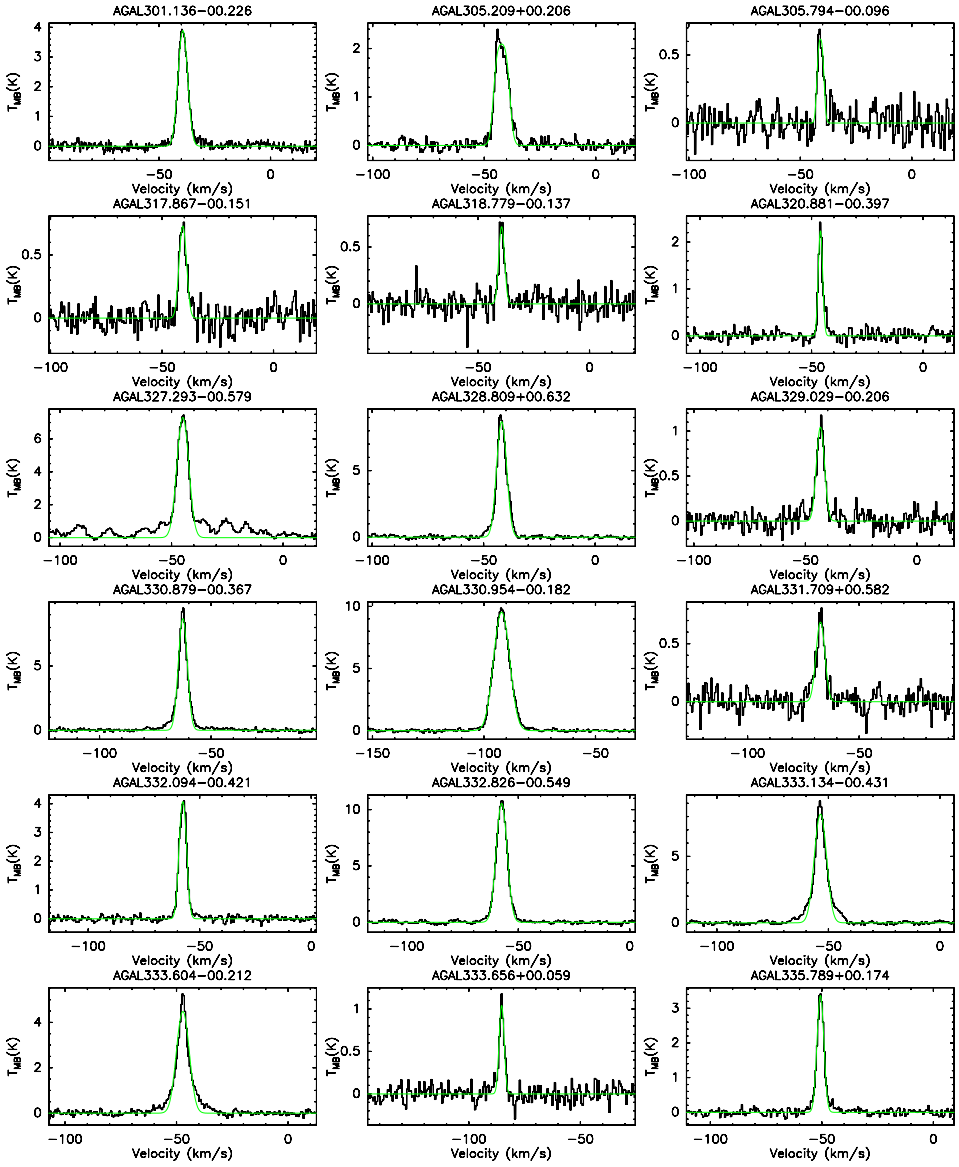

Figure C.4: $C^{17}O(3-2)$ for sub-sample S2. The fit is shown in green.

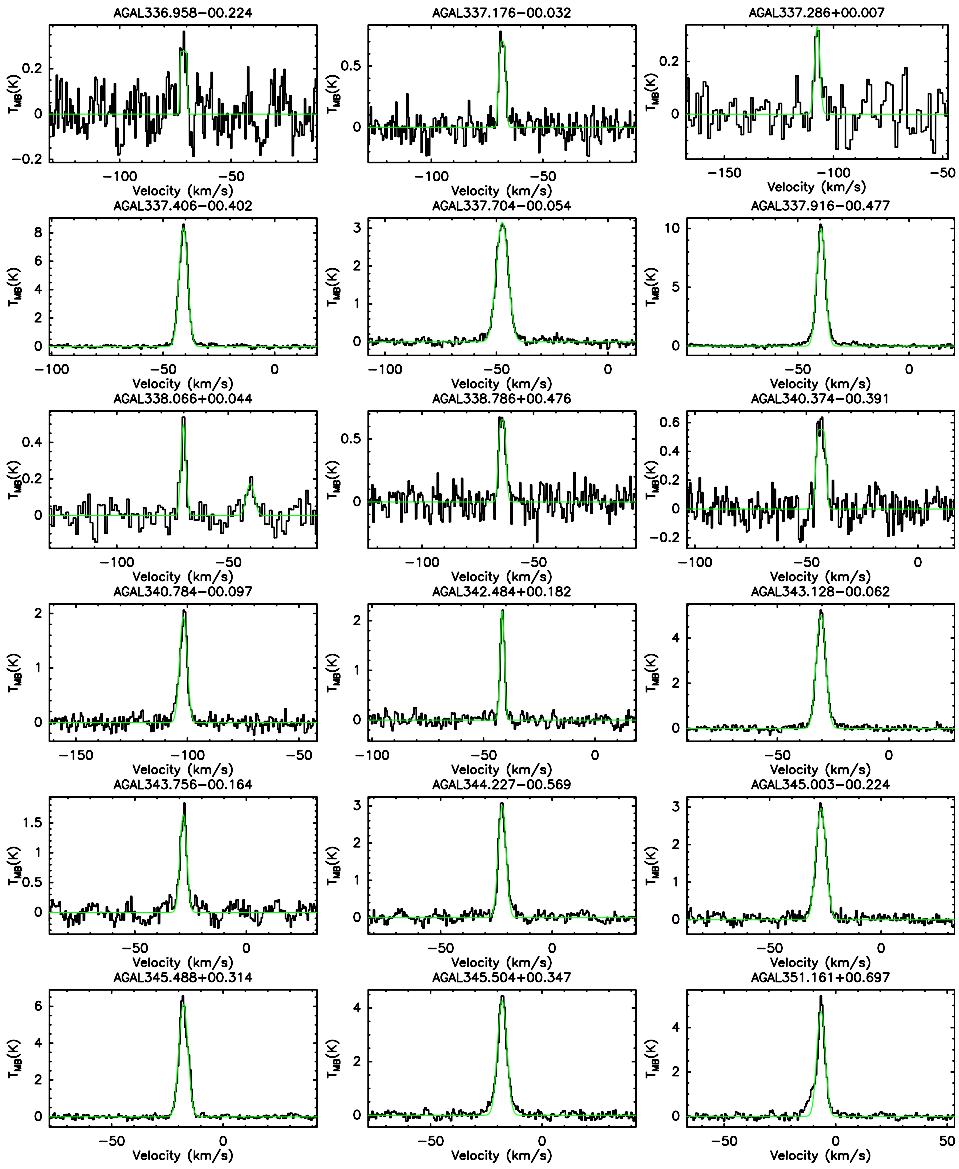

Figure C.4: Continued.

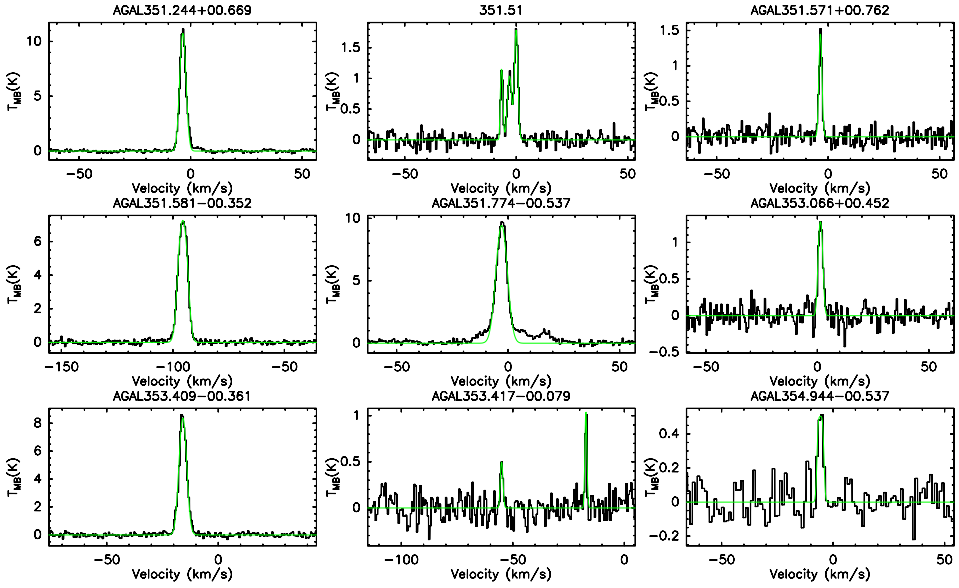

Figure C.4: Continued.

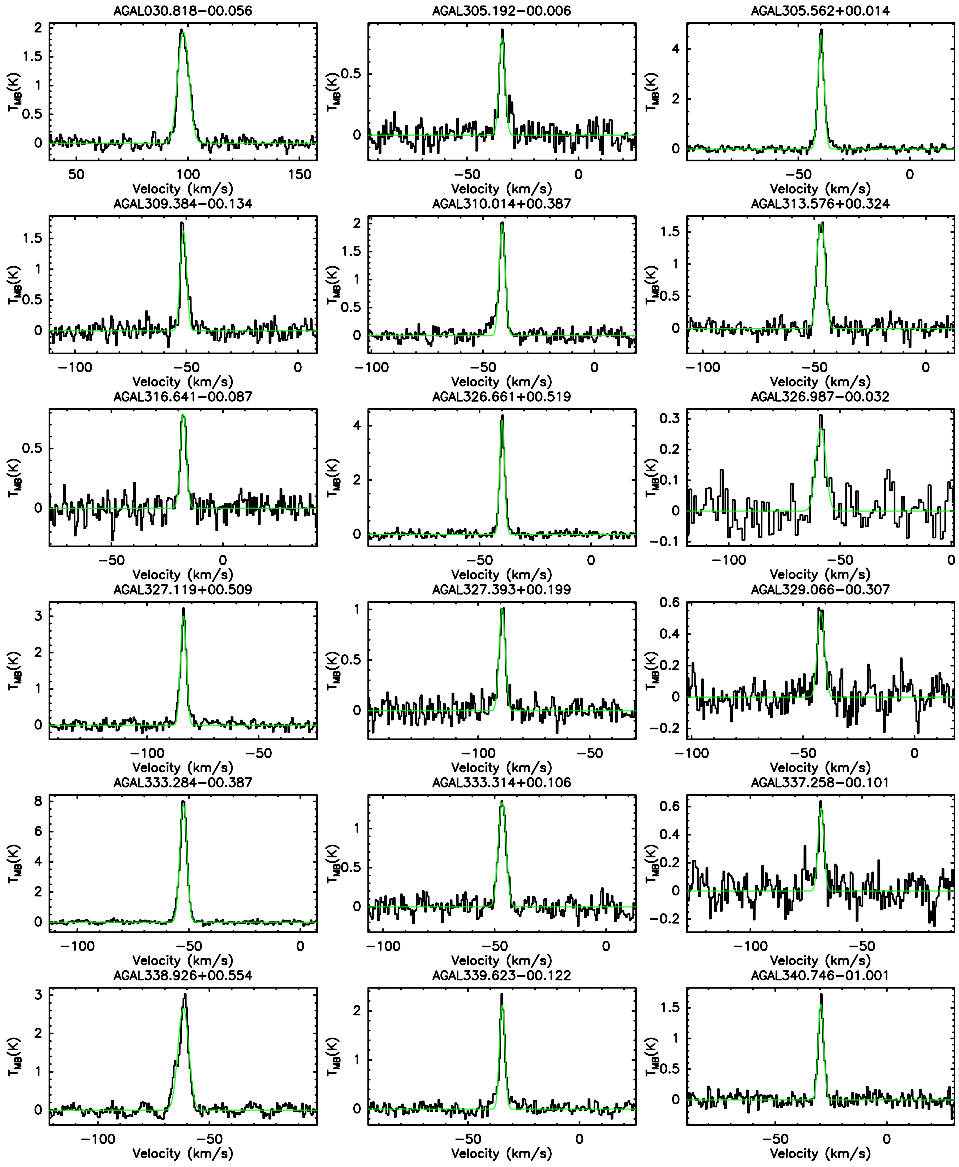

Figure C.5: $C^{17}O(3-2)$ for sub-sample S3. The fit is shown in green.

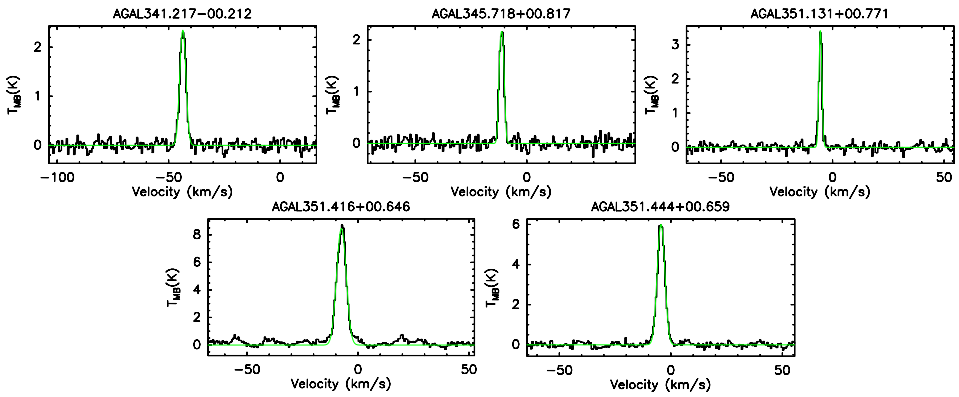

Figure C.5: Continued.

Acknowledgements

I would like to thank Dr. Jan Brand for the hours spent discussing both astrophysical and non-astrophysical topics. His patience in reading the papers and this work *n* times was epic, as were his comments, written in special ideograms referred to as "brandian", in which I am now expert. A curious fact about "brandian" is that the ideograms *must* be no larger than 2 mm $\times$ 2 mm in size.

I am in debt to Dr. Fabrizio Massi for the useful discussions about IR data, and for the help about this work. His witty emails will remain in history.

I would like to thank all the other people involved in this work, with a special mention to Riccardo Cesaroni, Francesco Fontani and Álvaro Sánchez-Monge for their important hints and comments.

I want to express my gratitude to Prof. Loretta Gregorini for the support and the wise advice given me during my work.

There are no words to thank my parents and my grandparents for everything they did since I was born, and for teaching me life. Furthermore, their interest in my formation and study has always been very important to me. They will always be a guide. I want to thank my brother, who is my example of determination, and to remind him to "resistere, resistere, resistere" for these three years. I am proud of him. I also want to thank those that cared about me over the years: a special thank you to Michou, who was such a good listener, to Maya, who regularly drives me mad, and to Tambo for the time spent together.

I obviously would like to mention my closest friends for the indescribable fun during these years. In particular (in alphabetic order) Stefano Baroni, Giacomo Falorni, Matteo Parri, Lorenzo Piscitelli and all the other not mentioned by name: I will always remember our sessions and "scozzoni", they were and are one of the best way to spend an afternoon or an evening "rolling on the floor laughing" (vai Armandowwwwwwwwwww!). Moreover, how can I forget to mention the parties in Casentino? They were terrific.

Last, but not least, I thank Barbara for being always by my side whenever I need it,

for her love and patience enduring the weekends and evenings of work. She is my strength and all that I will ever need. I will always love her.